

**DEVELOPMENT AND CHARACTERISATION OF A FIBRE-OPTIC  
ACOUSTIC EMISSION SENSOR**

by

**JONATHAN MARK BURNS**

A thesis submitted to the  
University of Birmingham  
for the degree of  
DOCTOR OF PHILOSOPHY



**UNIVERSITY OF  
BIRMINGHAM**

School of Metallurgy and Materials  
College of Engineering & Physical Sciences  
University of Birmingham  
September 2011

UNIVERSITY OF  
BIRMINGHAM

**University of Birmingham Research Archive**

**e-theses repository**

This unpublished thesis/dissertation is copyright of the author and/or third parties. The intellectual property rights of the author or third parties in respect of this work are as defined by The Copyright Designs and Patents Act 1988 or as modified by any successor legislation.

Any use made of information contained in this thesis/dissertation must be in accordance with that legislation and must be properly acknowledged. Further distribution or reproduction in any format is prohibited without the permission of the copyright holder.

## **Abstract**

A requirement for online monitoring has emerged owing to the susceptibility of fibre reinforced composite materials to sub-surface damage. Acoustic emission (AE) monitoring is understood to detect damage well before catastrophic failure; research in AE sensing therefore continues to attract significant attention.

The research presented herein provides a review of a fibre-optic-based AE sensor design. Developmental work was performed to evaluate both sensor fabrication and packaging-related issues. The characteristics of the sensor were found to be influenced by: (i) the type of optical fibre used for fabrication; and (ii) preparation of optical fibres prior to sensor fabrication. The use of a small-diameter packaging substrate revealed improvements in sensor performance. The fibre-optic AE sensor was successfully embedded in a uni-directional composite laminate that was fabricated using autoclave processing. The embedded fibre-optic sensor was found to provide higher sensitivity to simulated AE compared with a surface-mounted sensor.

Sensor characterisation trials were performed using simulated AE; a low directional sensitivity was observed. Modal analysis revealed a preferential sensitivity to the  $A_0$  wave-mode; this sensor design may therefore be suited to the detection of delamination in FRCs. Finally, the sensor was shown to successfully detect interlaminar crack propagation under Mode-I loading.

*To my family, both present and future.*

## **Acknowledgements**

I would first like to give thanks to the School of Metallurgy and Materials for providing me with the EPSRC funding that enabled me to complete this research. I would like to thank Professor Gerard Fernando for providing me with the opportunity to undertake this research and for his help and guidance throughout.

I would like to acknowledge Dr Rongsheng Chen and Dr Stephen Kukureka for their help and support at different stages of the project work.

I would like to acknowledge the financial support given by National Physical Laboratory and Doosan Babcock. The technical support offered by Mr Mike Gower (NPL) and Mr Graham Bryce (DB) was greatly appreciated.

The training and assistance in materials fabrication and testing from Mr Frank Biddlestone, Mr Mark Paget and Mr Mick Cunningham is gratefully acknowledged. I would also like to thank Mr Tim Bradshaw, Dr Surya Pandita, Dr Liwei Wang, Dr Venkata Machavaram and Dr Ramani Mahendran for their expert knowledge and useful discussions.

I am thankful to Nicholas Shotton-Gale and Phillip Reynolds for their encouragement and moral support throughout my research.

I would like to thank my family for their continued support, love and direction when I needed them the most. I also owe gratitude to my late father for his support and guidance when I doubted myself so many times. To you, I am truly indebted.

Finally, the greatest acknowledgement is to my future wife Mellissa, who has been patient and understanding every step of the way.

## Table of Contents

List of Figures -----	vii
List of Tables -----	xiii
Glossary -----	xv
<b>1 INTRODUCTION -----</b>	<b>2</b>
1.1 Introduction -----	2
1.2 Aims and Objectives of the Research -----	5
1.3 Structure of the Thesis -----	7
1.4 Research Publications -----	9
<b>2 LITERATURE REVIEW -----</b>	<b>12</b>
2.1 Fibre Reinforced Composite Materials -----	12
2.2 Structural Health Monitoring -----	20
2.3 Acoustic Emission (AE) -----	30
2.4 Fibre-Optic Acoustic Emission Sensors -----	44
2.5 Conclusions of the Literature Review -----	71
<b>3 EXPERIMENTAL -----</b>	<b>75</b>
3.1 Materials and Equipment -----	75
3.2 Acoustic Emission Sensors -----	77
3.3 Sensor Manufacture: Repeatability and Optimisation -----	84
3.4 Evaluation and Characterisation of the Fibre-Optic Acoustic Emission Sensor -----	100
3.5 Mechanical Testing: Interlaminar Crack Propagation -----	106
<b>4 EVALUATION OF THE SENSOR MANUFACTURING PROCESS -----</b>	<b>113</b>
4.1 Evaluation of the Sensor Fabrication Procedures -----	113
4.2 Evaluation of the Sensor Packaging Procedures -----	132
<b>5 OPTIMISATION OF THE SENSOR PACKAGING PROCEDURES -----</b>	<b>139</b>
5.1 Evaluation of the Circular U-channel Packaging Substrate -----	139
5.2 Embedment of the Fibre-Optic Acoustic Emission Sensor -----	147

<b>6</b>	<b>CHARACTERISATION OF THE FIBRE-OPTIC ACOUSTIC EMISSION SENSOR USING SIMULATED AE</b>	<b>155</b>
6.1	Evaluation of the Repeatability of the Hsu-Nielsen (HN) Source	155
6.2	Modal Analysis	166
6.3	Directional Sensitivity	175
<b>7</b>	<b>MONITORING OF INTERLAMINAR CRACK PROPAGATION USING ACOUSTIC EMISSION</b>	<b>218</b>
7.1	Interlaminar Fracture Toughness of Uni-directional Composite Materials	218
7.2	Monitoring of Interlaminar Crack Propagation using Acoustic Emission	223
<b>8</b>	<b>CONCLUSIONS AND SUGGESTIONS FOR FUTURE WORK</b>	<b>237</b>
8.1	Conclusions	237
8.2	Suggestions for Future Work	242
<b>9</b>	<b>REFERENCES</b>	<b>246</b>
	<b>APPENDICES</b>	<b>264</b>
	Appendix-A: Theory of the Fibre-Optic AE Sensor	264
	Appendix-B: Autoclave Processing	280

## List of Figures

Figure 1 Schematic illustrations of the common failure modes in fibre reinforced composite materials. ....	15
Figure 2 Schematic illustrations highlighting the three modes of failure in a composite that enable a crack to propagate at an interface. ....	16
Figure 3 Schematic illustration of a selection of AE features/parameters. ....	31
Figure 4 A schematic illustration of the fibre-optic Mach-Zehnder Interferometer. ....	46
Figure 5 A schematic illustration of the fibre-optic Michelson Interferometer. ....	51
Figure 6 A schematic illustration of the Fabry-Perot interferometer. ....	56
Figure 7 A schematic illustration of the Fibre Bragg grating sensor. ....	60
Figure 8 A schematic illustration of a 2x2 fused-tapered fibre-optic acoustic emission sensor; $P_0$ refers to optical input power and $P_1/P_2$ refer to the optical output powers. ....	67
Figure 9 A schematic illustration of the coupler fabrication unit (CFU) used to fabricate the fibre-optic AE sensor (not to scale). ....	78
Figure 10 A photograph of the instrument used to fabricate the fused-tapered fibre-optic AE sensor highlighting the location of the secondary fibre clamp. ....	79
Figure 11 A schematic illustration of the experimental setup used to interrogate the fibre-optic AE sensor. ....	81
Figure 12 A photograph of the WD piezoelectric transducer used in this study. ....	82
Figure 13 Screen-shots from the AEWIn™ software illustrating the acquisition setup values for: (a) AE channel setup; (b) waveform timing setup for metal specimens; and (c) composite specimens. ....	83
Figure 14 A screen-shot from the AEWIn™ software illustrating the AE parameters of interest. ....	83
Figure 15 Schematic illustrations of: (a) a typical sensor twist involving a pair of partially stripped optical fibres; and (b) measurement criteria for assessing overlapping twist repeatability (see Table 5 for details). ....	86
Figure 16 Schematic illustrations of: (a) a typical fibre-optic AE sensor; and (b) measurement criteria used for assessing the taper repeatability (see Table 6 for details). ....	88
Figure 17 Schematic illustrations of: (a) a square U-channel sensor packaging substrate; and (b) a circular U-channel packaging substrate. ....	89
Figure 18 A schematic illustration of the coupler fabrication unit used to fabricate the fibre-optic AE sensor. The magnetic clamping block and translation stage are highlighted (not to scale). ....	92
Figure 19 A schematic illustration of the close-up view of the magnetic clamping block (not to scale). ....	93
Figure 20 A schematic illustration of the close-up view of the support translation stage (not to scale). ....	94

Figure 21 Schematic illustrations highlighting the dimensions of: (a) the conventional capillary package; and (b) the precision micro-bore square capillary used to package the embeddable fibre-optic AE sensor. ....	95
Figure 22 A schematic illustration highlighting the a close-up view of the overhanging capillary and the translation stage capillary-carrier region (not to scale).....	96
Figure 23 A schematic illustration highlighting the locations of the embedded fibre-optic AE sensors in the composite specimen.....	97
Figure 24 Photographs of: (a) the fibre-optic flange assembly; and (b) location of the fibre-optic flange assembly on the autoclave. ....	98
Figure 25 A schematic illustration of a Hsu-Nielsen source (pencil lead break).....	100
Figure 26 A schematic illustration of the experimental setup used to characterise the directional sensitivity of the fibre-optic acoustic emission sensor.....	102
Figure 27 A schematic illustration of the experimental setup used to characterise the directional sensitivity of the fibre-optic acoustic emission sensor using a cross-ply composite plate (VTM-264). ....	105
Figure 28 A schematic illustration highlighting locations of pencil lead brakes used to confirm the response of the embedded fibre-optic AE sensors. ....	106
Figure 29 A schematic illustration of the 16-ply composite plate with a PTFE insert. Section removed to highlight dimensions of the Mode-I coupon. ....	107
Figure 30 A schematic illustration of the specimen of the 16-ply Mode-I test specimen (not to scale). ....	108
Figure 31 A photograph of the sensor locations on the mode-I coupon.....	109
Figure 32 A schematic illustration of: (a). custom-designed test fixture secured to Instron mechanical test equipment; and (b). loading blocks bonded to Mode-I test specimen. ....	110
Figure 33 SEM micrographs illustrating two stripped SM04-1 optical fibres: (a) coating removed with the Micro Electronics Inc stripping tool; and (b) coating removed with the Clauss stripping tool. ....	114
Figure 34 A scatter plot of the comparison of draw length vs. excess loss for sensor groups-1, 2 and 3. ....	118
Figure 35 A scatter plot of the comparison of draw length vs. coupling ratio for sensor groups-1, 2 and 3. ....	121
Figure 36 A scatter plot illustrating vacuum chuck displacement as a function of time for the left and right hand side chucks; the data sets are overlapped. ....	124
Figure 37 A schematic illustration of: (a) the definitions of the measurement zones that were used to quantify the sample-to-sample variation in a pair of double-twisted fibres; and (b) an optical micrograph of the double-twisted fibre pair.....	126
Figure 38 A schematic illustration of the definitions of the measurement zones that were used to quantify the sample-to-sample variation in post-fabricated fibre-tapers. ....	129

Figure 39 An example of a section of a collage of optical micrographs that have been enlarged and printed in order to obtain the measurement from the zones noted in Figure 38. ....	129
Figure 40 (a) and (b) SEM micrographs of two as received fused-silica square U-channel packages from the same batch; the micrographs illustrate a variation in the U-channel profile. ....	133
Figure 41 A schematic illustration of the cross-section of the square U-channel packaging substrate with the numerical coding system for the measurement zones. ....	134
Figure 42 A selection of column charts illustrating: (a) package width [1]; (b) package height [2]; (c) groove to base height [3]; (d) left upright width [4]; (e) right upright width [5]; (f) groove width [6]; and (g) groove height [7]. See Figure 41 for the coding system for the square U-channel package. ....	135
Figure 43 (a) and (b) Optical micrographs illustrating the positioning of the fibre-optic acoustic emission sensor within the square U-channel packaging substrate. ....	136
Figure 44 A SEM micrograph of the borosilicate circular U-channel packaging substrate. ....	139
Figure 45 A schematic illustration of the cross-section of the circular U-channel packaging substrate with the measurement coding. ....	140
Figure 46 A selection of column chart illustrating: (a) maximum groove width [1]; (b) minimum groove width [2]; (c) left upright width [3]; (d) right upright width [4]; (e) groove depth [5]; and (f) groove to base height [6]. See Figure 45 for the coding system for the circular U-channel package. ....	142
Figure 47 (a) and (b) SEM micrograph illustrating: (a) the square U-channel package where the fibre was bonded to the package with coating as received; and (b) the circular U-channel packaging substrate where the coating has been removed. ....	144
Figure 48 A column chart illustrating a comparison of the ASL values for pre- and post-packaged sensors housed in the square U-channel substrate. ....	146
Figure 49 A column chart illustrating a comparison of the ASL values for pre- and post-packaged sensor housed in the circular U-channel substrate. ....	147
Figure 50 A plot illustrating examples of the pressure and temperature profiles that were recorded during autoclave processing of the VTM-264 prepregs. ....	150
Figure 51 A photograph of uni-directional composite with embedded fibre-optic AE sensors. ....	151
Figure 52 A screen-shot of the AEwin™ software illustrating the time-driven average signal level produced by the fibre-optic sensor during processing. ....	153
Figure 53 A screen-shot of the AE analysis software highlighting: (a) a point-plot of the signal amplitude of each hit; and (b) an example of a typical discrete waveform recorded by the fibre optic sensor. ....	156
Figure 54 A screen-shot of the AEwin™ software highlighting: (a) a point-plot of the signal amplitude of each hit; and (b) an example of a typical discrete waveform recorded by the piezoelectric transducer. ....	156

Figure 55 A schematic illustration of the aluminium plate with the locations of the pencil lead break and fibre-optic sensor, highlighting examples of reflection paths. ....	157
Figure 56 A schematic illustration of the experimental setup used to obtain the differential time-of-arrival of a signal using two fibre-optic sensors. ....	159
Figure 57 Discrete waveform of the pencil lead break highlighting region of interest, i.e. 45 microseconds. ....	161
Figure 58 (a) A typical discrete waveform; and (b) corresponding FFT illustrating the peak frequency of the highlighted region; the signal was generated by a pencil lead break. ....	162
Figure 59 Scanning electron micrographs of a sample of three different pencil-leads which produced: (a) low-frequency; (b) medium-frequency; and (c) high-frequency acoustic signals. ....	164
Figure 60 Group velocity dispersion curve for an aluminium plate with a thickness of 1.6 mm with highlighted area of interest (see red box). ....	167
Figure 61 Expanded portion of a group velocity dispersion curve for an aluminium plate with a thickness of 1.6 mm; the red circle illustrates the approximated intersections of the mean signal velocity with the signal frequency. ....	168
Figure 62 A typical waveform for a signal recorded by the fibre-optic AE sensor in response to a pencil lead break. ....	169
Figure 63 Plot of the group velocity dispersion curve versus the time-frequency representation for a signal recorded by the fibre-optic sensor in response to a pencil lead break. ....	170
Figure 64 A typical waveform for a signal recorded by the wideband piezoelectric transducer in response to a pencil lead break. ....	172
Figure 65 Plot of the theoretical group velocity dispersion curve versus the short-time Fourier transform from the wideband sensor in response to a pencil lead break. ....	172
Figure 66 Typical examples of discrete waveforms captured using: (a) a one MSPS sampling rate; and (b) a ten MSPS sampling rate. ....	174
Figure 67 A radar plot illustrating the mean signal amplitude as a function of source orientation for the WD piezoelectric transducer. ....	177
Figure 68 A radar plot illustrating the mean signal amplitudes for the five fibre-optic sensors as a function of orientation; the sensors were fabricated using SM04-1 optical fibre. ....	179
Figure 69 A radar plot illustrating the mean signal amplitudes for the five fibre-optic sensors as a function of orientation; the sensors were fabricated using SM600 optical fibre. ....	182
Figure 70 A scatter plot illustrating the range of signal amplitudes and ASL values for the different source orientations as a function of taper length for three SM04-1 type fibre-optic sensors; the error bars represent the standard deviation from the mean for each source orientation. ....	186

Figure 71 Radar plot highlighting mean signal amplitude as a function of orientation for three fibre-optic sensors fabricated using SM04-1 optical fibre. ....	187
Figure 72 A scatter plot illustrating the variation in the mean signal amplitude range for repeated removal and remounting trials; the error bars represent the deviation from the mean for each source orientation. ....	189
Figure 73 A radar plot illustrating the mean signal amplitudes as a function of orientation for the four signal couplants. ....	192
Figure 74 An example of a typical waveform recorded by the fibre-optic AE sensor (SM04-010) in response to a pencil lead break for: (a) a sensor mounted to an aluminium plate using ultrasonic gel; and (b) a sensor mounted to an aluminium plate using a cyanoacrylate adhesive. ....	194
Figure 75 A radar plot highlighting the scatter in the data sets for SM04-1-type fibre-optic AE sensors, packaged using the circular and square U-channel substrates; the error bars represent the deviation from the mean for the two sensor groups. ....	198
Figure 76 Group-velocity dispersion curve for the VTM-264 composite specimen; the test specimen had a layup sequence of 0,90 <sub>2</sub> ,0 <sub>s</sub> . ....	201
Figure 77 (a) A typical discrete waveform; and (b) the corresponding FFT recorded by the fibre-optic sensor in response to a pencil lead break on the cross-ply composite specimen. ....	204
Figure 78 A typical discrete waveform recorded by the WD piezoelectric transducer in response to a pencil lead break performed on a 0/90° oriented composite plate. ....	205
Figure 79 A radar plot illustrating the mean signal amplitudes as a function of source orientation on the composite specimen for the fibre-optic and piezoelectric transducer; the error bars represent the deviation from the mean relating to lead break error. ....	206
Figure 80 A schematic illustration of the propagation paths for the wave travelling along 0°, 45° and 90° orientations. ....	207
Figure 81 A radar plot illustrating the mean signal amplitudes recorded by the fibre-optic AE sensor as a function of source orientation for both composite and aluminium test-plates; the error bars represent the deviation from the mean relating to lead break error. ....	208
Figure 82 Typical examples of discrete waveforms illustrating the response of the embedded fibre-optic sensor to pencil lead breaks at: (a) 25 mm; (b) 50 mm; (c) 75 mm from the centreline of the sensor. ....	211
Figure 83 A typical example of a discrete waveform highlighting the response of a surface-mounted fibre-optic AE sensor (SM04-1-type housed in a square U-channel package) to a pencil lead break at 75 mm from the centreline of the sensor. ....	213
Figure 84 An enlarged view of the discrete waveform in Figure 82(c). ....	214
Figure 85 An example of a load versus displacement curve for the 16-ply VTM264 uni-directional carbon fibre composite test coupon; non-linear (NL) and compliance +5% (C <sub>5%</sub> ) are highlighted. ....	219
Figure 86 Combined load versus displacement plots for all five 16-ply VTM-264 uni-directional carbon-fibre epoxy composite test coupons. ....	220

Figure 87 Photograph of fibre bridging from a post-tested sample.....	221
Figure 88 Resistance curve (R-curve) illustrating the $G_{IC}$ versus delamination length for the 16-ply VTM-264 uni-directional carbon-fibre epoxy composite test coupons. ....	222
Figure 89 Screen-shot from the AEwin™ software highlighting AE activity (hits) recorded during the DCB test (coupon 2) for: (a) the piezoelectric transducer; and (b) the fibre-optic sensor. ....	224
Figure 90 Screen-shot from the AEwin™ software highlighting signal amplitude versus time recorded during the DCB test (coupon 2) for: (a) the piezoelectric transducer; and (b) the fibre-optic sensor.....	226
Figure 91 Screen-shot from the AEwin™ software illustrating a log-sum amplitude distribution plot recorded during the DCB test (coupon 2) for: (a) the piezoelectric transducer; and (b) the fibre-optic sensor. ....	227
Figure 92 (a) and (b) SEM micrographs of the VTM-264 DCB coupon 2 specimen showing: (i) fibre and fibre bundle fracture; (ii) fibre-matrix debonding; and (iii) river markings. ....	229
Figure 93 Screen-shot from the AEwin™ software highlighting hit driven absolute energy versus time plot recorded during the DCB test (coupon 2) for: (a) the piezoelectric transducer; and (b) the fibre-optic sensor.....	231
Figure 94 A screen-shot from the AEwin™ software highlighting centroid frequency as a function of signal amplitude and test time for sample two. Data acquired by the fibre-optic sensor. ....	232
Figure 95 A typical discrete waveform and wavelet transform for a low amplitude signal recorded by the fibre-optic sensor during sample 2 mode-I test. ....	233
Figure 96 A typical discrete waveform and wavelet transform for a high amplitude signal recorded by the fibre-optic sensor during sample 2 mode-I test.....	234
Figure 97 A schematic illustration of a weakly-fused coupler cross-section.....	268
Figure 98 A schematic illustration of the simplified waist region of a fused-tapered coupler. ....	271
Figure 99 A schematic illustration of transverse beam vibration.....	274
Figure 100 A photograph of the autoclave that was used for processing the laminated prepregs. ....	280
Figure 101 Schematic illustrations of the vacuum plate that was used for assisting with the alignment and stacking of the prepreg lay-up: (a) trimetric view; and (b) rear view.....	283
Figure 102 A schematic representation of the vacuum bagging assembly (not to scale).....	284

## List of Tables

Table 1 A summary of selected conventional fibre reinforcements used in composite materials (Hull and Clyne, 1996). .....	13
Table 2 A summary of selected conventional matrices used in composite materials (Hull and Clyne, 1996). .....	13
Table 3 A literature survey comparison summarising the frequency range of different failure mechanisms; the units presented in the table are in kHz. ....	44
Table 4 Technical specifications of optical fibres used for fabrication of the fibre-optic AE sensor.....	75
Table 5 Details of the measurement criteria used for assessing the overlapping twist repeatability. ....	87
Table 6 Details of the measurement criteria used for assessing the dimensions of the 2x2 fused taper region with regards to the repeatability of the fabrication process. ....	88
Table 7 A summary of the fabrication characteristics for the 60 fibre-optic sensors from groups 1, 2 and 3; standard deviation in parentheses. ....	117
Table 8 A summary of the F-test statistical analysis obtained from evaluation of the SM04-1 fibre tests. ....	122
Table 9 A summary of the specified dimensions for the twisted region of five pairs of stripped optical fibres (see Figure 37 for measurement coding used – values in $\mu\text{m}$ ) (standard deviation in parentheses). ....	125
Table 10 A summary of the specified dimensions for the post-fabrication fibre taper repeatability (see Figure 38 for measurement coding used – values in $\mu\text{m}$ ) (standard deviation in parentheses) .....	128
Table 11 A summary of the fabrication characteristics for sensor groups-2 and 4. Group-2 refers to the square U-channel packaged sensors from section 4.1.2. Group-4 refers to the circular U-channel packaged sensors; standard deviation in parentheses. ....	144
Table 12 A summary of the fabrication characteristics of the seven sensors that were produced for embedment in composite materials (standard deviation in parenthesis).....	149
Table 13 A comparison of the mean fabrication characteristics for sensor groups-2, 4 and 5 (standard deviation in parenthesis). ....	149
Table 14 A summary of the sensor characteristics before and after processing.....	152
Table 15 Time of arrival calculations using two multiplexed fibre-optic sensors on a 1.6 mm thick aluminium plate; standard deviation in parentheses.....	160
Table 16 Physical and acoustic properties of the 30 pencil lead breaks; standard deviation in parenthesis. ....	163
Table 17 A summary of the directional sensitivities for the five SM04-1-type fibre-optic sensors; standard deviation in parentheses. ....	180
Table 18 A summary of the directional sensitivities for the five SM600-type fibre-optic sensors; standard deviation in parentheses. ....	183

Table 19 A summary of the signal-to-noise ratios for the square U-channel packaged SM04-1 and SM600-type fibre-optic sensors; standard deviation in parentheses. ....	184
Table 20 Summary table for sensor fabrication properties, average signal level, maximum signal amplitude and corresponding signal-to-noise ratios for five SM04-1 type sensors packaged using the square U-channel substrates. ....	185
Table 21 A summary of the mean signal amplitude values recorded using sensor SM04-010 as a function of orientation for the four coupling conditions; standard deviation in parentheses. ....	191
Table 22 A summary of the mean ASL, maximum signal amplitude and corresponding signal-to-noise ratios for the four coupling conditions; the sensors were packaged using the square U-channel substrates. ....	195
Table 23 A summary of the signal amplitudes recorded for the five circular packaged fibre-optic AE sensor during the directional sensitivity trials; standard deviations is shown in parentheses. ....	197
Table 24 A summary of the ASL, maximum amplitude and corresponding signal-to-noise ratios for the circular and square U-channel packaged fibre-optic AE sensors; the sensors were fabricated using SM04-1 optical fibre. ....	199
Table 25 A summary of the material properties used to define the group velocity dispersion curve. ....	201
Table 26 A summary of the time of arrival calculations using two surface-mounted fibre-optic sensors on a cross-ply composite plate; the measurements were obtained along the 90° axis relative to the longitudinal orientation of the sensor. ....	203
Table 27 A table of typical values for the directional sensitivities of the fibre-optic sensor; the typical values represent the response of the sensor under the different test conditions. Standard deviation is shown in parentheses. ....	216
Table 28 $G_{IC}$ values for the five 16-ply VTM-264 test coupons. Values obtained using corrected beam theory. ....	223
Table 29 A summary of the amplitude distributions for the five DCB mode-I tests; FOS refers to the fibre-optic sensor and PZT refers to the piezoelectric transducer. ....	230
Table 30 Details of the programmed processing schedule for the VTM264 prepregs. ....	281
Table 31 Descriptions of the components used for processing the prepregs in the autoclave. ....	285

## Glossary

<b>Absolute Energy:</b>	Absolute energy, measured in attojoules (aJ), is defined as the true energy of the AE hit. Absolute energy is obtained from the integral of the squared voltage signal divided by the reference resistance, i.e. 10 kilohm, over the duration of the AE waveform.
<b>Acoustic Emission (AE):</b>	Elastic waves generated by the rapid release of energy from sources within a material.
<b>Acoustic Impedance:</b>	A measurement of the resistance of a material to the transmission of sound waves. This material property is the product of the material density and sound velocity. Acoustic impedance of a material determines how much sound will be transmitted and reflected when the wave encounters a boundary with another material.
<b>AE Amplitude:</b>	The largest voltage peak in the AE signal waveform; customarily expressed in decibels to 1 microvolt at the preamplifier input (dB <sub>AE</sub> ).
<b>AE Channel:</b>	A single sensor and the related instrumentation for transmitting, conditioning, detecting and measuring a signal.
<b>AE Event Energy:</b>	The total elastic energy released by an acoustic emission event.
<b>AE Hit:</b>	The detection and measurement of an AE signal on a channel.
<b>AE Sensor:</b>	A device containing a transducer that turns physical wave motion into an electrical voltage.
<b>AE Source:</b>	The physical origin of one or more AE event(s).
<b>Attenuation:</b>	Loss of amplitude with distance as the AE signal propagates through the test structure.
<b>Average Signal Level:</b>	This is a measure of the varying and averaged amplitude of the AE signal. ASL differs from the RMS in that it is a measurement of dBAE and not voltage.
<b>Counts:</b>	The number of times an AE signal crosses the detection threshold. Also known as “ring-down counts” and “threshold crossing counts”.
<b>Centroid Frequency:</b>	The centre of mass of the power spectrum graph.
<b>C-Scan:</b>	A 2-dimensional data representation that is applied to UT techniques to yield a plane view of the specimen. Each C-scan image represents information at a pre-selected depth. Specific characteristics such as attenuation, thickness or the presence of reflectors are displayed.
<b>Coupling Ratio:</b>	The percentage of the optical power transferred to a second output port of a 2x2 coupler. This value is relative to the summation of the power of the two output ports.
<b>Detection:</b>	Recognition of the presence of a signal (typically accomplished by the signal crossing a detection threshold).
<b>Draw-length:</b>	A measurement used to define the length of draw used to achieve a 50% coupling ratio for the fibre-optic coupler; this value is measured by the coupler fabrication unit.

<b>Duration:</b>	The time from an AE signal's first threshold crossing to its last.
<b>Energy:</b>	Measured area under the rectified signal envelope (MARSE). This is derived from the integral of the rectified voltage signal over the duration of the hit.
<b>Excess-loss:</b>	The optical loss relative to the input optical radiation that does not emerge from the nominal operation ports of the device.
<b>H-N Source:</b>	Also known as Hsu-Nielsen or lead break; the industry standard calibration method, which involves fracturing a 0.5mm diameter, 3mm long, 2h propelling pencil-lead at 30 <sup>0</sup> orientation.
<b>Hit-definition time:</b>	The HDT is a time constant used to terminate the measurement of a signal.
<b>Hit-lockout time:</b>	The HLT is a time constant used to create "dead-time" after the end of a hit.
<b>Noise:</b>	Irrelevant indicators; signals produced by causes other than AE, or by AE sources that are not relevant to the purpose of the test.
<b>Peak-definition time:</b>	The PDT provides control over which peaks in the signal are used to define rise time and amplitude.
<b>Peak frequency:</b>	This is the point at which the maximum frequency magnitude occurs in the power spectrum or FFT plot.
<b>Rise time:</b>	The time from an AE signal's first threshold crossing to its peak.
<b>Signal Characterisation:</b>	Quantification of AE signal features from a certain type of damage mechanism or noise source.
<b>Signal Description:</b>	The result of the hit process: a digital (numerical) description of an AE signal.
<b>Signal Features:</b>	Measurable characteristics of the AE signal, such as amplitude, AE energy, duration, counts, risetime, that can be stored as a part of the AE hit description.
<b>Source Location:</b>	Relating to the use of multiple AE sensors for determining the relative positions of acoustic emission sources in 1, 2 or 3 dimensions.
<b>Threshold:</b>	Records the threshold of the AE setup. This value is only needed when using a floating threshold so that variations in the threshold can be quantified.
<b>Time-of-Flight:</b>	The time required for an ultrasonic signal to travel from the transmitter to the receiver via diffraction at a discontinuity edge or along the surface of the test object.
<b>Wavelet:</b>	Time-frequency representation of the time domain signal.

# CHAPTER 1

## Introduction

# 1 Introduction

---

## 1.1 Introduction

In recent decades, an increased utilisation of fibre reinforced composite (FRC) materials as structural components in engineering applications has been seen (Cantwell and Morton, 1981). This rise is primarily due to their low density, which provides materials with high specific-strength and stiffness. However, composite materials are susceptible to localised impact damage (Soutis and Curtis, 1996); this is often sub-surface and difficult to detect using visual inspection alone. This type of localised damage is often referred to as barely-visible impact damage (BVID). The nature of the ensuing damage is often complex due to the anisotropy of composite materials; this can result in a combination of matrix cracking, debonding, splitting, fibre fracture and delamination. Impact damage is understood to adversely affect the load bearing capacity of a composite (Soutis and Curtis, 1996; Cantwell and Morton, 1985). Therefore, there is significant merit in developing non-destructive evaluation techniques that can impart information on the integrity of composite materials over their lifetime.

Non-destructive evaluation (NDE) of composite materials using acoustic emission (AE) is a well established and well documented technique (Valentin et al., 1983; Short and Summerscale, 1984; Bertholet and Rhazi, 1990; Barre and Benzeggagh, 1994; Farrow, 1994; Benmedakhene et al., 1999; Johnson and Gudmundson, 2000; Bohse, 2000; Finlayson et al., 2001; Rotem, 2003; Waller et al., 2010). Electrical-based transducers are commonly used for

the detection of AE in engineering materials; piezoelectric transducers demonstrate high sensitivity to AE. The high sensitivity is a result of the piezoelectric crystal generating multiple resonances within the typical frequency range of interest (Doyle et al., 2002a). However, there are a number of disadvantages that preclude their use for *in-situ* damage detection in fibre reinforced composites. Examples of these limitations include: (i) the relatively large dimensions of piezoelectric transducers, e.g. 5-30 mm range, means that it is difficult and/or impractical for embedment within composite materials; (ii) the piezoelectric transducers are sensitive to electromagnetic interference; and (iii) conventional piezoelectric transducers and systems cannot be installed in hazardous environments, e.g. where there is a risk of explosion, or in environments that are corrosive. In contrast, optical fibre-based sensors do not suffer from these limitations (Fernando et al., 2003; Zheng et al., 1992; Paternotte, 1993; De Oliveria et al., 2008; Zhao et al., 2008) and are therefore ideal for remote and real-time structural integrity monitoring. Fibre-optic sensors (FOS) offer the following advantages.

- (a) Relatively small dimensions and uniform cross-section makes them capable of being surface-mounted or embedded into fibre reinforced composite materials.
- (b) Embedded fibre-optic sensors do not significantly compromise the static flexural (Lee et al., 2002) or tensile properties (Guemes et al., 2001) of the host materials.
- (c) Unlike electrical-based sensors, they are immune to electromagnetic interference (Bock et al., 1992).
- (d) They can be used to infer strain, temperature, pressure, humidity, vibration, specified chemicals, and acoustic emission (Fernando et al., 1997; Liu et al., 1998; Fernando and Degamber, 2006). In some cases, multiple properties may be accessed.

- (e) They are capable of remote data telemetry and on-line data acquisition (Fuhr et al., 1994; Fuhr et al., 1995).
- (f) Fibre-optic sensors can be multiplexed. Multiplexing refers to a technique whereby a number of similar or different sensors can be attached along a single optical fibre. With certain sensor designs, distributed sensing can also be achieved along the length of a fibre.
- (g) Fibre-optic sensors are intrinsically safe and can therefore be deployed in high risk environments, e.g. offshore oil and gas platforms for structural monitoring (Sun et al., 2007).
- (h) The cost of optical fibre is relatively low and the overall sensor system costs can be modest if: (i) the sensors are fabricated in-house; (ii) low-cost, off-the-shelf interrogation units are used; and (iii) telecommunications fibres are used.

A number of established fibre-optic configurations have been demonstrated for the detection of acoustic emissions (Giallorenzi et al., 1982; Zheng et al., 1992; Paternotte et al., 1993; Yo and Sirkis, 1994; Pierce et al., 1996; Tsuda et al., 1998; Liu et al., 1999; Tsuda et al., 1999; Tsuda et al., 2001; Perez et al., 2001; Doyle et al., 2002a; Betz et al., 2006). In addition, the development of novel fibre-optic systems for AE monitoring has received much attention; the fused-tapered fibre-optic coupler (Doyle et al., 2002a; Doyle et al., 2002b; Chen et al., 2003; Chen et al., 2004; Chen et al., 2008) presented herein provides an example of such developmental research.

## 1.2 Aims and Objectives of the Research

The aims and objectives of this research project were as follows:

- (a) To evaluate and optimise the manufacturing technique used for production of the fused-tapered coupler fibre-optic acoustic emission sensor.

The following aspects were investigated with a view to evaluating, characterising and optimising the sensor fabrication process: (i) the method of preparing the optical fibre prior to sensor fabrication; (ii) the repeatability of the fibre-optic coupling properties of the sensor, i.e. those parameters recorded by the coupler fabrication unit computer system during sensor manufacture; (iii) statistical analysis of the repeatability of the fabrication procedures with reference to the fibre-optic coupling properties; (iv) the reliability of the motion control processes, i.e. the reliability in the movement accuracy/consistency of the traversing platform on the coupler fabrication unit; and (v) the repeatability of the sensor geometry using image analysis.

- (b) To evaluate and optimise the packaging strategies for the fibre-optic acoustic emission sensor.

The substrates used to package the surface-mounted fibre-optic sensor were evaluated using image analysis to establish the repeatability in the design of the package. The parameters of interest were: (i) the dimensions and fabrication tolerances of two packaging substrates; and (ii) the surface-profiles of the two substrates.

A new method of packaging sensors destined for embedded applications was also evaluated. This involved the development of a retrofitted attachment, to increase control of the traversing of the capillary substrate along the fused-tapered region of the AE sensor. The substrates used to package the embedded sensors were also evaluated in order to improve the success of the packaging process. An investigation on the integrity of embedded fibre-optic AE sensors during composite fabrication was carried out. The laminated prepregs were autoclave processed.

(c) To evaluate the response of the fibre-optic sensor to simulated acoustic emissions.

Acoustic emissions were generated using the established Hsu-Nielson (HN) source, i.e. the fracture of a 0.5 mm 2H pencil lead on the surface of the material; the response of the sensor was characterised using this method of signal generation. Firstly, the repeatability of the HN source was evaluated to confirm the suitability of this technique for signal generation. Secondly, modal analysis was performed to examine the modal response of the AE sensor to the pencil lead breaks. Thirdly, the performance of the sensor was evaluated with reference to the following: (i) the performance of a piezoelectric transducer; (ii) the type of optical fibre and the physical properties of the fibre-optic sensor; (iii) the repeatability of surface-mounting of the sensor on the host material; (iv) the type of coupling media used to mount the sensor; (v) the type of packaging substrate used to house the sensor; and (vi) the properties of the test specimen on which the sensor was mounted. In addition, the response of embedded fibre-optic sensors were characterised using simulated AE.

(d) To study damage initiation and propagation in fibre reinforced composites using the fibre-optic acoustic emission.

The response of the AE sensor during mechanical testing of composite specimens was investigated. Mode-I double cantilever beam (DCB) tests were performed in order to demonstrate the feasibility of using the fibre-optic acoustic emission sensor for monitoring damage development in composite materials.

### **1.3 Structure of the Thesis**

#### **Chapter One: *Introduction***

The first chapter provides an overview of the research.

#### **Chapter Two: *Literature Review***

This chapter presents a review of the current research field relating to structural health monitoring of fibre reinforced composite materials. The review is presented in three sections, namely, an introduction to: (i) damage in fibre reinforced composite materials; (ii) conventional structural health monitoring techniques; and (iii) fibre-optic sensor technology.

#### **Chapter Three: *Experimental Procedures***

This chapter provides a description of the experimental procedures adopted for the research presented in Chapters four, five, six and seven.

**Chapter Four:** *Evaluation of the Sensor Manufacturing Process*

This chapter discusses the work carried out to characterise the manufacturing repeatability of the fibre-optic sensor; the results presented evaluate: (i) sensor fabrication consistency; (ii) a statistical analysis of sensor fabrication consistency; (iii) sensor packaging substrates; and (iv) sensor packaging procedures.

**Chapter Five:** *Optimisation of the Sensor Packaging Procedures*

This chapter discusses the works carried out to optimise the sensor packaging procedures used for surface-mounted and embedded sensors. A preliminary study on the embedment of the capillary-sealed fibre-optic AE sensor is also discussed.

**Chapter Six:** *Characterisation of the Fibre-Optic Acoustic Emission Sensor to Simulated AE*

This chapter provides an evaluation of the response of the fibre-optic sensor to simulated acoustic emissions using the Hsu-Nielson (HN) source. The results presented describe an evaluation of: (i) the reliability of the HN source for AE signal generation; and (ii) modal analysis of signals recorded by the sensor in response to the HN source. The chapter provides an evaluation of the directional sensitivity of the fibre-optic sensor using both isotropic and anisotropic materials. In addition, a preliminary review of the sensitivity of an embedded fibre-optic AE sensor is presented.

**Chapter Seven:** *Monitoring of Mode-I Crack Propagation using Acoustic Emission*

This chapter presents the results obtained from Mode-I DCB tests using uni-directional composite materials; the performance of the fibre-optic sensor is discussed.

## **Chapter Eight: Conclusions and Suggestions for Future Work**

Chapter eight summarises the conclusions of the research presented in Chapters four, five, six and seven. Suggestions for future work are proposed.

### **1.4 Research Publications**

The findings from the current research were presented at the following conferences:

1. Burns, J., Chen, R., Gower, M., Bryce, G., Fernando, G.F. (2009). “A fibre-optic sensor for acoustic emission detection in advanced fibre reinforced composite materials”. **In 15th International Conference for Composite Structures. Porto, 15-17 June 2009.**
2. Burns, J. (2009). A fibre-optic acoustic emission sensor for damage detection in fibre reinforced composite materials. *UK submission: SAMPE European Student Seminar 2009; Paris, France.*
3. Burns, J., Chen, R., Machavaram, V.R., Gower, M., Bryce, G., Fernando, G.F. (2008). “A Novel Fibre-optic Sensor for Simultaneous Detection of Acoustic Emission, Strain and Temperature”. **In ICCE-16 Composites/Nano Engineering. Kunming, 20-26 July 2008.**

The following publications were generated in collaboration with research colleagues during the course of the project:

4. Chen, R., Theobald, R., Gower, M., Malik, S., Burns, J., Fernandes, E., Bryce, G., Fernando, G.F. (2008). “A Novel Fibre-optic Acoustic Emission Sensor”. **Proceedings of SPIE, Vol. 6932; 693237.**

5. Chen, R., Bradshaw, T., Burns, J., Cole, P., Jarman, P., Pedder, D., Theobald, R., Fernando, G.F. (2006) Linear Location of Acoustic Emission using a Pair of Novel Fibre-optic Sensors. **Measurement Science and Technology**, 17: 2313-2318.
6. Chen, R., Burns, J.M., Bradshaw, T., Cole, P., Jarman, P., Theobald, R., Pedder, D., Fernando, G.F. (2006) Acoustic Emission Detection Using a Novel Fibre-optic Sensor. **Advanced Materials Research**, Vol 13-14: 99-104.

The following journal submissions are currently in preparation:

7. Burns, J.M., Bradshaw, T., Gower, M., Bryce, G., Fernando, G.F. Modal analysis and signal characterisation of the response of a fibre-optic sensor using simulated acoustic emissions. To be submitted to: **NDT&E International**.
8. Burns, J.M., Chen, R., Gower, M., Fernando, G.F. Monitoring Mode-I crack propagation in composite materials using a fibre-optic acoustic emission sensor. To be submitted to: **Journal of Composite Materials**.

# CHAPTER 2

## Literature Review

## 2 Literature Review

---

### 2.1 Fibre Reinforced Composite Materials

A fibre reinforced composite (FRC) is a material that typically consists of two constituent components held together by an interfacial layer (Drzal, 1990). The constituents of a composite include a strong and stiff fibrous reinforcement embedded within a continuous phase referred to as the matrix. The primary function of the reinforcing fibres is to provide strength and stiffness for the composite. The role of the matrix is to secure the fibres in position and to distribute and transfer the applied load to the fibres. In order to clearly define the properties of a composite material, the following must be specified (Bertholet, 1998): (i) the nature of the constituents and their properties; (ii) the geometry and distribution of the reinforcement; and (iii) the nature of the reinforcement-matrix interface. The properties of the material can therefore be modified by adjusting the nature, proportion and orientations of each component. The principle advantage of composite materials compared with metallic materials is their high specific-strength and stiffness (Cantwell and Morton, 1991); this results from the low densities of the individual constituents of the composite. The physical properties of selected constituents are presented in Table 1 and Table 2.

**Table 1 A summary of selected conventional fibre reinforcements used in composite materials (Hull and Clyne, 1996).**

<b>Material</b>	<b>Density (Mg/m<sup>3</sup>)</b>	<b>Young's Modulus (GPa)</b>	<b>Tensile Strength (MPa)</b>	<b>Failure Strain (%)</b>	<b>Fibre Diameter (µm)</b>	<b>Specific Modulus (GPa/Mg/m<sup>3</sup>)</b>	<b>Specific Strength (MPa/Mg/m<sup>3</sup>)</b>
E-glass	2.56	76	2000	2.6	10-16	29.69	781.25
Carbon (High Strength)	1.75	Axial 380 Radial 20	3400	1.1	7	217.14	1942.86
Carbon (High Modulus)	1.95	Axial 380 Radial 12	2400	0.6	10	194.87	1230.77
Kevlar™ 49	1.45	Axial 130 Radial 10	3000	2.13	12	89.66	2068.97

**Table 2 A summary of selected conventional matrices used in composite materials (Hull and Clyne, 1996).**

<b>Material</b>	<b>Density (Mg/m<sup>3</sup>)</b>	<b>Young's Modulus (GPa)</b>	<b>Tensile Strength (MPa)</b>	<b>Failure Strain (%)</b>	<b>Specific Modulus (GPa/Mg/m<sup>3</sup>)</b>	<b>Specific Strength (MPa/Mg/m<sup>3</sup>)</b>
Epoxy (Thermoset)	1.1 - 1.4	3 - 6	35 - 100	1 - 6	2.14 - 5.45	25 - 90.91
Polyesters (Thermoset)	1.2 - 1.5	2 - 4.5	40 - 90	2	1.33 - 3.75	26.67 - 75
PEEK (Thermoplastic)	1.26 - 1.32	3.6	170	50	2.73 - 2.86	128.79 - 134.92
Polypropylene (Thermoplastic)	0.9	1.0 - 1.4	200 - 400	50	1.11 - 1.56	222.22 - 444.44

Composite materials are however susceptible to damage owing to the relatively brittle properties of the fibre, matrix and the interface (Henneke, 1987; Hull and Clyne, 1996; Davies and Zhang, 1995; Konur and Matthews, 1989; Marshall et al., 1985). Their susceptibility to damage, particularly from low-velocity impacts, is further influenced by the lack of through-thickness reinforcement (Preuss and Clarke, 1988). The occurrence of damage in fibre reinforced composite materials is complicated due to the multifarious failure mechanisms. These failure mechanisms can either be fibre, matrix and interface dominated, or a combination of all three. For reference purposes, Figure 1 provides schematic illustrations of the typical failure modes in composite materials. Such mechanisms typically occur below the surface and can result in degradation in the strength and stiffness of the material (Kim and Sham, 2000).

Davies and Zhang (1995) proposed that owing to the brittle failure nature, composites are susceptible to impact damage resulting in a mixture of internal delaminations, lamina matrix cracks and fibre fracture (see Figure 1). Under increasing load, fibre fracture and further delamination was possible. Konur and Matthews (1989) noted that a brittle interface increased the fracture toughness of composites resulting in an increased likelihood of crack propagation both between and around the fibre reinforcement. Marshall et al., (1985) suggested that pre-failure damage in composite materials with high strength brittle reinforcements initiated from regularly spaced cracks in the matrix. In order to avoid complete failure at an early stage of applied stress under tension, it was assumed that the material was designed such that the fibre had a higher strain-to-failure than the matrix. Sela and Ishal (1989) noted that the limiting factor for the use of composite materials was the tendency for delamination or interlaminar separation; this could eventually lead to

degradation in the load-bearing properties of the material (Soutis and Curtis, 1996; Cantwell and Morton, 1985; Gu and Chattopadhyay, 1999). Delaminations can originate as a result of non-optimum cure during processing, inclusion of foreign bodies during processing as well as impact damage (Sela and Ishal, 1989).

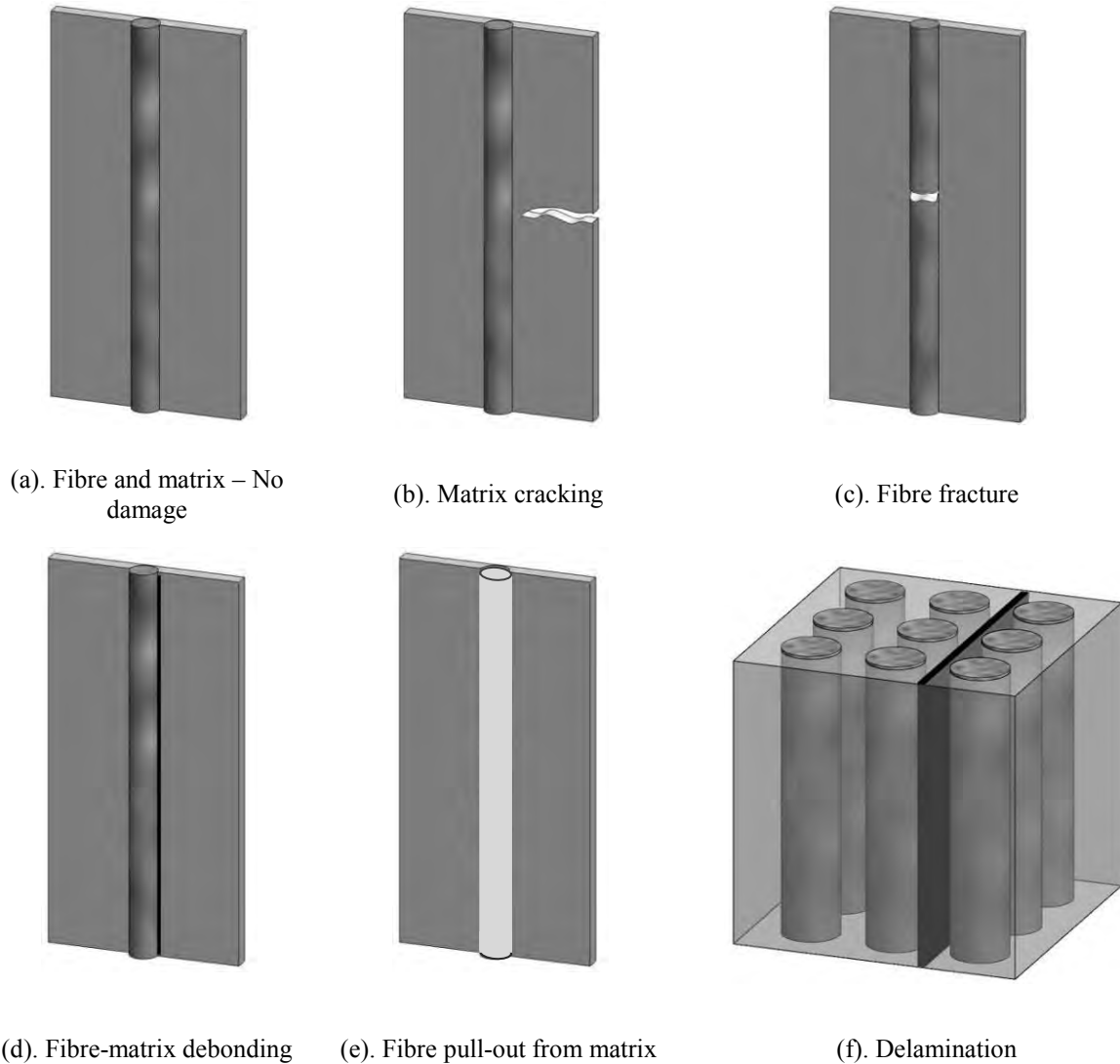


**Figure 1 Schematic illustrations of the common failure modes in fibre reinforced composite materials.**

Discrete sources of impact damage, for example, a dropped tool on a composite wing-section can be difficult to quantify through visual inspection alone; low-velocity impact damage can

induce a potential source of mechanical weakness within a structure (Chiang et al., 2008). Barely visible impact damage (BVID) is a commonly used term to define subsurface damage which is difficult to visually identify, yet is larger than the threshold level needed to induce damage (Bates et al., 2000). It is generally accepted that delamination is the most likely failure mechanism to result from BVID (Foote et al., 2004); this is predominantly driven by mode-II shear and matrix cracking resulting from transverse shear (Kim and Sham, 2000). Mode-I crack propagation is also said to occur during delamination (Miravete and Jimenez, 2004). Figure 2 illustrates the three modes of failure in a composite that enable a crack to propagate at an interface.

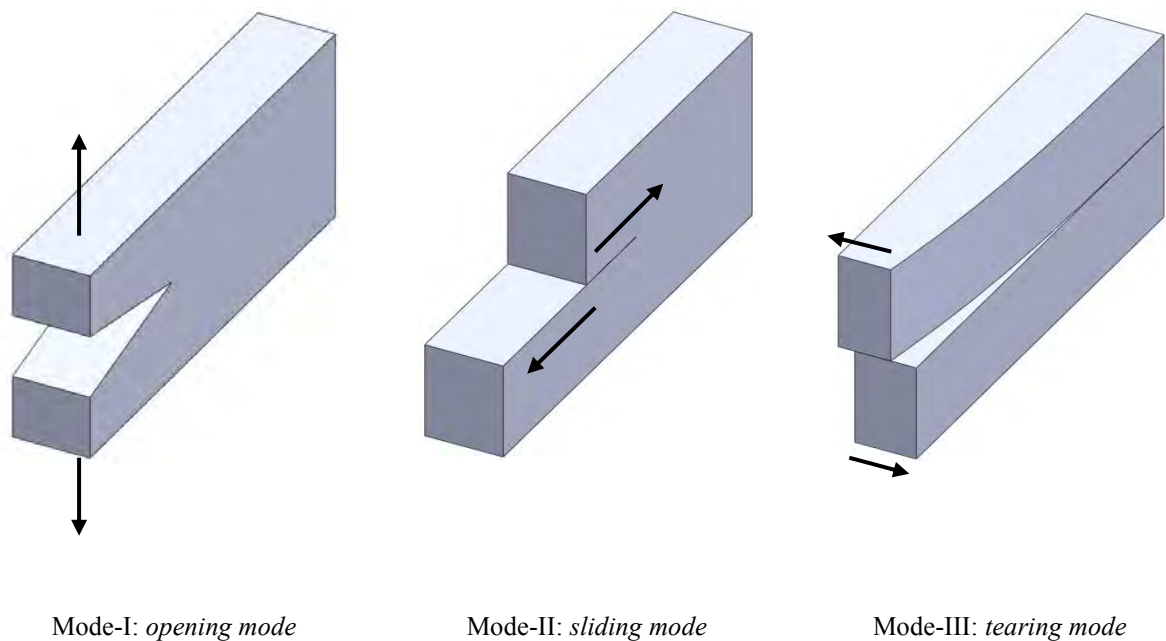


**Figure 2 Schematic illustrations highlighting the three modes of failure in a composite that enable a crack to propagate at an interface.**

Delaminations can initiate from the growth of transverse ply cracks under fatigue loading (Donaldson, 1987) or through applied compressive loading (Sela and Ishal, 1989); the latter results in local buckling, generating internal transverse tensile and shear stresses. The susceptibility of the composite to growth of delaminations is typically determined by the properties of the matrix (Gower, 2008). The resistance to delamination is defined by the interlaminar fracture toughness of the material (Donaldson, 1987); the simplest method of improving the interlaminar crack resistance is to toughen the matrix; this can be achieved through addition of rubbers, thermoplastics and hard inclusions, such as silica, to the epoxy matrix (Davies et al., 1998). Delamination can also occur as a result of matrix micro-cracking in the through-thickness direction within individual layers (Brewer and Lagace, 1988). Multi-axial stress states can develop from the effects of constraining the movement of the crack tip within a single layer; as such, high through-thickness tensile stresses can develop at the crack tip which can lead to delamination (Nairn and Hu, 1992). In order to achieve successful design solutions using composite materials, knowledge of how the material will respond when subjected to through-thickness tensile stresses is required.

A fracture mechanics approach can be considered when evaluating the interlaminar properties, particularly the Mode-I properties of composite materials. The fracture mechanics approach proposes an energy criterion that relates: (i) the extension of the crack face area; (ii) the work of the applied load; and (iii) the internal strain energy, to a material toughness parameter. The criterion is expressed in Equation (1).

$$\frac{d}{dA}(W - U) = G_C \quad \text{Eq. 1}$$

where  $A$  represents crack face area,  $W$  is the work of the applied loads,  $U$  is the strain energy and  $G_C$  is the material fracture toughness. The parameter  $d/dA(W-U)$  is referred to as the applied strain energy release rate and is typically assigned the symbol  $G$ . The fracture toughness is defined as the energy that is required to generate a unit increase in the crack surface area (Gower, 2008). This fracture mechanics approach is useful for determining the fracture toughness and strain energy release rates for the different modes of crack propagation.

A popular method of measuring the interlaminar fracture toughness of a material is based on the double cantilever beam (DCB) specimen method (BS ISO, 2001). A schematic illustration of this specimen configuration is shown in Figure 30. In this test, the specimen is loaded at an opening load  $F$ . The sample displacement  $\delta$  obtained directly from the cross-head displacement, and the crack length  $a$  are measured continuously. It is these parameters that are used to calculate the strain energy release rate (Al-Khodairi, 1996). An artificial starter-crack is typically generated in the composite during lamination of the prepregs; this is generally achieved by inserting a thin film at the composite mid-layer (Davies et al., 1989). The starter-crack simulates an existing delamination in the material (BS ISO, 2001).

In order to relate the parameters obtained from the DCB specimen test, i.e.  $F$ ,  $\delta$  and  $a$  above, to the fracture toughness of the material, a data reduction method is required; the compliance method is a commonly reported technique (Brunner et al., 2006; De Charentenay et al., 1984; Ashcroft et al., 2001; Davies et al., 1992). A relationship between the compliance and the crack length can be obtained using the Irwin-Kies relationship (Al-Khodairi, 1996). This is defined as:

$$G_{IC} = \frac{F^2}{2b} \cdot \frac{dC}{da} \quad \text{Eq. 2}$$

where  $F$  is the load required for crack initiation,  $b$  is the specimen width, or more appropriately, the length of the crack front (Bonesteel et al., 1978),  $C$  is the compliance and  $a$  is the crack length (Davies and Benzeggagh, 1989). The compliance is described as the inverse of stiffness and can be obtained from Equation (3).

$$C = \frac{\delta}{F} \quad \text{Eq. 3}$$

The compliance method can be divided into two discrete analysis methods, namely: (i) simple beam theory; and (ii) corrected beam theory (Al-Khodairi, 1996). The former, utilises classical beam theory to define the  $G_{IC}$  value from the DCB specimen. Equation (4) is used to relate the experimental parameters obtained from the test:

$$G_{IC} = \frac{3F\delta}{2ba} \quad \text{Eq. 4}$$

where  $F$  is the load,  $\delta$  is the sample displacement,  $b$  is the sample width and  $a$  is the length of the crack. The corrected beam theory was developed from the simple beam theory method; this method corrects for local and shear deformations that occur around the crack tip (Redder et al., 2002). This is achieved by assuming that the beam contains a longer crack length ( $a+\Delta$ ). The value of  $\Delta$  is obtained by plotting the cube root of compliance as a function of crack length. The corrected value for  $G_{IC}$  is therefore expressed as:

$$G_{IC} = \frac{3P\delta}{2b(a+\Delta)} \quad \text{Eq. 5}$$

In critical applications where reinforced composite materials are combined with a secondary bonded material, i.e. steel pipeline repairs, interfacial delamination between the dissimilar materials is of major concern. The properties of the bond-line are influenced by a number of factors, for example: (i) surface preparation of the pipeline; (ii) contamination of the surface; and (iii) insufficient wetting-out of the fibre reinforcement. Moreover, as the wet-layup repairs are typically cured using ambient temperature with no vacuum or pressure applied, high matrix voiding is likely, further reducing the performance of the material (Poole et al., 1994). However, due to difficulties using visual inspection in identifying damage in composite materials, it is beneficial to employ techniques that will provide reliable information on the integrity of the structure (Steiner et al., 1995).

## 2.2 Structural Health Monitoring

A structural health monitoring (SHM) system should be capable of detecting and interpreting variations in a material or structure (Kessler, 2002a). As such, the utilisation of SHM systems in engineering applications can be justified with respect to both safety as well as return-on-investment (Barthelds et al., 2004). A fundamental challenge in the development of a SHM system is the ability to determine which material property variations to investigate and how to interpret the recorded data (Kessler, 2002a).

The assessment of material integrity is performed using either destructive or non-destructive evaluation techniques. Destructive analysis is carried out off-line and inspection results in

additional damage to the material. Destructive testing methods, e.g. thermal deply, fractography and edge replication are typically used as a means of assessing the magnitude and mechanism of damage initiation and failure in the composite. These techniques can yield extensive characterisation of the extent of damage in a material (Hull and Shi, 1993). As the focus of the thesis relates to non-destructive evaluation methods, the above-mentioned techniques will not be discussed further. Non-destructive techniques, by nature, are non-invasive. As such, additional damage in the material resulting from the inspection is minimised. Ultrasonic (Compton, 1971; Lloyd, 1989; Teti and Alberti, 1990; Schuster et al., 1993; Kaczmarek and Maison, 1994; Blitz and Simpson, 1995; Hull and Clyne, 1996; Aymerich and Meili, 2000, Kinra et al., 2005), thermography (Ball and Almond, 1998; Wong et al., 1999; Bates et al., 2000; Avdelidis et al., 2003; D’Orazio et al., 2005; Steinberger et al., 2006; Pickering and Almond, 2008) and vibration-based (Cawley and Adams, 1988; Hou and Jeronimidis, 1999; Kessler et al., 2002b; Whittingham et al., 2006) techniques have been well documented as suitable methods for inspection of composite materials.

### 2.2.1 Ultrasonic Inspection

Ultrasonic-based (UT) inspection techniques measure the attenuation of reflected or transmitted waves in a material. A variation in the measured signal amplitude is used to infer the presence of discontinuities in the material. The image that is produced from a C-scan provides a superimposition of the through-laminate thickness damage network (Hull and Shi, 1993). The selection of an appropriate transducer is based on an appreciation that: (i) lower frequency probes provide higher material penetration; and (ii) the minimum detection limit increases with higher frequencies (Compton, 1971); this is due to the inverse relationship

between frequency and wavelength (Mix, 1987). It is understood that a discontinuity must be approximately one half of the wavelength of the propagating wave in order to be detected. Schuster et al. (1993) reported that the corresponding wavelength of the ultrasonic signal should be less than half the thickness of the specimen; this is in order to allow the front and back-wall echoes to be distinguished. Ultrasonic inspection of fibre reinforced composite materials is typically carried out using pulse frequencies between 0.5 and 25 MHz; the inspection of a thin sample necessitates the use of short pulses at frequencies between 10 and 25 MHz (Blitz and Simpson, 1995). Schuster et al. (1993) proposed that for samples greater than 4 mm in thickness, probe frequencies should be kept below 20 MHz due to high sound absorption of the material and short focal lengths.

Conventional normal-incidence inspection has been demonstrated for detection of discontinuities lying perpendicular to the inspection surface (Compton, 1971; Lloyd, 1989; Kaczmarek and Maison, 1994). Compton (1971) demonstrated detection of 0.4 mm holes in 10 mm thick carbon-fibre specimens using conventional 2-dimensional imaging. Lloyd (1989) demonstrated ply-by-ply analysis of 6 mm thick specimens using a 20 MHz probe. A similar procedure was presented by Kaczmarek and Maison (1994) for inspection of 2 mm thick plates. The authors demonstrated a combined procedure of amplitude and time-of-flight analysis of the received signal. Analysis of the time-of-flight of the received signal has been documented as a suitable method for locating the depth of flaws in composite materials (Preuss and Clarke, 1988; Teti and Alberti, 1990; Aymerich and Meili, 2000). Teti and Alberti (1990) obtained a depth detection accuracy of 0.125 mm for inspection of 4 mm thick samples using a 20 MHz probe. The same level of accuracy was demonstrated by Preuss and Clarke (1988); in this case, a 15 MHz probe was used for inspection of 56-ply carbon/epoxy

specimens. The authors observed comparatively larger delaminated areas at ply interfaces where the orientation of the reinforcing fibres was different. The principle limitation with normal-incidence inspection is the effect of masking of discontinuities that are positioned behind delaminations that are close to the surface (Lloyd, 1989; Kaczmarek and Maison, 1994).

Oblique-incidence techniques have been shown to detect flaws that lie parallel to the surface (Aymerich and Meili, 2000; Kinra et al., 2005). Aymerich and Meili (2000) presented a combined approach using both normal and oblique-incidence ultrasonic inspection; the authors demonstrated the detection of transverse matrix cracking resulting from low-velocity impact damage in 2.2 mm thick carbon/PEEK specimens. A 22 MHz probe was used. The normal-incidence method was used to determine the locations of delaminations. Time-of-flight of the returned UT signal rather than the measured reflected amplitude was used to size the cracks. An oblique angle of  $26^\circ$  was found to produce the highest reflected signal amplitudes; the angle was determined by manually adjusting the probe at the locations of the observed cracks until the highest amplitude signal was observed. A resolution of 3 cracks per mm was obtained using this technique. Kinra et al. (2005) observed matrix cracks running parallel with the fibre reinforcement using a  $25^\circ$  oblique angle to the surface of the specimen. Crack lengths of approximately 0.125 mm were located in individual plies of a quasi-isotropic 8-ply carbon/epoxy specimen. Owing to the low sample thickness, a 20 MHz probe was found to be effective, providing high resolution.

### 2.3.2 Thermographic Inspection

The use of transient infrared and lock-in thermography have been well documented for inspection of FRC's (Ball and Almond, 1998; Wong et al., 1999; Bates et al., 2000; Avdelidis et al., 2003; D'Orazio et al., 2005; Steinberger et al., 2006; Pickering and Almond, 2008). Thermography is typically used for inspection of carbon or metallic specimens where a sufficient level of thermal diffusivity can be achieved (D'Orazio et al., 2005). With reference to transient infrared thermography, a thermal pulse is applied to the surface of the material. The thermal diffusivity through the material is monitored as a function of time. In the presence of a material discontinuity, the thermal diffusivity will be reduced. Lock-in thermography uses a frequency modulated heat source, either via high power heat lamps (Pickering and Almond, 2008) or ultrasonic excitation (Bates et al., 2000). The sensitivity to defect depth is a function of the frequency used to excite the sample. Bates et al. (2000) proposed that the lower the modulation frequency, the greater the measurement depth accuracy. Wong et al. (1999) demonstrated the use of a 0.007 Hz modulation frequency for defect depth measurements of 2 mm. Infrared cameras are used to monitor the temperature field in the specimen. The camera is typically mounted at an oblique angle capturing reflections or is positioned either in front of or behind the specimen monitoring in a through-transmission mode at normal-incidence (Bates et al., 2000). The lock-in method utilises the phase lag between the heat source and the specimen to infer the condition of the material and the depth of existing defects (Pickering and Almond, 2008).

Ball and Almond (1998) evaluated the use of transient thermography for characterising low-velocity impact damage in woven composite specimens; 4, 8 and 16-ply specimens were

subjected to impact energies ranging between 3-38 Joules, 7.2-56 Joules and 12-75 Joules respectively. Thermographic images from the front (impacted) and back-faces of the specimens were obtained using a cooled thermographic camera; a temperature resolution of 0.2 °C and a spectral resolution between 2 and 5.6 micrometres was reported. A 500 W lamp was positioned at each side of the specimen; the samples were heated for 3 seconds during each measurement. With reference to the front-face images, the authors reported little correlation with ultrasonic C-scan data when attempting to size the damaged area. In contrast, estimations of the damage area in the back-face images for samples up to 8-ply thick were in close agreement with the ultrasonic inspection. This was attributed to a variation in the thermal diffusivity within the sample; the largest area of delamination was observed near to the back-face and therefore the damage was detected and sized more accurately by the cameras closest to this surface. Low correlation was reported by the authors for comparisons between the thermographic and ultrasonic methods for 16-ply samples. This was again due to a limitation with thermal diffusivity through the sample.

Bates et al. (2000) compared the use of transient and lock-in thermography for characterising low-velocity impact damage. Woven carbon/epoxy specimens with thicknesses between 1 and 5 mm were impacted at different energies ranging between 1-38 Joules. A 500 W halogen lamp, positioned at 0.2 metres from the specimen, was used to irradiate the samples; single-sided inspection was also chosen to replicate a realistic inspection of an in-service structure. The IR camera was positioned at a distance of 1.8 m and an angle of 30° to the specimen's surface. With reference to the lock-in method, modulation frequencies of 0.5, 1, 1.5 and 2 Hz were used. For the transient method, a heating period of 4 seconds was used to allow sufficient sample irradiation. A similar accuracy of detection from both techniques was

observed; both were suited to detection of BVID in thin samples where the damage was located in the first few layers just below the surface of the specimen. The lock-in technique gave greater image definition for sub-surface BVID compared with the transient method. For thin samples, i.e. 2 mm, a low modulation frequency of 0.5 Hz produced optimal image definition of the damage; a heating period of 4 seconds was applied. The authors noted that the lowest modulation frequency enabled greater depth measurement; a reduction in the modulation frequency did however increase the time required to obtain a measurement.

Avdelidis et al. (2003) reported on the use of transient thermography for the detection of a simulated delamination in a carbon fibre composite specimen. A medium-wave, i.e. 3-5  $\mu\text{m}$ , pulsed thermographic heat source was used to irradiate the specimen containing a PTFE insert; the insert was centrally embedded within a 6-ply specimen. In that study, two heat sources were positioned at oblique angles to the specimen surface and the IR camera was positioned at normal incidence for measuring the reflected signal. The simulated delamination was identified using the single-sided interrogation technique. The authors noted the following: (i) a short pulse time, i.e.  $< 1$  second, was required to define the dimensions of the defect accurately; and (ii) a longer pulse, i.e.  $> 3$  seconds, provided greater resolution and image contrast between the un-damaged and damaged regions.

Steinberger et al. (2006) presented an in-situ method of measuring the dissipation of heat from a composite specimen subjected to fatigue loading. Composite specimens were irradiated using pulsed thermography during the fatigue tests; the authors investigated the correlation between heat conductivity of the sample and the number of fatigue cycles that had been applied. Damage mechanisms such as matrix cracking, fibre fracture and ply delamination

were understood to result in an increase in the mechanical damping of the specimen. The damping effect resulted in the absorption of mechanical work producing a hysteretic heating effect. The dissipation of heat from the sample was shown to correlate with damage in the specimen. Fatigue tests were performed on samples that were loaded up to 75% of the ultimate tensile stress. An increase in the temperature of the sample of 14.5 °C was observed up to sample failure.

### 2.3.3 Vibration Monitoring

Vibration-based techniques have also been well documented in the literature (Cawley and Adams, 1988; Hou and Jeronimidis, 1999; Kessler et al., 2002b; Whittingham et al., 2006). When the specimen is excited, either by a piezoelectric actuator (Whittingham et al., 2006), loud-speaker (Hou and Jeronimidis, 1999) or an alternative “tapping” mechanism (Cawley and Adams, 1988), a signal is produced at the frequencies of the major structural vibration modes. The variation in the properties of the detected signal, e.g. frequency, can be correlated with a reference signal to infer the presence and severity of damage. The structural stiffness of the specimen is influenced by the presence of a defect; this results in a localised change in the impedance of the material (Cawley and Adams, 1988). Vibration-based techniques often utilise a variation in the resonant frequency of a recorded signal compared to a reference signal to infer the presence of discontinuities in composite materials (Hou and Jeronimidis, 1999; Kessler et al., 2002b; Whittingham et al., 2006).

Hou and Jeronimidis (1999) demonstrated a technique for correlating changes in the natural frequency of thin composite plates as a function of impact damage severity. 10-ply glass fibre

composite specimens were subjected to varying levels of impact damage with impact energies up to 45 Joules; the resonant frequencies of the samples were recorded at different levels of incremental damage and were correlated with signals from an un-damaged state. A reduction in the measured resonant frequency of approximately 12 Hz was observed, which correlated with the early onset of damage in the sample. The area of delamination corresponding to this frequency reduction was 4%. This was attributed to transverse matrix cracking and minor delaminations at the point of impact. Beyond this minimum, an increase in the resonant frequency of the sample was observed for higher impact damage energy levels, i.e. > 6% area of delamination. The authors attributed this to the separation of the plies within the composite which resulted in overall geometrical stiffening due to an increase in sample thickness.

Kessler et al. (2002b) presented a modal analysis technique for evaluating the effect of different damage modes on the natural frequencies and mode shapes. 8-ply quasi-isotropic carbon/epoxy specimens, measuring 250 x 50 x 1 mm<sup>3</sup>, were fixed in a cantilever beam arrangement and were excited using piezoelectric actuators; laser vibrometry was used to record the frequency response data. Damage resulting from fatigue induced matrix cracking, drilled holes and edge delaminations were evaluated. A broad frequency range between 5 and 500 Hz was evaluated; this range covered the first four bending modes (1, 2, 4 and 5) and the first two torsional modes (3 and 6). The authors noted that damage identification became more apparent during evaluation of higher frequencies, i.e. modes 3-6. Furthermore, the different damage states had varying influences on the mode shapes investigated. Artificial edge delaminations were shown to affect the symmetry of the specimen; the high frequency torsion mode shape (6<sup>th</sup> mode) was reduced by 9 Hz in this case. In the case of drilled holes and matrix cracks, the authors, attribute the reduction in the measured frequency response to

the reduction in the elastic properties of the material. The authors do however suggest that the orientation of the damage, e.g. whether parallel or perpendicular to the sensor position, can influence the natural frequency response; for a 50 x 20 mm<sup>2</sup> delamination, preferentially aligned along the length of the specimen, a greater reduction in the bending modes was observed. Delaminations aligned along the width of the specimen were found to have a greater influence on the torsional modes. A limitation with the proposed method was the inability to provide an indication of the location of the damage in the specimen.

Whittingham et al. (2006) also demonstrated the frequency response method for determining the presence of delaminations in simply supported beams. The frequency response from glass fibre composites with and without delaminations was examined. Piezoelectric transducers were used to initiate miniature “taps” into the composite specimens. Detection of the generated transients was carried out using a sensor positioned in close proximity to the actuating sensor. This method was successfully demonstrated for the detection of 50 mm, 100 mm and 150 mm long simulated delaminations in a 600 x 34 x 34 mm beam. A reduction in the natural frequency response from beams with simulated damage was reported; for a 50 mm long delamination, a 4 kHz shift from 6 kHz to 2 kHz was noted. These shifts occurred close to frequencies associated with dominant vibration modes. Moreover, peak broadening was found to occur, which was associated with a reduction in sample stiffness and specimen resonance. The authors highlight that changes in such low frequency regions were however audible.

## **2.3 Acoustic Emission (AE)**

### **2.3.1 Introduction to Acoustic Emission**

Acoustic emission (AE) is well established for online condition monitoring of structural components (Mba and Rao, 2006), for structural assessment during proof-load testing (Bunsell, 1977) and for mechanical characterisation of materials undergoing laboratory-based tests (Marec, 2008). When a composite material sustains damage, high frequency elastic waves are generated through the release of stored energy. The generation of these elastic waves in the material is traditionally referred to as stress wave emission as this does not imply restriction to audible frequencies (Pollock, 1967); the term acoustic emission is however more commonly used to describe this phenomena. The typical frequency range of interest for AE monitoring is between 20 kHz and 1 MHz (Doyle et al., 2002a). AE monitoring is a passive technique that is generally carried out using surface-mounted piezoelectric sensors (Di Scalea et al., 2006). The piezoelectric crystal is typically fabricated from a lead-zirconate-titanate or quartz-based ceramic; both materials have the ability to produce an electrical potential when deformed. This phenomenon is referred to as the piezoelectric effect (Song et al., 2006). The detection sensitivity of the piezoelectric transducer is dependent upon several factors, namely: (i) the properties of the stress wave, e.g. amplitude and frequency; (ii) the location of the sensor relative to the AE source; and (iii) the coupling between the sensor and the material (Colombo et al., 2005).

### 2.3.1.1 Properties of Acoustic Emission Signals

Parameter-based analysis with AE features such as amplitude and frequency can be used to infer the failure behaviour of materials (Shiotani, 2008); these quantitative parameters are derived from the discrete waveform (Green, 1969). Transient signals are captured by the AE sensor if a pre-defined voltage threshold is exceeded. A single discrete waveform is commonly referred to as a *hit*. A simplistic method of AE data analysis was performed by measuring activity using hit-rate data alone (Bachmaier, 2008). Once the signal voltage exceeds the threshold, AE features can be generated. Figure 3 provides a schematic illustration of an example of a discrete waveform. Examples of widely used AE features are illustrated in this figure.

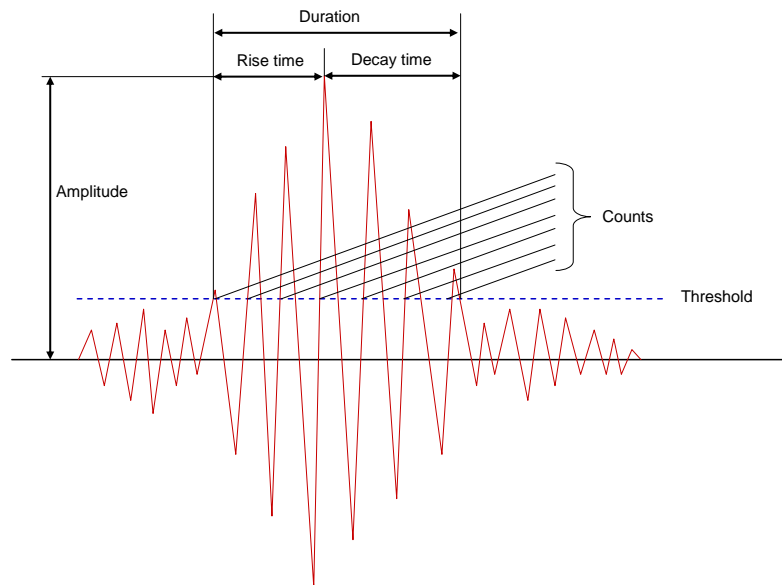


**Figure 3 Schematic illustration of a selection of AE features/parameters.**

More complex analysis can be performed by extracting modal parameters from the discrete waveforms; modal analysis is a method which applies fundamental wave mode theory to discriminate the different wave modes within the signal (Santulli, 2000). The two basic modes refer to the extensional wave (in-plane motion) and the flexural wave (out-of-plane motion). When acoustic emission is generated in a thin plate, transient Lamb waves are generated; these waves produce displacements in both the direction of wave propagation and perpendicularly to the plane of the plate. The two groups of Lamb waves can be described as symmetrical and anti-symmetrical. The following descriptions are used to distinguish the different Lamb wave modes: (i) the symmetrical mode propagates with symmetry about the mid-plane of the plate; and (ii) the anti-symmetrical mode propagates with anti-symmetry about the mid-plane (Viktorov, 1978). The subscripts *S* and *A* are assigned to the symmetrical and anti-symmetrical modes respectively. The use of dispersion curves enables identification of the propagation of Lamb waves in solid media (Kessler et al., 2002b); different Lamb modes travel at different frequencies and velocities in thin plates. The use of Lamb waves for damage identification in fibre reinforced composite materials has been documented in the literature (Maslov and Kundu, 1997; Seale et al., 1998; Badcock and Birt, 2000; Koh et al., 2002).

#### 2.3.1.2 Effect of Bonding Layer Properties on the AE Sensor Response

The effect of the bonding layer properties on the performance of AE sensors has been reviewed in the literature (Pietrzakowski, 2001; Dugmore et al., 2002; Colombo et al., 2005; Hensman et al., 2006; Qing et al., 2006; Han et al., 2008). The role of the couplant is to ensure contact between two surfaces to allow even pressure wave distribution (Physical

Acoustics Corporation, 2007). An optimal coupling layer needs to be as thin as possible with no voiding (ASTM, 2007). Higo and Inaba (1989) proposed that the entrapment of air-bubbles within the coupling layer influenced the frequency content of the recorded signal; additional peaks on the signal frequency spectrum around the resonance peak were observed. Variations in the thickness of the couplant layer are understood to contribute to uncertainties with the received signal (Enoki and Kishi, 2000). The thickness of the couplant layer can however be controlled by using a measured quantity of couplant and applying a known pressure to the sensor; this will ensure even distribution of the couplant at the interface (Dugmore et al., 2002). Han et al. (2008) proposed that since the modulus of the bonding layer was less than that of the sensor and the host material, the local stress distribution between the two would be influenced. The authors evaluated the effect of the bonding layer properties on the strain distribution along a sensor. The following conclusions were drawn from their study: (i) the effect of the shear modulus and thickness of the bonding layer is governed by the stiffness of the bonding layer; (ii) a reduction of 20% of the strain ratio was observed if the bonding layer was 80 micrometers thick compared with a perfectly bonded situation, i.e. close to zero thickness; and (iii) the effect of adhesive viscosity has little influence on the strain distribution. The viscosity of the couplant was also addressed using experimental investigation by Dugmore et al. (2002). A number of common couplant substances, e.g. vacuum grease, glycerin and ultrasonic gel, were evaluated to determine the signal reproducibility in response to an artificial acoustic emission (AAE) source. The authors observed larger signal amplitudes when using couplants with a higher viscosity. However, lower viscosity couplants such as ultrasonic gel provided greater measurement reproducibility in comparison with a vacuum grease. Qing et al. (2006) observed a variation in the amplitude of a recorded signal as a function of the couplant layer thickness; this trend

was however dependent upon the frequency of the signal. An experimental setup consisting of two sensors configured in a pulse-receive arrangement were used to evaluate this effect. Signals were generated at varying frequencies as a function of bonding layer properties. At lower frequencies, i.e.  $\leq 300$  kHz, the amplitude of the signal for an adhesive bond-line of 10 micrometers was approximately three times the magnitude compared with a 40 micrometer bond-line. At 500 kHz, this result was found to reverse. In addition, at lower frequencies, the tensile modulus of the adhesive was shown to have little effect on the sensor performance. At 500 kHz, the adhesive with the lowest modulus, i.e. 723 MPa compared with 2750 and 4940 MPa, gave higher recorded amplitudes. The results presented by Pietrzakowski (2001) further confirm the findings presented by Qing et al. (2006) and Han et al. (2008). The author does however note that an adhesive with a high stiffness can increase the susceptibility to shear stress concentrations at the bonding region.

### 2.3.2 Wave Propagation in Fibre Reinforced Composite Materials

As a result of the anisotropic properties of fibre reinforced composite materials, the onset of damage can result in multiple concurrent failure modes. Analysis of wave propagation in fibre reinforced composite materials is more complex than for isotropic materials. For example, in  $0/90^\circ$  orientated composites, the elastic modulus along the fibre direction is higher. According to Equation (6) (Rose, 2004), the velocity in the axial direction of the reinforcing fibres will therefore be higher.

$$v = \left( \frac{E}{\rho} \right)^{\frac{1}{2}}$$

**Eq. 6**

where  $v$  refers to the acoustic wave velocity,  $E$  is the elastic modulus and  $\rho$  is the density of the material. In the case of a  $0/90^\circ$  cross-ply laminate, the phase and group velocities of the first order symmetrical ( $S_0$ ) mode are direction dependant (Percival and Birt, 1997; Thursby et al., 2008); that is, the velocity along the fibre axis, i.e.  $0^\circ$  and  $90^\circ$ , is greater compared with the  $45^\circ$  orientation. Thursby et al. (2008) proposed that the  $S_0$  wave velocity is approximately 1.4 times faster along the fibre than in the off-axis orientation. This was said to be due to the predominant particle displacement of this wave mode being concentrated along the in-plane direction. Less pronounced directional dependency was observed for the anti-symmetrical ( $A_0$ ) mode (Thursby et al., 2008). The  $A_0$  mode produces out-of-plane wave motion, i.e. through the thickness of the material, and therefore the propagation velocity is less dependent upon the layup orientation of the laminate. Percival and Birt (1997) reported group velocities in a  $0/90_{2s}$  carbon fibre/epoxy specimen for the  $A_0$  mode to be 1.6, 1.6 and 1.5 ( $\pm 0.1$ ) mm/us for the  $0^\circ$ ,  $45^\circ$  and  $90^\circ$  respectively. Thursby et al. (2008) proposed that the energy of the  $S_0$  mode was predominantly concentrated along the  $0/90^\circ$  directions, whilst the  $A_0$  mode was said to be more uniformly distributed through all angles in the plate. These models further confirm the difference in the directional sensitivity between the two modes.

The variation in wave properties as a function of fibre orientation increases the complexity of defect location, particularly if the AE source is generated from a location that is away from the axial orientation of the fibre (Percival and Birt, 1997). Moreover, since the attenuation of the anti-symmetrical wave is higher than that of the symmetrical wave (Percival and Birt,

1997), monitoring of large components may not be practical owing to the need for a large number of sensors. In addition, at low frequencies, the wavelength of the  $A_0$  mode is smaller than the  $S_0$  mode and therefore it is more sensitive to the detection of defects with smaller dimensions (Chen et al., 2010). The signal amplitude of the  $A_0$  mode has also been shown to be higher than the  $S_0$  mode in thin composite plates (Toyama et al., 2001).

### 2.3.3 Damage Identification in Fibre Reinforced Composite Materials using AE

The acoustic emission technique can be used to detect damage long before catastrophic failure (Finlayson et al., 2001). The intensity and/or rate of acoustic emissions are understood to increase proportionally with the level of damage generated in the material (Barre and Benzeggagh, 1994; Waller et al., 2010). It is the change in the slope of AE activity (hit rate) with time that is commonly interpreted as the onset of structural damage. This change in the slope of AE activity can be related to the change in a materials stress-strain curve (Santulli, 2000; Johnson and Gudmundson, 2000). Johnson and Gudmundson (2000) made reference to the correlation of AE activity with the “knee” in associated stress-strain curves that were recorded during mechanical tests; the authors evaluated uni-directional, cross-ply and angle-ply glass fibre composites that were subjected to tensile loading. Samples with different layup sequences were selected in order to generate different failure modes. A signal classification criterion was developed to characterise emitted signals at different stages of loading. The activity and signal classification was correlated with the “knee” in the stress-strain curves plotted for each sample. The acquired signals were grouped into nine classifications based on: (i) waveform features; (ii) the corresponding stress level of the sample at which they occurred; and (iii) emissions from a particular specimen layup sequence.

The amplitude of the signal was not used for failure mechanism classification; the authors proposed that signal amplitudes from the same failure mechanism can produce very different amplitudes, i.e. fracture of single fibre or fibre bundles can provide mis-leading information. Analysis and location of failure mechanisms as a function of depth in the specimen was also demonstrated; the analysis was based on the generation of different wave-modes resulting from non-symmetrical and symmetrical loading when cracks were located in different plies of the specimen. For example, matrix cracking in the central plies of a 0/90<sub>2s</sub> specimen would result in symmetrical loading and therefore generate extensional modes only. In the case where cracking developed in an outer ply, non-symmetrical loading would occur resulting in the generation of flexural and extensional modes. The different modes were interpreted by adding and subtracting waveforms recorded by different sensors mounted at different positions on the sample. In contrast to Johnson and Gudmondson (2000), several studies have presented the use of single parameter analysis for discriminating failure mechanisms in composite materials. Signal amplitude clustering has been proposed as a suitable method for the discrimination of failure mechanisms in composite materials (Valentin et al., 1983; Short and Summerscales, 1984; Bertholet and Rhazi, 1990; Barre and Benzeggagh, 1994; Farrow et al., 1994; Benmedakhene et al., 1999; Bohse, 2000; Rotem, 2003).

Valentin et al. (1983) investigated the use of a *b*-value criterion for classifying failure mechanisms. The “*b*-value” criterion (Pollock, 1981) is defined through correlation of the cumulative event-count as a function of amplitude. The authors proposed that the amplitude distribution of signals generated from uni-directional and cross-ply composites, under load, could yield information on the failure mechanism. Composite specimens were loaded in tension at different orientations between 0 and 90°. With reference to the uni-directional

specimens, a high number of low amplitude signals, i.e.  $> 30000$ , were reported when the samples were loaded in tension; in this case, fibre fracture was understood to be the dominant failure mode. The authors propose that whilst the energy release per unit area during failure of a single fibre was large, the cross-sectional area of the fibre was small and therefore the measured energy was small. As the loading angle was increased beyond  $30^\circ$ , fewer high amplitude emissions were recorded during failure of the specimen; a total of 50 hits were recorded. The dominant failure mechanism associated with a loading orientation of  $30^\circ$  was matrix cracking parallel to the fibres; the high signal amplitudes were attributed to the high interfacial energy released during crack propagation. Analysis of amplitude distributions in cross-ply composites loaded at different orientations was more complex; this was due to the dominance of inter-laminar failure processes and the restraining movement of fibres in the  $0^\circ$  and  $90^\circ$  orientations. The authors proposed that mechanisms other than fibre fracture became dominant in  $0/90^\circ$  oriented composites as the loading direction moved towards  $45^\circ$ ; these mechanisms resulted in the generation of fewer high amplitude emissions that were the result of interlaminar shear stresses at the fibre-matrix interface.

Betholet and Rhazi (1990) reported on the use of AE for monitoring failure in uni-directional specimens that were subjected to flexural loading. It was proposed that the amplitude of the signal could be used to identify the key failure modes during specimen failure. The variation in signal amplitude was related to the energy required to initiate a specific mechanism. The authors indicated that the energy required to initiate transverse matrix cracking was thirty times lower than fibre fracture and as such, the signal amplitude was lower. The energy required to produce longitudinal cracking and delamination were equivalent to transverse cracking and as such, the amplitudes were within the same distribution. It was further

proposed that the observation of higher amplitude signals resulting from longitudinal cracking may not be related to the failure mechanism itself, but instead, to the frictional rubbing of the crack surfaces. Source discrimination based on the length of signals was however more difficult since both high and low energy fracture processes produced very similar durations.

Farrow et al. (1994) evaluated the release of stored energy from different types of fibre reinforcement that were subjected to tensile loading; the release of energy was shown to have a linear correlation with the amplitude of the AE signals. This relationship was defined using the expression presented in Equation (7):

$$U = \frac{P^2 L}{2EA} \quad \text{Eq. 7}$$

where  $U$  is the strain energy,  $P$  is load at failure,  $L$  is the fibre length,  $E$  is Young's modulus and  $A$  is the cross-sectional area. Fibres with greater ultimate tensile strains exhibited higher signal amplitudes when fractured. The authors further noted that the amplitude of signals associated with the fracture of bare fibres was higher compared with when the fibres were embedded within a matrix. A difference of 18 dB<sub>AE</sub> was reported between single fibre fractures and those from micro-composite specimens. The reduced amplitude was attributed to an attenuation effect from the surrounding matrix as well as the degree of elastic fibre relaxation post-fracture; as the fibre was constrained within the matrix, the reduction in the relaxation of the fibre resulted in a short signal duration with a low amplitude. In contrast, Favre et al. (1989) and Bohse (2000a) proposed that the amplitude of fibre fracture was a function of its dimensions and the distribution of fibre strengths throughout a single bundle.

Brittle fibre fracture can occur alone and/or be accompanied by: (i) matrix cracking around the fractured fibre surface; and (ii) fibre/matrix debonding (Bohse, 2000a). Multiple failure modes occurring concurrently can result in an overlapping of signal amplitudes adding complexity to data interpretation.

Barre and Benzeggagh (1994) monitored damage development in short-glass fibre composite specimens using acoustic emission. The specimens were subjected to quasi-static tension, tension-fatigue and crack propagation (crack tension) tests. Owing to the short fibre lengths, it was not anticipated that signals would be associated with fibre fracture. Instead, the research focused on amplitude discrimination of matrix cracking and interfacial debonding between the fibres and the matrix. The stress-strain behaviour of the samples under tensile loading produced a pronounced non-linearity; AE activity was observed at strain level of 0.125 %, confirming that the quality and performance of the samples were poor. In both the tension and tension fatigue tests, a dominance of AE activity was observed in the range of 40-60 dB<sub>AE</sub>. At high stress levels, i.e. > 75% of the ultimate stress, an increase in the number of high amplitude events was observed indicating increased levels of damage. Samples with different fibre-matrix interfacial adhesion strengths were compared. The authors found that specimens with poor interfacial adhesion produced a distinct amplitude peak at 65 dB<sub>AE</sub>. This peak in the amplitude-event response was attributed to the onset of interfacial failure; it was concluded that amplitudes greater than 65 dB<sub>AE</sub> were associated with fibre pull-out due to high energy release resulting from the fibre slipping/rubbing against the matrix. The proposed failure mechanisms were confirmed using scanning electron microscopy.

Benmedakhene et al. (1999) evaluated crack growth in double-cantilever beam (DCB) and single-cantilever beam (SCB) specimens; the growth of delaminations in woven glass-fibre samples subjected to different crack opening velocities were characterised using acoustic emission. DCB samples were loaded at velocities of 2, 100 and 500 millimetres per minute. The SCB samples were used to evaluate high-velocity crack propagation; in this case, the samples were loaded at 3 and 6 ms<sup>-1</sup>. The authors proposed that by varying the loading velocity, different failure mechanisms were initiated during crack growth. With reference to the DCB specimens, the crack principally travelled through the resin with indications of fibre/matrix interfacial failure at regions where the crack front met with the woven fibre bundle; fibre bridging was also observed at the 2 mm/min loading rate. Dominant signal amplitudes in the range of 40-60 dB<sub>AE</sub> were observed during slow crack opening; these signals were attributed to matrix crack propagation. In addition isolated peaks at 65 dB<sub>AE</sub> in the amplitude-event plots were also noted. These signals were attributed to interfacial cracking prior to final failure. For high crack opening velocities, the dominant failure mechanisms were decohesion in the inter-ply interface and the fibre-matrix interface. At high crack opening velocities, the dominant amplitude range was between 60-70 dB<sub>AE</sub>. These signals were attributed to the release of high energy resulting from interfacial failure. Microscopic analysis supported the proposed failure mechanisms inferred by the AE data.

Due to the variability with interpreting and relating time-domain waveform properties to failure mechanisms in composite materials, alternative analysis methods have been proposed that evaluate the frequency content of acquired signals (de Groot et al., 1995; Bohse, 2000a; Ni and Iwamoto, 2002; Ramirez-Jimenez et al., 2004). The frequency content of a discrete time-domain signal is conventionally presented using a fast Fourier transform (FFT)

(Bergland, 1969). The FFT provides a plot of the magnitude of energy versus frequency for a given signal. The time-domain signal is assumed to be composed of a summation of sinusoids of multiple frequencies; the FFT provides a summation of the amplitude of each individual sinusoid as a function of frequency. The fast Fourier transforms can be used to provide real-time frequency determination of acoustic signals relating to specific failure mechanisms in materials (Surgeon and Wevers, 1999).

Analysis of the frequency content for AE signals emitted during various mechanical tests was reported by de Groot et al. (1995). Loading methodologies were chosen in order to isolate modes of failure within each test. The authors reported unambiguous separation of failure mechanisms within the following frequency bandwidths: (i) pure resin samples loaded in tension emitted signals in the range of 50-180 kHz associated with matrix cracking only; (ii) fibre pull-out produced signals in the range of 180-240 kHz; (iii) double-cantilever beam tests emitted signals in the range of 240-310 kHz which were associated with debonding; and (iv) uncured prepreg samples loaded in tension emitted signals above 300 kHz.

Bohse (2000a) also investigated the use of frequency discrimination of AE signals. The author proposed that each failure mechanism had varying visco-elastic relaxation processes, with each one having its own intrinsic frequency. This relationship is defined in Equation (8) (Bohse, 2000a):

$$f_i \sim \frac{1}{\tau_i} \sim c_i \sim \sqrt{\frac{E_i}{\rho_i}} \quad \text{Eq. 8}$$

where the intrinsic frequency  $f_i$  and the elastic acoustic velocity  $c_i$  of the elastic relaxation process for the fibre and matrix are related to the relaxation time  $\tau_i$ , modulus  $E_i$  and density  $\rho_i$ . As such, matrix cracking produces signals in the lower bandwidth limit (100-350 kHz), whereas fibre fracture signals were found at higher frequencies (350-700 kHz).

Ni and Iwamoto (2002) observed that the detected frequency of a signal was independent of the propagation distance; unlike signal amplitude, analysis of signal frequencies was not influenced by variations in the source-to-receiver distance. Ni and Iwamoto (2002) presented a method using frequency discrimination of failure mechanisms in single fibre carbon composite (SFC) specimens; the single carbon fibre was embedded in an epoxy matrix. Visual identification of damage mechanisms was permitted owing to the transparency of the sample. The SFC's were subjected to a specific load, unloaded, inspected for damage, and then reloaded. This process was repeated for four different loads. The FFT's were calculated for each time domain signal acquired. Three failure modes were observed during the mechanical trials, namely matrix cracking, debonding and fibre fracture. The authors concluded that each mechanism could be grouped into a distinct frequency band; the frequency bands used were <100 kHz, 200-300 kHz and 400-450 kHz respectively.

The work by Ramirez-Jimenez et al. (2004) supports the conclusions proposed by de Groot et al. (1995). The authors demonstrated simple frequency-based analysis to identify micro-failure mechanisms in glass/polypropylene composites. FFT's were calculated from the time-domain signals during tensile tests. The peak frequency was used to determine the dominant frequency of the signal. Samples were prepared such that specific failure modes could be eliminated. The following events were classified into the corresponding frequency bands: (i)

matrix cracking at ~100 kHz; (ii) fibre-slippage and fibre pull-out between 200 and 300 kHz; and (iii) fibre breakage beyond 400 kHz. A comparison of published literature relating to source discrimination using signal frequency content is presented in Table 3.

**Table 3 A literature survey comparison summarising the frequency range of different failure mechanisms; the units presented in the table are in kHz.**

Reference	Material	Matrix Cracking	Debonding	Fibre pull-out	Fibre Fracture	Delamination
de Groot (1995)	Carbon/epoxy	50-180	240-310	180-240	> 300	-
Russell and Henneke (1977)	Carbon/epoxy	50-150	-	-	140-180	-
Suzuki et al. (1988)	Glass/polyester	30-150	180-290	180-290	300-400	30-150
Suzuki et al. (1991)	Glass/PET	80-130	-	250-410	250-410	-
Komai et al. (1991)	Carbon/epoxy	< 300	< 300	300	> 500	-
Suh et al. (1991)	Carbon/epoxy	60-80	60-80	400	1900	-
Bohse (2000a)	Glass/epoxy	100-350	-	-	350-700	-
Ni and Iwamoto (2002)	Carbon-fibre/epoxy	<100	200-300	-	400-450	-
Ramirez-Jimenez et al. (2004)	Glass/PP	100	-	200-300	>400	-
Kim et al. (2005)	Glass/epoxy	≤ 200	≤ 200	-	500	-

## 2.4 Fibre-Optic Acoustic Emission Sensors

Piezoelectric transducers are typically used for AE monitoring in composite materials due to their high sensitivity to signals within the bandwidth of interest. There are however accepted limitations that preclude their use for *in-situ* damage detection in FRC's. In addition to those limitations outlined in Section 1.1, piezoelectric transducers have to be located in close proximity of the interrogation equipment if a preamplifier is not used. They tend not to be used in harsh environments in the presence of corrosive agents or under exposure to high

temperatures, i.e.  $> 150\text{ }^{\circ}\text{C}$ ; corrosive agents and high temperatures can degrade the materials and components that are used to manufacture the sensors. Moreover, regulatory organisations often apply stringent requirements that limit the current of electrical devices in hazardous and explosive risk areas; an example of this can be found in the aircraft regulation code SFAR-88 (Giordano and Zielinski, 2007). These regulations limit the current of devices within aircraft fuel tanks to levels well below that required by electrically wired acoustic emission systems.

In contrast, fibre-optic sensors do not suffer from the drawbacks that limit the use of conventional electrical-based sensors. As such, the use of fibre-optic technologies provides an alternative sensing option; a number of fibre-optic sensor configurations have been developed for the detection of acoustic emissions and ultrasound; the most common configurations in recent decades refer to the Mach-Zehnder interferometer (Zheng et al., 1992; Paternotte et al., 1993; Pierce et al., 1996), Michelson interferometer (Liu et al., 1990; Tsuda et al., 1998; Tsuda et al., 1999; Tsuda et al., 2001), extrinsic Fabry-Perot interferometer (Read et al., 2002; De Oliveria et al., 2008; Zhao et al., 2008) and fibre Bragg grating (Perez et al., 2001; Tsuda et al., 2004; Takeda et al., 2005; Betz et al., 2006) sensor designs. The following provides a review of commonly reported fibre-optic AE sensing configurations. A review of the fused-tapered coupler (Doyle et al., 2002a; Doyle et al., 2002b; Chen et al., 2003; Chen et al., 2004; Chen et al., 2008) fibre-optic sensor is also presented.

#### 2.4.1 Mach-Zehnder Interferometer

The fibre-optic Mach-Zehnder interferometer, illustrated in Figure 4, has two single-mode fibre paths of equal length which are referred to as the reference and sensing arms; generally

the reference arm remains in a stress-free state and as such, is isolated from mechanical vibrations (Paternotte et al., 1993). Two optical couplers are used to configure the sensor; the first coupler serves to divide the light between the sensing and reference arms and the second coupler recombines the beam to generate the interference signal.

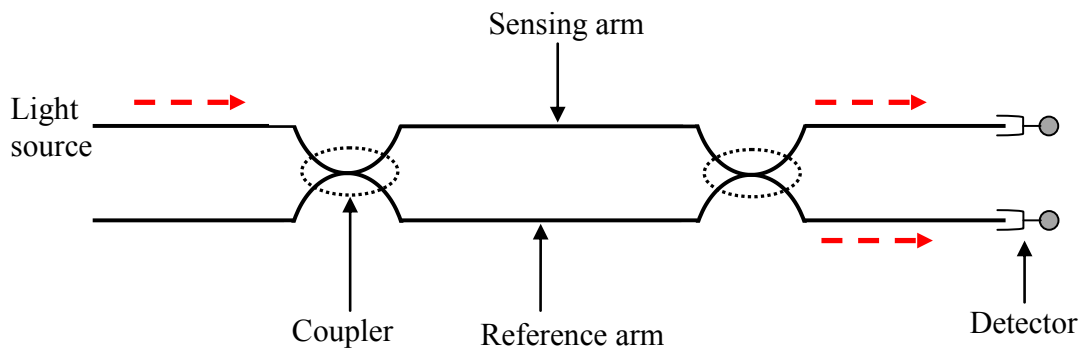


**Figure 4 A schematic illustration of the fibre-optic Mach-Zehnder Interferometer.**

Zheng et al. (1992) proposed that the fibre-optic Mach-Zehnder interferometer should be considered as having two parts, namely: (i) a sensing element that produces a phase shift in the optical radiation carried by the optical fibre in response to a vibration; and (ii) an interferometer in which the phase shift modulates the light so that signal recovery can be achieved using photoelectric detection. The phase shift occurs in both the  $x$  and  $y$  polarisation states within the optical fibre. Interferometric demodulation is performed through a comparison of the difference in phase shift for one of the polarisation states against a reference signal (Zheng et al., 1992).

Zheng et al. (1992) demonstrated the sensitivity of the fibre-optic Mach-Zehnder interferometer to the detection of AE using a HN source. The sensor configuration was as follows: light was launched into one arm of a directional coupler that served to divide the

beam between the sensing and reference fibres. Two polarisation controllers were positioned before and after the sensing element; the two devices served the purpose of: (i) selecting a specific polarisation eigenmode; and (ii) controlling the fringe visibility. Phase modulation in the reference arm of the sensor was achieved by coiling the optical fibre around a piezoelectric (PZT) tube; the PZT tube was also used to remove any environmental phase perturbations, i.e. thermal and low frequency acoustics. This method was referred to as active homodyne demodulation (Yo and Sirkis, 1994). This was achieved by applying a voltage to the PZT tube to maintain phase quadrature. The sensing fibre was held in position on the surface of a steel plate via a weighted steel block. No coupling media was used in this study. An increase in the mass of the block from 10 g to 300 g resulted in a doubling of the signal amplitude. The authors reported that the pencil lead break produced a near-step in the surface displacement of the material thereby producing a broadband spectral response. As a result, the HN source was justified for evaluating the frequency response of sensors. The authors proposed that the interferometer exhibited a resonant response; the signal peaked within a specific frequency range and then rolled off as the frequency of signal changed. Interferometer noise was reported and was attributed to frequency-related noise from the He-Ne laser source.

Paternotte et al. (1993) noted that phase shifts in the light transmitted within the fibre resulted from pressure-induced variations of the refractive index and fibre length. The sensitivity of the device can therefore be optimised by varying the applied pressure and the interaction length. In the study by Paternotte et al. (1993), the interference signal was measured by an optoelectric (OE) converter that was positioned at phase quadrature. The output current from the OE converter was proportional to the detected light intensity and

therefore was directly related to the induced phase shift. The authors demonstrated the use of the Mach-Zehnder interferometer for detection of high frequency radial displacements of a piezoelectric transducer. The sensing arm was bonded to the surface of the transducer; the transducer was then excited at its resonant frequency of 171 kHz resulting in radial displacement of the surface of the probe. A linear relationship between a change in the interferometric signal and radial displacement of the transducer was observed. The output from the interferometer was found to be proportional to the elongation of the sensing fibre arm.

Pierce et al. (1996) proposed the use of the fibre-optic Mach-Zehnder interferometer for detecting simulated AE signals in thin steel plates. An active homodyne demodulation method was also proposed for signal recovery. Signal recovery was as follows: an analogue-compensation was applied to the reference arm of the sensor to enable signal demodulation of the output response of the sensor; in this study, the reference fibre was coiled around a piezoelectric cylinder. In a stable state, the sensor remained in the quadrature condition. In the presence of a mechanical perturbation, both the phase of the sensing and reference signals were found to drift. In the event of this signal fading (Giallorenzi et al., 1982), a voltage was applied to the cylinder to maintain quadrature by introducing bias phase; the voltage applied to the cylinder was proportional to the change in the optical path (Yo and Sirkis, 1994). An advantage of this configuration was that amplitude fluctuations resulting from slow varying measurands, i.e. strain and temperature, are eliminated since they are common mode to both arms of the sensor (Giallorenzi et al., 1982). The homodyne method was used to avoid low-frequency drifting owing to the long lengths of optical fibre used to construct the sensor, i.e. > 3 metres. The simulated AE signals were generated in the thin steel plate using a

piezoelectric pulser operating at 300 kHz. The pulser was positioned within a water column that was attached to the plate; the water column enabled coupling of the AE signals. Two methods were evaluated for mounting the fibre-optic sensor to the test plate. These were: (i) the use of a second water column to couple the signal to the sensor; and (ii) surface-mounting using a quick-drying lacquer, i.e. nail polish. The out-of-plane anti-symmetrical mode was generated in the plate by pulsing at an oblique angle of  $35^\circ$ . With reference to the water-coupled sensor, a maximum peak-to-peak signal amplitude of 212 mV was achieved in response to the generated pulse. The same waveform shape was observed when the sensor was bonded directly to the plate; the amplitude of the signal was however dramatically reduced to less than 50 mV. An acute pulsing angle of  $17^\circ$  was evaluated in an attempt to generate both the symmetrical ( $S_0$ ) and anti-symmetrical ( $A_0$ ) modes into the thin steel plate. Sensitivity to both wave modes was observed from the surface-mounted sensor. In that study, smaller out-of-plane displacements were generated and therefore the amplitude of the signal corresponding to the  $A_0$  mode was reduced to less than 10 mV. A peak-to-peak signal amplitude of  $\sim 5$  mV was achieved with reference to the  $S_0$  mode. The authors noted that the properties of the sensor bonding layer may influence the response of the sensor with regards to the in- and out-of-plane sensitivities; the stress transferred from the plate normal to and parallel to the fibre may not be equal.

Pierce et al. (1996) also reported on the embedment of the Mach-Zehnder sensor in a 3 mm thick composite plate. Simulated signals were generated in the plate from an ultrasonic transducer positioned in a water column. The angle of incidence was chosen to generate the  $S_0$  mode. The authors proposed that the full length of the embedded fibre was sensitive to the simulated wave since the whole plate was insonified by the signal from the transducer. As a

result, the sensitivity of embedded sensor was found to be higher than that of the surface-bonded sensor; an increase in the maximum signal amplitude of approximately 500 mV was observed. Limitations with embedment of the fibre-optic sensor were however reported; variations in the quality of the interfacial bonding between the coated fibre and the resin produced fluctuations in the signal amplitude by more than 1 V along the length of the embedded fibre. This was attributed to an inconsistency in the sensitivity to the stress wave perturbations at distinct regions of the embedded length. In addition, protection of the fibres where the sensor protrudes from the edge of the composite must be considered in order to avoid damage (Friebele et al., 1999). In contrast, an embedded sensor is completely protected from minor surface damage and may be integrated into the structure regardless of the surface properties of the material.

#### 2.4.2 Michelson Interferometer

Detection of acoustic emission has also been demonstrated using the fibre-optic Michelson interferometric sensor design. The Michelson interferometer utilises a single coupler to recombine the optical signals from the reference and sensing arms of the sensor (Machavaram, 2006). The optical signal is reflected back from the mirrored face at the end of each arm. A differential path length between the mirrored ends of the two fibres is used to form the sensing region (Liu et al., 1990). The sensing principle is based on a change in the optical path length resulting from a phase shift in the interference signal (Tsuda et al., 1999). The interference signal is produced from the combined signals from the reference and sensing arms; the change in this signal results from a mechanical strain acting on the fibre. A schematic illustration of the fibre-optic Michelson interferometer is presented in Figure 5.

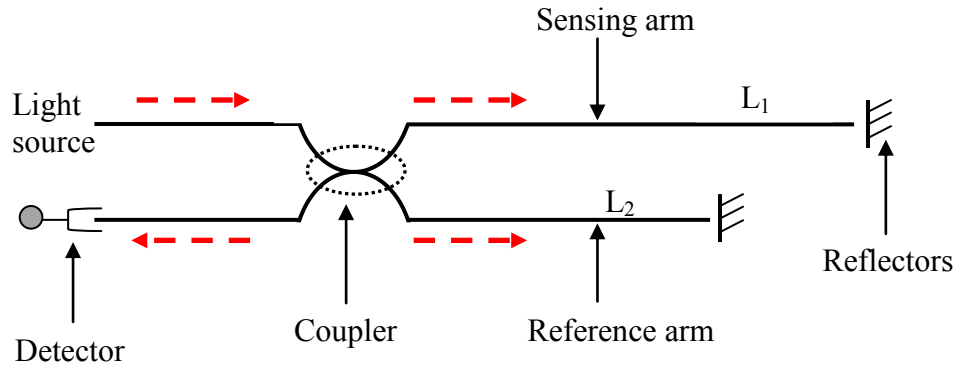


**Figure 5 A schematic illustration of the fibre-optic Michelson Interferometer.**

In order to achieve maximum sensitivity, the phase shift is measured at the quadrature point, i.e. where the phase change and light intensity are linear (De Oliveria et al., 2008). The reference arm of the sensor typically remains in a strain-free state (Tsuda et al., 2001); this is in order to maintain sensitivity to small fluctuations in the phase of the optical signal. Photodiodes are used to convert the received interference signal to a voltage for measurement of AE activity (Liu et al., 1990; Tsuda et al., 1999; Tsuda et al., 2001). The main limitations with the conventional sensor configuration are the susceptibility to thermal and mechanical-induced fluctuations in the phase of the signal from the reference arm.

Liu et al. (1990) also evaluated the use of the Michelson interferometer for detecting AE signals in fibre reinforced composites. The authors proposed the use of a sensor that was embedded in the composite. In this study, the sensor was configured such that both the reference and sensing arms were embedded; as a result, both the reference and sensing fibres were subjected to the same perturbation-inducing phase shifts. The sensing region was formed by the differential in the path length of the two fibres of unequal lengths. The active

homodyne signal demodulation technique was used for signal recovery; the concept of the active homodyne signal demodulation was presented by Yo and Sirkis (1994). Liu et al. (1990) demonstrated the sensitivity of the Michelson interferometer to acoustic emissions during a tensile test; AE signals were observed during specimen loading. The authors proposed that the main limitation with this sensor design was the fluctuation in laser wavelength during measurement; laser wavelength switching is often related to a phenomenon referred to as mode-hopping (Gray and Roy, 1991). In a semi-conductor laser, side modes share the total power with the main transmitted mode. Mode hopping results from switching between the main and side modes which induces laser noise. Fluctuations in the temperature of the laser case and the injection current driving the laser are understood to be the main causes for this phenomenon (Gray and Roy, 1991). In addition, Liu et al. (1990) proposed that the sensitivity of the sensor was dependent upon the propagating and polarisation direction of the waves with respect to the orientation of the sensor.

Tsuda et al. (1999) demonstrated the use of the continuously changing interference signal received from a Michelson interferometer to infer the onset of damage in a composite during tensile loading. The authors proposed that the stress wave emitted from the release of strain energy during matrix cracking and fibre fracture could be detected. A low sampling rate of 1.5 kHz was used for data acquisition; as a result, a maximum signal frequency of 750 Hz was achievable. This frequency range was well below that of typical acoustic emissions of between 20 kHz and 1 MHz. The sensor was configured in a conventional manner such that the reference fibre remained in a strain-free state and the sensing fibre was bonded to the composite test specimen. A conventional acoustic emission sensor was used for comparison; data from the conventional AE sensor was compared with strain measurement data in an

attempt to show correlation with a change in material properties. Data from the tensile test were presented which corresponded to three distinct stages, namely: (i) stage one, whereby only small-scale damage occurred, i.e. matrix cracking; (ii) stage two, where some AE signals were saturated suggesting minimal fibre fracture; and (iii) stage three, whereby the stress-strain curve showed non-linear behaviour with many high amplitude signals recorded. The authors of that study proposed that these signals were understood to be associated with multiple fibre fracture and eventual sample failure. The sample and fibre-optic sensor failed at approximately 1.6% strain.

With reference to the fibre-optic sensor response, fluctuations in the continuously oscillating interference signal were monitored and correlated with the response from the conventional AE sensor. The authors observed erroneous low-frequency oscillations of less than 1 Hz at the start of the test; these were thought to be associated with disturbances in the optical signals due to the thermal drift of the laser source. Higher frequency oscillations between 1 and 2 Hz were observed from the fibre-optic sensor prior to and at the same time as the first detected AE signals were recorded by the conventional AE sensor. The authors therefore proposed that the sensitivity of the Michelson interferometer to small scale damage was higher than the conventional sensor. During stage three, significant oscillations in the interference signal were time correlated with periods of high AE count rate. The authors proposed that the frequency of the oscillations observed close to final failure were in the region of 100 Hz; in some cases, multiple frequency peaks were observed which were attributed to multiple failure modes, resulting in displacements of different speeds. These signals were observed more clearly when 20 kHz high-pass filters were used.

Tsuda et al. (2001) further evaluated the use of the Michelson interferometer for detecting simulated transient AE sources in carbon-fibre composites; a higher sampling rate of 10 MHz was utilised. The effect of the direction of the wave motion on the fibre-optic sensor response was addressed; wave motion was defined as either in-plane or out-plane. Pencil lead breaks were generated in the centre and at the edge of the specimen to simulate both in-plane and out-of-plane wave motion respectively. The configuration of the sensor was the same as presented by Tsuda et al. (1999). The authors proposed that mechanisms such as delamination in a composite produce predominantly out-of-plane motion whereas fibre fracture and matrix cracking produce in-plane motion; as such, there was a need to understand the sensors response to the two modes. The response of the fibre-optic sensor was compared against a conventional piezoelectric AE sensor. With reference to the pencil lead break at the centre of the plate, the Michelson sensor demonstrated an obvious sensitivity to the flexural mode; oscillations in the signal of gradually increasing amplitude were observed. The observed oscillation frequency was lower than that of the piezoelectric sensor. It was therefore proposed that the resonance of the two devices was dissimilar. The arrival of the extensional mode at the fibre-optic sensor was observed and was indicated by a small but stable increase in the measured voltage; no oscillatory response was however observed. It was proposed that the sensors low sensitivity to this mode was due to the low amplitude generated by the wave motion. The time-of-arrival of the extensional mode was confirmed from the response of the electrical-based sensor; here, the amplitude of the signal was significantly lower than that of the flexural mode. With reference to the pencil lead break at the edge of the test plate, the arrival of the extensional wave mode was observed at both sensors simultaneously. The signal oscillated with high amplitude from the point of

detection; this indicated that the in-plane motion resulted in a more dramatic effect on the optical interference signal compared with the out-of-plane wave motion.

### 2.4.3 Fabry-Perot Interferometer

In addition to the Mach-Zehnder and Michelson interferometers, the Fabry-Perot interferometer has been demonstrated for detection of acoustic emissions. The extrinsic Fabry-Perot interferometer (EFPI) is fabricated using two optical fibres fixed at a pre-defined gauge length, typically within a precision-bore capillary; the capillary serves the purpose of fibre alignment (Read et al., 2002; De Oliveria et al., 2008; Zhao et al., 2008). The fibres are positioned within the capillary such that there is a set distance providing a cavity length between the cleaved faces of the two fibres. The sensing principle relies on the interference of reflected light from the cleaved ends of the two fibres (Kersey et al., 1983). When illuminated, Fresnel reflections occur at the glass-air interface of the first fibre and the air-glass interface of the second fibre. These reflections have an observed optical path difference which produces interference fringes. The length of the cavity is influenced by external parameters such as applied low frequency mechanical strain and temperature (Zhao et al., 2008). A change in cavity length of the EFPI sensor will result in a shift in the interference fringe pattern with respect to wavelength (Machavaram, 2006). Machavaram (2006) proposed the following limitations with the EFPI sensor design: (i) non-reproducible cavity lengths; (ii) difficulty determining the exact gauge lengths; (iii) accidental damage to cleaved ends during fibre insertion into the capillary; and (iv) misalignment during fusion splicing or adhesive bonding.

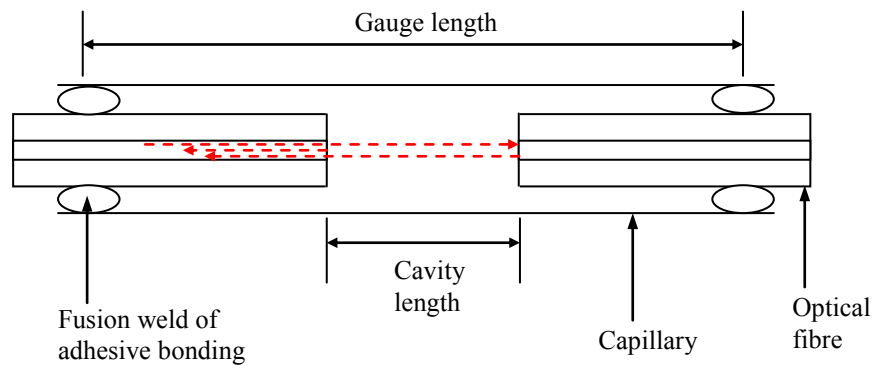


**Figure 6 A schematic illustration of the Fabry-Perot interferometer.**

Read et al. (2002) investigated the fibre-optic Fabry-Perot interferometer for detecting AE signals in composite materials. In order to avoid the effects of a continuously changing cavity length owing to a constant strain change from dynamic loading, a signal processing scheme was used; the processing scheme identified small changes in light intensity as a function of the signal phase shift. The small intensity changes were used to infer the presence of AE. Details of the processing scheme were as follows: the point of maximum sensitivity for detecting the change in light was at the quadrature position of the phase signal. As such, two lasers with fixed wavelengths that were separated by a quarter of the sensors free spectral range were used to illuminate the EFPI sensor. Monitoring of two distinct wavelengths ensured that at least one wavelength was amplitude modulated at the quadrature point at any one time regardless of the effects of external parameters, e.g. temperature, on the cavity length. In order to monitor the two discrete wavelengths separately at the photo-detector, two fibre Bragg grating sensors were used. The role of the Bragg filters was for wavelength rejection of one of the two wavelengths; therefore, each detector received only one wavelength. The performance of the EFPI sensor was evaluated using a pencil lead break.

The results from this trial demonstrated that the sensor had high directionality. This was anticipated owing to the sensitivity in the strain response along the length of the fibre. A 75% reduction in sensor sensitivity to the pencil lead break was observed when the source was generated at an angle of  $90^\circ$  to the orientation of the optical fibre. The frequency response of the sensor was limited to the low frequency range, i.e. less than 215 kHz. Beyond this frequency range, the authors reported that the signal became lost in noise.

De Oliveria et al. (2008) demonstrated the use of a low-finesse EFPI sensor for AE signal detection. The sensor was embedded within a uni-directional carbon-fibre composite specimen. The authors proposed a signal demodulation scheme using a pair of fibre Bragg gratings; the Bragg gratings were located on the output arms of a fibre-optic coupler and therefore received the reflected signal from the EFPI sensor. The role of the two Bragg gratings was to filter two signals with their phase in quadrature from their respective resonant wavelengths. A broadband light-source was used to illuminate the EFPI sensor. As reported by Read et al. (2002), the Bragg wavelengths were chosen to ensure that the two signals were in quadrature of phase and in such a way to operate at the linear region of the response curve. The phase of the signal was correlated with the length of the cavity. As a result, when small elastic waves were generated through the release of energy in the material, i.e. acoustic emissions, the length of the cavity would change; a fluctuation in the measured light intensity at the quadrature position would then occur. The fibre-optic sensor was embedded within a carbon-fibre composite constructed of both woven and uni-directional prepreps. The sensors were embedded within the central layer of the composite along the same orientation as the reinforcing fibres; the central plies consisted of uni-directional prepreps. A pair of high frequency, high bandwidth photo-detectors was used to measure the optical intensity. The performance of the sensor was evaluated using simulated AE signals using: (i) the pencil lead

break; and (ii) impact loading. The sensor was found to detect fluctuations in the optical intensity to both modes of signal excitation. Signal interference, i.e. optical-borne noise, was observed from the signals detected at each photodiode; a noise floor of  $\sim 10$  mV was reported. Maximum signal amplitudes of  $\sim 70$  mV and  $\sim 40$  mV were recorded for the pencil lead break and impacts respectively. The authors proposed that the signal response could be increased if high-gain photo-detectors were used; a limitation of this approach would have been a reduction in the bandwidth of the system.

Zhao et al. (2008) evaluated the fibre-optic Fabry-Perot interferometer for AE signal monitoring. A method was proposed utilising a dense wavelength division multiplexing (DWDM) approach; this method was used in order to provide greater stabilisation of the quadrature point of operation. The authors proposed that the conventional methods of dual wavelength evaluation, i.e. using Bragg filters, which rely on the approximations of two wavelengths within the optical signal, are less sensitive; the reduction in sensitivity results from a lack of precision in identifying the quadrature position within the approximated signals. In this study, dual wavelength analysis of the reflected optical signal from the EFPI sensor was carried out using the DWDM unit. The DWDM was used to generate two quadrature phase-shifted signals; in using the DWDM, the quadrature position could be maintained throughout monitoring enabling precise intensity measurements to be made. The performance of the sensor was evaluated with respect to: (i) AE signal detection in response to a pencil lead break; and (ii) sensing stability. The EFPI sensor demonstrated higher sensitivity than the conventional electrical-based sensor to the extensional signal component of the pencil lead break; the observed signal amplitude was  $\sim 30\%$  higher. This was attributed to the higher sensitivity of the EFPI sensor to in-plane strains generated by this wave mode. A broadband frequency response was observed from the EFPI sensor up to 300 kHz. With

respect to measurement stability, an 11% quadrature error, i.e. phase difference between the two wavelength signals, was reported. The authors also report a high noise floor from the EFPI sensor at  $\sim 80$  mV; the maximum signal response that could be generated from the sensor was 3.2 V. In addition, results from a thermal-stress test revealed that as the sensor was heated, both signals independently drifted away from the quadrature point. Owing to the dual wavelength strategy used, only one signal was reported to show signal fading at a single temperature and therefore AE measurements were still possible.

#### 2.4.4 Fibre Bragg Grating

Fibre Bragg gratings (FBG) provide an alternative sensing concept for detecting acoustic emissions. A Bragg grating is a periodic perturbation of the refractive index within the core of an optical fibre. The perturbations are formed by exposing the core of the fibre to an intense optical interference pattern (Tsuda et al., 2004). When the fibre is illuminated with a light-source, a narrow band of the incident optical radiation is reflected by successive and coherent scattering from the perturbations of the refractive index (Hill and Meltz, 1997). This produces a defined reflection peak of a specific wavelength corresponding to the Bragg wavelength. A schematic illustration of the fibre Bragg grating is presented in Figure 7.

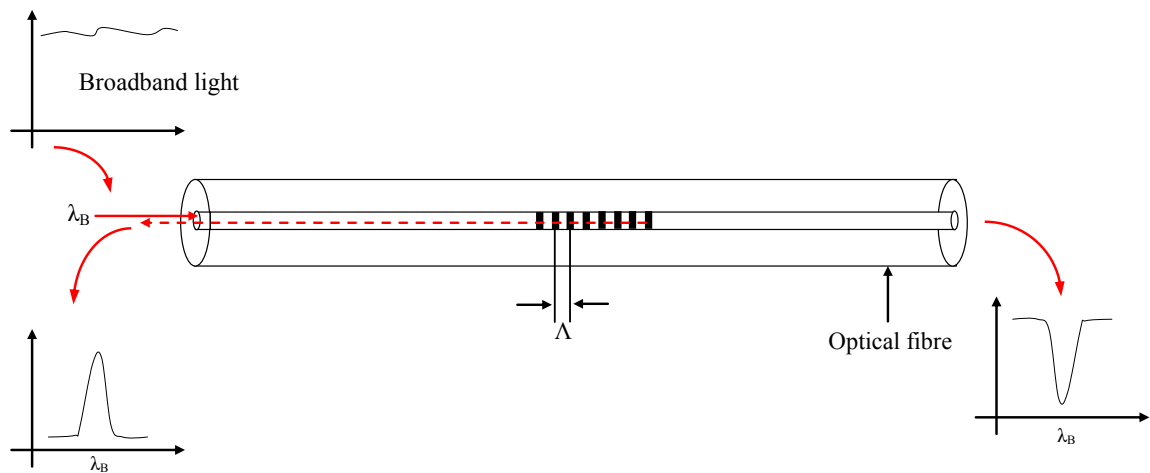


**Figure 7 A schematic illustration of the Fibre Bragg grating sensor.**

When the sensor is subjected to mechanically induced strain, the length of the fibre increases which results in a change in the grating pitch ( $\Lambda$ ) and the refractive index of the fibre (Kersey, 1996). The sensor also demonstrates sensitivity to a change in temperature due to the thermal expansion properties of the material and the temperature dependence of the refractive index (Kersey, 1996). With reference to acoustic emission sensing using FBG's, high-speed strain changes in a material result from the propagation of ultrasonic Lamb waves; the strain changes are in the microstrain range (Tsuda et al., 2004; Betz et al., 2006). Conventional FBG signal interrogation methods are ineffective for AE measurement owing to the low sampling rate (Tsuda et al., 2004). In order to measure the high-speed strain change resulting from wave propagation, demodulation schemes that relate the shift in the Bragg peak wavelength with an optical power change are proposed (Takeda et al., 2005). Active and passive sensing methodologies using FBG technologies have been presented in published literature (Perez et al., 2001; Tsuda et al., 2004; Takeda et al., 2005; Lee and Tsuda, 2005; Betz et al., 2006). For active sensing, the presence of damage in a material affects the propagation characteristics of

an ultrasonic wave; therefore damage can be identified when the properties of a received signal generated by a simulated source, e.g. a piezoelectric transducer, deviate from a reference signal.

Perez et al. (2001) evaluated the use of FBG sensors for detecting simulated AE signals. Fibre Bragg gratings were surface-mounted to the face of a piezoelectric transducer. The transducer was swept through various resonant frequencies ranging between 200 kHz and 2 MHz. The response of the FBG was characterised at six frequencies within this range, namely: 235, 330, 332, 525, 1100 and 2150 kHz. The greatest sensitivity achieved by the FBG sensor to the simulated AE signals was observed between 332 and 525 kHz using a 2 mm tunable FBG filter. In this study, a tunable matching fibre Bragg grating filter was employed to demodulate the intensity of the optical response signal; conversion of the optical signal to a voltage was achieved using a high-speed photo-detector. The minimum detectable displacement of the transducer face that the FBG could register was 0.02 microstrain. This was achieved with a pulser voltage of 10 V at a resonant frequency of 2 MHz. The authors claimed that this detection sensitivity was approaching existing AE detection methods. The performance of the sensor to signals generated at different orientations was also examined on an aluminium test specimen. High gain amplifiers, i.e. 60 dB<sub>AE</sub> gain, were used to increase the signal level. High directionality was observed; the highest signal response was observed from a source emanating parallel to the axial orientation of the sensor. This was due to the preferential strain sensitivity along the length of the fibre when the AE wave elongates and compresses the fibre. The maximum signal level referenced to a 310 mV noise level was 20 dB<sub>AE</sub>. Away from the 0° orientation, the magnitude of the received signals was reduced by approximately 6 dB<sub>AE</sub>. The authors also demonstrated the response of the FBG sensor to

pencil lead breaks. In order to detect the pencil lead break, the amplified gain was increased to 80 dB<sub>AE</sub>. In addition, the bandwidth of the sensor response was limited to 30 kHz; the authors proposed that this limitation was due to available electronic filters and the choice of amplifier that was used.

Tsuda et al. (2004) evaluated the use of fibre Bragg gratings for detecting the presence of impact damage in 0/90° oriented CFRP specimens. The FBG was surface mounted to the specimen. A wavelength-intensity conversion technique was adopted for signal recovery. A narrowband optical filter was used to transmit specific wavelengths of light that were reflected by the sensing FBG. The intensity of the light transmitted through the filter was therefore directly proportional to the strain applied to the sensing FBG; in this case, the optical filter was a second FBG. As such, the area under the Bragg reflection peak that overlapped with the transmissivity peak of the filter corresponded to the light intensity measured at the photo-detector. Therefore, when the sensor was subjected to a compressive strain, the light intensity through the filter was reduced; under tensile strain, the opposite was observed. A broadband amplified-spontaneous-emission (ASE) light-source was used to illuminate the FBG via a 2x1 optical coupler. The role of the optical coupler was to direct light reflected by the sensing FBG into the optical filter. The intensity of the light transmitted through the FBG filter was measured using a photo-detector with a response frequency of >10 MHz. A piezoelectric transducer was positioned in two places such that the received signal propagated through both the damaged and intact areas of the specimen before being detected by the FBG. The transducer-to-sensor spacing was 105 mm. For the reference signal, i.e. the wave propagating through the intact region, an arrival time of 13.6 microseconds was reported with a period of 5.9 microseconds. Close agreement was observed with the arrival of the S<sub>0</sub>

mode; this was based on a calculated velocity of  $7270 \text{ ms}^{-1}$ ; the wave velocity was obtained from the relationship with Young's modulus and specimen density. In contrast, when the wave propagated through the damaged region, the arrival time was 11.6 microseconds. The former was attributed to the separation of the  $0^\circ$  and  $90^\circ$  plies due to the impact damage. As a result, the wave propagated along the  $0^\circ$  layer; the wave velocity was estimated to be  $10,020 \text{ ms}^{-1}$  along the axial direction of the fibres due to a higher Young's modulus. Moreover, the amplitude of the signal was lower and the period was double that of the signal passing through the intact region. This was a function of wave attenuation and dispersion at the damaged region. The waveform broadening resulted in a lower frequency response for the signal passing through the impact damaged region. The authors reported similar observations from a conventional piezoelectric transducer.

Takeda et al. (2005) evaluated the use of small-diameter optical fibres for detecting ultrasonic Lamb waves in composite materials. An active sensing method was also proposed for detecting the optical power change in the Bragg peak reflection signal. The authors noted that signal analysis systems with mechanically moving parts could not provide the high-speed sampling rate required to detect a transient strain change. The sensing FBG was illuminated using an ASE light-source. An optical circulator was used to direct the reflected light to an optical amplifier. The amplified optical signal was transmitted through an array waveguide grating (AWG); this consisted of two narrowband Bragg filters closely separated in the wavelength domain. The two adjacent filters were used to modulate the signals into respective optical powers  $P_1$  and  $P_2$ ; two filters were used in order to provide a higher resolution intensity measurement. The changes in the optical power, i.e.  $P_1$  and  $P_2$ , were detected using photodiodes. The relationship between the wavelength of the Lamb wave and

gage length of the sensor was defined in order to ensure sufficient sensitivity of the FBG sensor without interference effects from other sources of mechanical strain; a gauge length of one-seventh of the wavelength of the Lamb wave was proposed since this produced a narrow Bragg spectrum providing high resolution to the transient strain changes associated with ultrasonic wave propagation. With reference to the  $S_0$  and  $A_0$  modes, suitable gauge lengths of 3 and 0.6 mm were proposed. This information was obtained from the calculated dispersion curves for the defined composite material. The directional sensitivity of the optical fibre sensor was obtained for orientations between  $0^\circ$  and  $180^\circ$  at  $22.5^\circ$  increments. The FBG sensor was surface-mounted to a glass plate; a piezoelectric transducer was used to generate signals within the plate and was mounted at a distance of 100 mm. The authors observed high sensitivity from the sensor along the axial orientation of the fibre. When the angle was increased from  $0^\circ$  to  $90^\circ$ , the amplitude of the signal decreased to almost zero voltage. This was attributed to the low sensitivity to strain variations away from the axial orientation of the sensor. With reference to the damage detection capabilities, a sensor with a gauge length of 1 mm was shown to discriminate the  $A_0$  and  $S_0$  modes propagating within a CFRP sample. The authors also demonstrated the feasibility of detecting simulated delaminations. As reported in Tsuda et al. (2004), the waveform characteristics for a received signal travelling through intact and damaged regions were different; in this case, an additional mode was observed in the waveform. This mode was attributed to: (i) the separation of the  $A_0$  mode along two propagation paths, namely the  $0^\circ$  and  $0/90^\circ$  paths; and (ii) mode conversion of the  $A_0$  mode into the  $S_0$  and  $A_0$  modes at each propagation path. Since the  $S_0$  mode in the  $0^\circ$  layer travels faster than other modes, the time of arrival decreased inversely proportional to an increasing delamination length. In addition, the presence of delaminations in the sample resulted in a reduction in the measured signal amplitude.

Lee and Tsuda (2005) evaluated the use of FBG sensors for detecting damage development in composite materials subjected to tensile loading and impact damage. The authors utilised a tunable light-source where the central wavelength was focused on the linear region of the side lobe of the Bragg peak. A change in the grating pitch ( $\Lambda$ ) of the FBG resulting from an interaction of an AE wave could be demodulated by a variation in the reflected intensity. In support of Takeda et al. (2005) and Betz et al. (2006), it was reported that the length of the grating should be significantly smaller than the expected ultrasonic wavelength. This was proposed in order to avoid erroneous signal capture from local strain gradients in the material and distorted spectra due to non-uniform strain along its length. A novel sensing design was presented in which a conventional 1 mm FBG was bonded on to a 1.6 mm thick acrylate plate; the acrylate plate was used to support the sensor and could be surface-mounted to a host material and removed without risk of damage to the sensor head. The sensor was coupled to the host material using grease couplant. As the acrylate plate was not mechanically fixed to the specimen, the sensor was insensitive to low-frequency strain changes during mechanical loading. For evaluation, the sensor design was surface-mounted to a CFRP test specimen which was subjected to tensile loading. The fibres in the composite were oriented at  $90^\circ$  to the loading direction and therefore the sample was expected to fail by matrix cracking only. The response of the FBG sensor to this failure mode showed close agreement with a conventional electrical-based sensor; the FBG demonstrated a  $10 \text{ dB}_{\text{AE}}$  higher signal-to-noise ratio than the piezoelectric device. With reference to the frequency response, both sensors demonstrated sensitivity to signals within the range of 100 to 375 kHz.

Betz et al. (2006) proposed an alternative method of acousto-ultrasonic sensing using a tunable laser rather than a broadband light-source; the purpose of the tunable laser was to emit

a defined optical signal at a known wavelength. The central wavelength of the signal from the laser was selected at the linear region of the spectrum, i.e. between 20-80% of the gratings maximum reflectivity. Any movement of the Bragg wavelength in response to an ultrasonic wave resulted in a change in the optical power output at this region of the spectrum. The authors proposed that the length of the grating region was an important consideration for the following reasons: (i) a constant strain change over the entire length of the grating was required; and (ii) if the sensor was too short, there would be a risk of heightened sensitivity to localised strain gradients. With reference to (i), a change in strain over the entire grating length ensured a linear response with the incident acoustic strain amplitude. The authors of that study found that a practical grating length of 1 mm was suited to the detection of all frequencies up to 1.6 MHz for a typical application using a 1 mm thick aluminium plate. Moreover, the authors proposed that a grating length of 1 mm ensures a linear relationship of the observed sensor signal with the applied acoustic amplitude.

#### 2.4.5 Fused-Tapered Coupler

The feasibility of deployment of the fused-tapered coupler fibre-optic sensor for acoustic emission detection has been demonstrated previously (Doyle et al., 2002a; Doyle et al., 2002b; Chen et al., 2003; Chen et al., 2004; Chen et al., 2008). Research focused on the fused-tapered sensor design, cited herein, have attempted to define: (i) the principles of operation of the sensor; and (ii) the sensitivity of the sensor to acoustic emissions. A schematic illustration of the fused-tapered coupler is presented in Figure 8.

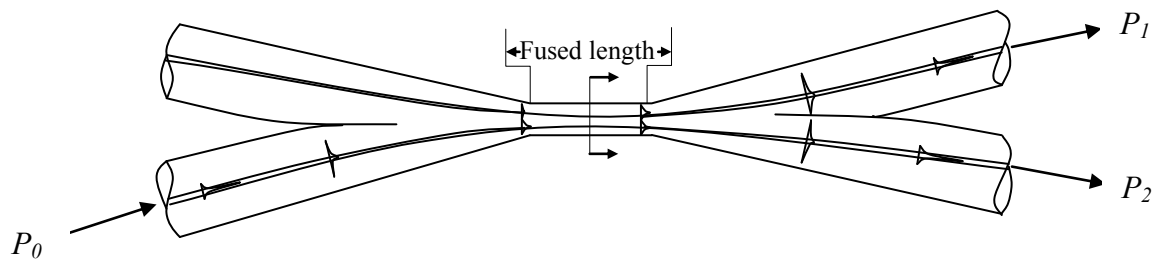


**Figure 8** A schematic illustration of a 2x2 fused-tapered fibre-optic acoustic emission sensor;  $P_0$  refers to optical input power and  $P_1/P_2$  refer to the optical output powers.

The mode of operation for the fused-tapered coupler for acoustic emission sensing is as follows: with reference to Figure 8, the operating principle of the 2x2 fused-tapered fibre-optic sensor is based on monitoring the differential light intensities at the output ports  $P_1$  and  $P_2$ . Light is launched into the coupler at  $P_0$  using a laser operating at a wavelength of 630 nm; the optical radiation is coupled to the second optical fibre at the region where the fibres are fused together; this region is tapered to a diameter of approximately 15 microns and therefore acts as a stress concentrator (Chen et al., 2003). Details of the fabrication process of the sensor are given in Section 3.2.1. When an external acoustic field interacts with the sensor, an acoustic wave is excited at one end of the device and propagates along its length. This induces a variation in the strain field around the sensing region. The strain field in a tapered optical fibre was modelled in Chen et al. (2008); the authors found that the length of fibre with the narrowest waist region demonstrated the highest sensitivity to induced strain. The perturbation of the strain field in the narrow tapered region of the coupler results in a change in the refractive index of the fibres and an elongation of the sensing region. The refractive index change is due to the strain-optic effect within the optical fibres and will result in a variation in the coupling ratio; a variation in the coupling ratio will therefore influence the

optical intensities at the output ports of the sensor. The effects of strain and the length of the coupling region on the performance of the fused-tapered coupler were modelled in Chen et al. (2003). Appendix-A provides a detailed description of the derivation of the equations used to describe the influence of these parameters on the performance of the sensor; the equations that are presented in Appendix-A make reference to: (i) the influence of the strain-optic effect on the coupling ratio of the sensor; (ii) the magnification of the mechanical strain effects; and (iii) the effect of the un-bonded length of the sensor on the response of the AE sensor.

With reference to evaluating the performance of the sensor, Doyle et al. (2002a) reported on the use of the fused-tapered coupler for detecting AE in composite materials; simulated AE signals were generated using an ultrasonic pulser. The authors proposed that the overall laser noise of a fibre-optic based sensing configuration could be reduced by monitoring the optical intensity at two output ports using differential detection; a reduction in the signal triggering threshold and/or improvements to the sensors sensitivity could be realised from reduced laser noise. A fibre-optic coupler was surface-mounted on a 16-ply +/- 45° oriented glass fibre composite. The sensor, a 2x2 coupler operating at a central wavelength of 630 nm, was packaged within a circular V-groove with an outside diameter of 4 mm. For reference, the sensor response was compared with the response from a piezoelectric transducer. A second piezoelectric pulser was used to excite acoustic signals in the plate; an attenuation test was performed on the plate to determine the distance at which the signal could no longer be detected. Signals were generated at 0°, 45° and 90° orientations around the sensor. Detection of signals along the orientation of the reinforcing fibres, i.e. 45°, was observed up to 30 cm from the sensor. The source-to-receiver distance was reduced to ~22 cm for the 0° and 90° orientations. Noise levels of 36 dB<sub>AE</sub> and 26 dB<sub>AE</sub> were achieved for a 5 mW laser diode and

a 10 mW He-Ne laser source resource respectively. The authors proposed that the higher noise from the laser diode was due to a reduced efficiency of common-mode rejection at the photodiode. This results from a mismatch between the laser wavelength and the wavelength peak sensitivity of the two photodiodes; for a differential detection scheme, the optical intensities should be equal at both photodiodes to achieve effective common mode rejection. If the wavelength mismatch is present between the two photodiodes, there is the potential for the coupling ratio to drift from the optimal 50:50 ratio thereby increasing the noise level. With reference to the maximum detectable signal level, a signal with an amplitude of 80.4 dB<sub>AE</sub> was recorded using a pulsing distance of 2 cm. The maximum signal level was 17 dB<sub>AE</sub> lower for the He-Ne laser. The maximum recorded signal-to-noise ratio obtained using the laser diode was 45 dB<sub>AE</sub>. The signal frequency characteristics of the signal recorded by the fibre-optic sensors were also examined. Frequency peaks between 50 and 200 kHz were observed; the resonance of the device was therefore understood to be dominated by a mechanical effect rather than an acousto-optic effect.

Doyle et al. (2002b) further evaluated the fibre-optic sensor performance during mechanical testing. In this study, the sensor was packaged in a borosilicate capillary with an outer diameter of 1.5 mm and was embedded within the central plies of a 16-ply +/- 45° composite; the composite specimen was prepared by the wet-layup process and was cured at room temperature. Specimens with embedded sensors were cut to the desired dimensions and prepared for tensile tests by end-tapping. The samples were loaded and AE signals were acquired by the coupler sensor and a reference piezoelectric transducer. Both sensors produced similar trends with reference to cumulative hits versus time. The authors reported that increases in the recorded activity from the fibre-optic sensor were in response to high

energy and high amplitude signals; these signals were believed to correspond to fibre fracture rather than matrix cracking. It is therefore worth noting that whilst the fused-tapered coupler sensor did not respond to low amplitude signals owing to a high noise floor, detection of critical damage mechanisms were possible. Failure of the fibre-optic sensor occurred at approximately 1 % strain, after which, the test was aborted.

Chen et al. (2003) demonstrated that the coupling ratio change due to the interaction of an acoustic perturbation was dependent upon several factors, namely: (i) the effective amplitude of the acousto-elastic effect which relates to the acoustic energy, material properties and the sensor packaging; (ii) the coupling co-efficient that relates to the structure of the coupling region and the cross-power points; (iii) the properties of the acoustic wave, e.g. the acoustic frequency or wavelength; and (iv) the geometry of the sensing region, e.g. the length, width and taper angle of the coupling region. In addition, Chen et al. (2004) proposed that the sensitivity of the device could be optimised through improvements to the profile of the coupling region, i.e. the length and width of the tapered region, as well as the nature of the sensor packaging.

Chen et al. (2004) evaluated the properties of an “in-house” fabricated fused-tapered coupler. A coupler sensor with a 50:50 coupling ratio was packaged within a fused-silica V-groove with dimensions of 25 x 2 x 2 mm and was bonded at each end using an epoxy adhesive. The performance of the sensor was evaluated using pulsed signals from a piezoelectric transducer; the sensor and transducer were both immersed in a water bath. The directional characteristics of the sensor were obtained at 0°, 45° and 90° orientations using a source-to-receiver distance of 100 mm. A low variation in the signal amplitude was observed as a function of orientation;

the maximum peak-to-peak signal variation was 17 mV suggesting that the sensor had little directional sensitivity. The response of the sensor to pencil lead breaks was also determined; here the sensor was surface mounted to a glass fibre reinforced epoxy plate. A piezoelectric transducer was used as a reference. In this study, pencil leads were fractured at a distance of 10 mm from the sensor. The recorded signal amplitudes from the fibre-optic and piezoelectric transducers were  $\sim 500 \mu\text{V}$  and 200 mV respectively. A frequency peak at 155 kHz was observed from the FFT of the signal recorded by the piezoelectric transducer. A higher frequency response was observed from the fibre-optic sensor; several distinct peaks around 300 kHz were observed. The authors attribute this result to the natural resonant frequencies of the sensor system.

## **2.5 Conclusions of the Literature Review**

A number of conclusions can be drawn from this literature review with reference to: (i) damage susceptibility in advanced fibre reinforced composite materials; (ii) conventional structural health monitoring techniques; and (iii) fibre-optic sensing methods for acoustic emission monitoring. The key points to note are:

The utilisation of composite materials has increased in recent decades, primarily due to the high specific properties they offer to the end user. However, this class of materials are susceptible to damage, e.g. low-velocity impacts that generate specific damage modes. Therefore, it is beneficial to provide continuous online monitoring of a materials integrity.

It is generally accepted that delamination is the most likely failure mechanism to result from impact damage. The resistance to delamination and crack propagation at an interface is given by the interlaminar fracture toughness of the material. A popular method of measuring the interlaminar fracture toughness of a material is based on the double cantilever beam (DCB) method.

Due to difficulties using visual inspection for the identification of damage in composite materials, it is beneficial to employ techniques that will provide reliable information on the integrity of the structure. Structural health monitoring (SHM) ensures that variations in a material or structure can be detected and interpreted.

Ultrasonic, thermography and vibration-based techniques have been well documented as suitable SHM methods for inspection of composite materials. However, these techniques have limitations as they typically require the structure to be removed from service for inspection or have very complex processing methods that are limited only to laboratory practises.

In contrast, acoustic emission (AE) is well established for online condition monitoring of structures, for structural assessment during proof-load testing and for mechanical characterisation of composite materials undergoing laboratory-based testing. AE provides real-time monitoring of the material/structure and can infer the onset, propagation and location of damage well in advance of visual indications.

Piezoelectric transducers are typically used for AE monitoring in composite materials due to their high sensitivity to signals within the bandwidth of interest. There are however accepted limitations that preclude their use for *in-situ* damage detection, e.g. large dimensions, susceptibility to electromagnetic interference and are unsuitable for use in hazardous environments.

In contrast, fibre-optic sensors do not suffer from the drawbacks that limit the use of conventional electrical-based sensors. A number of fibre-optic sensor configurations have been developed for the detection of AE; the most common configurations in recent decades refer to the Mach-Zehnder, Michelson, extrinsic Fabry-Perot and fibre Bragg grating sensor designs.

Limitations with the interferometric and Bragg grating sensor designs include: (i) sensitivity to environmental-induced perturbations, e.g. thermal and mechanical; (ii) high associated costs due to the equipment required to ensure measurement stability; (iii) high directional sensitivity; and (iv) complex signal recovery methods.

The fused-tapered fibre-optic coupler sensor has been proposed as an alternative sensing principle. A relatively simple sensing methodology based on a differential intensity measurement was proposed. Preliminary research has shown that the sensor is sensitive to simulated AE and demonstrates relatively low directional sensitivity.

# CHAPTER 3

## Experimental

## 3 Experimental

---

### 3.1 Materials and Equipment

#### 3.1.1 Optical Fibres

Two types of optical fibre were used during this research for fabrication of the fibre-optic acoustic emission (AE) sensor, namely: (i) SM04-1; and (ii) SM600. The specifications for the named fibre types are presented in Table 4.

**Table 4 Technical specifications of optical fibres used for fabrication of the fibre-optic AE sensor.**

<b>Fibre type</b>	<b>Design wavelength (nm)</b>	<b>Numerical aperture</b>	<b>Mode fibre diameter (<math>\mu\text{m}</math>)</b>	<b>Outside diameter (<math>\mu\text{m}</math>)</b>	<b>Coating</b>
SM04-1 <sup>*1</sup>	633	0.13	4.2	245 $\pm$ 10	Acrylate
SM600 <sup>*2</sup>	633 - 680	0.1 - 0.14	4.3 - 4.6	245 $\pm$ 5%	Acrylate

\*1 Beijing Aomolin Photoelectrical Technology Co. Ltd, China

\*2 Fibercore Ltd, UK

SM04-1 and SM600 fibres were used for fabricating the AE sensor owing to the nature of the step-index profile. The regular and homogenous refractive index profile along the fibre provides a smooth evanescent field at the location of the co-joined fibre cores of the coupler. As a result, consistent optical guidance along the tapered length can be achieved with minimal output loss.

### 3.1.2 Fusion Splicer

A commercial fusion splicer (FSM-40PM; Fujikura Ltd, UK) was used for joining optical fibres. The equipment was required for: (i) connecting optical fibres together to extend the fibre length; and (ii) connecting optical fibre to connectors. The fusion splicer provided accurate core-to-core alignment which ensured minimal optical loss. In the event that optical loss, measured at the splice, was greater than 0.02 dB, the fusion process was repeated. The splice region was protected with a 40 mm steel reinforced heat-shrink polymer tube.

### 3.1.3 Optical Fibre Cleaver

A high-precision cleaver (CT-30, Fujikura Ltd, UK) was used for preparation of the end-face of an optical fibre prior to fusion splicing. The fibre was stripped of its polymeric coating using a fibre-optic stripper (CF2; Clauss, USA) and cleaned. In all subsequent cases, the fibres were cleaned of surface debris using iso-propanol alcohol and piece of lint-free tissue. The fibres were then cleaved. Cleave angles equal to or less than  $0.5^\circ$  were achievable.

### 3.1.4 Optical Fibre Connector

A single type of optical fibre connector was used for connecting the AE sensor to the interrogation equipment; the connector was an FC/PC (fibre connector/physical connection) type. The connectors were cleaned prior to use using a tape cleaning tool (Type-A cassette cleaner; Cletop.com, USA).

## 3.2 Acoustic Emission Sensors

### 3.2.1 Fabrication of the Fibre-Optic Acoustic Emission Sensor

With reference to Figure 8 (see Section 2.4.5), the 2x2 fused-tapered fibre-optic AE sensor was fabricated by fusing two single-mode optical fibres together using a hydrogen flame. Unless otherwise stated, the fibre type used for sensor fabrication was SM04-1. The fabrication procedure was performed using a commercial coupler fabrication unit (JW2102; Shanghai Joinwit Optoelectronic Tech Co Ltd, China) and was as follows: A 12 mm section of the acrylate coating was removed from each optical fibre using a mechanical stripper and was cleaned. The two stripped sections were positioned within intimate contact using an overlapping twist. The fibres were then secured within two vacuum clamps such that the stripped region was located directly beneath the hydrogen torch. The flow rate of the hydrogen gas used to fuel the flame was set at 110 standard cubic centimetres per minute (sccm). The hydrogen flame was ignited using a conventional spark igniter. The fibres were then heated and drawn at a constant rate of 1 mm/min to form the bi-conical tapered region. The length and diameter of the tapered region for a typical sensor was approximately 7 mm and 15  $\mu\text{m}$  respectively. The coupling ratio was monitored during fabrication by launching light into one fibre and monitoring the intensity of the two output fibres. The output detector ports were located within the fused bi-conic taper system and the optical signal was recorded via a computer-based data acquisition system. The fused-tapered sensors were fabricated to yield a 50:50 coupling ratio ( $\pm 10\%$ ). A schematic illustration of the coupler fabrication unit is presented in Figure 9.

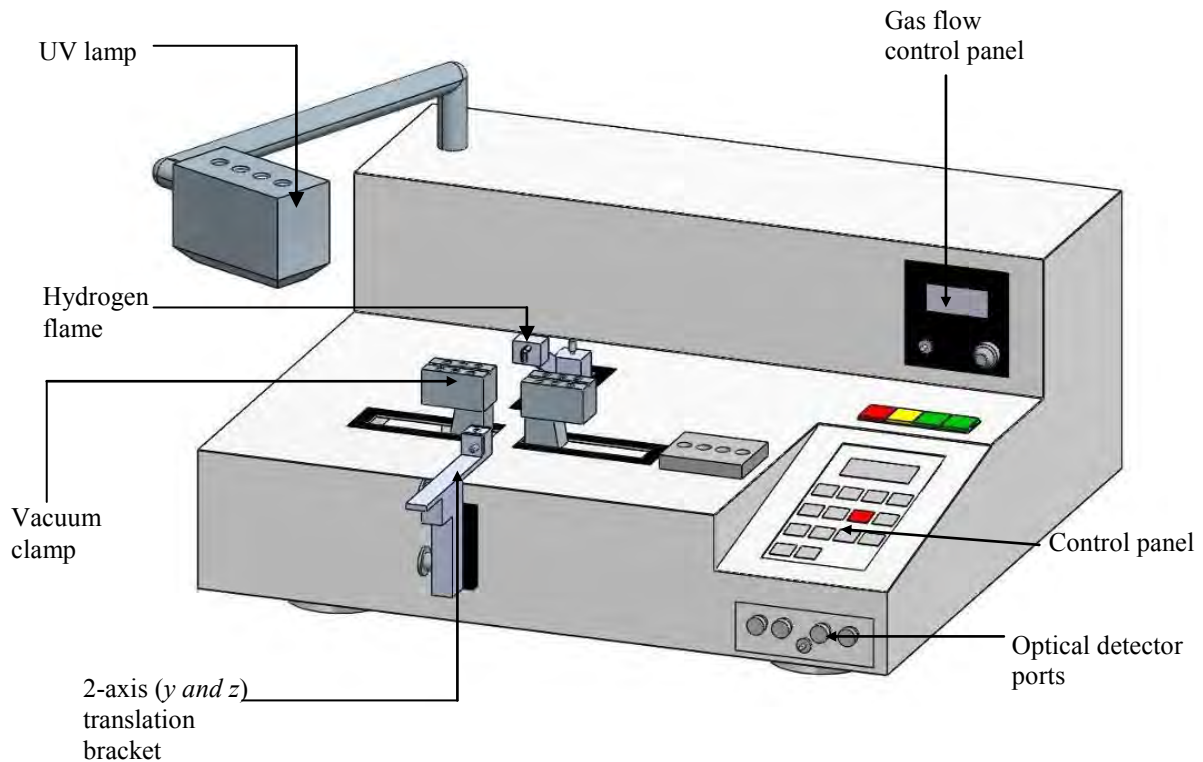


**Figure 9 A schematic illustration of the coupler fabrication unit (CFU) used to fabricate the fibre-optic AE sensor (not to scale).**

### 3.2.2 Packaging of the Fibre-Optic Acoustic Emission Sensor

(a) Surface-mounted sensors: The fused-tapered sensor was secured within a fused-silica U-channel with approximate dimensions of 30 mm (l) x 1500  $\mu\text{m}$  (w) x 1500  $\mu\text{m}$  (d). The U-channel packaging was positioned using a coarse-movement translation stage that was mounted onto the front of the coupler fabrication unit. The translation stage provided movement in the  $y$  and  $z$ -axes. A 30 mm package length was used in order to accommodate a small section of unstripped fibre at both ends of the tapered region. The fused-silica U-channel was positioned so that the unstripped fibre made contact with the U-channel surface.

The sensor was then secured using a UV-curable epoxy resin (UV403-T; Shanghai Jiyuan Ltd, China) at both ends of the package.

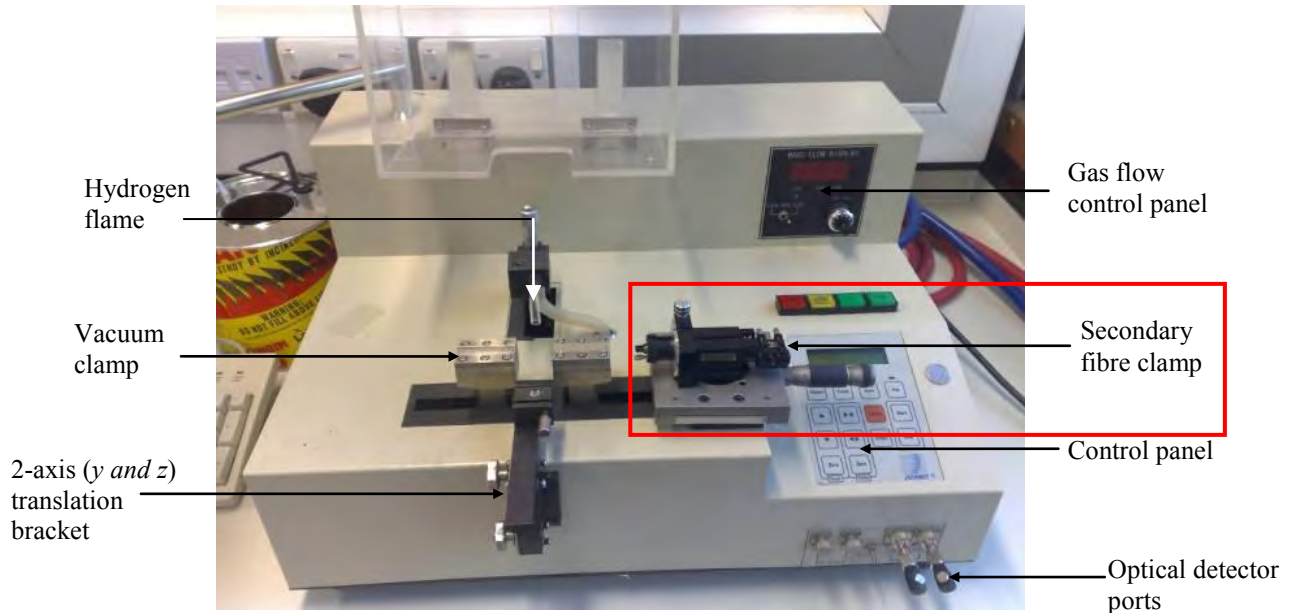


**Figure 10 A photograph of the instrument used to fabricate the fused-tapered fibre-optic AE sensor highlighting the location of the secondary fibre clamp.**

(b) Embeddable sensors: The fused-tapered sensor was packaged within a borosilicate capillary with inner and outer diameters of 500  $\mu\text{m}$  and 700  $\mu\text{m}$  respectively. The capillary package was positioned onto the two output fibre leads prior to fusion splicing the fibres to the output connectors. During fabrication of the sensor, the capillary was located on the outer edge of the right vacuum chuck. After fabricating the sensor, a secondary fibre clamp (see Figure 10) was temporarily fixed to the coupler fabrication unit. This clamp was necessary in order to maintain fibre tension whilst the right vacuum chuck was switched off. The vacuum was removed to allow movement of the capillary across the surface of the chuck groove, and into position around the tapered sensor. The capillary was translated manually with the use of

a crochet needle; the crochet needle was used to allow finer movement control of the capillary. The vacuum chuck was turned back on when the capillary was in position covering the stripped tapered region. The package was secured to the fibres using a UV-curable epoxy resin. Resin was applied at both ends of the capillary.

### 3.2.3 Interrogation of the Fibre-Optic AE Sensor

Interrogation of the fibre-optic acoustic emission sensor was performed using a custom-designed pin-photodiode module. The interrogation module housed a 635 nm pig-tailed laser (PLD635SM3.0; Fibercore Ltd, UK) which was used to illuminate the sensor;  $P_0$  in Figure 8 refers to the fibre connected to the laser. The output power from the laser, measured at the fibre pig-tail, was 1.8 mW. The output optical signal from the fibre-optic AE sensor, i.e.  $P_1$  and  $P_2$ , was directed to a pin-photodiode preamplifier (TA10; Theoptics Ltd, UK). The interrogation module also housed a pair of pin-photodiodes. The input and output fibre leads were connected to the interrogation hardware via FC/PC connectors. A phantom power source was used to power the interrogation unit; the 28-volt phantom power supply was obtained directly from a PCI-2 data acquisition card installed in the acoustic emission computer. The PCI-2 card provided a facility to acquire signals from two AE channels in real-time. The acquired AE data was analysed using a Microsoft<sup>®</sup> windows-based acquisition software (AEwin<sup>™</sup>; Physical Acoustics Corporations, USA). Post-processing of AE data were also performed using advanced signal processing software (Noesis<sup>™</sup>; Envirocoustics, Greece). Figure 11 provides a schematic illustration of the hardware setup.

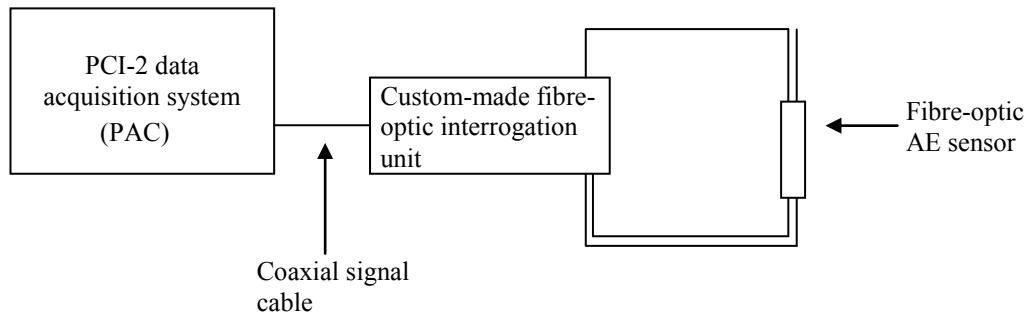


**Figure 11** A schematic illustration of the experimental setup used to interrogate the fibre-optic AE sensor.

### 3.2.4 Piezoelectric Transducers

A conventional electrical-based piezoelectric transducer was utilised during this research project. A WD (wideband frequency response) piezoelectric transducer was used for comparison with the fibre-optic acoustic emission sensor; the sensor was supplied by Physical Acoustics Corporation, USA. A photograph of the piezoelectric transducer is provided in Figure 12. The WD sensor is a broadband sensor with bandwidth of 0.1 to 1 MHz. The dimensions of the sensor were 18 mm dia. x 17 mm. The piezoelectric element was packaged within aluminium housing and sealed using an epoxy adhesive. The sensor had a ceramic face-plate for contact with the host material. The electrical connection cable measured 1 metre in length.



**Figure 12 A photograph of the WD piezoelectric transducer used in this study.**

The WD sensors was interrogated using a commercial interrogation system (PCI-2; Physical Acoustics Corporation, USA). The sensors were connected to the PCI-2 data instrumentation card described in Section 3.2.3 via a 2/4/6 low-noise preamplifier (Physical Acoustics Corporation, USA). The 2/4/6 preamplifier provided a selectable signal gain feature (20/40/60 dB<sub>AE</sub>) and was connected to the interrogation system using a BNC connection. Details of the acquisition setup used for data capture are presented in Figure 13. Descriptions of the waveform-acquisition timing parameters, namely: (i) peak definition time (PDT); (ii) hit definition time (HDT); and (iii) hit lock-out time (HLT) are presented in the glossary section. The AE parameters that were of interest are presented in Figure 14.

AE Channel	Threshold			Gain dB	Pre-Amp dB	Analog Filter		Waveform Setup		
	Type	dB	FTBnd			Lower	Upper	Sample Rate	Pre-Trigger	Length
<input checked="" type="checkbox"/> 1	FIXED	40	6	0	40	20kHz	1MHz	1MSPS	50	1k
<input checked="" type="checkbox"/> 2	FIXED	40	6	0	40	20kHz	1MHz	1MSPS	50.0000	1k
<input checked="" type="checkbox"/> 3	FIXED	40	6	0	40	20kHz	1MHz	1MSPS	50.0000	1k
<input checked="" type="checkbox"/> 4	FIXED	40	6	0	40	20kHz	1MHz	1MSPS	50.0000	1k

(a)

AE Channel	PDT	HDT	HLT	Max Duration
	microseconds	microseconds	microseconds	milliseconds
<input checked="" type="checkbox"/> 1	200	800	1000	100
<input checked="" type="checkbox"/> 2	200	800	1000	100
<input checked="" type="checkbox"/> 3	200	800	1000	100
<input checked="" type="checkbox"/> 4	200	800	1000	100

(b)

AE Channel	PDT	HDT	HLT	Max Duration
	microseconds	microseconds	microseconds	milliseconds
<input checked="" type="checkbox"/> 1	50	100	300	100
<input checked="" type="checkbox"/> 2	50	100	300	100
<input checked="" type="checkbox"/> 3	50	100	300	100
<input checked="" type="checkbox"/> 4	50	100	300	100

(c)

**Figure 13** Screen-shots from the AEwin™ software illustrating the acquisition setup values for: (a) AE channel setup; (b) waveform timing setup for metal specimens; and (c) composite specimens.

**Hit Data Set**

- Amplitude
- Energy
- Counts
- Duration
- RMS
- ASL
- Threshold
- RiseTime
- Counts to Peak
- Average Frequency
- Reverberation Frequency
- Initiation Frequency
- Signal Strength
- Absolute Energy

**Hit Parameters:**

1    2

Cycle Counter / RPM

**Spectrum Features:**

- Frequency Centroid
- Peak Frequency
- Partial Power

0 Segments Defined   Define...

**Time Driven Parameters:**

1    2    3    4    5    6    7    8

Cycle Counter / RPM

**Time Driven Channel Data:**

RMS    ASL

Threshold    Absolute Energy

Time Driven Rate:  ms    seconds

milliseconds

**Constants:**

RMS/ASL Time Constant:  ms

Energy Reference Gain:  dB

**Figure 14** A screen-shot from the AEwin™ software illustrating the AE parameters of interest.

### **3.3 Sensor Manufacture: Repeatability and Optimisation**

#### **3.3.1 Repeatability of Sensor Fabrication**

The repeatability of the procedures that were used to fabricate the fibre-optic acoustic emission sensor were investigated. To achieve this, twenty sensors were fabricated using the manufacturing procedure outlined in Section 3.2.1; the sensors were packaged in a fused-silica U-channel and were designed for surface-mounted applications. The performance of the sensors was assessed using the following criteria: (i) excess-loss; (ii) coupling ratio; and (iii) draw-length. These terms are defined within the glossary. Data from (i)-(iii) were obtained from the coupler fabrication unit. Three batches of sensors were compared; the three batches were fabricated using two different reels of SM04-1 fibre, as well as a reel of SM600 optical fibre.

#### **3.3.2 Statistical Analysis of the Repeatability of Sensor Fabrication**

Statistical analysis was performed on the data obtained from the sensor repeatability trials. A single factor analysis of variance ( $F$ -test) was performed on the acquired data to determine the statistical correlation between the three experimental factors highlighted in Section 3.3.1. Only the two batches of SM04-1 sensors were analysed and compared using statistical analysis.

### 3.3.3 Reliability of the Process Control for Sensor Fabrication

The reliability of the draw-control settings of the coupler fabrication unit that were used to provide consistent vacuum chuck displacement was investigated. This test was performed to assess the contribution of the fabrication equipment reliability on the consistency of the sensor properties. The draw-control was evaluated with regards to: (i) the velocity of both vacuum chucks during tapering; (ii) a comparison between chuck displacement and the control panel display; and (iii) the return chuck position relative to its original starting position ( $x$  and  $z$ -axes).

The traverse speed of the vacuum chuck was calculated using displacement and time measurements. The displacement of the chuck was monitored with the aid of a measurement scale attached to the coupler fabrication unit. A scale was located on the bed of the equipment adjacent to the chuck. The time was recorded at every 1 mm interval as the chuck traversed along the scale. All static displacement measurements were made using an electronic calliper with a measurement accuracy of  $\pm 0.03$  mm.

### 3.3.4 Repeatability of the Double-Twist

The repeatability of the overlapping twist that was used to bring the individual fibres of the coupler into intimate contact was investigated. Analysis was carried out using optical microscopy. A 12 mm section of the acrylate coating was removed from each length of optical fibre using a mechanical stripper and was cleaned. The fibres were positioned within intimate contact via a single overlapping twist and secured under vacuum. A borosilicate

glass slide was used to mount the twisted fibres for image analysis. A UV-curable adhesive was used to bond the fibres to the slide.

A 1.3 megapixel CMOS camera (PL-A662; PixeLINK, Canada) was attached to the trinocular port of an optical microscope (Axioskop, Carl Zeiss AG, Germany). The fibre twist was sectioned into a maximum of eight images due to a limitation with the microscope's field of view. A measurement scale was imprinted onto the slide to enable accurate reconstruction of the image. The repeatability of the twist was characterised according to the pre-defined measurement criteria outlined in Figure 15 and Table 5.

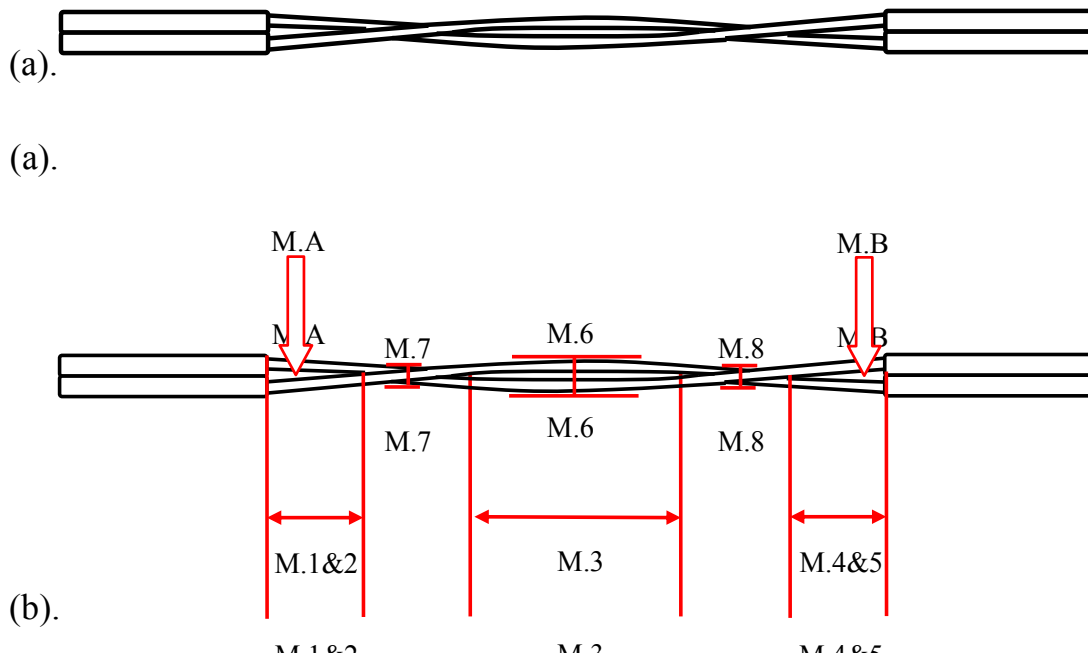


**Figure 15 Schematic illustrations of: (a) a typical sensor twist involving a pair of partially stripped optical fibres; and (b) measurement criteria for assessing overlapping twist repeatability (see Table 5 for details).**

**Table 5 Details of the measurement criteria used for assessing the overlapping twist repeatability.**

<b>Measurement</b>	<b>Description of measurement</b>
M.1	Upper left coating distance to sensor twist
M.2	Lower left coating distance to sensor twist
M.3	Length of twist “eyelit”
M.4	Lower right coating distance to sensor twist
M.5	Upper right coating distance to sensor twist
M.6	Width of twist “eyelit” (mean of 3 locations at eyelit mid-point)
M.7	Width of left sensor twist (mean of 3 locations at twist mid-point)
M.8	Width of right sensor twist (mean of 3 locations at twist mid-point)
M.A	Appearance of left contact between upper and lower fibre
M.B	Appearance of right contact between upper and lower fibre

For reference, the double-twist image analysis samples were assigned the coding of DT-xxx where xxx refers to the database number.

### 3.3.5 Repeatability of the Fibre Taper

The repeatability of the fibre taper was evaluated using image analysis. Fibre-optic sensors were fabricated and packaged within square U-channel substrates. The sensors were secured temporarily to a borosilicate glass slide using polyester tape and image analysis was performed using the same equipment and procedures specified in 3.3.4. The taper was sectioned using a maximum of fifteen images, which were later reconstructed for analysis. The repeatability of the fibre taper was characterised according to the pre-defined measurement criteria outlined in Figure 16 and Table 6. For reference, all sensors manufactured using the SM04-1-type optical fibre were assigned the coding of SM04-xxx, where xxx refers to the database number.

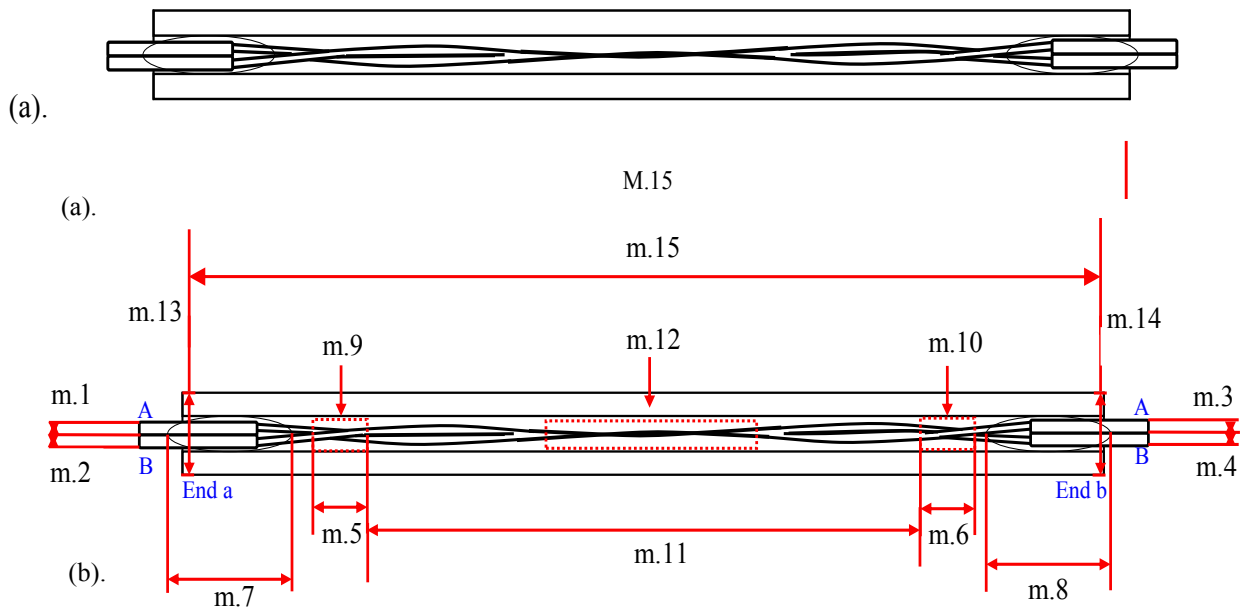


**Figure 16 Schematic illustrations of: (a) a typical fibre-optic AE sensor; and (b) measurement criteria used for assessing the taper repeatability (see Table 6 for details).**

**Table 6 Details of the measurement criteria used for assessing the dimensions of the 2x2 fused taper region with regards to the repeatability of the fabrication process.**

Measurement	Description of measurement
m.1	Diameter of fibre A - end a
m.2	Diameter of fibre B - end a
m.3	Diameter of fibre A - end b
m.4	Diameter of fibre B - end b
m.5	Length of twist at end a
m.6	Length of twist at end b
m.7	Length of resin at end a
m.8	Length of resin at end b
m.9	Width of twist at end a
m.10	Width of twist at end b
m.11	Length between twists
m.12	Width measurement at narrowest region
m.13	Width of capillary - end a
m.14	Width of capillary - end b
m.15	Length of u-groove package

### 3.3.6 Evaluation of the AE Sensor Packaging Procedures

An alternative packaging substrate was investigated with the aim of: (i) reducing the dimensions of a packaged sensor; and (ii) improving the sensitivity response to acoustic emissions. The dimensions of the square U-channel package were approximately 30 mm ( $l$ ) x 1500  $\mu\text{m}$  ( $w$ ) x 1000  $\mu\text{m}$  ( $d$ ). The dimensions of the U-channel in the square package were 750  $\mu\text{m}$  ( $w$ ) x 550  $\mu\text{m}$  ( $d$ ). A circular U-channel substrate was evaluated for use as an alternative sensor package. The dimensions of the circular substrate were 30 mm ( $l$ ) x 700  $\mu\text{m}$  ( $dia.$ ). The maximum dimensions of the U-channel were 500  $\mu\text{m}$  ( $w$ ) x 350  $\mu\text{m}$  ( $d$ ). A comparison of the square and circular U-channel packaging substrates is presented in Figure 17.

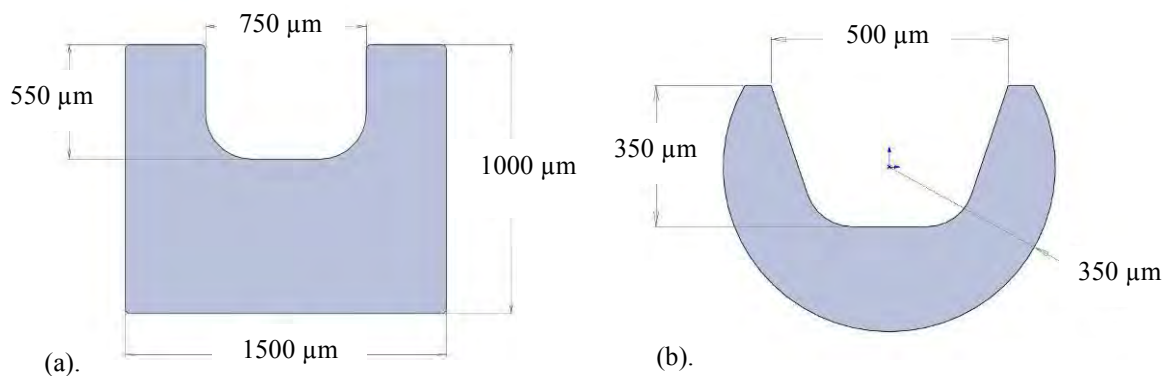


**Figure 17 Schematic illustrations of: (a) a square U-channel sensor packaging substrate; and (b) a circular U-channel packaging substrate.**

With reference to Figure 17, the two packaging substrates were examined using optical and electron microscopy. Image analysis was performed on the sensor package to investigate

dimensional consistency and visual roughness of the U-channel groove and the outer surfaces; samples were selected at random from a single batch of packaging substrates. The substrates were supplied by the manufacturer in a standard length of 50 mm. The length was reduced using a diamond-tipped pen-cleaver to the required packaging dimensions, i.e. ~30 mm.

### 3.3.7 Consistency of the Sensor-to-Packaging Bonding Region

The positioning of the sensor within the packaging substrate was examined using optical microscopy. Details of the AE sensor packaging procedure can be found in Section 3.2.2. The end-profile of the sensor package was imaged to address: (i) the location of the fibres with respect to the U-channel; and (ii) the degree of resin flow around the fibres. Five square U-channel packaged surface-mounted sensors were potted within a cold-setting embedding resin (Epofix; Struers Ltd, UK) and cured at room temperature for a minimum period of 8 hours. The surface of the potted sensors was abraded using silicon-carbide grinding papers (800-2500 grit). The samples were then polished using a 1  $\mu\text{m}$  diamond solution and a synthetic polishing cloth (MD Nap; Struers Ltd, UK) to enhance the image quality. A 1.3 megapixel CMOS camera (PL-A662; PixeLINK, Canada) was used for capturing the end-profile image of the sensors. The camera was attached to the trinocular port of an optical microscope (Axioskop, Carl Zeiss AG, Germany).

### 3.3.8 Evaluation of the Sensors Pre- and Post-Packaging Average Signal Level (ASL)

The average signal level (ASL) of the fibre-optic sensor was determined before and after packaging. The ASL was obtained as follows: The output fibres of a pre-packaged fibre-optic

sensor were removed from the optical detector ports (see Figure 9) of the coupler fabrication unit and were connected to the fibre-optic sensor interrogation unit. During this process, the sensor was retained in the vacuum clamps. The acoustic emission data acquisition system was connected to the fibre-optic sensor interrogation unit as shown in Figure 11. The threshold level for signal acquisition was set at a value to ensure that a continuous “noise” signal from a fabricated sensor could be obtained. The 40 dB<sub>AE</sub> threshold corresponds to a signal voltage of 10 mV based on an amplified gain of 40 dB<sub>AE</sub>. The optical noise level of the laser was first obtained using the same procedure of lowering the threshold into a region whereby continuous signals were recorded. The preset threshold required by the AE system in order to avoid continuous noise from the laser was 42 dB<sub>AE</sub>. ASL was measured over a 1-minute period to ensure adequate sampling. The output fibres were re-connected to the output detector ports of the coupler fabrication unit and the sensor was packaged according to the procedure defined in Section 3.2.2. The ASL was then obtained after packaging for comparison using the same procedure. The ASL was obtained for both the square U-channel and circular U-channel packaged sensors.

### 3.3.9 Optimisation of the Repeatability of the Packaging Process used for Sensors Destined for Embedded Applications

During the initial stages of this research project, approximately 10% of sensors destined for embedment in composite materials survived the packaging process. This was understood to relate to the inexperience of the operator as well as limitations associated with the procedures that were used to carry out the packaging process. The limitations included: (i) the need for an additional temporary fibre clamp when the vacuum was removed from the chuck; (ii) manual

traversing of the capillary package using a crochet needle; and (iii) no lateral support for the traversing capillary. The secondary fibre clamp is highlighted in Figure 10. Due to the combined effects of the three limitations discussed, the likelihood of sensor fracture was high.

To overcome the abovementioned limitations, a permanent magnetic clamping block and translation stage were integrated onto the coupler fabrication unit. The additional components provided: (i) a permanent mount for retaining the optical fibres during packaging within the small-diameter capillary; and (ii) controlled movement and lateral support for the small-diameter package when traversed along the bare tapered fibres. A schematic illustration of the modified coupler fabrication system with: (a) the magnetic clamping block; and (b) the translation stage are presented in Figure 18.

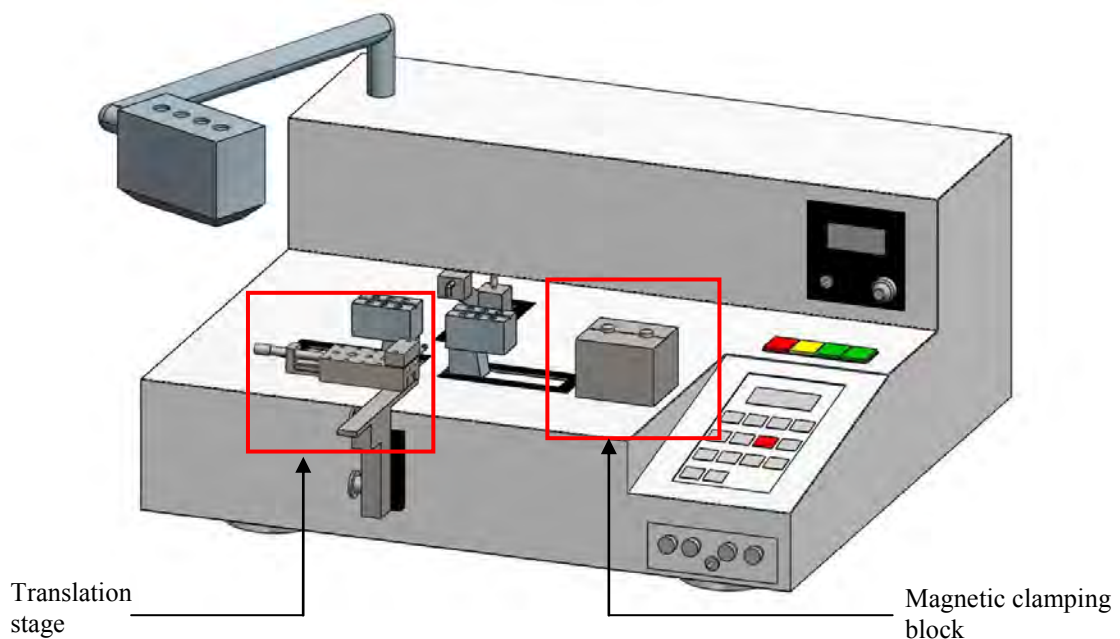


**Figure 18** A schematic illustration of the coupler fabrication unit used to fabricate the fibre-optic AE sensor. The magnetic clamping block and translation stage are highlighted (not to scale).

(a) Magnetic Clamping Block

The magnetic clamping block was designed as a replacement tool for the secondary fibre clamp. The block was machined using a standard-grade carbon steel. The dimensions of the block were 30 (*w*) x 40 (*l*) x 36.35 mm (*d*). A 500  $\mu\text{m}$  groove was machined into the top surface of the block to accommodate two coated optical fibres. The height of the groove was aligned with the vacuum chuck to avoid fibre bending. Two magnetic fibre clamps were used to secure the fibres within the groove during sensor fabrication. The block was bonded to an existing mount attached to the upper face of the coupler fabrication system. An enlarged view of the magnetic clamping block is presented in Figure 19.

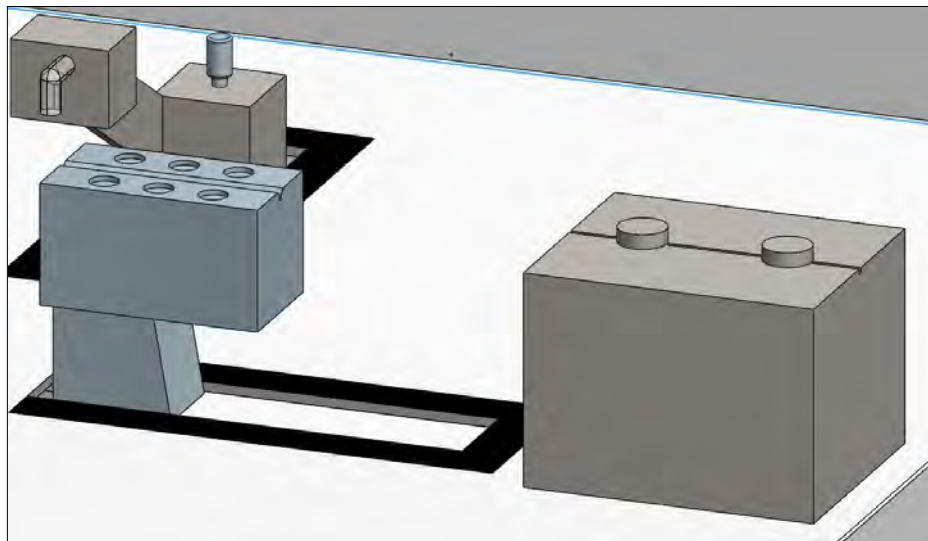


**Figure 19** A schematic illustration of the close-up view of the magnetic clamping block (not to scale).

(b) Supported Translation Stage

A 25 mm linear motion translation stage (422-1sa; Newport Spectra-Physics Ltd, UK) was fixed to the existing 2-axis ( $y$  and  $z$ ) translation bracket on the coupler fabrication unit. The linear stage was screw-driven and provided high resolution motion; this was made possible by the precision pitch angle of the screw. A custom aluminium fixture was machined and attached to the upper-face of the linear translation stage. The purpose of this attachment was to provide lateral support for the capillary as it was traversed during packaging. The custom fixture had a protruding arm onto which the capillary could attach itself during motion. Sensor fabrication trials were undertaken using the additional components. An enlarged view of the translation stage is presented in Figure 20.

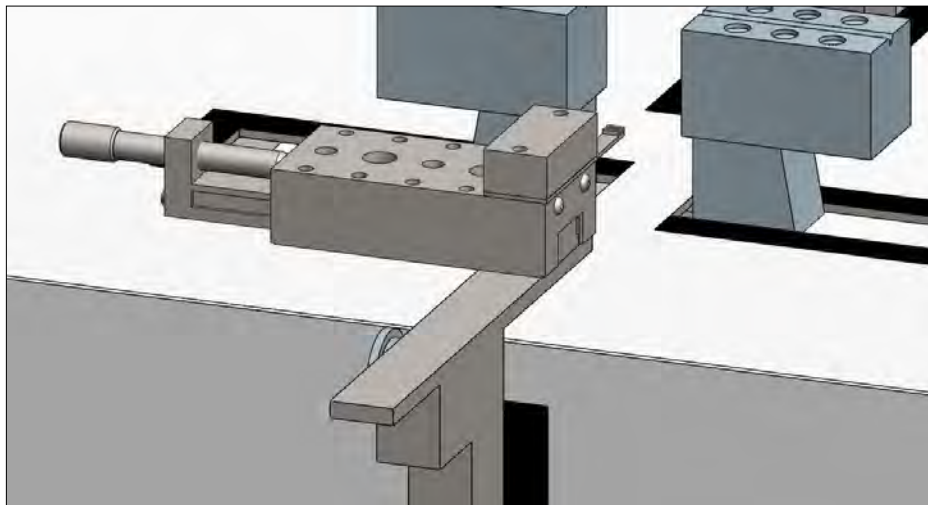


**Figure 20** A schematic illustration of the close-up view of the support translation stage (not to scale).

### 3.3.10 Optimisation of the Packaging Substrate Design used for Sensors Destined for Embedded Applications

An optimised packaging substrate was evaluated to determine if the fabrication success rate could be improved; the optimised package was a precision micro-bore square capillary. The cross-sectional area of the capillary bore was larger than the conventional package and was therefore more likely to accommodate the bare tapered optical fibre when traversed without risk of damage. The dimensions of the micro-bore square capillary were 700  $\mu\text{m}$  and 500  $\mu\text{m}$  for outer and inner widths respectively. A schematic illustration of the different packaging media are presented in Figure 21.

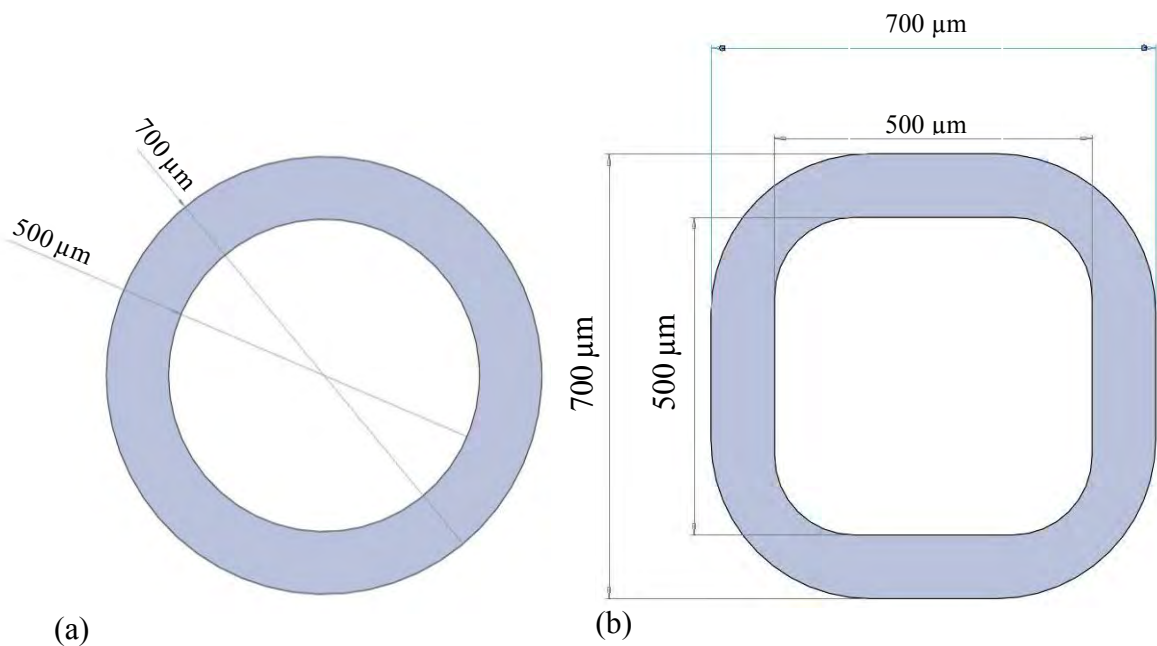


**Figure 21 Schematic illustrations highlighting the dimensions of: (a) the conventional capillary package; and (b) the precision micro-bore square capillary used to package the embeddable fibre-optic AE sensor.**

Post sensor fabrication, the output fibres leads were positioned within the precision aligned groove of the magnetic clamping block and clamped at two locations using fibre magnets. At this stage, vacuum was removed from the clamp whilst maintaining tension on the fibres. The capillary was fed along the vacuum chuck groove using a metal rod and positioned with a 2 mm length overhanging beyond the end of the chuck; the overhanging capillary is highlighted in Figure 22. The supported translation stage was positioned so that the capillary carrier region was in contact with the overhanging capillary. The capillary could then be traversed along the tapered fibre section, maintaining lateral support along the length of the sensors tapered region.

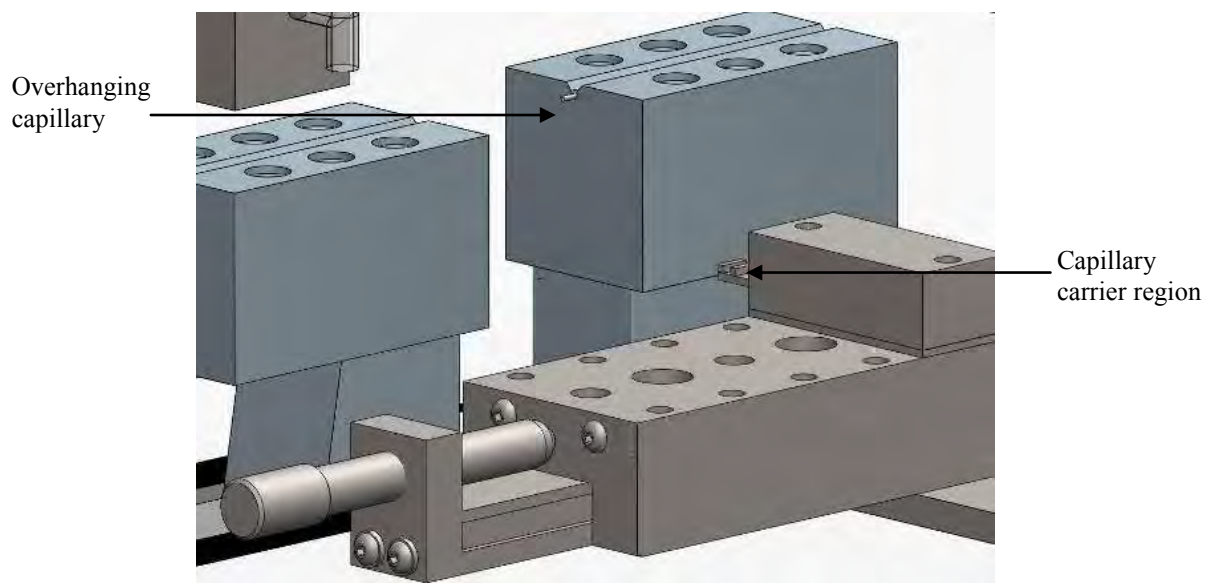


**Figure 22 A schematic illustration highlighting the a close-up view of the overhanging capillary and the translation stage capillary-carrier region (not to scale).**

### 3.3.11 Embedment of the Fibre-Optic AE Sensor

Composite specimens with the embedded fibre-optic AE sensors were fabricated using VTM-264 prepregs (Advanced Composites Group, UK). All composite specimens used within this research project were autoclave processed; the procedures and details of the materials used in the production of the composite specimens are provided in Appendix-B. The fibre-optic sensor was embedded in the prepregs at the lamination stage. The AE sensors were embedded in 8-ply uni-directional prepregs. The sensors were positioned between the central 2-ply along the same orientation as the adjacent reinforcing fibres. The sensors were packaged using the precision micro-bore capillary and were cleaned prior to the lamination stage. After lamination of the 8-ply prepregs, the lead-out portions of the AE sensor were protected at the composite-air interface using Teflon tubing. Temperature resistant tape was used to seal the end of the Teflon tubing to minimise resin flow beyond the end of the tubing.

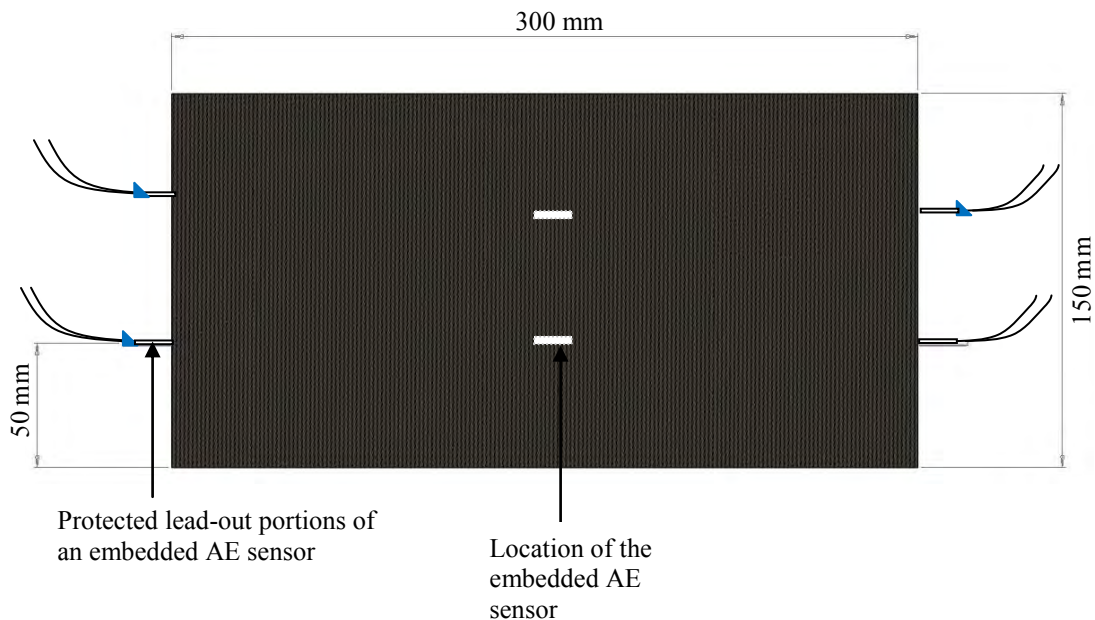


**Figure 23** A schematic illustration highlighting the locations of the embedded fibre-optic AE sensors in the composite specimen.

For reference, all sensors embedded in composite specimens were assigned the coding of EM04-xxx, where xxx refers to the database number.

### 3.3.12 Online Monitoring of the Fibre-Optic AE Sensor during Composite Fabrication

The autoclave used to process the prepregs was instrumented with a fibre-optic flange assembly; the purpose of the flange was to allow for real-time on-line monitoring of the fibre-optic AE sensor response during processing of the carbon-fibre prepregs. The AE sensors input and output fibres were fusion spliced to individual optical fibres inside the autoclave and connected to the acoustic emission interrogation unit via the external fibres of the fibre-optic flange assembly.

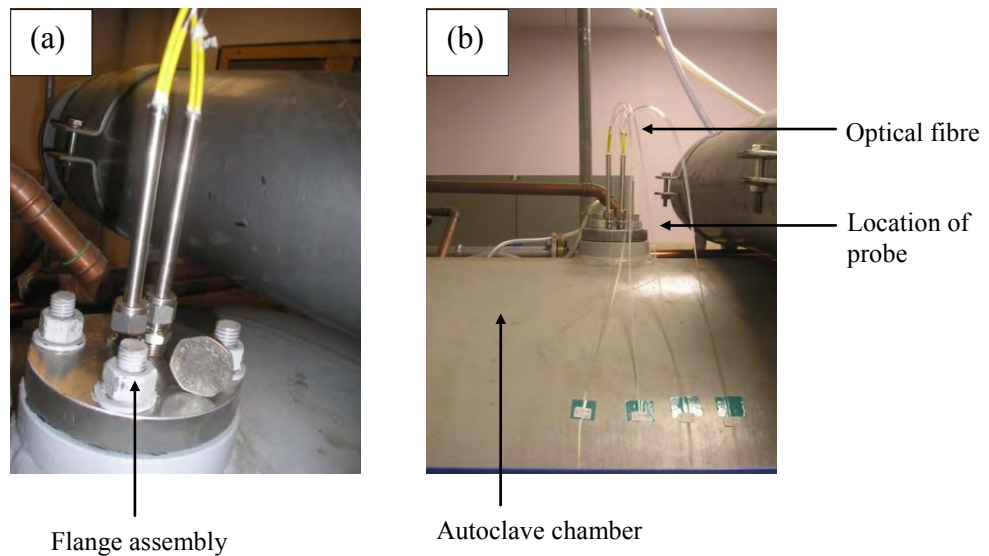


**Figure 24 Photographs of: (a) the fibre-optic flange assembly; and (b) location of the fibre-optic flange assembly on the autoclave.**

The fibre-optic flange assembly was located on the top of the autoclave and was designed to bolt onto a redundant pressure fixture, enabling fibres to be fed directly into the internal chamber. Fibre leads were also accessible on the outside of the autoclave for connection to sensor interrogation equipment. A photograph of the fibre-optic probe is presented in Figure 24. The flange assembly was pressure tested for safety prior to any work being undertaken.

The data acquisition system was setup to monitor the change in the average signal level of the sensor during composite processing. The recorded data could then be used to determine: (i) if the sensor had failed at any time during processing; (ii) the stage of processing any failure did occur; and (iii) any changes in the sensor performance with reference to the ASL as a result of cure. Data were acquired continuously throughout the cure process and during subsequent cooling.

### 3.3.13 Analysis of the Pre- and Post-Embedment Sensor Coupling Ratio Analysis

The effect of sensor embedment on the coupling ratio of the fibre-optic AE sensor was evaluated pre and post-processing. The AE sensors input and output fibre leads were fusion spliced to commercial FC/PC connectors. The input fibre was connected to the laser-source housed within the interrogation system. The measured power at each fibre output was obtained using an optical power meter (PM100; Thorlabs Ltd, UK) and the coupling ratio was defined.

### 3.4 Evaluation and Characterisation of the Fibre-Optic Acoustic Emission Sensor

#### 3.4.1 Evaluation of the Consistency of the Hsu-Nielsen (HN) Source

The repeatability of the Hsu-Nielsen (HN) source with reference to acoustic signal generation was investigated. A schematic illustration of a Hsu-Nielsen source is presented in Figure 25.

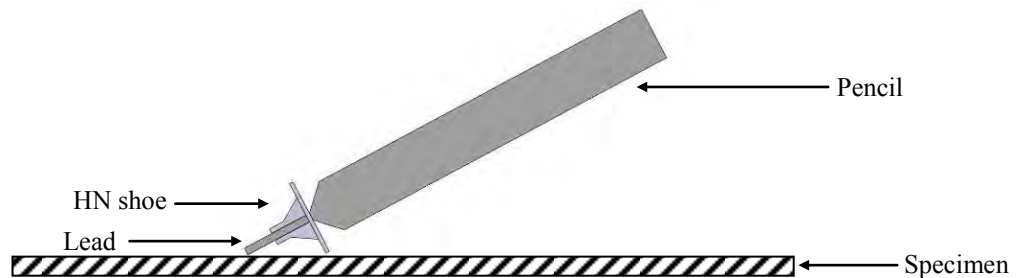


**Figure 25** A schematic illustration of a Hsu-Nielsen source (pencil lead break).

With reference to Figure 25, a pencil lead break was performed by making contact between the host material and pencil and applying sufficient force to fracture the lead. A HN source generates a broadband acoustic signal similar to a realistic acoustic event. The AE signal is not actually generated by the lead fracture but instead, it is the release of the materials surface displaced by the lead tip. A 2H pencil-lead with a diameter of 0.5 mm and a length of 2.5 mm was used as per ASTM E976–05 (ASTM, 2005). A collar was attached to the end of the pencil to ensure that the incident angle between the lead and the material was constant; this was used in order to improve the repeatability in the lead break. A Pentel<sup>®</sup> retractable pencil was used to perform all of the pencil lead breaks during this project.

A square U-channel packaged fibre-optic AE sensor was surface-mounted in the centre of an aluminium plate using an ultrasonic coupling gel (UGEL250; Anagel UK). The dimensions of the plate were 300 mm ( $l$ ) x 300 mm ( $w$ ) x 1.6 mm ( $d$ ). Thirty pencil lead breaks were performed on the aluminium plate at a distance of 100 mm along the 90° axis in relation to the longitudinal axis of the sensor. The signal response from each lead break was recorded using the PCI-2 acoustic emission data acquisition system. The mass and length of each pencil lead was noted. The repeatability of the pencil breaks were evaluated with respect to: (i) the length and mass of each lead; and (ii) the acoustic signature of each lead break with respect to signal amplitude and dominant frequency content. The response of the fibre-optic AE sensor was compared with a conventional electrical-based AE sensor.

#### 3.4.2 Evaluation of the Directional Sensitivity of the Fibre-Optic Sensor

The directional sensitivity of the fibre-optic AE sensor was assessed using pencil lead breaks. A square U-channel packaged fibre-optic sensor was surface-mounted in the centre of an aluminium plate (see Section 3.4.1) using ultrasonic coupling gel (UGEL250; Anagel, UK). Pencil lead breaks were performed at 0°, 45° and 90° orientations in relation to the longitudinal orientation of the sensor. The pencil breaks were performed at a distance of 100 mm. The recorded signal amplitude at each orientation was obtained from the mean value of ten pencil lead breaks. The signal response from five sensors fabricated using the SM04-1 optical fibre were characterised and compared with five sensors fabricated using the SM600 fibre. The response of a WD piezoelectric transducer was obtained as a comparison for the fibre-optic AE sensor. The WD sensor was positioned in the same location as the fibre-optic

sensor in order to obtain a direct comparison. A schematic illustration of the experimental setup is presented in Figure 26.

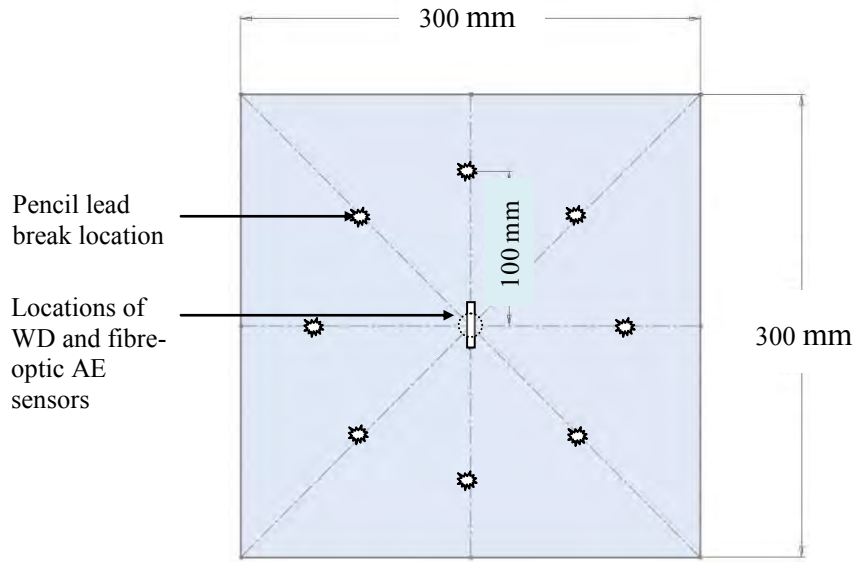


**Figure 26 A schematic illustration of the experimental setup used to characterise the directional sensitivity of the fibre-optic acoustic emission sensor.**

### 3.4.3 Evaluation of the Sensor Remounting Procedure

The effect of removing and remounting the fibre-optic AE sensor on the directional sensitivity response was investigated. The de-bonding tests were performed on the aluminium plate. The fibre-optic AE sensor was surface-mounted as per Section 3.4.1. Pencil lead breaks were used to assess the response of the sensor as indicated in Figure 26. Ten lead breaks were performed at each location. The directional sensitivity response was recorded and the sensor was carefully de-bonded using rubber-tipped tweezers. The package was cleaned and the

sensor was re-mounted to the test specimen and the directional response was recorded. Data from five removal and remounting cycles was obtained and compared.

#### 3.4.4 Evaluation of the Coupling Medium used for Sensor Mounting

The response of a surface-mounted acoustic emission sensor as a function of the coupling medium was characterised using pencil lead breaks. A square U-channel packaged fibre-optic sensor was surface-mounted in the centre of an aluminium plate as per Section 3.4.1. Three adhesives were used to evaluate the effect of bonding properties on the signal response, namely: (i) an ultrasonic coupling gel (UGEL250; Anagel, UK); (ii) a non-corrosive silicone rubber adhesive (494-118; RS Components, UK); and (iii) a cyanoacrylate adhesive (CN; TML Ltd, UK). Pencil lead breaks were performed as indicated in Figure 26. Ten pencil lead breaks were performed at each location. Five fibre-optic sensors were evaluated; the response of each sensor was evaluated using all three adhesives (four conditions). The sensor was removed from the plate using rubber-tipped tweezers after each adhesive test and cleaned. The order in which the adhesives were tested was as follows: (i) ultrasonic coupling gel; (ii) un-cured silicone rubber; (iii) cured silicone rubber (20-hour cure); and (iv) cyanoacrylate adhesive.

#### 3.4.5 Directional Sensitivity of the Small-Diameter Circular U-Channel Packaged Sensor

The directional sensitivity procedure outlined in Section 3.4.2 was repeated to obtain the orientation response of the AE sensor packaged using the small-diameter U-channel packaging substrate. Owing to the size and low weight of the small-diameter sensor package,

ultrasonic coupling gel was not used to mount the sensor; the use of a low viscosity couplant would increase the likelihood of the sensor rolling over under the weight of the optical fibre during the test. A silicone rubber coupling adhesive was used in place of the ultrasonic coupling gel to provide greater bonding stability.

#### 3.4.6 Evaluation of the Directional Sensitivity of the AE Sensor in Composite Materials

The directional sensitivity of the fibre-optic AE sensor was assessed using pencil lead breaks. A square U-channel packaged fibre-optic sensor was surface-mounted in the centre of an 8-ply cross-ply carbon-fibre epoxy composite specimen. The composite plate was fabricated from VTM-264 prepregs (Advanced Composites Group, UK) and had dimensions of 300 mm ( $l$ ) x 300 mm ( $w$ ) x 2.5 mm ( $d$ ) and a lay-up sequence of  $0,90_2,0_s$ . Pencil lead breaks were performed at  $0^\circ$ ,  $45^\circ$  and  $90^\circ$  orientations in relation to the longitudinal orientation of the sensor. The pencil breaks were performed at a distance of 100 mm. The recorded signal amplitude at each orientation was obtained from the mean value of ten pencil lead breaks. The signal response from sensors fabricated using the SM04-1 optical fibre were characterised. For comparison, the response from a WD piezoelectric transducer to the pencil lead breaks was obtained. A schematic illustration of the experimental setup is presented in Figure 27.

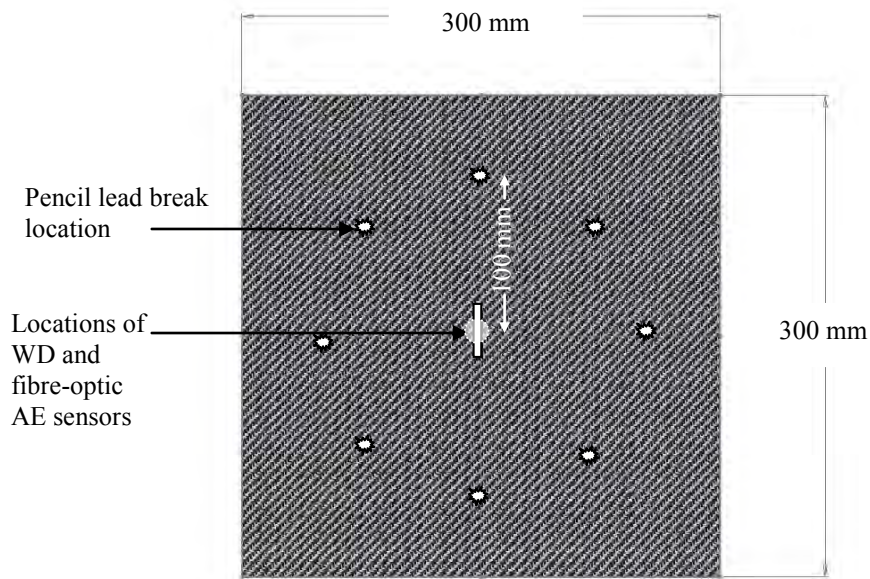


**Figure 27** A schematic illustration of the experimental setup used to characterise the directional sensitivity of the fibre-optic acoustic emission sensor using a cross-ply composite plate (VTM-264).

### 3.4.7 Evaluation of the response of an Embedded Fibre-Optic AE Sensor in Composite Materials

The response of the embedded AE sensors was obtained using pencil lead breaks. The preliminary tests were performed to ensure that the sensor had survived processing. Pencil lead breaks were performed at incremental distances from the embedded fibre-optic sensor. The locations of the pencil lead breaks relative to the sensor are highlighted in Figure 28.

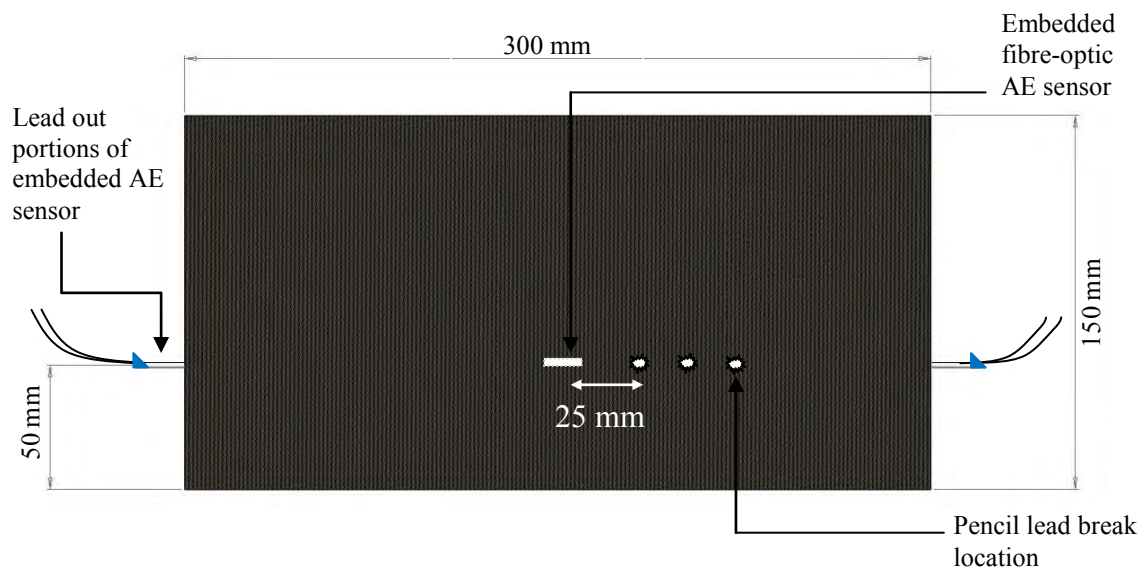


**Figure 28** A schematic illustration highlighting locations of pencil lead brakes used to confirm the response of the embedded fibre-optic AE sensors.

### 3.5 Mechanical Testing: Interlaminar Crack Propagation

#### 3.5.1 Monitoring of Mode-I DCB tests using the Small-diameter Circular U-Channel Packaged Sensor

The response of the small-diameter Circular U-channel packaged fibre-optic AE sensor was characterised using the Mode-I double-cantilever beam (DCB) test. The purpose of the test was to determine if sensors packaged in the circular U-channel packaging substrate were sensitive to acoustic emissions generated from interlaminar crack propagation in uni-directional composite specimens. The test methodology was as follows:

Test specimens were fabricated in accordance with BS ISO 15024:2001 (BS ISO, 2001). A 16-ply uni-directional composite plate was fabricated using VTM-264 prepregs (Advanced

Composites Group, UK) and was processed in an autoclave. The dimensions of the composite plate were 300 mm ( $l$ ) x 300 mm ( $w$ ). A 13  $\mu\text{m}$  thick polytetrafluoroethylene (PTFE) insert with dimensions of 350 mm ( $l$ ) x 122 mm ( $w$ ) was embedded between plies eight and nine during lamination. The composite plate was cut to the required specimen dimensions of 150 mm ( $l$ ) x 20 mm ( $w$ ) using a diamond-tipped rotating wheel cutter. Due to the width of the cutting blade, 2 mm was lost from the length of the plate. The PTFE insert was embedded to create an initial delamination of 60 mm. A schematic illustration of the plate with the embedded PTFE insert is presented in Figure 29.

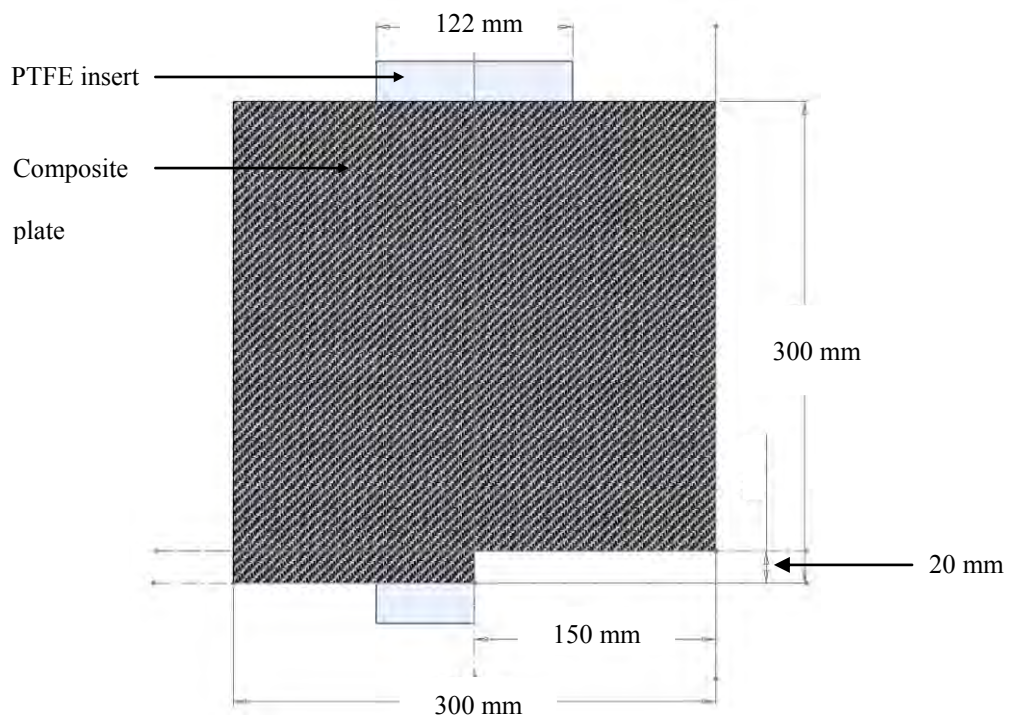


**Figure 29** A schematic illustration of the 16-ply composite plate with a PTFE insert. Section removed to highlight dimensions of the Mode-I coupon.

Stainless steel loading blocks (see Figure 32 (b)) with dimensions 15 mm ( $l$ ) x 20 mm ( $w$ ) x 15 mm ( $d$ ) were bonded onto the composite specimens in the locations shown in Figure 30. An 8 mm pin-hole was machined through the blocks to allow for attachment to a custom-designed loading fixture. The loading blocks were bonded using a toughened structural adhesive (Scotchweld 9323; 3M, UK). The adhesive was cured at 66 °C for 120 minutes. Correction fluid was applied along one edge of the specimen; the start point of the correction fluid was the edge of the PTFE insert. Markers were inscribed on the correction fluid along the specimen length for reference purposes during loading. Marker points corresponding to the first 10 mm in 1 mm increments and thereafter every 10 mm up to 50 mm were drawn on using black ink. 1 mm increments were also marked for measurements between 50 and 55 mm. The test specimens were stored in a desiccator at ambient temperature until required.

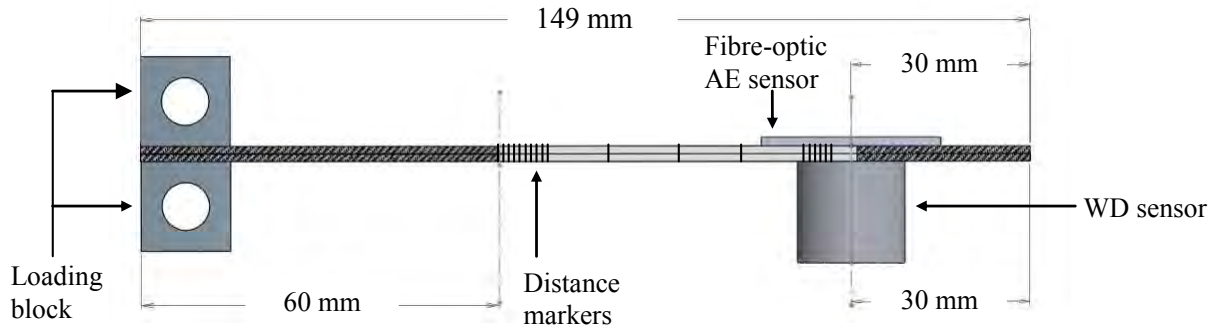


**Figure 30** A schematic illustration of the specimen of the 16-ply Mode-I test specimen (not to scale).

A small-diameter circular U-channel packaged fibre-optic AE sensor was bonded to the top face of the specimen at a distance of 30 mm from the unloaded edge. For reference purposes, a WD piezoelectric transducer was positioned on the bottom face of the coupon. The WD sensor was positioned at a distance of 30 mm from the edge and was bonded using a silicone

rubber adhesive. The locations of the acoustic emission sensors are presented in Figure 30. A photograph of the sensor locations is provided in Figure 31.

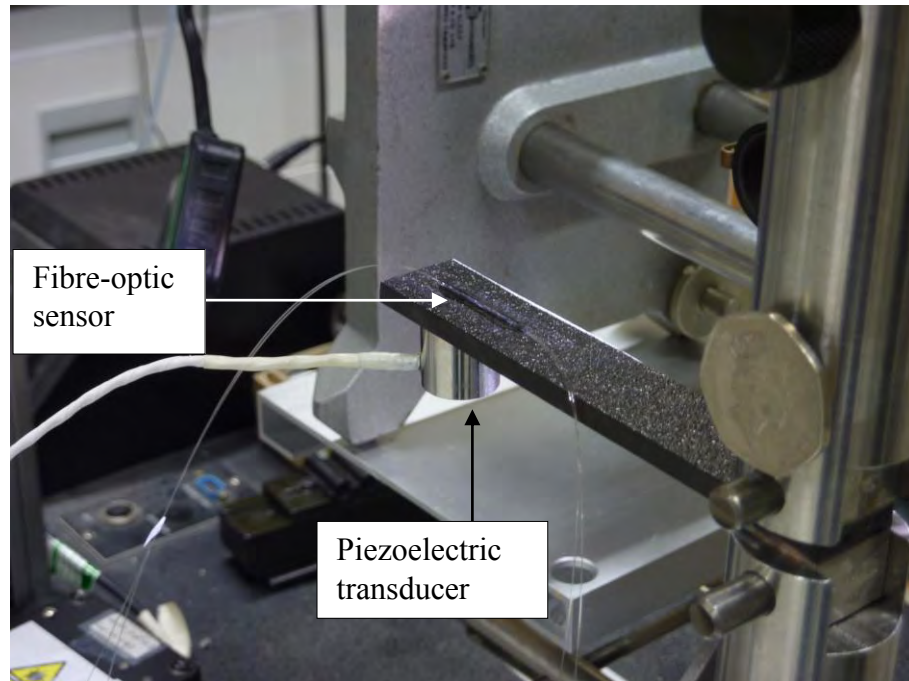


**Figure 31** A photograph of the sensor locations on the mode-I coupon.

The test procedure was performed in accordance BS ISO 15024:2001 (BS ISO, 2001). The composite specimen was secured by aligning the holes of the test fixture and loading blocks using a steel pin. Two test fixtures (see Figure 32(a)) were secured onto a universal tensile test machine (Model no.5566; Instron, UK); one fixture was mounted to the travelling cross-head and the other to the load cell at the base of the Instron.

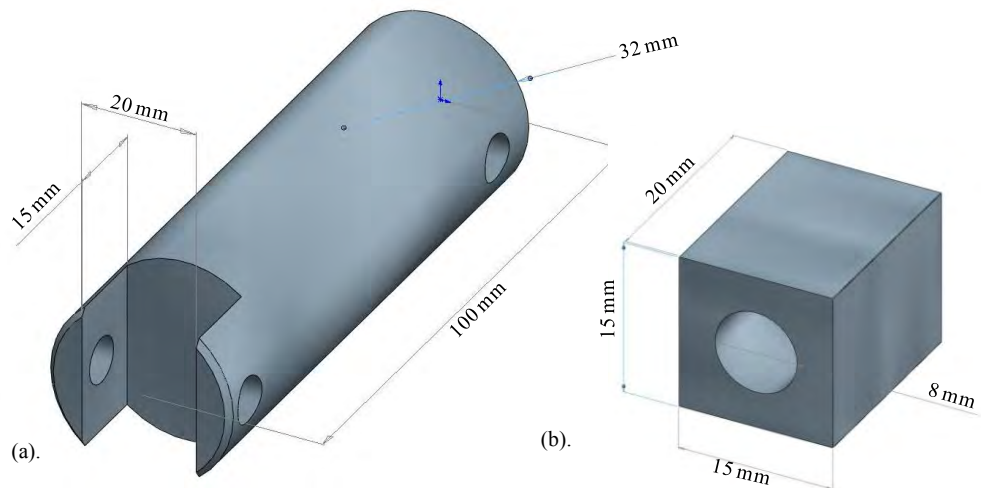


**Figure 32** A schematic illustration of: (a). custom-designed test fixture secured to Instron mechanical test equipment; and (b). loading blocks bonded to Mode-I test specimen.

A microscope capable of  $x$ -axis translation was positioned in-line with the mid-plane of the composite specimen. The microscope was used to continuously monitor the propagation of the delamination during loading. A constant displacement rate of 1 mm/min was used to propagate the starter delamination. The specimen was pre-loaded in tension until the crack-tip had propagated 3 mm along the composite specimen. The sample was unloaded using a cross-head displacement rate of 5 mm/min. The sample was then re-loaded at a cross-head displacement rate of 1 mm/min until the crack-tip had propagated past the 55 mm marker point. During the initial pre-load and re-load, an electronic pulse was sent to the AE-win system each time the crack-tip passed a reference marker point. A signal generator (Model no.33220A; Agilent Technologies, USA) was used to initiate the electronic pulse time-stamp. Time-stamping was required to enable cross-referencing between the crack-tip position and the load-displacement output. Five pencil lead breaks were performed on each specimen prior to loading to confirm that the sensor was in working order. Data from the acoustic emission

sensors was acquired continuously during the test. Five specimens were evaluated as recommended in the standard.

# CHAPTER 4

## Evaluation of the Sensor Manufacturing Process

## 4 Evaluation of the Sensor Manufacturing Process

---

### 4.1 Evaluation of the Sensor Fabrication Procedures

This section discusses the parameters that were considered to be important with regard to the production of the fibre-optic acoustic emission sensor. These parameters were as follows:

- (i) optical fibre surface cleanliness prior to fusion;
- (ii) draw-rate and draw-length of the taper profile;
- (iii) symmetry of the cross-over points of the stripped optical fibre pair prior to fabrication;
- and (iv) symmetry of the taper profile.

It is important to note that some of the above-mentioned parameters are inter-related. For example, the symmetry of the cross-over points of the stripped optical fibres would dictate the taper profile of the fibre-optic sensor. Precise control of the draw length and the temperature profile at the region of fibre fusion has also been shown to influence the geometry and mechanical properties of the coupler; the use of a high temperature flame source, i.e.  $> 1300$  °C enables greater fusion of the cladding between the two optical fibres; this is thought to improve the mechanical properties of the device (Shi and Wu, 2002). The parameters that can be measured directly from the coupler fabrication unit include the following: (i) excess-loss (dB); coupling ratio; and (iii) draw-length. The relationships between each of these parameters will be discussed in the following sections.

#### 4.1.1 Preparation of the Optical Fibre for Sensor Fabrication

A 20 mm section of the acrylate coating from a sample of the SM04-1 optical fibre was removed using a hand-held micro-stripping tool. Once the coating was removed, the surface was cleaned using iso-propanol alcohol and a piece of lint-free tissue. Two types of micro-stripping tool were evaluated to determine the volume of residual coating on the fibre surface after stripping. The two micro-stripping tools evaluated were: (i) CFS-2; Clauss, USA; and (ii) MS-1-FS; Micro Electronics Inc, USA. Scanning electron micrographs (SEM) of the stripped and cleaned sections of optical fibre are presented in Figure 33. The two micrographs highlight the surface cleanliness after coating removal using the two different stripping tools.

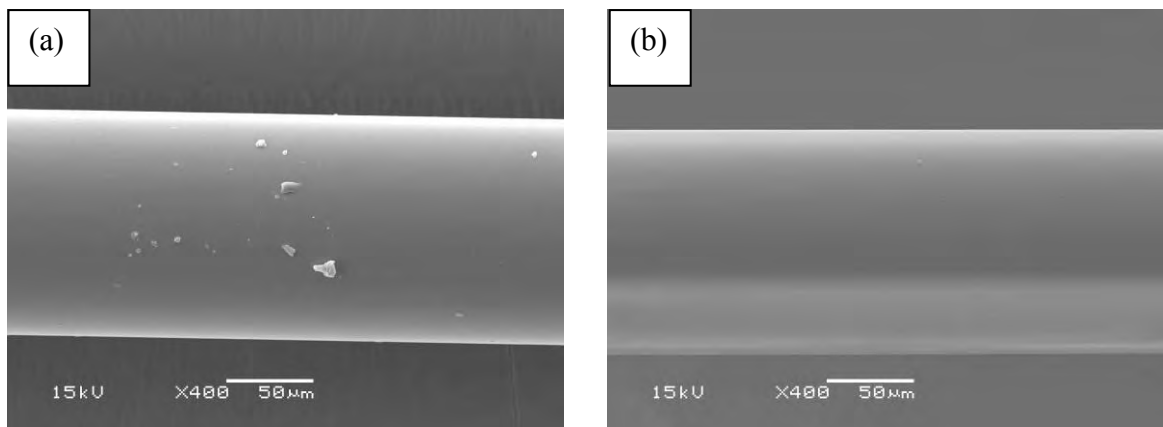


**Figure 33 SEM micrographs illustrating two stripped SM04-1 optical fibres: (a) coating removed with the Micro Electronics Inc stripping tool; and (b) coating removed with the Clauss stripping tool.**

With reference to Figure 33(a), fragments of the acrylate coating are visible on the surface of the optical fibre. In contrast, no residual coating is visible on the section of optical fibre in

Figure 33(b). The effect of coating removal on the residual properties of an optical fibre has been reviewed in the literature (Nagata et al., 1994; Matthewson et al., 1997; Barnier et al., 2000; Jacobs, 2001; Tarpey et al., 2002; Mia et al., 2004; Schmid and Toussaint, 2007; Lee et al., 2011). Various methods of coating removal have been proposed, including: (i) mechanical stripping using hand-held tools; (ii) chemical etching; and (iii) laser ablation. These methods are reported to have a negative influence on the resistance of the fibres to damage. Miao et al. (2004) suggested that chemical etching reduced the fatigue resistance by 10%. Barnier et al. (2000) evaluated laser ablation and found that both CO<sub>2</sub> and KrF lasers degraded the optical fibre; no quantitative values were given. Exposure of the surface of the glass fibre to moisture within the environment has been shown to increase the susceptibility to fibre damage; fatigue cracks were found to propagate from surface defects in the glass-fibre resulting from the breakdown of the Si-O bonds (Schmid and Toussaint, 2007). Previous research has also indicated that mechanical stripping and cleaning of the fibres using alcohol-based substances increased the likelihood of surface cracking (Nagata et al., 1994; Matthewson et al., 1997). Nagata et al. (1994) evaluated the effects of mechanical stripping on the fibres integrity and found that approximately 15% of all stripped fibres fractured prematurely. The quality of the blade was attributed to an increased probability of damage; the authors proposed that a blunt or chipped blade resulted in additional force required to remove the jacket from the fibre. Tarpey et al. (2002) also evaluated the effects of removing polyimide coatings from optical fibres. The authors concluded that poor handling of the fibres was the contributing factor in the degradation of the fibres properties. In the current study, no apparent defects were visible on the surface of fibre after cleaning. All subsequent sensors were prepared using a single wipe of the bare fibre surface using an iso-propanol saturated cloth and were stripped using the Clauss stripping tool; a single wipe over the fibre

was assumed to be sufficient for optimal surface preparation (Jacobs, 2001). In addition, after removal of the fibre coating, handling was kept to a minimum in order to: (i) reduce the likelihood of degradation in the mechanical properties (Nagata et al., 2004); and (ii) minimise possible surface contamination (Barnier et al., 2000).

#### 4.1.2 Repeatability of the Characteristics of the Fabricated Sensors

The repeatability of the procedures used to manufacture the fibre-optic sensor were evaluated to assess if the characteristics of the sensors were consistent. Three batches of optical fibre were compared. Twenty sensors were fabricated from each of the following fibre reels for comparison: (i) a reel of SM04-1 optical fibre that was manufactured in 2005; (ii) a reel of SM04-1 optical fibre that was purchased in 2008; and (iii) a reel of SM600 optical fibre that was purchased in 2008. The three reels were assigned to groups-1, 2 and 3 respectively. With reference to group-1, the history of the fibre with respect to storage conditions was not known at the time of sensor manufacture. For groups-2 and 3, the fibre was stored in the dark under ambient conditions until required. The characteristics of the sixty sensors were analysed with respect to: (i) excess-loss; (ii) coupling ratio; and (iii) draw-length. The expression used to define the excess loss parameter was (Joinwit, date unknown):

$$Excess - loss (dB) = -10 \log \frac{\sum_m P_m(o)}{P_n(i)} \quad \text{Eq. 9}$$

where  $P_m(o)$  is the output power detected at a single port and  $P_n(i)$  is the incident power from the light source that was used to illuminate the lead-in fibre. Excess-loss was used as a

quality control parameter during the fabrication of the sensors; a low excess-loss, i.e. < 3 dB, was taken to represent a sensor with an acceptable output light intensity. The coupling ratio was also used as a quality control parameter during the fabrication of the fibre-optic sensor. The coupling-ratio was defined as (Joinwit, date unknown):

$$R_m = \frac{P_m(o)}{\sum_{m=1} P_m(o)} (\%) \quad \text{Eq. 10}$$

where  $R_m$  is the coupling ratio and  $P_m(o)$  is the output power detected at a single port. The coupling ratio is presented as a percentage. A variation in the 50% coupling ratio of approximately  $\pm 10\%$  was deemed to be acceptable. The characteristics of the sensors from the three groups are shown in Table 7.

**Table 7 A summary of the fabrication characteristics for the 60 fibre-optic sensors from groups 1, 2 and 3; standard deviation in parentheses.**

Batch	Excess-loss (dB)	Coupling ratio (%)	Draw-length (mm)
	Mean	Mean	Mean
Sensor group-1	2.20 (0.9)	51.8 (5.9)	9.93 (0.2)
Sensor group-2	1.13 (0.6)	55.1 (2.8)	10.28 (0.2)
Sensor group-3	1.92 (1.0)	52.4 (5.3)	10.05 (0.4)

With reference to sensor group-1, a mean excess-loss of 2.20 dB was recorded with a standard deviation of 0.9 dB. The overall spread of data is presented in Figure 34; a large variance in the set of data was observed. In comparison, a 1.1 dB excess-loss was reported from sensor group-2. A value of 1.1 dB correlates with previously reported literature; Pal et al. (2006) reported excess-loss values within the range 0.5-1.1 dB. The high excess-loss from the

couplers was attributed to the smaller mean taper length of sensors in group-1. Matthews et al. (1987) and Hsieh et al. (2001) proposed that couplers with small taper lengths exhibited sharper taper steps, i.e. a sharp taper angle, and were therefore likely to have high loss due to inefficient coupling of the optical radiation into the second fibre. The mean excess-loss and draw-length measurements for group-3 lie mid-way between groups-1 and 2. The same conclusion can therefore be drawn relating shorter draw lengths to higher loss.

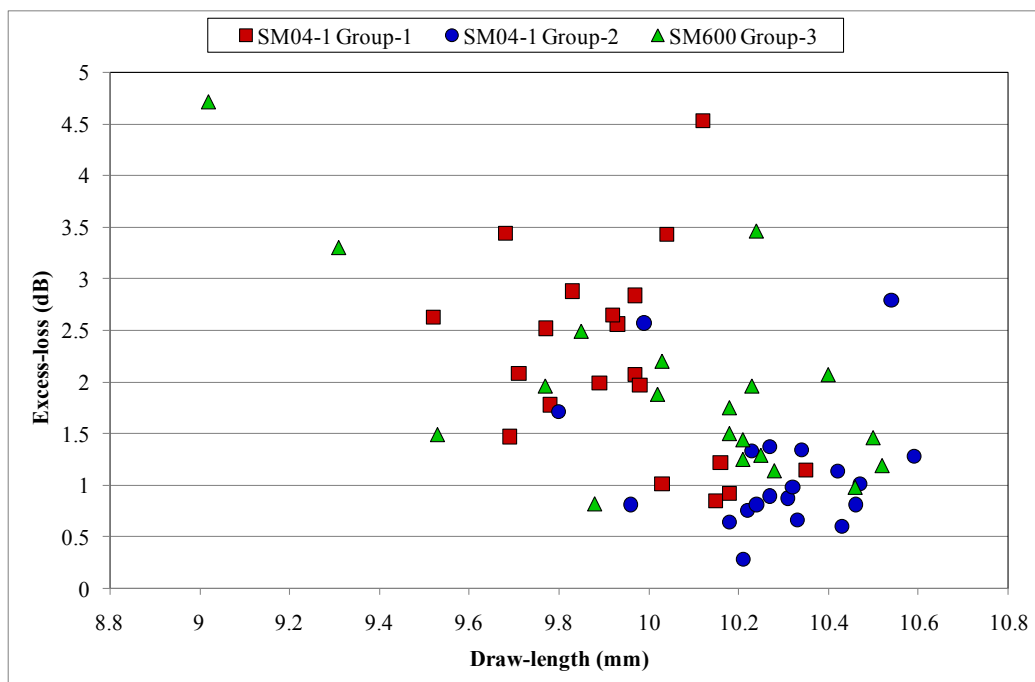


Figure 34 A scatter plot of the comparison of draw length vs. excess loss for sensor groups-1, 2 and 3.

Bures et al. (1983) and Payne et al. (1985) evaluated the effects of optical coupling and insertion-loss in single-mode couplers. The authors noted that the  $LP_{01}$  mode is initially guided along the core of the fibre through the input arm. Upon reaching the start of the tapered region, the mode is decomposed into plane waves. As the angle of incidence equals that of the critical angle, the  $LP_{01}$  mode will refract out of the co-joined cores; it is then

considered a field of the entire cross-section of the coupler. It was proposed that this refraction out of the fibre core occurs close to the neck of the taper and that the main coupling action in mono-mode fibre couplers is between the two lowest-order modes, namely: (i)  $LP_{01}$ ; and (ii)  $LP_{11}$ ; the full cross-section of the co-joined tapered fibres becomes the waveguide for the optical signal. The air-glass interface therefore acts as the boundary between two media with different refractive indices. Beyond the taper, this cladding mode cannot be recaptured by the core. It is proposed that this effect is a significant cause of loss in optical couplers (Burns et al., 1986).

Georgiou and Boucouvalas (1985) further proposed that the excess-loss of the coupler could be minimised by reducing the pulling time required to achieve a defined coupling ratio. The authors inferred that improved fusion of the two fibres could be achieved for slower pull speeds. In the current trials, a pulling rate of 1 mm/min was used to fabricate the coupler; this speed was found to be lower than values obtained from the literature, i.e. 1 mm/second (Hsieh et al. 2001) and 1.2 mm/min (Bilodeau et al. 1990). The effect of hydroxyl content has also been shown to influence the properties of optical fibres as well as the excess-loss in couplers (Lemaire et al. 1993; Takeuchi, 1996). In addition, Takeuchi et al. (1996) proposed that the type of fibre fusion source used to fabricate the coupler could also influence the amount of optical loss. The authors explained that the activation energy required to generate diffusion of the  $\text{OH}^-$  ions did not change during fusion; instead, during elongation, the Si-O bonds are broken due to stress on the fibre which results in the interaction between Si-O and  $\text{OH}^-$ . For a standard oxy-hydrogen flame, as used herein, the diffusion of hydroxyl ions was thought to be small since the activation energy does not change with the fusion conditions. The authors suggested that the use of a micro-heater can increase the water content in the air which leads

to increased diffusion of hydroxyl ions into the fibre. The refractive index (RI) profile of different fibre types is also understood to influence loss in couplers. Georgiou and Boucouvalas (1985) evaluated three types of fibre with different RI cladding profiles, namely; (i) depressed clad; (ii) matched clad; and (iii) raised clad. The authors reported the lowest excess loss from the fibre with the uniform matched clad design. The increased loss in groups-1 and 3 may therefore be attributed to: (i) environmental ageing and UV exposure; (ii) increased diffusion of hydroxyl ions; and/or (iii) a non-uniform RI cladding profile.

With reference to the coupling ratio of the three sensor groups, the variability for draw-length for all groups of sensors was relatively low; the deviation from the mean was approximately  $\pm 10\%$ , which was deemed acceptable with respect to fabrication consistency. The standard deviation for group-2 was the lowest for all three groups. A scatter plot illustrating the relationship between coupling ratio and draw-length for all sixty sensors is presented in Figure 35. Anomalous results were observed in both groups-1 and 3; sensors with coupling ratios of  $\sim 40\%$  were included in the results presented in Table 7. Removal of the anomalous results from the data sets only marginally improved the variation in the recorded mean values.



performance of the sensors, namely: (i) substrate design used to package the sensor; (ii) quality and consistency of the packaging.

Statistical analysis was performed on the data obtained from sensor group-1 and -2. Details of the methodology used can be found in Section 3.3.2. All tests were evaluated based on 95% confidence, i.e. a  $P$ -value of 0.05. The analysis was performed on sensor groups-1 and 2 only, for the following reasons: (i) the fibre was obtained from the same manufacturer, ensuring greater consistency within the results; and (ii) the outcome from the sensor fabrication trials demonstrated an observed variation in sensor properties for the two sensor batches. With reference to Table 8, no statistical significance was reported from tests 1-4; this result indicates that the fabrication parameters do not influence each other. Results from test 5 and 6 do however confirm that the data sets from the two groups were statistically significant.

**Table 8 A summary of the F-test statistical analysis obtained from evaluation of the SM04-1 fibre tests.**

<b>Test Number</b>	<b>Parameters evaluated</b>	<b><math>P</math>-value</b>	<b><math>F</math>-Test value</b>	<b>Statistical significance</b>
1	Draw-length vs. coupling ratio for sensor group-1	3.9	0.27	None
2	Draw-length vs. excess loss for sensor group-1	3.9	0.49	None
3	Draw-length vs. coupling ratio for sensor group-2	3.9	0.82	None
4	Draw-length vs. excess loss for sensor group-2	3.9	0.16	None
5	Excess loss: sensor group-1 vs. sensor group-2	<b>4.1</b>	<b>17.3</b>	<b>High</b>
6	Draw-length: sensor group-1 vs. sensor group-2	<b>4.1</b>	<b>29.7</b>	<b>High</b>

#### 4.1.3 Reliability of the Coupler Fabrication Unit Draw-Control

The reliability and repeatability of the coupler fabrication unit was evaluated with respect to the displacement of the vacuum chucks; the vacuum chucks were used to retain the two optical fibres during fabrication of the fibre-optic sensor. The reliability and repeatability was addressed with reference to: (i) traverse velocity of the vacuum chuck; (ii) the correlation between chuck displacement and the data displayed on the control panel; and (iii) the returning chuck position after sensor fabrication relative to their original starting positions ( $x$  and  $y$ -axis). The relative displacement of the left and right vacuum chucks was evaluated to determine any deviations in the lateral velocity; the relationship between displacement as a function of time for each chuck is shown in Figure 36. The displacement of the chuck was measured manually using a scale that was temporarily bonded to the coupler fabrication unit, adjacent to the chuck.

With reference to Figure 36, both chucks were found to travel at equal velocities. Assuming no slippage of the optical fibres within the chucks, no irregularities in the taper profile were anticipated. Measurement error was found to be small; the error bars are not visible.

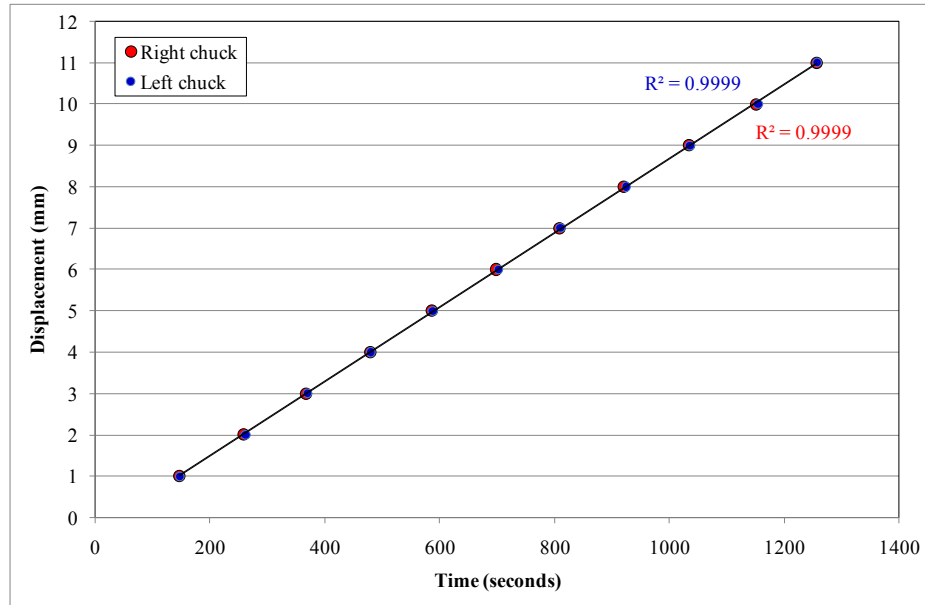


**Figure 36 A scatter plot illustrating vacuum chuck displacement as a function of time for the left and right hand side chucks; the data sets are overlapped.**

Manual measurements of the chuck displacement were compared against the read-out display of the coupler fabrication unit; both measurements were in close agreement. The vacuum chucks were found to return to their initial “home” positions when the fabrication equipment was reset. A consistent chuck spacing of 26.4 mm was recorded. The chuck spacing was defined by the distance between the internal faces of the two chucks. The vertical displacement of the vacuum chucks was also examined; measurements of chuck height, i.e. base of right/left fibre slot in the chuck to the top face of coupler system were made at 1 mm increments along a total displacement of 11 mm. A chuck height of 45.3 mm was consistently measured along the 11 mm length. The presented results indicate that the coupler fabrication unit was repeatable and as such, it was proposed that the any inconsistencies in fabricated sensor characteristics were deemed not to be related to an error with the equipment.

#### 4.1.4 Double-Twisted Stripped Fibres

The repeatability of the double-twist that was used to position the two optical fibres within intimate contact was evaluated. Five double-twisted (DT) optical fibre pairs were imaged using optical microscopy. Due to the small field-of-view on the microscope, multiple images were collected and a single image was created using post-processing image reconstruction. Eight measurements were made in order to characterise the dimensions of the twisted pair. Two qualitative indicators were also obtained for characterisation. A description of these measurements can be found in Section 3.3.4. The values obtained from image analysis of the five twisted pairs are presented in Table 9.

**Table 9** A summary of the specified dimensions for the twisted region of five pairs of stripped optical fibres (see Figure 37 for measurement coding used – values in  $\mu\text{m}$ ) (standard deviation in parentheses).

Measurement	DT-001	DT-002	DT-003	DT-004	DT-005	Mean
<b>M.1</b>	2101	1465	2337	2140	2555	<b>2119 (408)</b>
<b>M.2</b>	1945	1725	2352	2142	2338	<b>2100 (268)</b>
<b>M.3</b>	4942	4846	4811	5681	4798	<b>5016 (376)</b>
<b>M.4</b>	1658	1621	1709	2143	1784	<b>1783 (210)</b>
<b>M.5</b>	1368	1907	1844	2080	1910	<b>1822 (268)</b>
<b>M.6</b>	208	210	209	239	199	<b>213 (15)</b>
<b>M.7</b>	123	131	123	135	120	<b>126 (6)</b>
<b>M.8</b>	124	133	121	136	119	<b>127 (8)</b>
<b>M.A</b>	Separated	Full contact	Separated	Full contact	Separated	-
<b>M.B</b>	Full contact	Full contact	Partial contact	Partial contact	Partial contact	-

All measurements were made with reference to the two anchor points, i.e. (M.7) and (M.8), highlighted in Figure 37(a). An example of an optical micrograph of the twisted pair is presented in Figure 37(b). The anchor points in this image are illustrated.

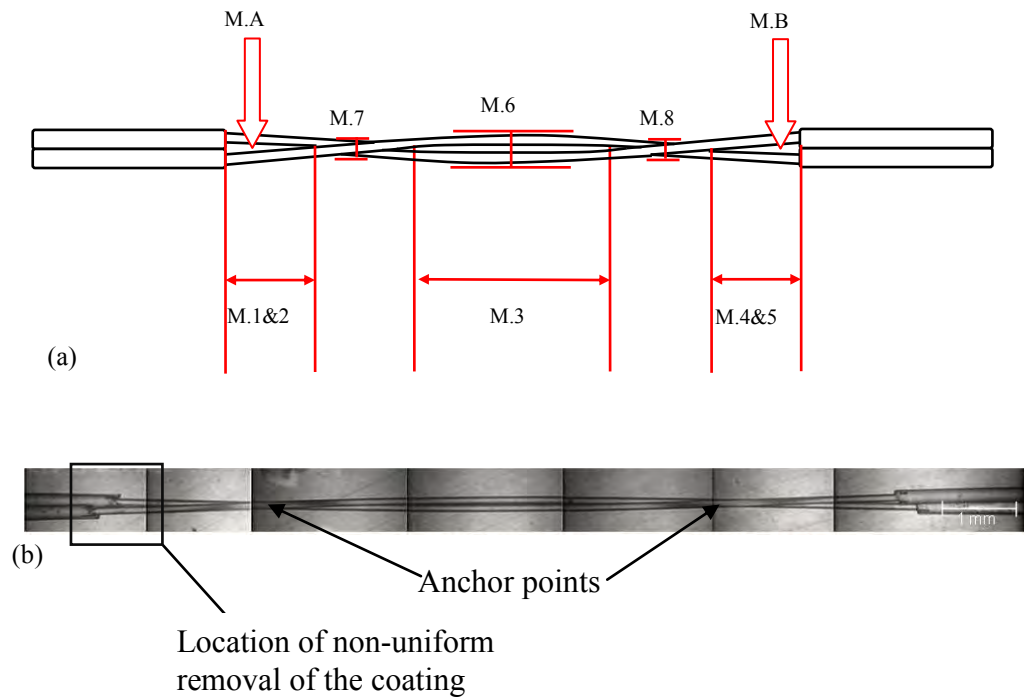


**Figure 37 A schematic illustration of: (a) the definitions of the measurement zones that were used to quantify the sample-to-sample variation in a pair of double-twisted fibres; and (b) an optical micrograph of the double-twisted fibre pair.**

With reference to Table 9, low repeatability for the twisted pairs was observed. The mean recorded measurements for (M.1), (M.2), (M.4) and (M.5) had a standard deviation greater than 10 %. The contact points (M.A) and (M.B) show a combination of full and partial contact, and full separation at each end of the double-twist. The observed variations were attributed to: the effects from the non-uniform regions of the polymer coating; and/or (ii) variable tension in the twisted fibre pair prior to fusion. The non-uniform removal of the optical fibre coating is highlighted in Figure 37(b); this was observed in all of the five samples that were imaged. The condition of the coating in this region implies that the blades of the stripping tool may have been blunt or chipped. This effect was reported previously and was found to influence the mechanical reliability of the fibres (Nagata et al., 1994). The variation in measurement (M.3) indicates that the tension applied between the anchor points

was not consistent at the start of fabrication. Birks (1989) reported that the taper tension influenced the degree of fusion within fibre-optic couplers. Shi et al. (2002) also proposed that mode coupling at the tapered region was less efficient for couplers where the cores are further apart. Measurement (M.6) indicates that the two fibres were not aligned adjacent to each other in the transverse direction; a measurement of 250  $\mu\text{m}$  would be expected as the diameter of a single fibre was 125  $\mu\text{m}$ . The mean width at this region was 213  $\mu\text{m}$ , suggesting that the two fibres were overlapped. As a consequence, the twisted fibre pair may be exposed to different temperatures owing to the distribution of heat within the flame tip. Alegria (2001) proposed that the alignment of fibres prior to fabrication of a fused-tapered coupler was necessary in order to avoid non-uniformities in the coupler geometry as well as high insertion loss. For a tapered coupler with varying waist geometry, the strain response along the tapered region was found to be non-uniform (Chen et al. 2008). As a result, it is assumed that the influence of an acoustic perturbation on the strain response of the coupler could vary along the sensing region.

#### 4.1.5 Repeatability of the Fused Fibre-Optic Taper

Optical microscopy was also used to evaluate the repeatability of five fibre-optic sensors that were packaged in the square U-channel packaging substrate. The five sensors (SM04-001 to 005) were imaged and measurements were recorded according to the zones referenced in Figure 38. Owing to the small dimensions of the fibre-optic sensor and the limitations with the field of the view of the microscope and the camera, the individual images were printed on A4-size paper and the coupler image was reconstructed on a large surface. Measurements were made manually using a steel-rule; the measurements were then referenced against the

scale-bar from the optical micrograph. A photograph showing a section of a reconstructed optical micrograph of a fused-tapered coupler is shown in Figure 39.

**Table 10 A summary of the specified dimensions for the post-fabrication fibre taper repeatability (see Figure 38 for measurement coding used – values in  $\mu\text{m}$ ) (standard deviation in parentheses)**

<b>Measurement</b>	<b>SM04-001</b>	<b>SM04-002</b>	<b>SM04-003</b>	<b>SM04-004</b>	<b>SM04-005</b>	<b>Mean</b>
<b>m.1</b>	245	271	258	258	271	<b>260 (11)</b>
<b>m.2</b>	245	271	258	258	245	<b>255 (11)</b>
<b>m.3</b>	271	258	245	245	245	<b>253 (12)</b>
<b>m.4</b>	245	232	258	245	258	<b>248 (11)</b>
<b>m.5</b>	580	632	658	787	722	<b>676 (80)</b>
<b>m.6</b>	567	696	645	941	890	<b>748 (161)</b>
<b>m.7</b>	2553	UNCLEAR	1341	3275	3598	<b>2692 (775)</b>
<b>m.8</b>	2269	UNCLEAR	2411	3456	3030	<b>2792 (428)</b>
<b>m.9</b>	142	129	142	142	129	<b>137 (7)</b>
<b>m.10</b>	142	142	142	142	142	<b>142 (0)</b>
<b>m.11</b>	17202	18246	18607	19291	18298	<b>18329 (755)</b>
<b>m.12</b>	13	19	13	13	13	<b>14 (3)</b>
<b>m.13</b>	1560	1651	1547	1625	1651	<b>1607 (50)</b>
<b>m.14</b>	1638	1651	1586	1573	1663	<b>1622 (40)</b>
<b>m.15</b>	26150	28962	28007	30831	29800	<b>28750 (1788)</b>

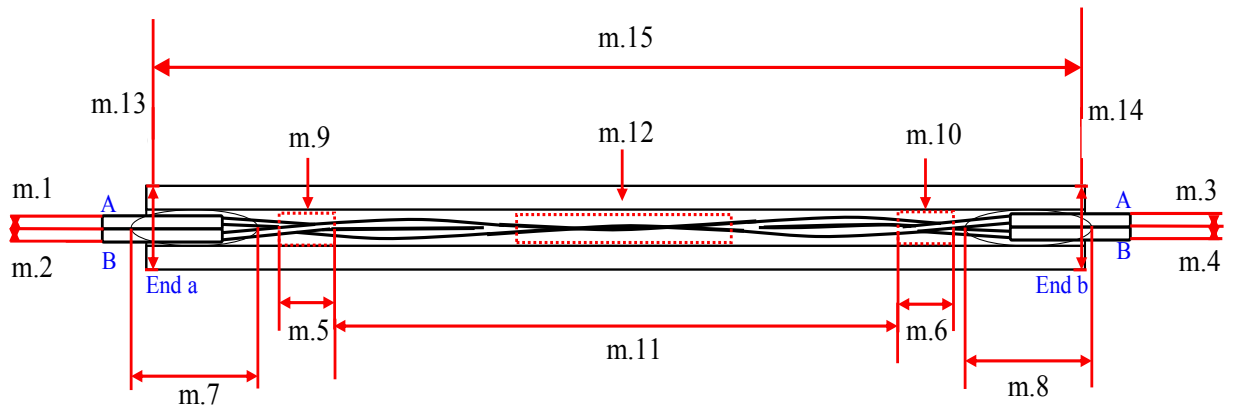


**Figure 38** A schematic illustration of the definitions of the measurement zones that were used to quantify the sample-to-sample variation in post-fabricated fibre-tapers.

For clarity of the sensor in the photograph, only a section of the sensor reconstruction is shown in Figure 39.



**Figure 39** An example of a section of a collage of optical micrographs that have been enlarged and printed in order to obtain the measurement from the zones noted in Figure 38.

With reference to the measurements in Table 10 the following observations can be made:

Variations in the anticipated and observed diameters of the optical fibre were reported, i.e. (m.1), (m.2), (m.3) and (m.4). The error was attributed to image distortion due to the circular profile of the fibres. The values shown in Table 10 should therefore be used as relative measurements and not absolute.

A variation in the length of the cross-over points (m.5) and (m.6) for each sensor was observed; this indicates a difference in tension from one end of the sensor to the other prior to the fusion process and/or slippage of the fibre in the vacuum chuck. Relaxation at the cross-over points (m.9) and (m.10) was also proposed based on the comparison of the representative mean values for before and after sensor fabrication; the comparison was made between results presented in Table 9 and Table 10. Further analysis is required to understand these variations. Xie (1991) evaluated the causes of un-even coupling ratios in fibre-optic couplers and proposed that this was due to: (i) inhomogeneous heating; (ii) drooping or bending of softened fibres; (iii) unequal tension on the fibres; and (iv) asymmetric positioning of the fibres. It is proposed here that all of the factors noted may have had an influence on the recorded measurements. Alegria (2001) also proposed that air draughts or gas pressure fluctuations in the flame gas could be attributed to non-uniformities in the taper profile.

In general, the measurement values for four of the five sensors with reference to the length of the adhesively bonded regions, i.e. (m.7) and (m.8), show close agreement. With reference to specimen SM04-003, a 1070  $\mu\text{m}$  variation in the length of the adhesive bonding was recorded. The adhesive bond performance was assumed to influence the signal-coupling between the

sensor and the substrate. Pierce et al. (1996) proposed that the response of an embedded fibre-optic sensor was influenced by the extent of surface contact between the coated fibre and the matrix resin; the same principle can be applied here. An increased sensitivity to stress wave perturbations can be achieved if the bonding length covers a larger region. The bonded length should therefore be similar for both ends of the coupler in order to achieve directional insensitivity. Hill and El-Dardiry (1981) proposed a multi-layer approach for acoustic signal transmission through couplant layers; the authors suggested that the properties of the layers that facilitate the signal should be considered when designing a transducer. The acoustic impedance of the different layers should be of the same order where possible and be significantly higher than air to avoid attenuation of the signal (Theobald et al. 2008). In addition, Theobald et al. (2008) proposed that stiffness of the bond can increase the sensitivity of the sensor to certain modes; rigid bonds provide good signal transmission for shear waves.

A 2 mm variation between sensors in the length of the overall tapered region (m.11), i.e. between the two cross-over points, was observed. A review of the effects of the length and width of the taper and the taper angle on the performance of the sensor can be found in Sections 2.4.5 and 4.1.2. respectively. A comparison of the response of SM04-1, SM04-002 and SM04-004 to simulated acoustic emissions is discussed in Chapter six.

A low variation in the diameter of the waist region (m.12) of the taper was observed for four of the five sensors; waist diameters of 13  $\mu\text{m}$  were recorded for sensors SM04-001, SM04-003, SM04-004 and SM04-005. A 19  $\mu\text{m}$  waist region was recorded for the SM04-002. This was attributed to the shorter draw length achieved during fabrication and therefore a reduction in the degree of fusion at the taper waist region. Shi et al. (2002) proposed that in order to

produce highly reliable couplers with low insertion-loss, high mechanical strength and stable optical properties, the following parameters should be considered: (i) fusion temperature; (ii) draw-length; and (iii) flame type. The authors found that a mixture of hydrogen and oxygen produced higher flame temperatures, enabling greater fusion of the fibres cladding and reduced excess-loss. The use of oxygen-butane flames have also been demonstrated for coupler fabrication. This flame type does however suffer from the following limitations: (i) the oxy-butane gas can produce by-products which results in contamination of the coupler; (ii) the size of the oxy-butane flame is too small to control the length of the fused region; and (iii) the temperature of the oxy-butane gas flame is easily influenced by the surrounding environment (Alegria, 2001; Chen, 2010). The influence of a wider taper region on the response of the sensor to simulated acoustic emissions will be reviewed in Chapter six.

Variations in the length and width measurements of the packaging substrates, obtained from (m.13), (m.14) and (m.15), were recorded. This was anticipated as a consequence of using a pen-cleaver to fracture the substrate to the required length.

## **4.2 Evaluation of the Sensor Packaging Procedures**

### **4.2.1 Manufacturing Consistency of the Square U-Channel Packaging Substrate**

The consistency of the fused-silica square U-channel packaging substrate used to house the fibre-optic acoustic emission sensor was evaluated using scanning electron microscopy (SEM). The purpose for evaluating the sensor packaging was to assess the consistency of the U-channel profile with respect to dimensional repeatability. Figure 40 presents two SEM

micrographs showing examples of the U-channel substrate. With reference to these images, both U-channels appear to have different profiles.

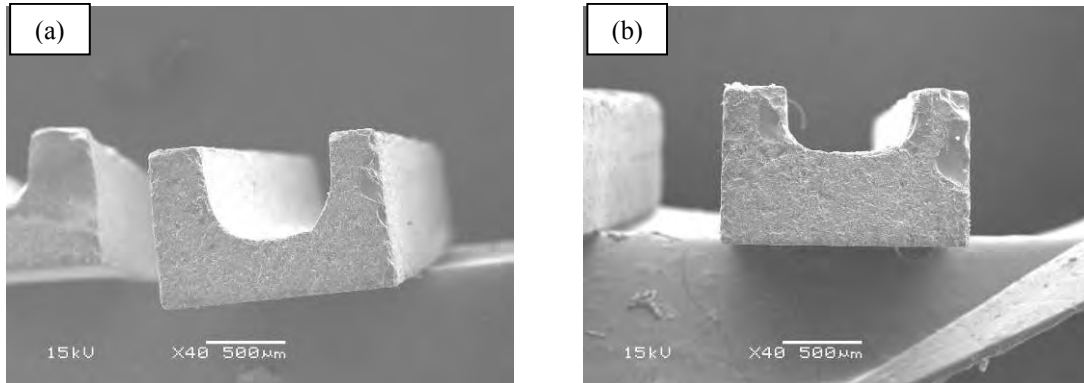


**Figure 40 (a) and (b) SEM micrographs of two as received fused-silica square U-channel packages from the same batch; the micrographs illustrate a variation in the U-channel profile.**

To illustrate the variation in the dimensions of the U-channel, a sample of five substrates were selected at random and measurements were recorded. Figure 41 presents a schematic illustration of the cross-section of the square (SQ) U-channel package with measurement coding. The histograms in Figure 42 illustrate the recorded measurements.

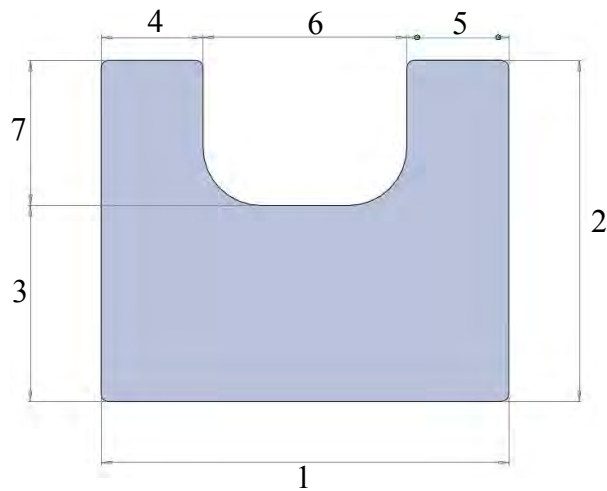


**Figure 41 A schematic illustration of the cross-section of the square U-channel packaging substrate with the numerical coding system for the measurement zones.**

With reference to Figure 42, a large variation in the measurement zones of the substrates was observed. Inconsistencies were observed in the measurements with respect to: (i) the width of the substrate; (ii) U-channel symmetry; and (iii) the depth of the U-channel. As a consequence, it can be concluded that the positioning of the fibre-optic sensor within the U-channel could vary from sensor-to-sensor. For a shallow channel depth, there is a possibility that the sensor would be positioned such that it protrudes beyond the top of the package, therefore increasing the susceptibility to damage and/or damping of the AE signal.

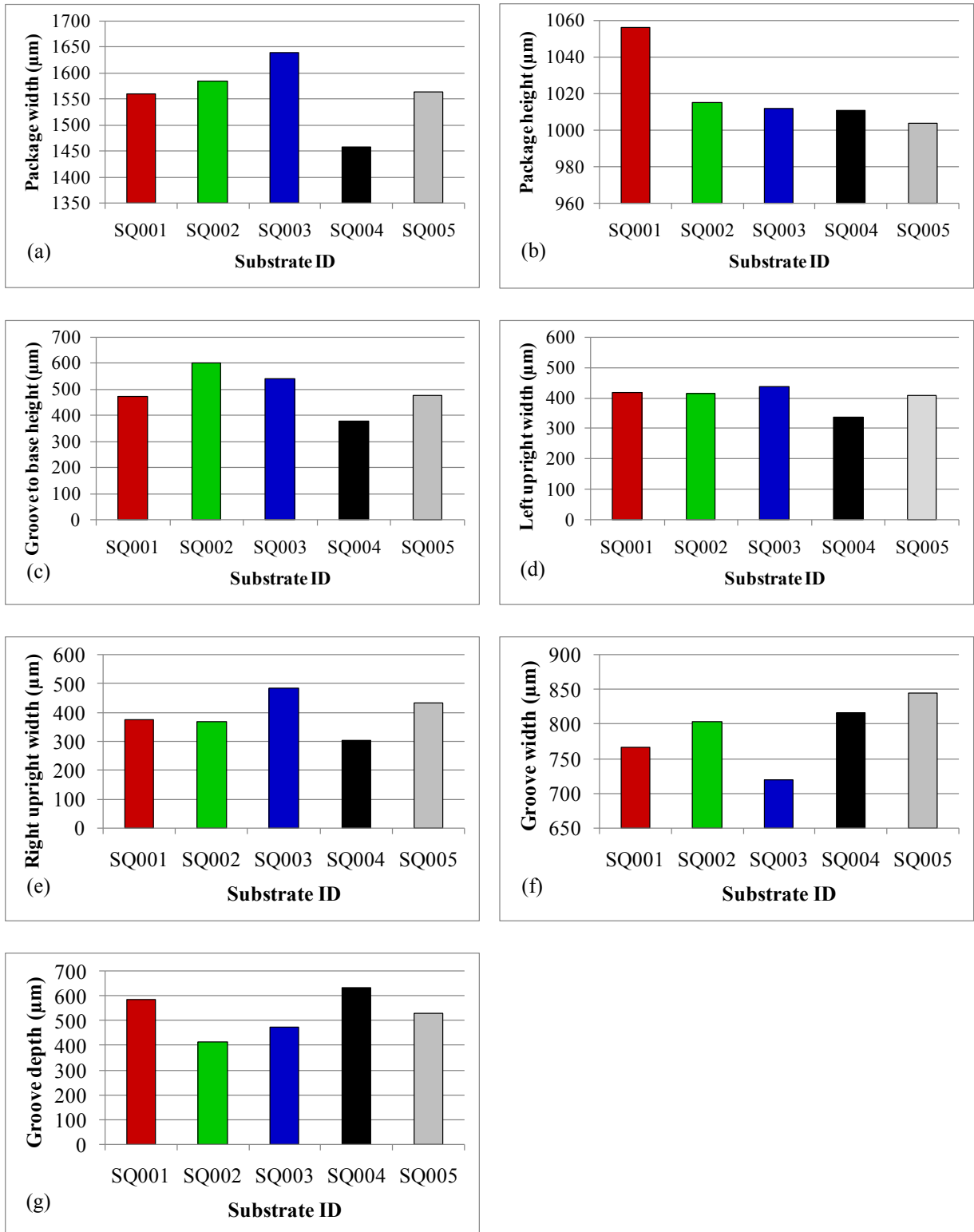


**Figure 42** A selection of column charts illustrating: (a) package width [1]; (b) package height [2]; (c) groove to base height [3]; (d) left upright width [4]; (e) right upright width [5]; (f) groove width [6]; and (g) groove height [7]. See Figure 41 for the coding system for the square U-channel package.

#### 4.2.2 Location of the Sensor and Fibre-to-Package Bonding Region

The consistency of adhesive bonding between the fibre-optic sensor and the square U-channel packaging substrate was evaluated. Samples of the square U-channel packaged sensors were evaluated using optical microscopy. The packaged sensors were potted in an epoxy resin and prepared for image analysis by abrading and polishing the ends. The purpose of the image analysis was to evaluate: (i) the positioning of the sensor with respect to the U-channel; and (ii) the consistency of the adhesive bonding. Typical examples of two potted sensors are shown in Figure 43 (a) and (b).

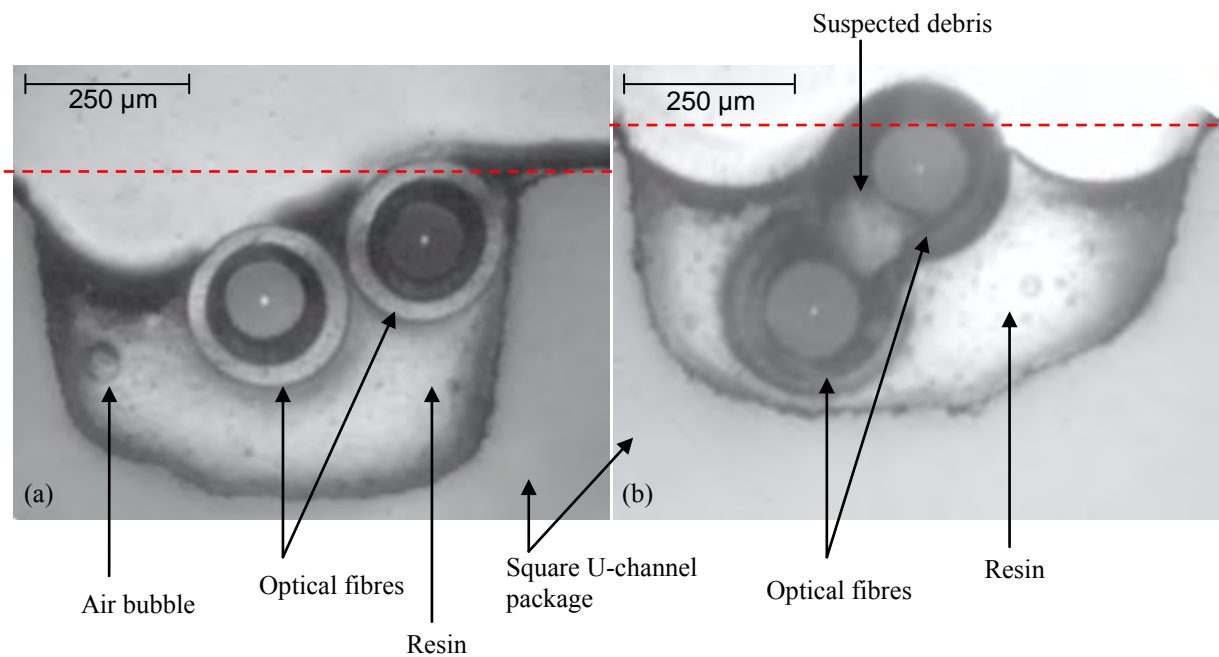


**Figure 43 (a) and (b) Optical micrographs illustrating the positioning of the fibre-optic acoustic emission sensor within the square U-channel packaging substrate.**

With reference to the Figure 43 (a) and (b), it can be noted that the fibres do not sit parallel to each other within the channel. This observation supports the assumption that the two fibres may not be parallel prior to fusion (see Section 4.1.2.2). In addition, a large portion of the

optical fibre protrudes from the top of the package beyond the resin bonding layer. As a consequence, this fibre would be more susceptible to damage through accidental impact caused by general handling.

A rigid adhesive bond that encapsulates the sensor is required in order to achieve efficient transmission of the stress-wave from the host material to the fibre-optic sensor (Theobald et al. 2008). It is clear from Figure 43 that the volume of adhesive used to bond the sensors varies from sensor-to-sensor. Resin flow within the gap between the fibres and the package was observed in all of the micrographs that were analysed; complete encapsulation of the sensor was however not consistent (See Figure 43(b)). It is therefore proposed that the poor consistency in the bonding properties may result in variations in the sensitivity and response of the fibre-optic AE sensor. The effect of non-uniform bonding of the sensor and surrounding resin on the sensitivity to stress-wave perturbations was investigated in Pierce et al. (1996) (see Section 2.4.1).

Owing to the large variation in the substrate-to-substrate dimensions, a second packaging substrate was sourced and evaluated.

# CHAPTER 5

## Optimisation of the Sensor Packaging Procedures

## 5 Optimisation of the Sensor Packaging Procedures

---

### 5.1 Evaluation of the Circular U-channel Packaging Substrate

#### 5.1.1 Manufacturing Consistency of the Small-Diameter Circular U-Channel Package

The second packaging substrate that was evaluated was circular in profile and had an outer diameter of 750  $\mu\text{m}$ ; this represented approximately a 50% reduction in packaging size. The manufacturing consistency of this package was evaluated using image analysis. A SEM micrograph of the circular package is shown in Figure 44. With reference to the micrograph, the surface profile of the package appears to be smooth with no visual surface pitting. In comparison, the profile of the square package discussed previously was heavily pitted leading to the potential entrapment of air bubbles within the adhesive layer.

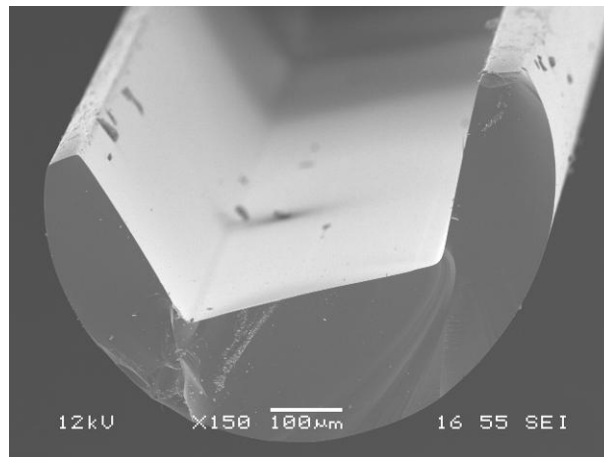


**Figure 44** A SEM micrograph of the borosilicate circular U-channel packaging substrate.

Theobald et al. (2008) proposed that the presence of air at the interface between the sensor and the specimen results in high acoustic absorption, i.e. greater than 50% at frequencies above 100 kHz. Higo and Inaba (1991) also reported a reduction in the resonant sensitivity of an AE sensor if air bubbles were present in the couplant layer between the sensor and the host material. A weighted mass is often used to improve consistency with sensor coupling and to force air-bubbles from the interfacial layer (Theobald et al., 2008). In the case of the square U-channel packaged sensors, where the optical fibre protruded from the silica groove, this method was not practical and may have resulted in damage to the sensor.

The uniformity of the circular profile (CP) with respect to the dimensional consistency was evaluated. To illustrate the variation in the dimensions of the circular U-channel package, a sample of five substrates were selected at random and measurements were recorded. The cross-section of the circular U-channel with measurement coding is presented in Figure 45. The histograms in Figure 46 illustrate the recorded measurements.

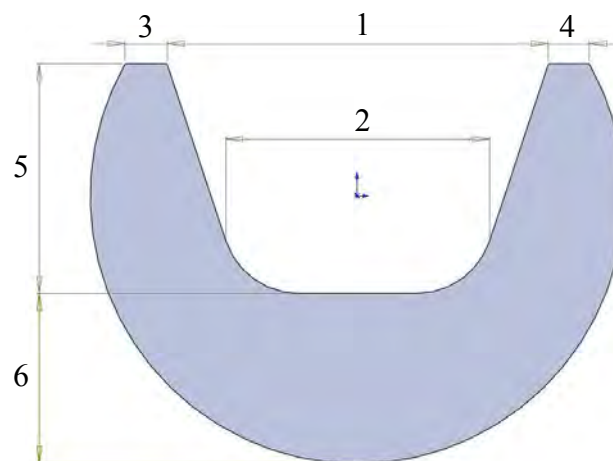


**Figure 45 A schematic illustration of the cross-section of the circular U-channel packaging substrate with the measurement coding.**

With reference to Figure 46, the consistency of the circular U-channel packaging dimensions was significantly better than the consistency of the square U-channel. As a result, it was anticipated that the repeatability of the sensor positioning within this package would be improved. In addition, owing to the smaller dimensions of the circular U-channel package, a precision fit was achieved with respect to fibre positioning. As a consequence of the width at the base of the U-channel being  $\sim 350 \mu\text{m}$ , only fibre that had been stripped of its polymeric coating could be accommodated. As a result, the UV-curable adhesive was applied directly to the glass-fibre; in the case of the square U-channel package, the fibre-optic sensor was bonded with the acrylate coating as received.

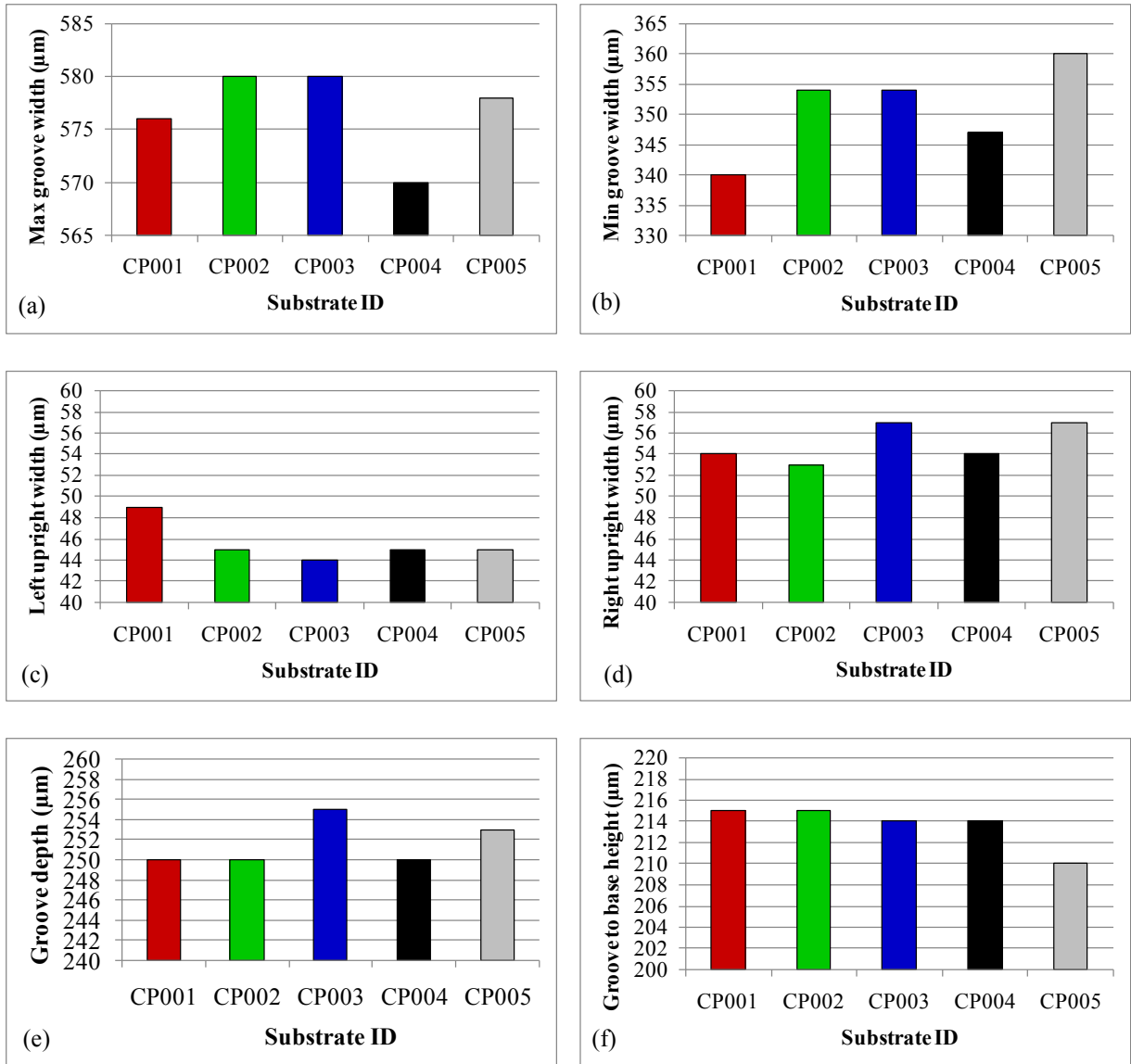


**Figure 46** A selection of column chart illustrating: (a) maximum groove width [1]; (b) minimum groove width [2]; (c) left upright width [3]; (d) right upright width [4]; (e) groove depth [5]; and (f) groove to base height [6]. See Figure 45 for the coding system for the circular U-channel package.

Figure 47 (a) and (b) show examples of the fibre bonding regions for the square and circular U-channels respectively. It should be noted that the region where the coating has been removed outside of the substrate for the circular package, the fibre has been reinforced with

the UV-curable epoxy for protection. It was anticipated that AE coupling would be optimised for glass-resin-glass bonding compared with glass-resin-polymer bond; the lower modulus of the polymeric coating would result in a reduction in the sensitivity to the stress wave perturbation. Pierce et al. (1996) proposed the use of chemical etching to remove the buffer coating prior to embedment of a fibre-optic sensor in a composite. By removing the coating, localised variations in the bonding between the buffer and the resin were likely to be minimised. Wei et al. (2001) also recommended the removal of the polymeric coatings from optical fibre strain sensors; the authors found that bare fibres embedded within resin samples subjected to tensile loading were more sensitive to strain development. The bare fibres demonstrated a close correlation with conventional strain sensing compared with coated fibres.

With reference to Figure 47 (a), it is also noteworthy that the fibres do not protrude beyond the top surface of the groove. The resin conceals all of the fibre within the U-channel. As such, it is less likely that the sensor may be damaged from careless handling or accidental impact. The implementation of a packaging lid would further minimise the chance of accidental damage; an evaluation of suitable substrates for this purpose is suggested as a topic for future work to enhance the sensors survivability.

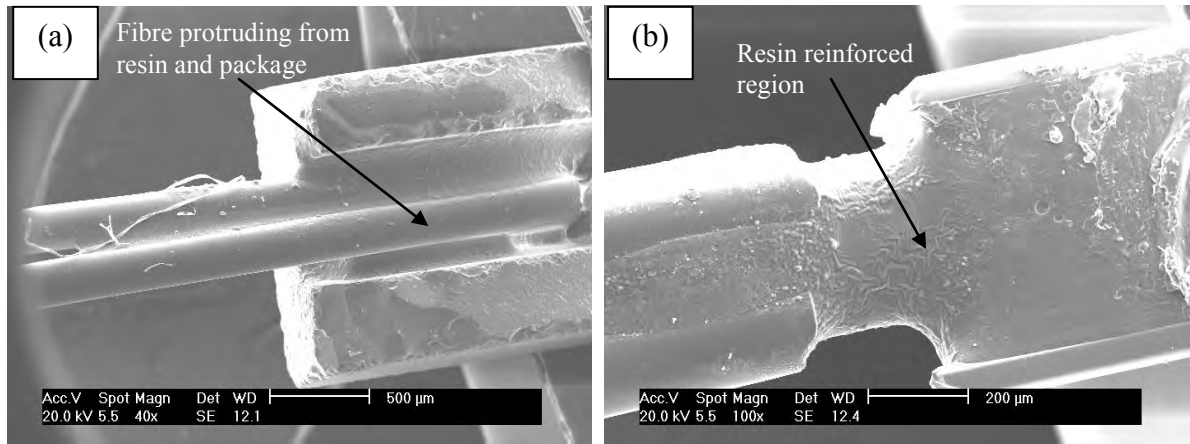


**Figure 47 (a) and (b) SEM micrograph illustrating: (a) the square U-channel package where the fibre was bonded to the package with coating as received; and (b) the circular U-channel packaging substrate where the coating has been removed.**

The characteristics of the sensors fabricated using the circular U-channel packaged sensors were comparable to the square U-channel packaged sensors. This indicates that the process of mounting the sensors in the precision-fit circular U-channel does not influence the fabricated properties of the sensor. The mean fabrication characteristics from a sample of sensors manufactured from SM04-1 optical fibre (reel purchased in 2008) and housed within the circular package (CP) are presented in Table 11.

**Table 11 A summary of the fabrication characteristics for sensor groups-2 and 4. Group-2 refers to the square U-channel packaged sensors from section 4.1.2. Group-4 refers to the circular U-channel packaged sensors; standard deviation in parentheses.**

Batch	Excess-loss (dB)	Coupling ratio (%)	Draw-length (mm)
	Mean	Mean	Mean
Sensor group-2	1.13 (0.6)	55.1 (2.8)	10.28 (0.2)
Sensor group-4	1.00 (0.3)	54.5 (1.3)	10.22 (0.1)

### 5.1.2 Pre- and Post-Packaging Average Signal Level (ASL)

The average signal level (ASL), i.e. baseline noise level, produced by the fibre-optic sensor before and after packaging was evaluated. The ASL values for five sensors, each packaged using the square U-channel and circular U-channel substrates, are presented in Figure 48 and Figure 49 respectively. With reference to both plots, the recorded ASL decreased after the sensor was packaged; this observation was true for all of the sensors evaluated and both packaging substrates. The decrease in ASL was attributed to damping of vibrations emanating from the vacuum chucks; as the optical fibre was retained by the vacuum chuck, the vibrations travelled along the fibre-optic coupler. Vibration damping was achieved as a result of: (i) increasing the mass of the device (Mead, 2000) by mounting the coupler on the glass package; and (ii) the adhesive bond used to attach the coupler to the substrate. The latter was due to a difference in the acoustic impedance of the optical fibre and the resin at the bonded region; signal transmission through the resin was therefore reduced. Birks et al. (1996) proposed that a fibre-optic coupler would bend periodically when an acoustic wave/vibration impinged on the device. As a result of this periodic bending, a change in the refractive index distribution occurs within the fibre, together with a lengthening of the fused region. Both mechanisms are understood to influence mode coupling at the tapered region. It is therefore proposed that vibrations induced in the optical fibres when retained by the vacuum chucks would result in fluctuations in the signal coupling. The measured signal amplitude would therefore be higher for an un-damped optical coupler. For reference, further details of the acousto-optic coupling are provided in Appendix-A. The fused-tapered coupler sensor has previously been demonstrated for vibration monitoring applications (Jian and Bin, 2010). Hati et al. (2008) also proposed that when optical fibres are subjected to vibrations,

phase shifts in the optical signal can occur; such phase shifts result in intensity fluctuations in the optical signal. Packaging of the sensor also ensured that the device was less susceptible to air draughts.

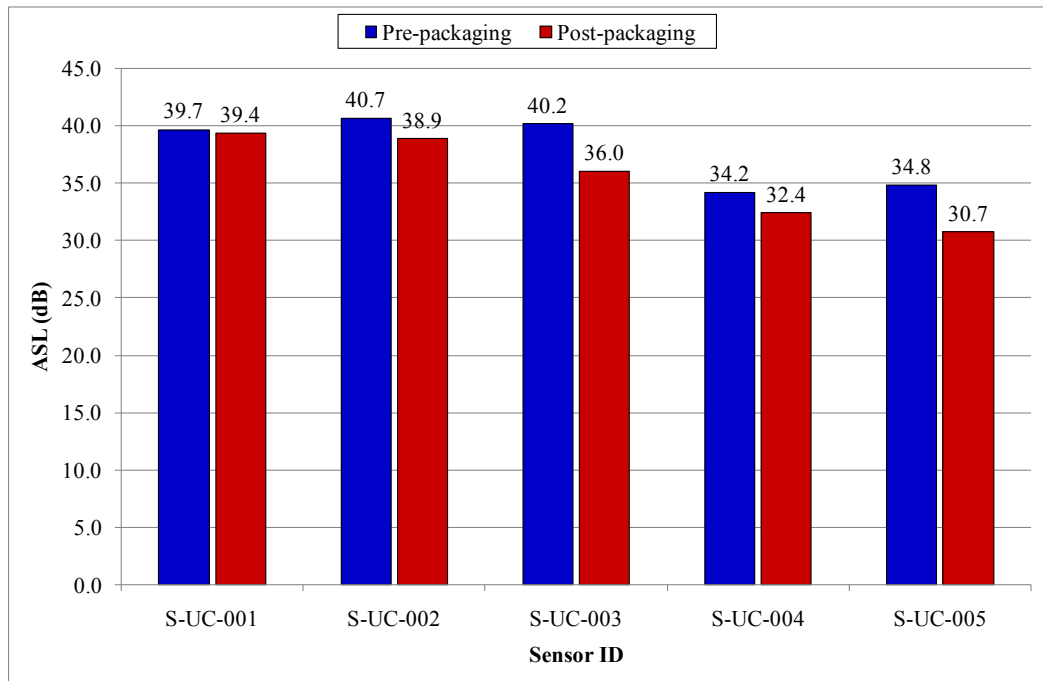


**Figure 48** A column chart illustrating a comparison of the ASL values for pre- and post-packaged sensors housed in the square U-channel substrate.

The mean reductions in ASL after packaging were 2.4 and 3.8 dB<sub>AE</sub> for the square and circular U-channel substrates respectively. It was therefore proposed that the process of mounting and bonding the sensor to the package improved the stability of the coupler with respect to baseline noise level. A lower mean ASL was observed from the circular U-channel packaged sensor; the mean ASL was 33.9 dB<sub>AE</sub> compared with 35.5 dB<sub>AE</sub> for sensors housed in the circular and square packages respectively.

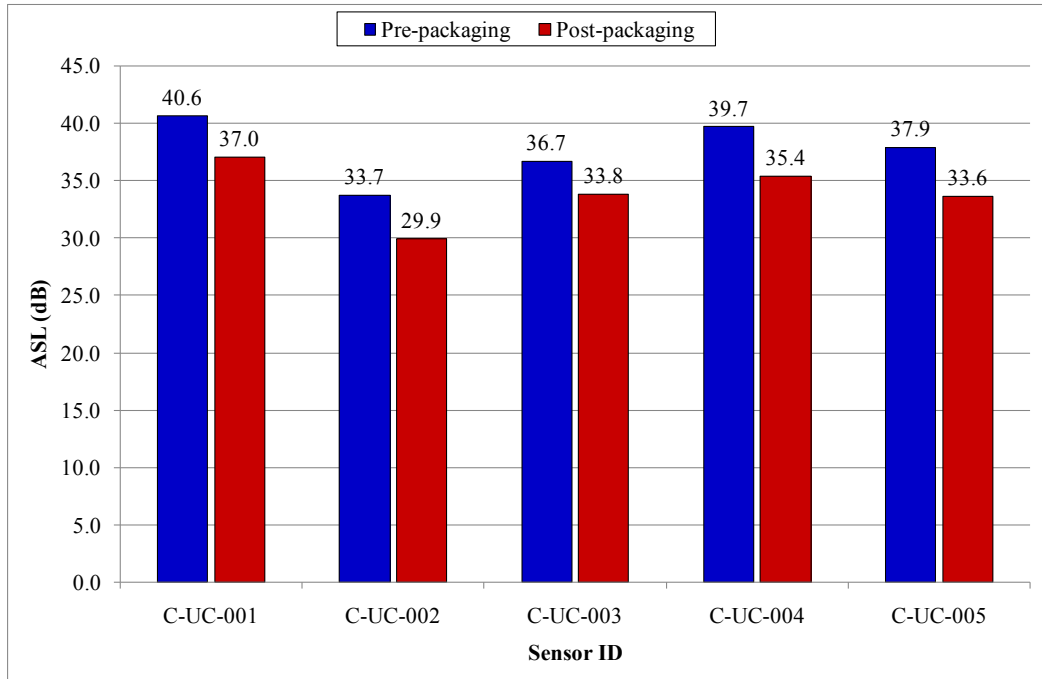


**Figure 49** A column chart illustrating a comparison of the ASL values for pre- and post-packaged sensor housed in the circular U-channel substrate.

In conclusion of these findings, it is proposed that the circular U-channel sensor offers: (i) a reduction in the overall sensor dimensions; (ii) potentially greater sensitivity to stress-wave perturbations owing to the removal of the coating at the package ends; and (iii) a reduction in the recorded ASL.

## **5.2 Embedment of the Fibre-Optic Acoustic Emission Sensor**

### **5.2.1 Optimisation of the Packaging Procedure for Sensors Destined for Embedment**

An improved fabrication procedure was developed for manufacturing fibre-optic sensors that were destined for embedment in composite materials. In brief, the improvements to the

fabrication process were intended to minimise operator dependency by: (i) providing support for the capillary when traversing it along the fused-tapered fibres; (ii) providing continuous tension on the fibres, through the use of a magnetic clamp, when the vacuum chuck was switched off to allow to capillary to be traversed; (iii) increasing the inner bore cross-sectional area of the package to minimise the likelihood of impacting the tapered region when traversing the capillary. Further details can be found in Sections 3.3.9 and 3.3.10.

A study was undertaken to evaluate the success rate for fabricating sensors using the improved packaging procedure. An attempt was made to fabricate ten capillary-sealed sensors; of the ten sensors fabricated, three were damaged at the packaging stage. The sensors were fabricated using the SM04-1 optical fibre (reel purchased in 2008). The suspected mode of failure of the three sensors was mis-alignment of the traversing capillary; as a result, the narrow waist region was fractured upon contact with the leading edge of the capillary. The characteristics of the seven sensors that were fabricated are shown in Table 12. The mean fabrication characteristics are also compared with sensor groups-2 and 4 in Table 13. Sensor group-2 refers to the square U-channel packaged sensors and group-4 to the circular U-channel packaged sensors. With reference to Table 13, the characteristics are in close agreement with those measured for the surface-mounted sensors.

**Table 12 A summary of the fabrication characteristics of the seven sensors that were produced for embedment in composite materials (standard deviation in parenthesis).**

<b>Characteristic</b>	<b>EM04-001</b>	<b>EM04-002</b>	<b>EM04-003</b>	<b>EM04-004</b>	<b>EM04-005</b>	<b>EM04-006</b>	<b>EM04-007</b>	<b>Mean</b>
Excess-loss (dB)	1.10	1.42	1.00	0.76	0.01	1.02	2.37	1.09 (0.7)
Coupling ratio (%)	58.2	54.2	60.5	53.7	56.9	54.9	54	56.1 (2.6)
Draw-length ( $\mu\text{m}$ )	10.29	10.58	10.31	10.14	10.35	10.58	10.45	10.39 (0.2)

**Table 13 A comparison of the mean fabrication characteristics for sensor groups-2, 4 and 5 (standard deviation in parenthesis).**

<b>Batch</b>	<b>Excess-loss (dB)</b>	<b>Coupling ratio (%)</b>	<b>Draw-length (mm)</b>
	<b>Mean</b>	<b>Mean</b>	<b>Mean</b>
<b>Sensor group-2</b>	1.13 (0.6)	55.1 (2.8)	10.28 (0.2)
<b>Sensor group-4</b>	1.00 (0.3)	54.5 (1.3)	10.22 (0.1)
<b>Sensor group-5</b>	1.09 (0.7)	56.1 (2.6)	10.39 (0.2)

### 5.2.2 Online Monitoring of the Embedded Sensor during Composite Processing

A preliminary investigation was undertaken to evaluate the feasibility of embedment of the capillary-sealed fibre-optic AE sensors in an autoclave-cured carbon-fibre composite laminate; the composite was fabricated using VTM-264 prepregs (Advanced Composites Group, UK). Details of the procedures used to lay-up the prepregs and the positioning of the fibre-optic sensors are provided in Section 3.3.11. The prepreg stack was cured using

conventional autoclave processing. Further details of the autoclave processing schedule are provided in Appendix-B. An example of the temperature and pressure profiles from the autoclave control system are provided in Figure 50.

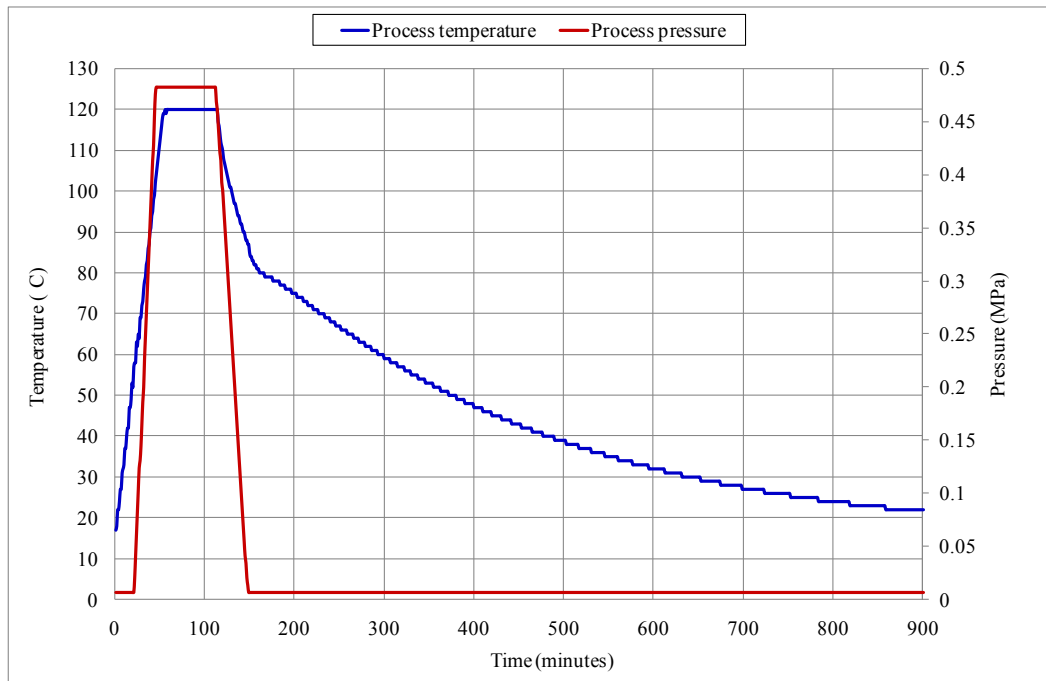


**Figure 50** A plot illustrating examples of the pressure and temperature profiles that were recorded during autoclave processing of the VTM-264 prepregs.

The tooling material that was used to process the prepregs was chosen in order to minimise the residual strain in the laminate. De Oliveria et al. (2008) evaluated the residual strain development in autoclave processed uni-directional laminates as a function of the tooling material. Fibre Bragg grating strain sensors were embedded in the prepregs to monitor the development of strain in the laminate during both the cure and the cool-down phases; aluminium and carbon-fibre tooling plates were evaluated. The authors proposed that a lower thermal expansion mis-match between the tooling plate material and the composite would

result in a lower value of residual strain in the laminate. In uni-directional laminates, residual strain values of 19.4 and 1303  $\mu\epsilon$  were recorded by the FBG sensors for carbon-epoxy and aluminium tool plates respectively. As a result, in the current study, a carbon-fibre tool plate was utilised with the intention of minimising the process-induced residual strain in the laminate and reducing the likelihood of sensor failure.

Two sensors, namely EM04-006 and EM04-007 (see Table 12) were embedded during the preliminary investigation. A photograph of the composite specimen with the embedded sensors is shown in Figure 51; both sensors survived embedment.

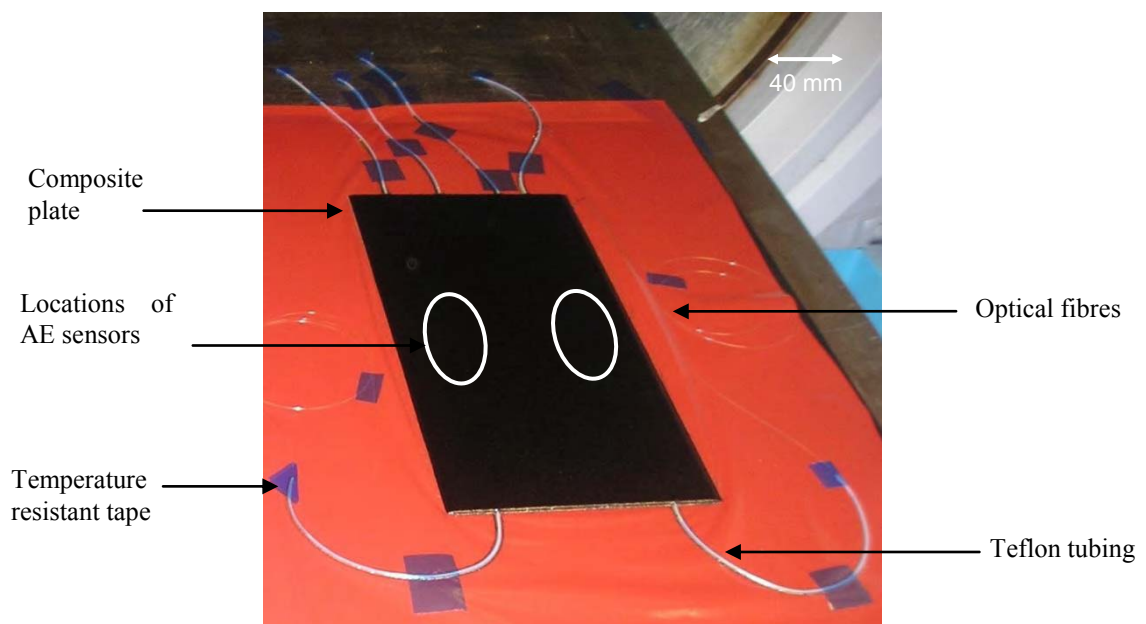


**Figure 51** A photograph of uni-directional composite with embedded fibre-optic AE sensors.

The coupling ratios of the two sensors were compared before and after embedment to determine the effects of autoclave processing on the characteristics of the AE sensor; Table 14 provides a summary of this data.

**Table 14 A summary of the sensor characteristics before and after processing.**

<b>Sensor ID</b>	<b>Characteristic</b>	<b>Pre-processing</b>	<b>Post-processing</b>	<b>Difference</b>
<b>EM04-006</b>	Coupling Ratio (%)	54.9	39.3	-15.6
	Excess-Loss (dB)	1.02	2.11	1.09
<b>EM04-007</b>	Coupling Ratio	54	57.5	3.5
	Excess-Loss	2.37	1	-1.37

With reference to Table 14, a variation in the post-processing properties of the two sensors was observed. This was attributed to an increase in the axial strain acting on the sensor; the axial strain results from the residual strain development in the uni-directional laminate (Kuang et al., 2001; De Oliveria et al., 2008). In addition to the pre and post-fabrication measurements, the time-driven ASL from the fibre-optic sensor was monitored in real-time during processing; time-driven data acquisition is independent of the signal threshold crossing and can therefore be used to trend the response of the sensor over a period of time. The ASL measurements for sensor EM04-007 is presented in Figure 52. The sensor was fusion-spliced to the optical fibres housed within the autoclave flange attachment. The ASL was recorded at 1-second intervals throughout the cure cycle; acquisition was aborted prior to opening the autoclave door after the composite had been fabricated. With reference to Figure 52, a 2 dB<sub>AE</sub> increase in the ASL was observed after packaging. Large fluctuations in the ASL were observed during the cure and cooling phases of the process. These fluctuations were

attributed to a change in temperature, pressure and rheological properties of the prepregs. Further work is however required to evaluate the correlation between these parameters and the response of the fibre-optic sensor. With reference to the results presented herein, it was therefore assumed that the performance of the fibre-optic sensor was not significantly degraded after embedment in the composite. The assumption was based on: (i) a minimal variation in the sensor characteristics measured after embedment; and (ii) a minimal increase in the ASL recorded by the sensor after embedment.

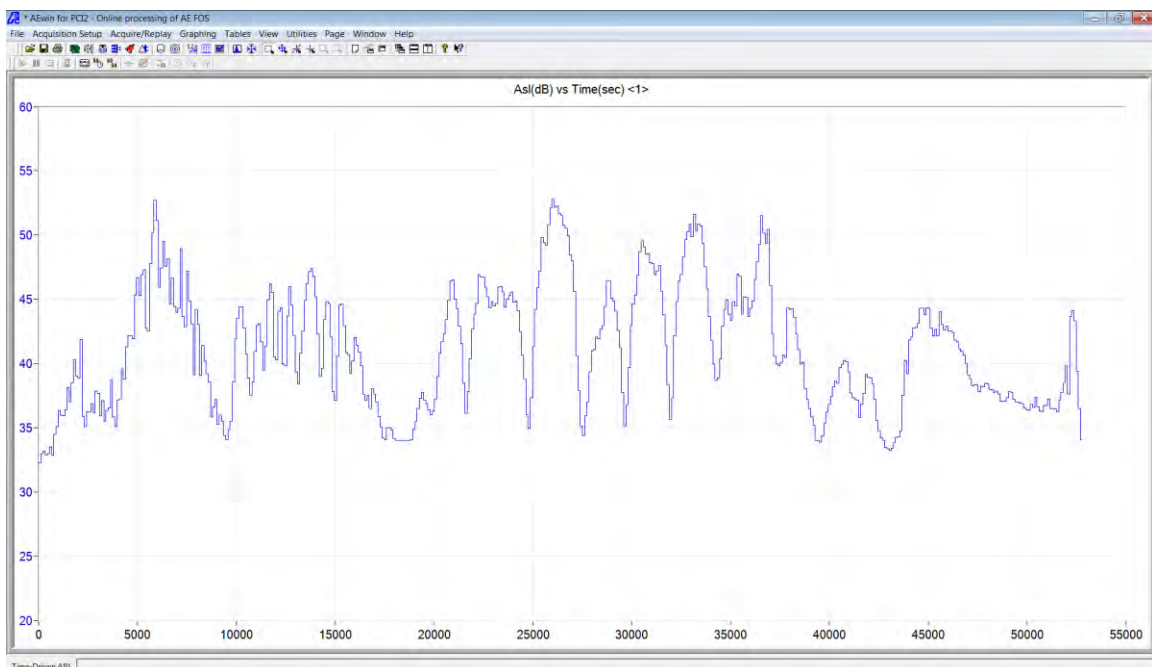


**Figure 52** A screen-shot of the AEwin™ software illustrating the time-driven average signal level produced by the fibre-optic sensor during processing.

# CHAPTER 6

## Characterisation of the Fibre-Optic Acoustic Emission Sensor using Simulated AE

## 6 Characterisation of the Fibre-Optic Acoustic Emission Sensor using Simulated AE

---

### 6.1 Evaluation of the Repeatability of the Hsu-Nielsen (HN) Source

The consistency of the Hsu-Neilson (HN) source was investigated to determine if this AE signal generation technique could be reliably used to evaluate the response of the fibre-optic sensor. A fibre-optic AE sensor (SM04-006) was manufactured using SM04-1 optical fibre (reel purchased in 2008) and was packaged within the square U-channel substrate. Thirty pencil-leads were fractured on the surface of an aluminium plate; further details of the experimental setup are provided in Section 3.4.1. The signals that were generated from the lead breaks were recorded by the fibre-optic sensor. Figure 53 presents a screen-shot from the AE analysis software illustrating the thirty pencil lead break signals. As a reference, the consistency of the HN source was also validated using a piezoelectric transducer. The test was repeated with the WD sensor; the results from the two sensors were compared. Figure 54 presents a screen-shot from the AE analysis software illustrating the signals recorded by the piezoelectric transducer. Both sensors demonstrated consistency in their response to the pencil lead break. The mean signal amplitudes for the fibre-optic and piezoelectric transducers were 80.7 (2.7) and 89.1 (1.7) dB<sub>AE</sub> respectively; the standard deviation is shown in parentheses. The observed deviation from the mean was found to be within the  $\pm 3$  dB<sub>AE</sub> limit specified in ASTM E-976 (ASTM, 2005). The maximum signal amplitude was obtained from the largest peak in the discrete waveform along the full time window of 1024 microseconds.

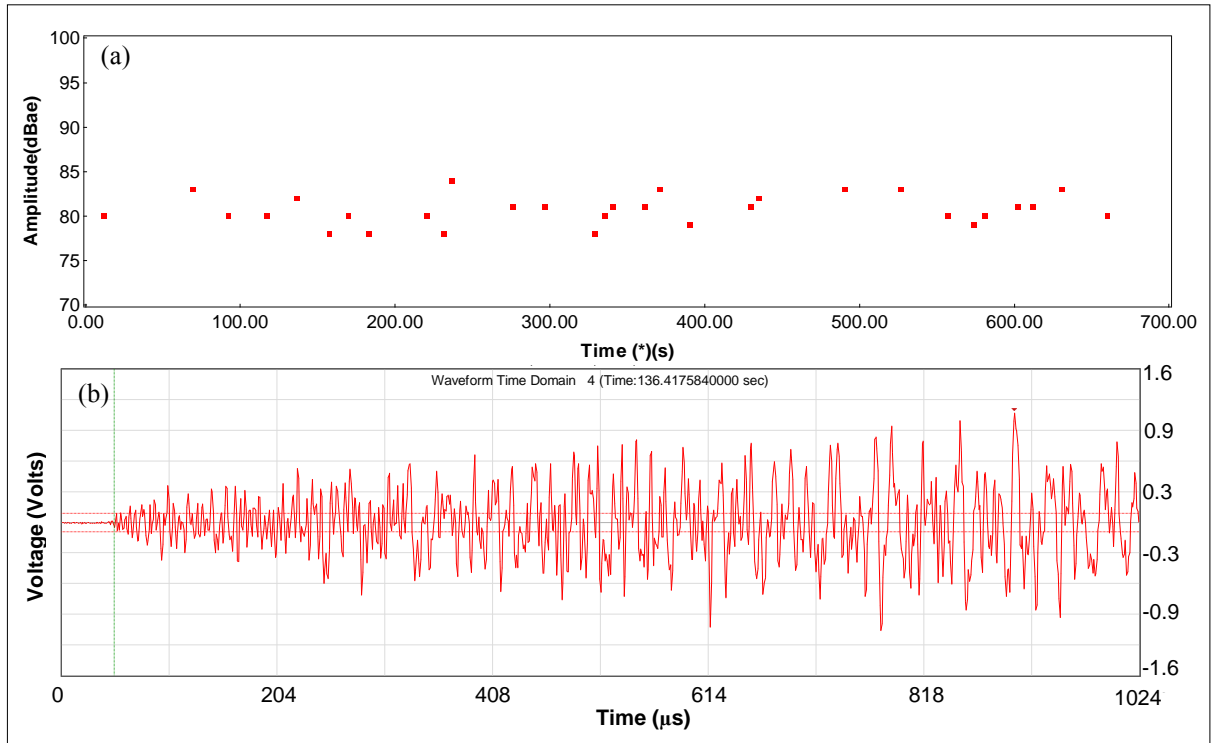


**Figure 53** A screen-shot of the AE analysis software highlighting: (a) a point-plot of the signal amplitude of each hit; and (b) an example of a typical discrete waveform recorded by the fibre optic sensor.

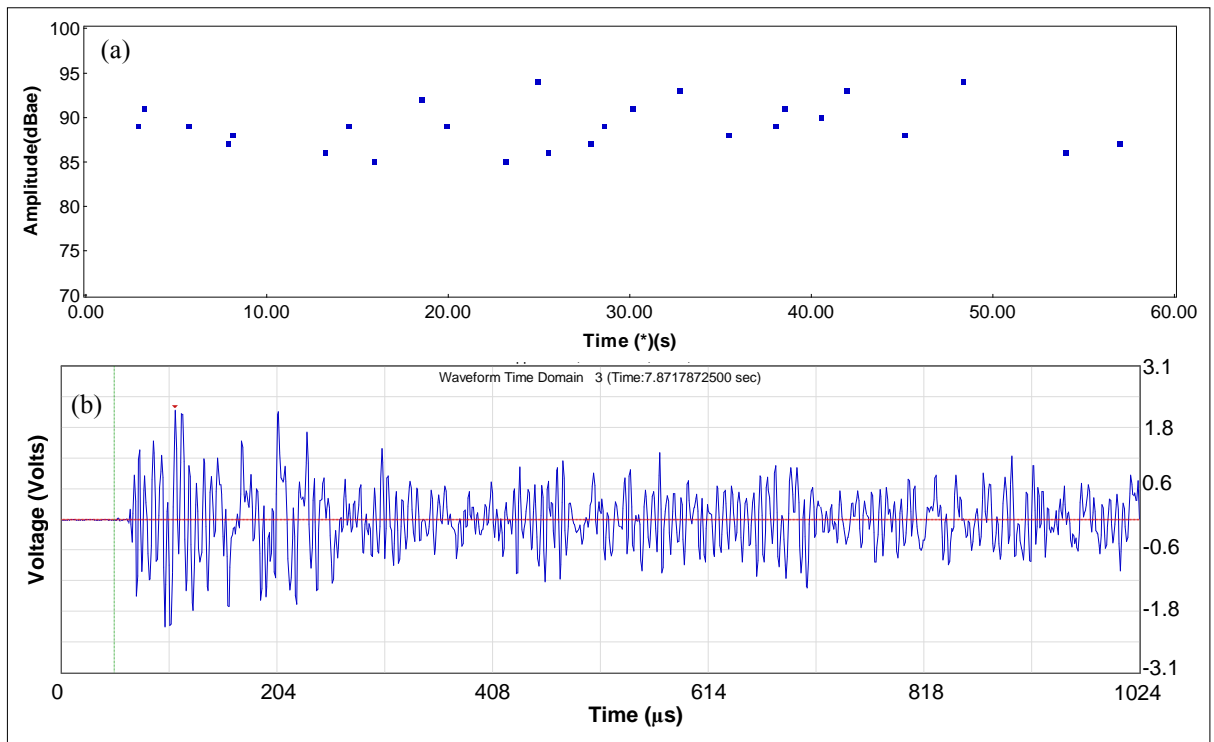


**Figure 54** A screen-shot of the AEwin™ software highlighting: (a) a point-plot of the signal amplitude of each hit; and (b) an example of a typical discrete waveform recorded by the piezoelectric transducer.

With reference to the discrete waveforms presented in Figure 53 (b) and Figure 54 (b), all of the pencil lead break signals were found to have durations in excess of 15667 and 46022 microseconds for the fibre-optic and piezoelectric transducers respectively; little or no signal ring-down was observed in these waveforms. The long durations were attributed to interference from edge reflections generated at the boundaries of the aluminium plate; the longer duration for the piezoelectric transducer compared with the fibre-optic sensor was attributed to the increased sensitivity to multiple reflections. Figure 55 provides a simplified diagram that illustrates the possible paths taken by reflections at the edge of the plate.

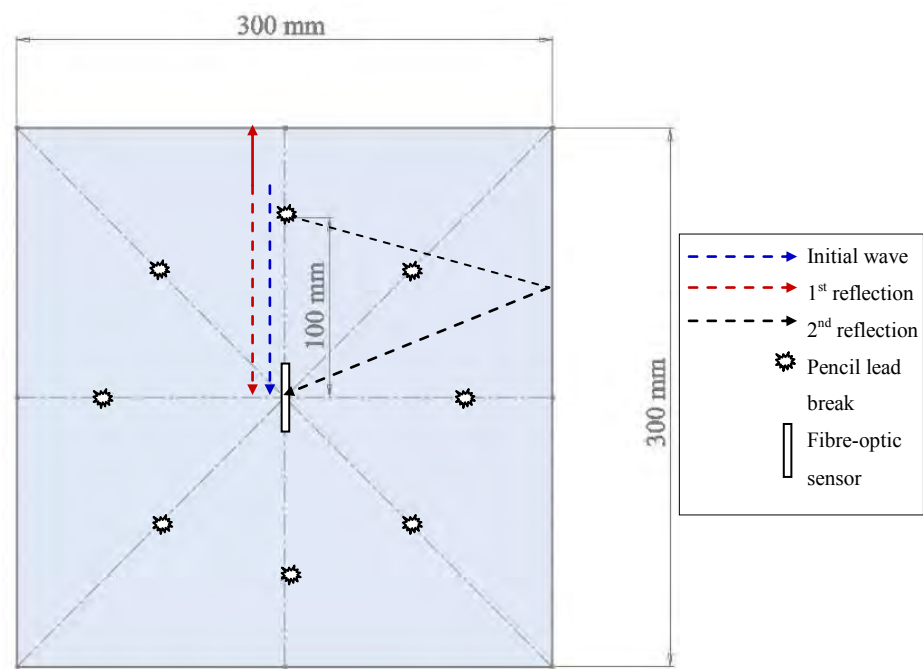


**Figure 55 A schematic illustration of the aluminium plate with the locations of the pencil lead break and fibre-optic sensor, highlighting examples of reflection paths.**

With reference to Figure 55, AE signals recorded by the fibre-optic sensor were assumed to be representative of a minimum of three separate signals each with a discrete arrival time.

Prosser et al. (1999) investigated the influence of plate boundary reflections on the recorded AE signal waveform. Pencil lead breaks were performed on the surface of thin isotropic specimens; various pencil lead break locations relative to the positioning of the sensor on the specimen were evaluated to determine the influence of normal and oblique-incidence reflections on the received signal. The authors inferred that the plate geometry and source-to-receiver distance were contributing factors to the observed signal interference. In the case where the direct arrival wave and first reflection propagation distances were similar, the two signals were superimposed. Signal separation was achieved when the direct arrival wave propagation distance was significantly shorter than that of the first boundary reflection. In all trials, the authors observed multiple reflection signals in the recorded waveforms; the multiple signals were attributed to waves that had reflected from the edge of the plate with different incident angles.

In the current study, superposition of the direct arrival and subsequent boundary reflection signals was observed. This indicated that the propagation distance of the first reflection was similar to the direct arrival wave. Constructive/destructive interference was observed in the recorded waveform; as a consequence, the recorded signal amplitude, obtained from the AE analysis software, was not an accurate representation of the true amplitude of the signal. An alternative method was therefore proposed to define the signal amplitudes recorded by the fibre-optic sensor.

Due to the small dimensions and low attenuation properties of the aluminium test plate, little separation in the arrival times of the primary signal and the boundary reflections was observed. However, as the distance between the source (pencil lead break) and the fibre-

optic-sensor was fixed, the difference in the arrival time of the initial wave and the arrival time of the first boundary reflection could be calculated. To enable calculation of the first boundary reflection, the wave speed in the aluminium plate was obtained using the differential time-of-arrival (TOA) of the signal at two surface-mounted fibre-optic sensors; the two sensors (SM04-006 and SM04-007) were spaced at a distance of 100 mm. An effort was made to ensure that each channel was triggered on the same region of the waveform to avoid timing errors associated with varying sensor sensitivities; this was achieved by manually correcting the time of arrival/threshold crossing of each channel within the software. A schematic illustration of this setup is shown in Figure 56. The results of ten TOA measurements are presented in Table 15.

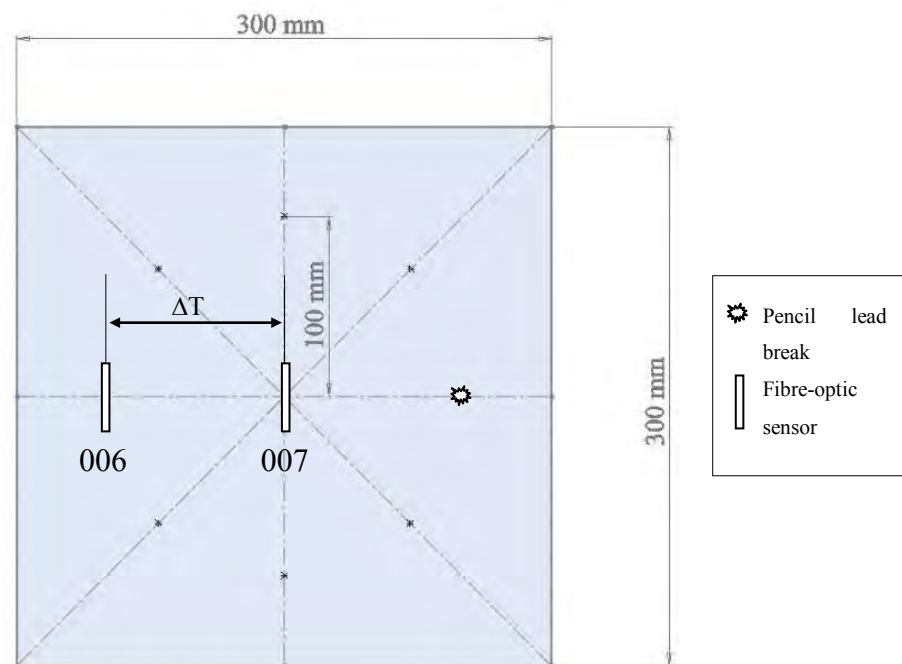


**Figure 56 A schematic illustration of the experimental setup used to obtain the differential time-of-arrival of a signal using two fibre-optic sensors.**

**Table 15 Time of arrival calculations using two multiplexed fibre-optic sensors on a 1.6 mm thick aluminium plate; standard deviation in parentheses.**

Signal No.	Delta TOA (seconds)	Distance (metres)	Velocity (ms <sup>-1</sup> )
1	4.3E-05	0.1	2325.6
2	4.63E-05	0.1	2159.8
3	4.48E-05	0.1	2232.1
4	4.66E-05	0.1	2145.9
5	4.7E-05	0.1	2127.7
6	4.34E-05	0.1	2304.2
7	4.71E-05	0.1	2123.1
8	4.48E-05	0.1	2232.1
9	4.47E-05	0.1	2237.1
10	4.46E-05	0.1	2242.2
<b>Mean</b>	-	-	<b>2212.9 (71.4)</b>

An average wave speed of 2213 ms<sup>-1</sup> was calculated from the ten TOA tests. In order to obtain the arrival time of the first reflection, the additional distance travelled by the reflected wave was calculated. Based on the dimensions of the aluminium test plate and the location of the pencil lead break (see Figure 55), the additional distance travelled by the first boundary reflection was 0.1 metres; this was assumed based on the normal-incidence back-wall reflection. Using the calculated wave speed of 2213 ms<sup>-1</sup>, a first reflection arrival time of 45x10<sup>-6</sup> seconds was obtained from the initial threshold crossing, i.e. 0.1/2213 = 45 microseconds. Figure 57 provides an example of a typical discrete waveform showing the initial 45 microseconds from the threshold crossing only. This portion of the discrete waveform was believed to relate to the first arrival wave only. A pre-trigger of 50 microseconds was used during acquisition to record any signal activity prior to the threshold crossing. Constructive/destructive interference was observed in all acquired waveforms captured during evaluation of the fibre-optic sensor using the 300 x 300 mm aluminium plate. As a result, all pencil lead break signal amplitudes and frequency responses were calculated

directly from the time-gate between signal crossing and the initial 45 microseconds of each recorded signal. Theobald et al. (2008) proposed the same procedure for time-gating the direct arrival wave.

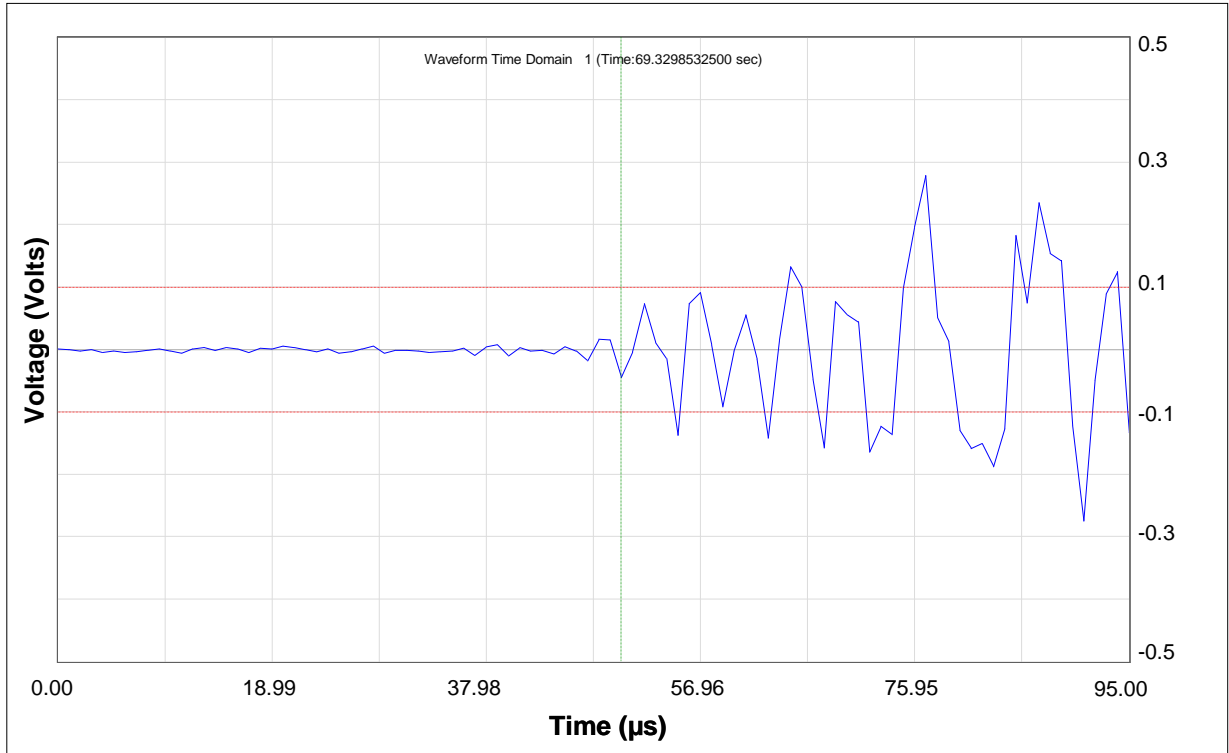


**Figure 57** Discrete waveform of the pencil lead break highlighting region of interest, i.e. 45 microseconds.

A sampling rate of one million samples per second (MSPS) was used for waveform acquisition. The sampling rate was selected based on the frequency bandwidth of interest. As the frequency filter of the fibre-optic sensor interrogation unit was 10 – 500 kHz, a sampling rate twice the maximum frequency component was deemed adequate for acquisition. Figure 58 provides a typical example of a fast Fourier transform (FFT) for the first 45 microseconds after threshold crossing. With reference to the FFT, the peak frequency of the pencil lead break was observed at 218 kHz.

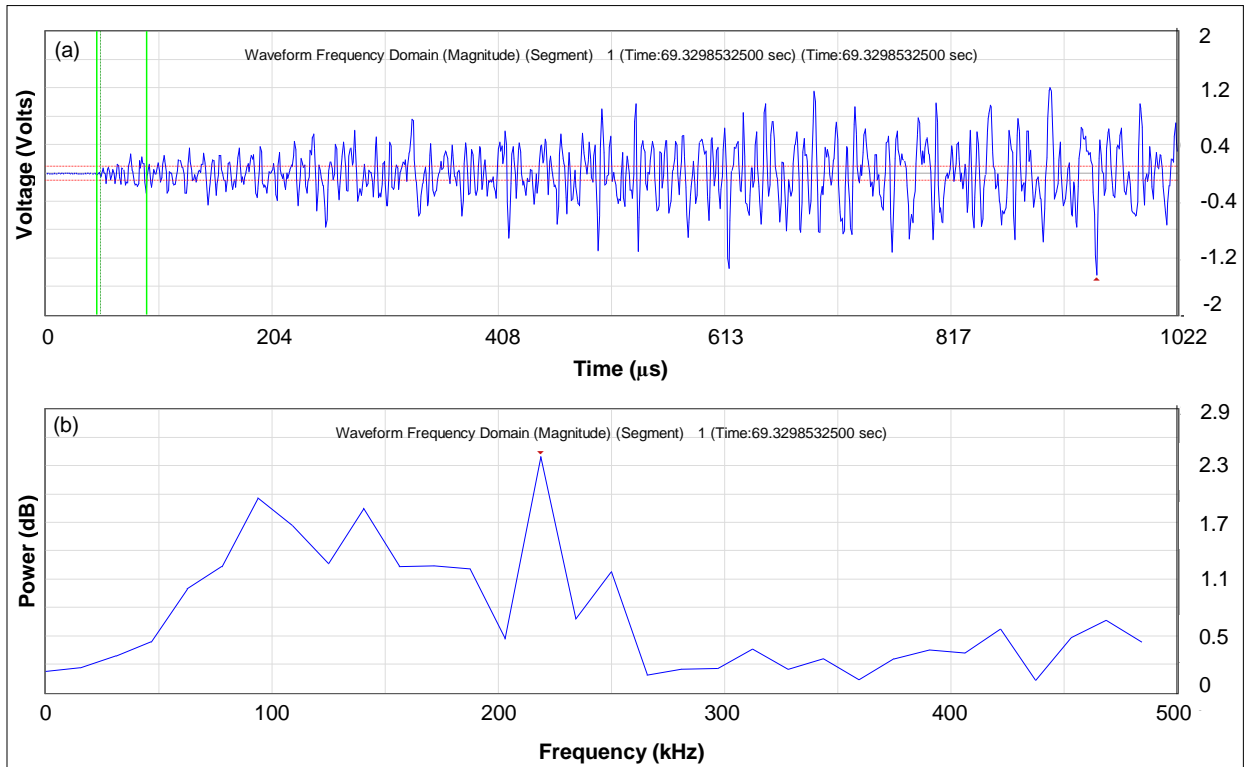


**Figure 58 (a) A typical discrete waveform; and (b) corresponding FFT illustrating the peak frequency of the highlighted region; the signal was generated by a pencil lead break.**

The thirty pencil lead breaks were evaluated with respect to their physical properties, i.e, their mass and length. The physical properties of the each lead were compared with the characteristics of the AE signal generated from the pencil lead break. The mass and lengths of each fractured lead are presented in Table 16. The maximum signal amplitude and peak frequency are also shown for correlation. The signal voltage was converted to  $dB_{AE}$  using the following equation:

$$Amp (dB_{AE}) = \log 20 \left( \frac{Max\ signal\ peak\ (volts)}{1\ \mu volt} \right) * preamp\ gain \quad Eq. 11$$

**Table 16 Physical and acoustic properties of the 30 pencil lead breaks; standard deviation in parenthesis.**

<b>Pencil-lead number</b>	<b>Pencil mass (µg)</b>	<b>Pencil length (mm)</b>	<b>Recorded amplitude (dB<sub>AE</sub>)</b>	<b>Peak frequency (kHz)</b>
1	9.8	2.19	66.6	218
2	10.5	2.36	68.9	218
3	10.8	2.91	65.3	218
4	9.9	2.32	65.3	218
5	9.9	2.54	67.3	218
6	9.2	2.61	64.0	218
7	9	2.19	66.6	218
8	15	2.18	65.7	218
9	12.6	3.04	65.3	218
10	9.8	2.55	65.1	218
11	15.4	3.00	70.3	78
12	8.3	1.99	67.9	218
13	8.1	1.93	67.3	218
14	13.9	2.95	65.1	93
15	10	2.25	67.3	218
16	10.2	2.25	67.2	218
17	15.6	3.30	65.5	218
18	10.2	2.23	69.3	218
19	11.4	2.58	66.5	218
20	10.7	2.05	65.3	218
21	10.4	1.91	66.3	78
22	9.3	1.83	68.7	218
23	10	2.03	65.9	218
24	12.6	2.33	64.3	218
25	10.3	2.38	66.5	218
26	10.4	2.10	65.8	218
27	9.3	2.15	64.8	78
28	10.8	2.15	65.8	218
29	10.2	2.06	65.8	218
30	12.5	2.38	67.1	218
<b>Mean</b>	<b>10.87 (1.96)</b>	<b>2.36 (0.37)</b>	<b>66.4 (1.5)</b>	<b>-</b>

With reference to Table 16, a low standard deviation for lead mass and length was observed. The observed length of the pencil lead breaks also complied with the value stated in the reference standard, ASTM E-976 (ASTM, 2005); the standard proposed that each lead should measure between 2 and 3 mm. With respect to the signal amplitude, a mean amplitude of

66.4 dB<sub>AE</sub> was recorded with a standard deviation of  $\pm 1.5$  dB<sub>AE</sub>. This error lies within the accepted range of  $\pm 3$  dB<sub>AE</sub> (ASTM, 2005). Consistency with the peak frequency of the recorded signals further supports the reliability of this method for repeatable signal generation; 86 % of the pencil lead breaks recorded were found to have a peak frequency of 218 kHz. The remaining 14 % of signals had peak frequencies of 78 and 93 kHz. The fracture surfaces of the pencil lead breaks corresponding to the low, medium and high frequency signals, i.e. 78, 93 and 218 kHz respectively, were examined using scanning electron microscopy (SEM). The SEM micrographs are presented in Figure 59.

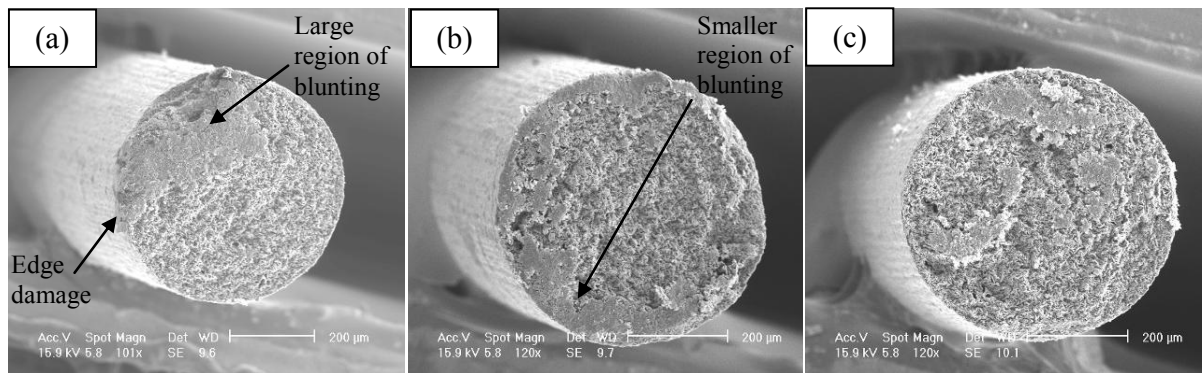


**Figure 59 Scanning electron micrographs of a sample of three different pencil-leads which produced: (a) low-frequency; (b) medium-frequency; and (c) high-frequency acoustic signals.**

The micrograph corresponding to the low frequency signal illustrates significant surface blunting in a single discrete region. This blunting may be attributed to a higher applied force at this region during fracture of the pencil-lead; through applying a greater force, the fracture of the lead was assumed to be typical of a crushing mechanism. A fracture dominated by a crushing mechanism would be less dynamic and it is therefore assumed that this mode of

failure would exhibit a lower frequency response. The smaller region of blunting is observed in Figure 59(b); this implies that the crushing force was lower. A more uniform surface profile was observed from Figure 59 (c) suggesting dynamic failure from a discrete location. To the best of the author's knowledge, no research studies have been undertaken to evaluate the frequency response of pencil lead breaks that were fractured by different mechanisms. Bohse (2000a) proposed that different failure mechanisms in composite materials have varying visco-elastic relaxation process and therefore different intrinsic frequencies. It is proposed here, that the assumed difference in the fracture mechanism of the pencil lead was related to varying relaxation times of the surface of the material that was displaced by the fracturing of the pencil lead; a crushing failure mode was believed to be less dynamic and therefore would result in a slower relaxation. As a result, the observed frequency content of the signal would be lower.

With reference to other AE parameters of interest, e.g. signal energy, counts and rise time, no further correlations were drawn from analysis of the physical properties of the pencil leads. It was anticipated that any variations in the response of the sensor due to pencil lead break error can be minimised through adequate sampling; a mean value from ten pencil lead breaks at each measurement location was used in all subsequent trials. In view of the low variation in the data presented in Table 16, the HN-source was used in all subsequent trials for evaluating the response of the fibre-optic sensor. Support of the use of this method for verifying the response of an acoustic emission sensor is presented in Nielsen (1980), Hamsted (1982) and Ohtsu et al. (1998).

## 6.2 Modal Analysis

Modal analysis was utilised for the evaluation of the sensitivity of the fibre-optic sensor to different wave modes present within the discrete waveforms; modal analysis was performed on signals generated in response to pencil lead breaks. An explanation of modal analysis is presented in Section 3.4.1.1. In order to demonstrate clear separation of the different modes within the acquired waveforms, the test was performed on a 1 m x 1 m x 1.6 mm aluminium plate. Hamstad et al. (2002) utilised modal analysis to show separation of wave modes in wavelet transforms. The authors inferred that as the source-to-receiver distance was increased, the separation of the two modes became more defined owing to the differences in the wave propagation velocities. Figure 60 provides the group velocity dispersion curve the aluminium plate; the red area highlighted in the figure illustrates the frequency range of interest based on the filter settings within the fibre-optic sensor interrogation unit, i.e. 10 – 500 kHz.

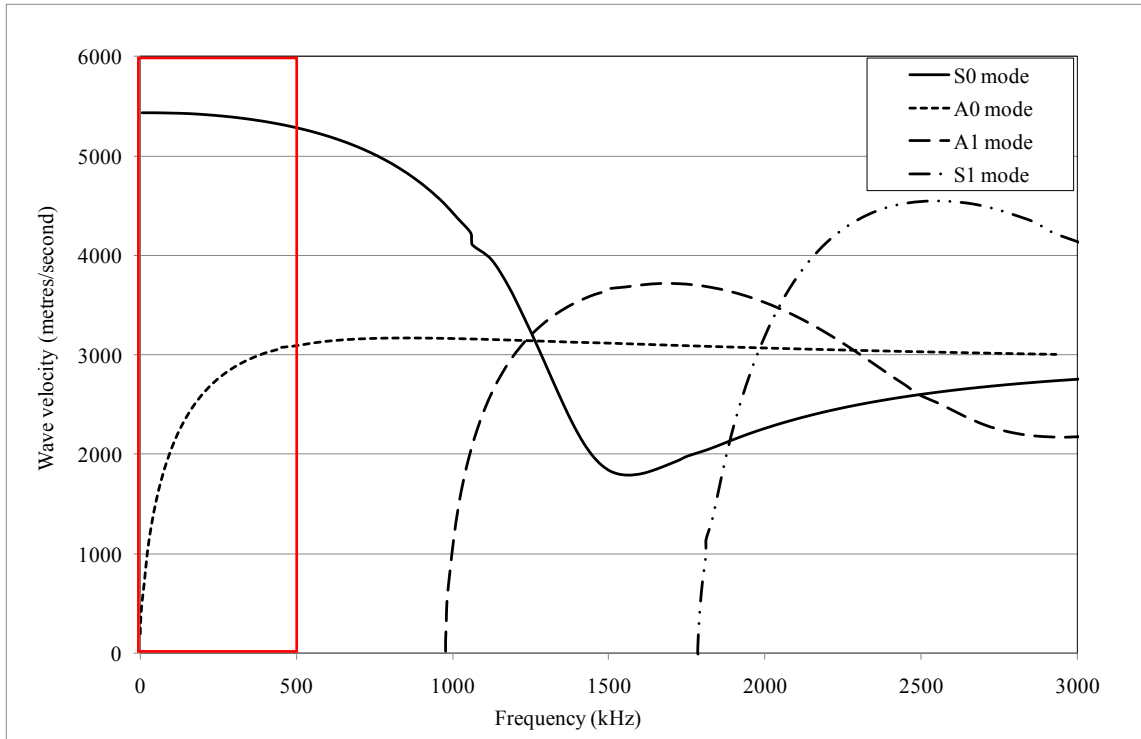


**Figure 60 Group velocity dispersion curve for an aluminium plate with a thickness of 1.6 mm with highlighted area of interest (see red box).**

An expanded portion of Figure 60 is presented in Figure 61. With reference to the recorded wave speed of  $2213 \text{ ms}^{-1}$  obtained from the TOA calculation reported in Section 6.1, the frequency range and thus the proposed mode of interest can be defined; the red circle in Figure 61 indicates the approximated region at which the  $y$ -axis intersects with the curve of the  $A_0$  mode at  $\sim 2213 \text{ ms}^{-1}$ . It is therefore proposed that the fibre-optic sensor was sensitive to the higher amplitude out-of-plane anti-symmetrical mode.

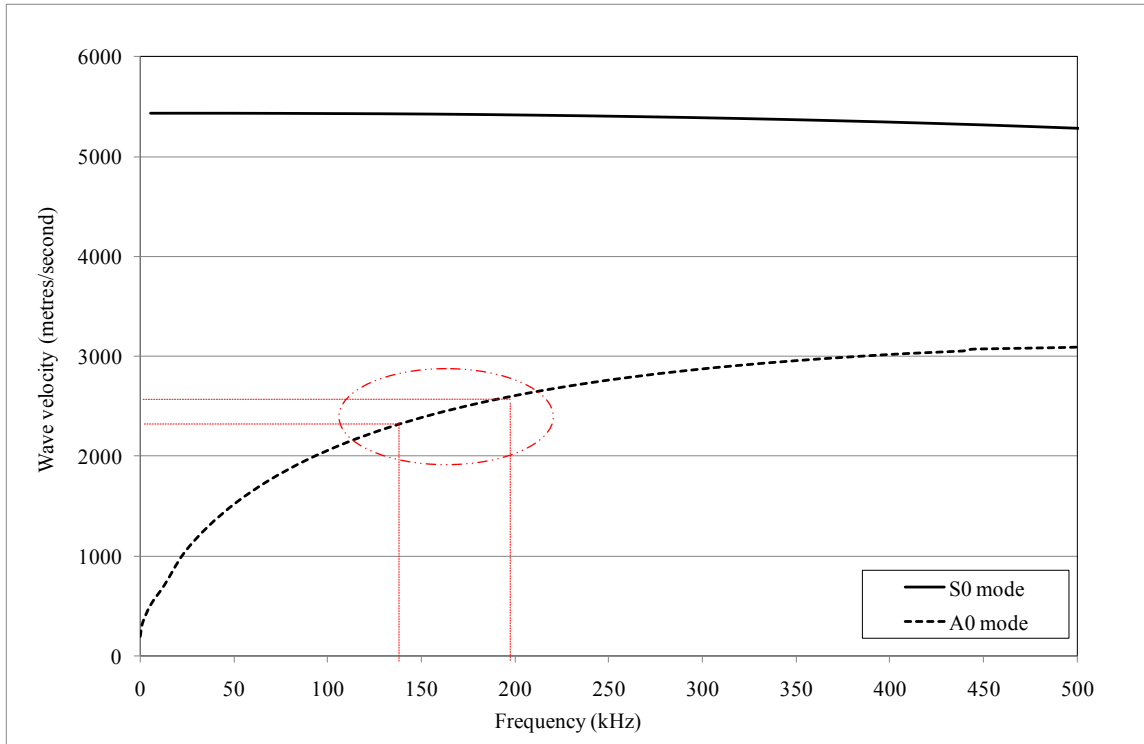


**Figure 61 Expanded portion of a group velocity dispersion curve for an aluminium plate with a thickness of 1.6 mm; the red circle illustrates the approximated intersections of the mean signal velocity with the signal frequency.**

In addition, wave mode evaluation software (PerfPAC™, Physical Acoustics Corporation; USA) was utilised to compare the calculated time-frequency signal representation with the theoretical group velocity dispersion curve. The discrete waveform highlighted in Figure 62 was analysed using the PerfPAC™ software. The waveform in this figure corresponds to a pencil lead break performed at a distance of 800 mm from the sensor.

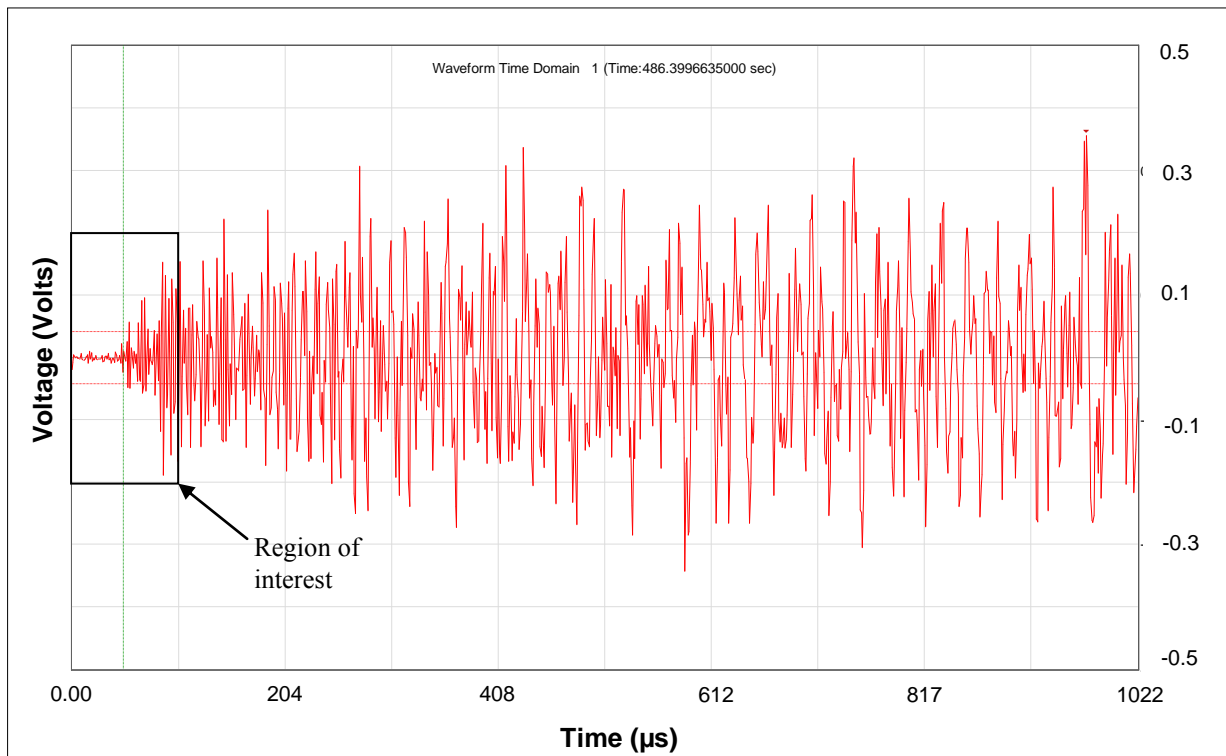


**Figure 62 A typical waveform for a signal recorded by the fibre-optic AE sensor in response to a pencil lead break.**

Figure 63 highlights the analysed signal using the PerfPAC™ software. It is noteworthy to mention that no clear separation in the wave modes was observed. Hamstad (2011) proposed that time-frequency analysis using wavelet transforms (WT) communicated useful information on the energy contained within the different modes present within an AE signal.

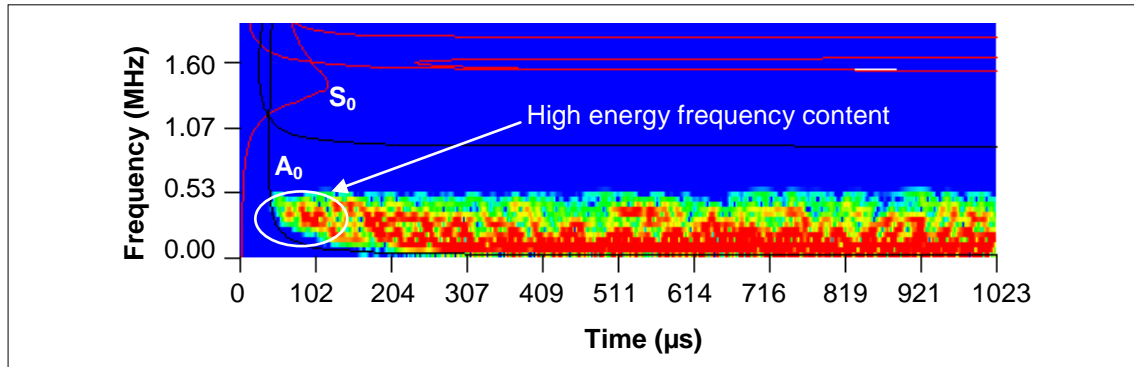


**Figure 63 Plot of the group velocity dispersion curve versus the time-frequency representation for a signal recorded by the fibre-optic sensor in response to a pencil lead break.**

With reference to Figure 63, signals beyond  $\sim 500$  kHz were not recorded due to the frequency cut-off of the filter used in the fibre-optic sensor interrogation unit. With respect to the wave mode correlation, the time-frequency representation is in close agreement with the  $A_0$  wave mode on the dispersion curve; a region of high energy at around 100-250 kHz was observed at the point of the threshold crossing. This frequency range correlates well with the marker on the curve of the  $A_0$  mode illustrated in Figure 61. No indication of the  $S_0$  mode was observed in the data.

It has been documented in the literature that a pencil lead break on the surface of a thin plate produces predominantly out-of-plane displacements (Gorman and Prosser, 1991; Prosser et al., 1999; Tsuda et al., 2001). As a result, high amplitude flexural modes were expected with little extensional mode content. With reference to the results presented, it is therefore proposed that the fused-tapered fibre-optic sensor would show high sensitivity to failure modes in composites that result in large out-of-plane displacements; Tsuda et al. (2001)

proposed that impact loading and delaminations result in the generation of signals with high amplitude flexural modes.

For comparison, the PerfPAC™ software was used to analyse a discrete waveform recorded by the piezoelectric transducer. The signal was recorded in response to a pencil lead break performed at a distance of 800 mm from the sensor. With reference to Figure 64, clear mode separation was observed within the first 300 microseconds (see highlighted region). Figure 65 presents the dispersion curve versus time frequency representation correlation plot. With reference to this figure, both the  $S_0$  and  $A_0$  dispersion curves correlate well with the frequency content observed in time-frequency analysis plot. The piezoelectric transducer demonstrated sensitivity to both extensional and flexural wave modes. Prosser et al. (1999) proposed that although a surface-fractured pencil lead break produced predominately anti-symmetrical wave motion, a piezoelectric transducer had sufficient sensitivity to detect the small extensional wave travelling in thin plates. The second low amplitude peak in Figure 64 correlates with the reflection signal of the  $S_0$  mode, i.e.  $S_{0R}$  from a normal incidence boundary reflection (see Figure 55).

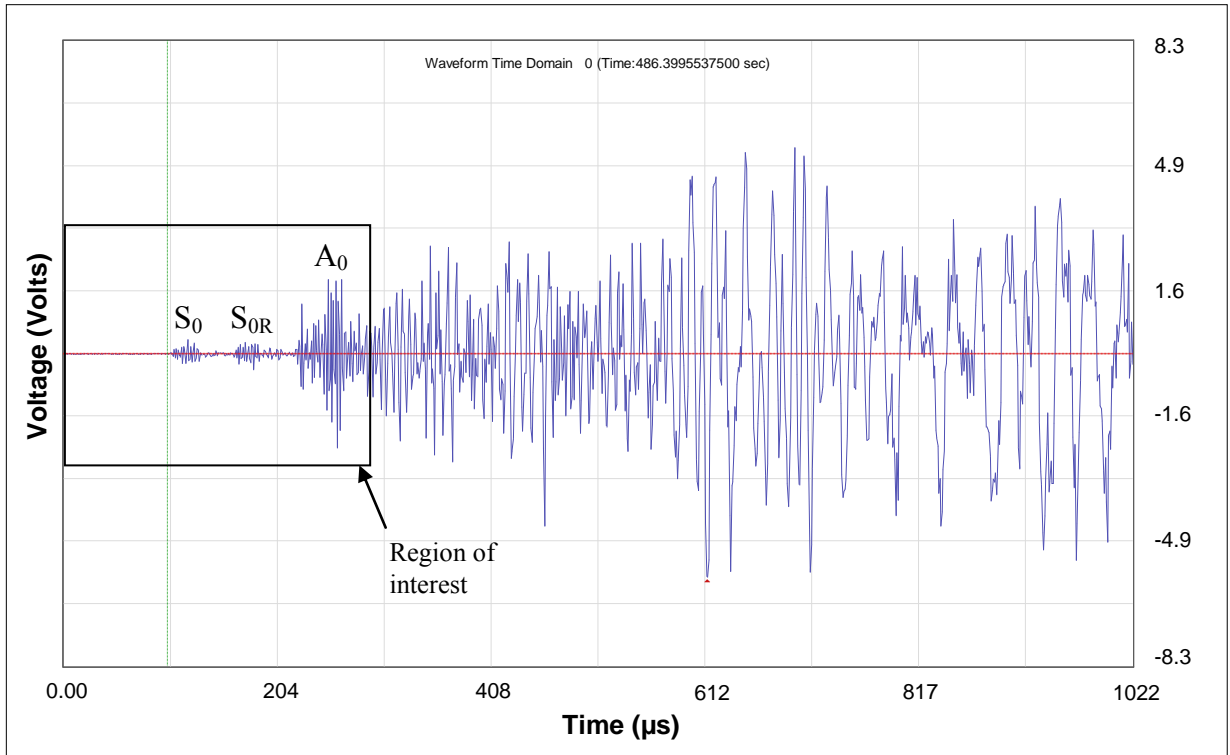


Figure 64 A typical waveform for a signal recorded by the wideband piezoelectric transducer in response to a pencil lead break.

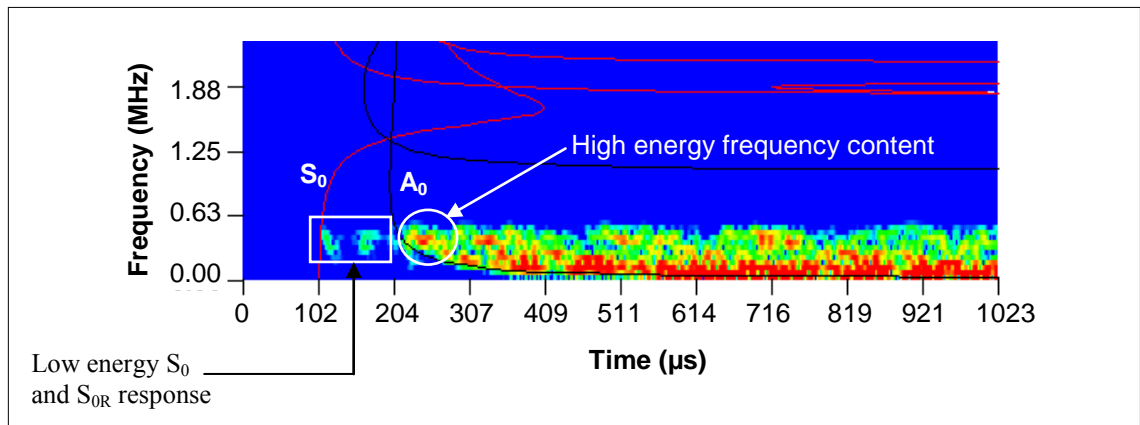
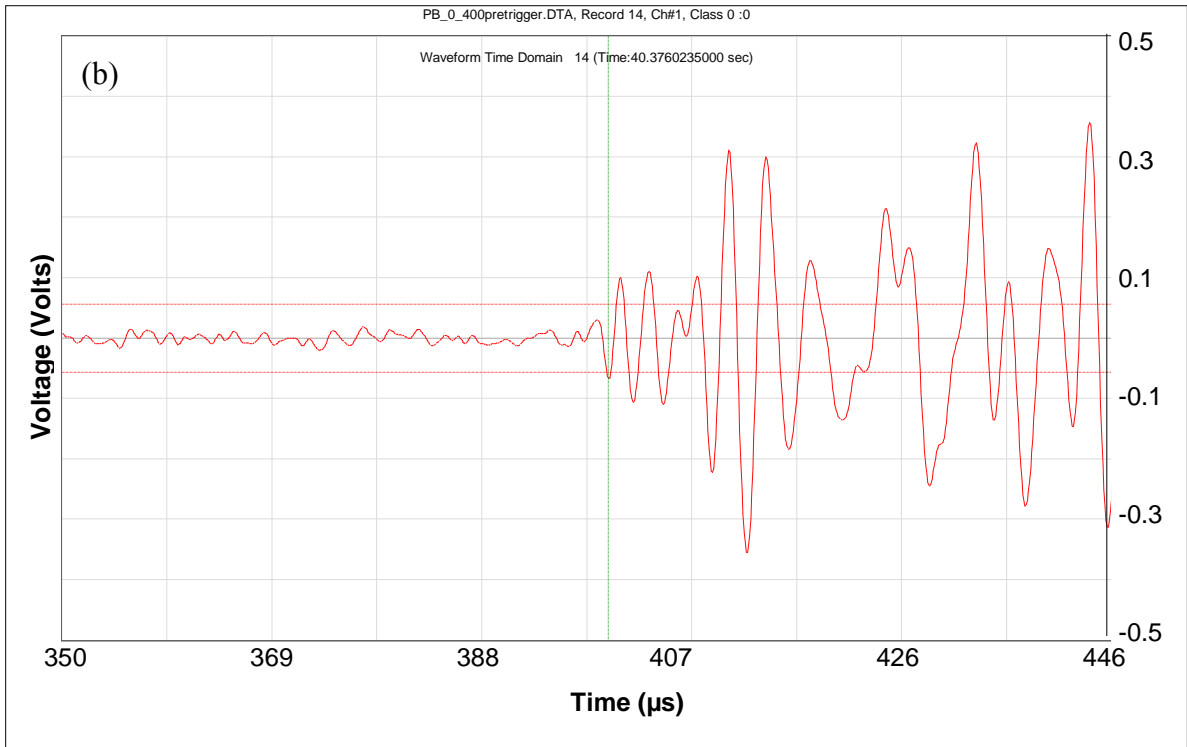
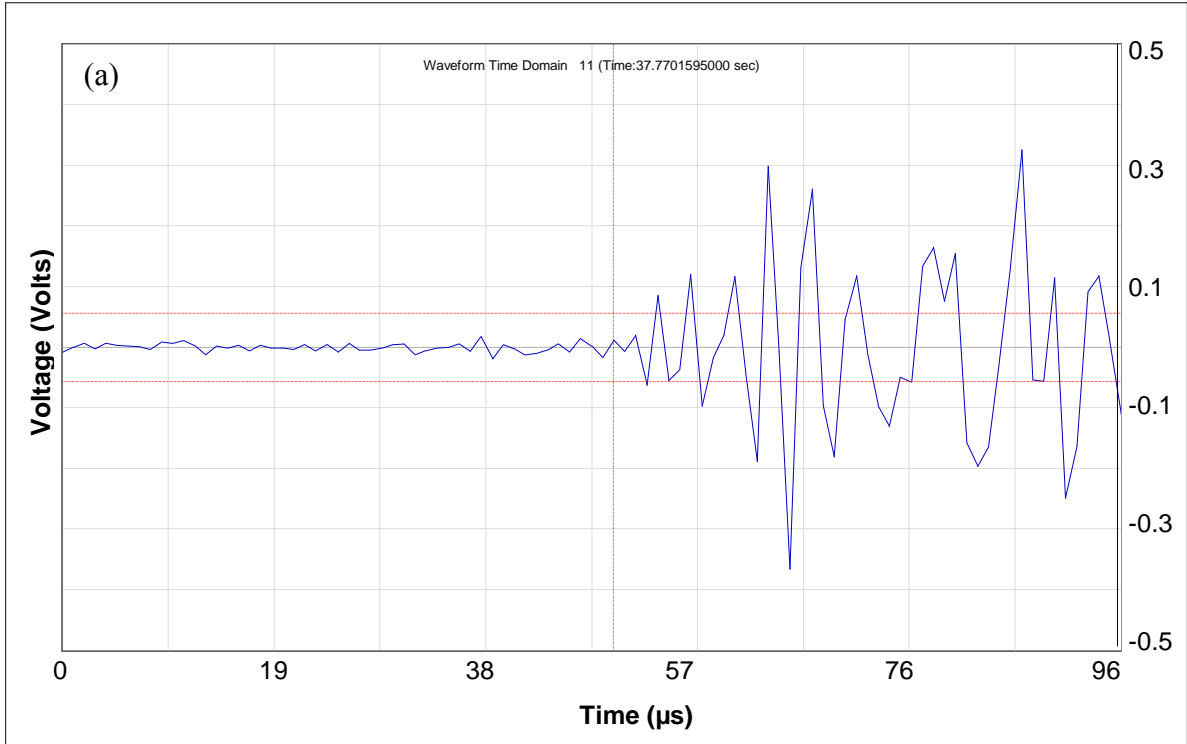


Figure 65 Plot of the theoretical group velocity dispersion curve versus the short-time Fourier transform from the wideband sensor in response to a pencil lead break.

The effect of increasing the sampling rate used for data acquisition was evaluated. This was in order to determine if the sensitivity of the fibre-optic sensor to the symmetrical mode could be improved. Pencil lead breaks were performed on the surface of a 1.6 mm thick aluminium plate; the acquired data was sampled at both one and ten MSPS. Figure 66 (a) and (b) provide examples of typical discrete waveforms recorded at one MSPS and ten MSPS respectively; minimal resolution in the data was lost from sampling at the lower rate. The observed waveforms at the lower sampling rate appear to be less rounded; the loss of resolution had no influence on the observed maximum signal level. No additional wave mode information was extracted from the fibre-optic sensor at the higher sampling rate. The waveform presented in Figure 66 (b) had a 400 microsecond pre-trigger. It is therefore proposed that the acquired waveforms were sampled appropriately at one MSPS without loss of meaningful data, e.g. wave-mode identification, amplitude or frequency response. Prosser and Gorman (1992) proposed that for signals with a peak frequency content of  $\sim 200$  kHz, a 1 MHz sampling rate would be high enough to avoid inaccuracies with the frequency response of the signal.



**Figure 66 Typical examples of discrete waveforms captured using: (a) a one MSPS sampling rate; and (b) a ten MSPS sampling rate.**

### 6.3 Directional Sensitivity

This section discusses the trials that were carried out in order to characterise the directional sensitivity of the fibre-optic AE sensor. The trials were performed with the aim of characterising the response of the AE sensor with reference to:

- (i) the performance of a piezoelectric transducer;
- (ii) the type of optical fibre and the physical properties of the fibre-optic sensor;
- (iii) the repeatability of surface-mounting of the sensor on the host material;
- (iv) the type of coupling media used to mount the sensor;
- (v) the type of packaging substrate used to house the sensor; and (vi) the properties of the test specimen on which the sensor was mounted.

In addition to the above-mentioned trials, a preliminary study investigating the sensitivity of a fibre-optic AE sensor that was embedded in a uni-directional composite is presented.

The directional sensitivities of the piezoelectric and fibre-optic sensor are presented using radar plots; the maximum recorded signal amplitude, obtained using the time-gating method outlined in Section 6.1, was presented as a function of the orientation of the pencil lead break. The maximum amplitude, reported using the logarithmic  $\text{dB}_{\text{AE}}$  scale, was obtained from the peak voltage from each waveform recorded in response to a pencil lead break. A comparison of the sensor performance from each trial condition is presented in a summary table at the end of this section.

### 6.3.1 Directional Sensitivity of the Electrical-Based Piezoelectric transducer

The directional sensitivity of the WD piezoelectric transducer was evaluated using the HN source; the performance of the electrical-based sensor was obtained for comparison with the response of the fibre-optic sensor. Pencil lead breaks were performed around the 360° orientation of the sensor at 45° intervals. A source-to-receiver distance of 100 mm was used in order to avoid saturation of the signals (ASTM, 2005). Saturation of the signal occurs when the maximum voltage exceeds the limit of the preamplifier; as a result, the maximum peak of the waveform becomes truncated (Farrow et al., 1994). In this study, the sensor was mounted on a 1.6 mm thick aluminium plate using ultrasonic gel; further details of the experimental setup can be found in Section 3.4.2. Ultrasonic gel was used for ease of sensor removal after measurements were recorded. Colombo et al. (2005) reported that a similar type of the couplant did not require setting-time and would permit removal of the sensor without the risk of damage. In addition, the sensor could be easily cleaned of this aqueous-based couplant.

Figure 67 illustrates the recorded directional sensitivity of the surface-mounted WD sensor; the sensor was repeatedly mounted and the response was characterised. The plot in Figure 67 illustrates a typical response from the sensor; the response from the device was found to be consistent. The error bars represent the standard deviation from the mean for ten pencil lead breaks performed at each location. The observed variation in the signal amplitude was attributed to pencil lead break error; the maximum variation, i.e. 1.8 dB<sub>AE</sub>, was within the accepted tolerances outlined in ASTM E-976 (ASTM, 2005). The WD sensor demonstrated a uniform response as a function of orientation of the source relative to the sensor; a difference

of 2.5 dB<sub>AE</sub> was reported between the highest and lowest mean values. The minimal variations in the amplitude of the signal were assumed to be related to small non-uniformities with sensor mounting.

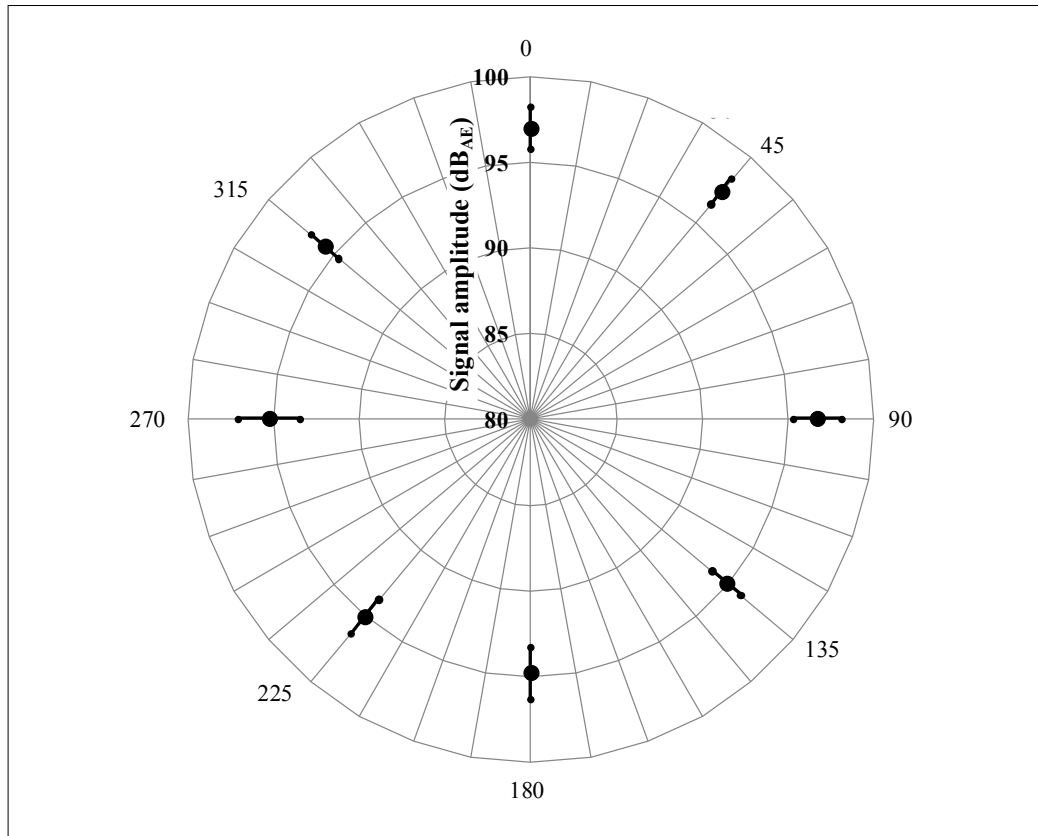


**Figure 67 A radar plot illustrating the mean signal amplitude as a function of source orientation for the WD piezoelectric transducer.**

In comparison with the results presented in this study, Chen et al. (2006) reported similar directional sensitivities from a surface-mounted piezoelectric transducer on an aluminium plate. Barbezat et al. (2004) presented nominal variations in the orientation response for a piezoelectric transducer mounted on an isotropic PMMA specimen. The authors inferred that the small fluctuations in the amplitude of the signal were due to variations in the pencil lead

break. Hill and El-Dardiry (1981) also proposed that fluctuations in the thickness of the coupling layer between the sensor and the host material could influence the sensitivity of the sensor. Buttle and Scruby (1989) indicated that sensors that do not exhibit an omnidirectional response would not be suitable for accurate localisation of acoustic sources.

The ASL recorded by the WD sensor was also obtained in order to calculate the signal-to-noise ratio of the device. A mean value of 14.2 dB<sub>AE</sub> was obtained from the pre-trigger region of the recorded waveforms. The corresponding signal-to-noise ratio of the WD sensor was greater than 80 dB<sub>AE</sub>; it is therefore inferred that the sensitivity of the piezoelectric transducer would permit the detection of low-amplitude AE signals that were emitted from failure mechanisms that generate a low release in energy, e.g. matrix cracking (Favre et al., 1989).

### 6.3.2 Directional Sensitivity of the Fibre-Optic Sensor

The directional sensitivity of the fibre-optic sensor was also characterised using the HN source. Five fibre-optic AE sensors were each manufactured from reels of the SM04-1 and SM600 optical fibre; both reels of fibre were stored in the dark under ambient conditions prior to sensor fabrication. All of the sensors were housed using the square U-channel package. In order to minimise damage to the sensors during handling and storage, the sensors were manufactured and then characterised immediately using pencil lead breaks. Ten pencil lead breaks were performed around the 360° orientation of the sensor at 45° intervals. An average of the ten lead breaks was used to represent the mean signal response for each sensor. The directional sensitivities of the ten sensors, i.e. five SM04-1 and five SM600-type sensors, were compared. In this study, the sensors were coupled to the aluminium plate using

ultrasonic gel. Further details of the experimental setup are provided in Section 3.4.2. The radar plot in Figure 68 illustrates the mean directional sensitivity obtained from the five SM04-1 fibre-optic sensors for all pencil lead breaks orientations relative to the sensor; the error bars represent the standard deviation for the average of the five sensors.

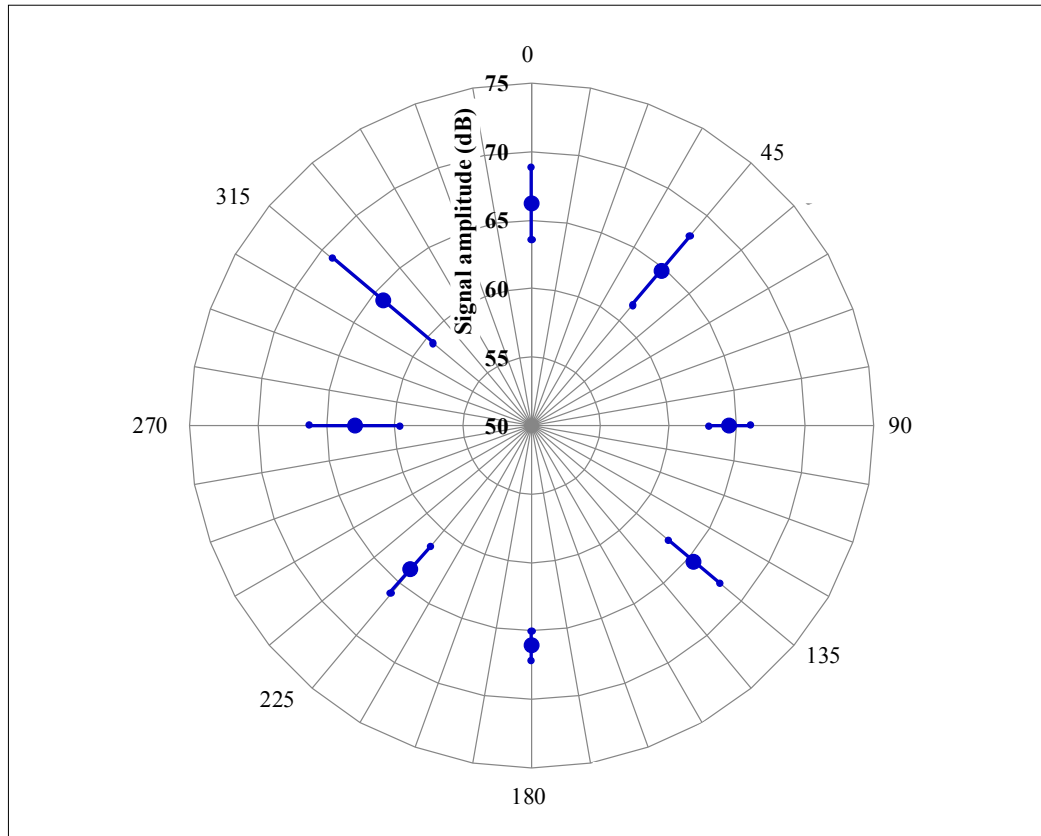


**Figure 68** A radar plot illustrating the mean signal amplitudes for the five fibre-optic sensors as a function of orientation; the sensors were fabricated using SM04-1 optical fibre.

Two noteworthy observations can be made from a review of Figure 68. Firstly, the amplitudes of the signals recorded by the fibre optic sensor were more than 25 dB<sub>AE</sub> lower than those recorded by the piezoelectric transducer. Secondly, the spread in the measured data was relatively high. This indicates that the sensitivities of the five sensors were not consistent.

From a comparison of the sensor-to-sensor signal response, a large scatter was observed. With reference to a single axis of measurement, a maximum variation of more than 10 dB<sub>AE</sub> was recorded; the minimum and maximum values corresponding to this variation in sensitivity are highlighted in blue in Table 17. The inconsistency in the sensor-to-sensor response was anticipated owing to the low fabrication repeatability reported in Section 4.1. For reference, the individual signal amplitudes for each of the SM04-1 sensors are shown in Table 17.

**Table 17 A summary of the directional sensitivities for the five SM04-1-type fibre-optic sensors; standard deviation in parentheses.**

Orientation	Amplitude (dB <sub>AE</sub> )					
	SM04-008	SM04-009	SM04-010	SM04-011	SM04-012	Mean
0°	63.1 (1.3)	68.3 (1.4)	65.9 (1.1)	64.3 (2.4)	69.3 (1.7)	<b>66.2 (2.6)</b>
45°	61.0 (1.4)	68.6 (1.5)	66.6 (1.4)	61.8 (1.2)	65.7 (2.1)	<b>64.7 (3.2)</b>
90°	65.4 (1.8)	61.9 (1.3)	64.5 (1.3)	65.9 (1.1)	64.4 (1.6)	<b>64.4 (1.5)</b>
135°	63.4 (1.9)	69.6 (1.2)	66.0 (1.5)	64.2 (2.2)	64.3 (1.0)	<b>65.5 (2.5)</b>
180°	65.7 (1.7)	66.8 (0.5)	64.3 (0.8)	66.6 (1.1)	67.0 (1.5)	<b>66.1 (1.1)</b>
225°	60.3 (1.3)	66.1 (0.7)	64.3 (1.3)	62.8 (2.0)	64.9 (1.9)	<b>63.7 (2.2)</b>
270°	58.5 (0.7)	60.7 (1.8)	63.6 (1.3)	65.0 (1.2)	66.6 (1.8)	<b>62.9 (3.3)</b>
315°	59.0 (0.8)	63.3 (1.2)	65.6 (1.7)	61.5 (1.5)	71.6 (1.3)	<b>64.2 (4.8)</b>

A low standard deviation at each measurement location was observed; this result indicates that there was little error in the pencil lead breaks. A maximum deviation of 2.4 dB<sub>AE</sub> was observed from evaluation of sensor SM04-011. This maximum deviation value represents a percentage error of less than 4 % of the maximum recorded amplitude; this was deemed to be an acceptable measurement error. Barbezat et al. (2004) observed a typical deviation of  $\pm 2$  dB<sub>AE</sub> when using the pencil lead break technique. The error observed in the current study is in agreement with their findings.

No directional sensitivity was anticipated from the response of the sensor owing to the isotropic properties of the aluminium plate. With reference to Table 17, sensors SM04-010 and 011 demonstrated a uniform directional response; the lowest directional sensitivity was observed from SM04-010. A higher directional sensitivity was reported for sensors SM04-008, 009 and 012. This was attributed to a combination of: (i) a non-uniform couplant layer between the sensor and the host material around the sensor package (Hill and El-Dardiry, 1981); (ii) non-uniformity in the structure of the sensor taper as discussed in Section 4.1.6; and (iii) a variation in the adhesive bonding of the sensor at both ends of the sensor package. The latter would have resulted in a non-uniform sensitivity to the stress-wave around the sensor (Pierce et al., 1996). Poor coupling efficiency was deemed to be the most feasible cause for the variation in the directional sensitivity response of the sensors; this was proposed as low amplitude measurements were found in concentrated areas around the sensor, e.g. signals with lower amplitudes were located between 225 and 315° for SM04-008.

The directional sensitivities of five fibre-optic sensors fabricated using the SM600 optical fibre were recorded. For reference, all sensors fabricated using the SM600-type optical fibre were assigned the coding of SM600-xxx, where xxx refers to the database number. The response of the SM600-type sensors was compared with the response of the SM04-1-type sensors. The radar plot in Figure 69 illustrates the mean directional sensitivity obtained from the five SM600 fibre-optic sensors; the error bars represent the standard deviation from the average value for the five sensors at each pencil lead break orientation around the sensor. The following observations were made: (i) the greatest sensitivity was found to be parallel to the sensor package, i.e. 0 or 180°; (ii) the mean signal amplitudes were typically higher compared with the SM04-1 sensors; (iii) a low standard deviation was observed for the pencil lead break

error; and (iv) a large scatter, i.e. greater than 10 dB<sub>AE</sub>, was evident in the sensor-to-sensor sensitivities. The minimum and maximum values corresponding to the large variation in the sensor-to-sensor performance are highlighted in blue in Table 18.

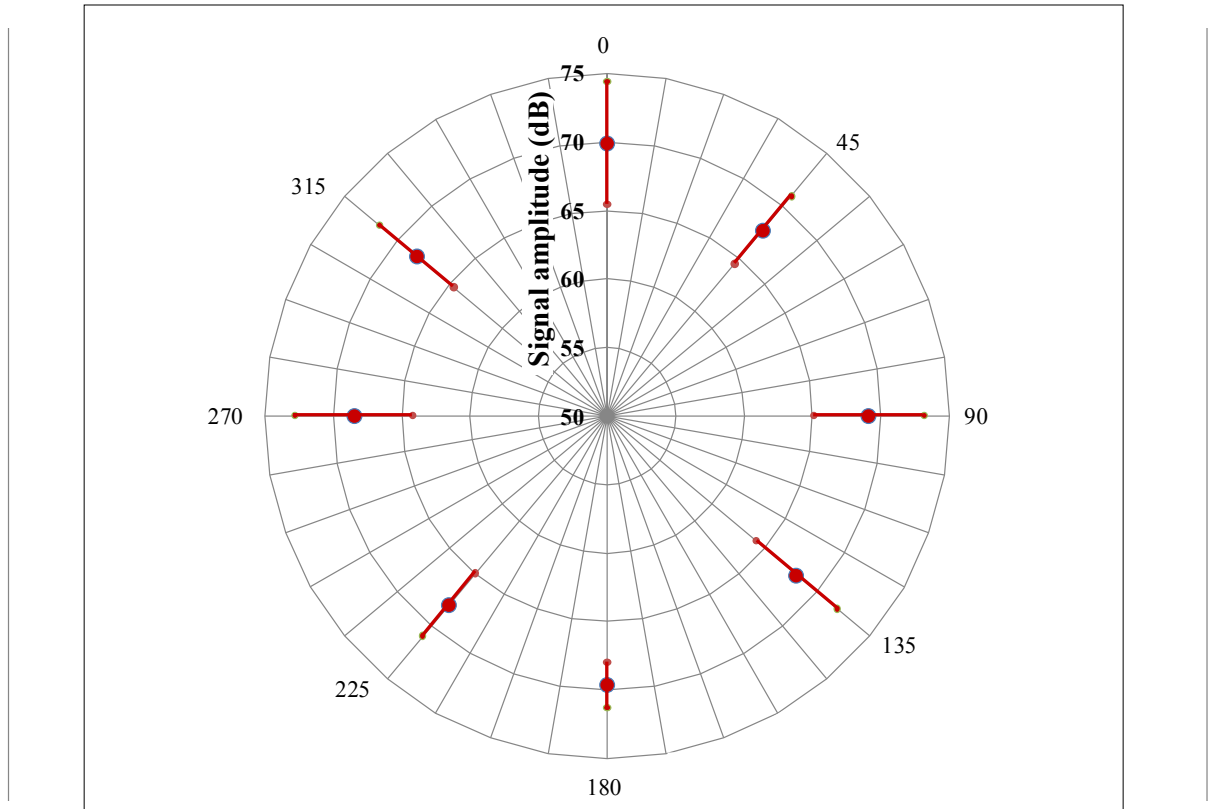


**Figure 69** A radar plot illustrating the mean signal amplitudes for the five fibre-optic sensors as a function of orientation; the sensors were fabricated using SM600 optical fibre.

With reference to Figure 69, the maximum signal amplitudes recorded by the SM600 sensors in response to the pencil lead break were higher than the values recorded by the SM04-1 sensors. The dynamic range, highlighted by the signal-to-noise ratio, was however lower for the SM600 sensors. The higher maximum signal amplitude may be attributed to optimised mode coupling ratio at the sensing region; the mean coupling ratio for the SM600 sensors was

52.4 %; this ensured efficient evanescent mode coupling at the tapered region. A mean coupling ratio of 55.1 % was reported for the sensors fabricated using the SM04-1 fibre. The draw lengths for both the SM04-1 and SM600 fibre-optic sensors were similar. It is therefore proposed that the taper widths of both sensor types were within a similar range. Due to time constraints with the project, no image analysis was performed on SM600 fibre to confirm this assumption. For reference, the mean signal amplitudes for all five of the SM600-type sensors are shown in Table 18.

**Table 18 A summary of the directional sensitivities for the five SM600-type fibre-optic sensors; standard deviation in parentheses.**

Orientation	Amplitude (dB <sub>AE</sub> )					
	SM600-001	SM600-002	SM600-003	SM600-004	SM600-005	Mean
0°	70.1 (0.6)	75.1 (1.1)	72.8 (1.1)	68.0 (1.3)	63.5 (1.4)	<b>69.9 (4.5)</b>
45°	68.9 (1.5)	71.6 (0.7)	67.0 (1.1)	68.2 (0.9)	62.7 (1.4)	<b>67.7 (3.3)</b>
90°	69.7 (1.3)	73.3 (0.8)	72.5 (1.1)	65.1 (1.3)	64.7 (0.9)	<b>69.1 (4.0)</b>
135°	68.3 (2.0)	70.8 (1.5)	71.5 (0.9)	68.0 (2.0)	61.6 (1.0)	<b>68.0 (3.9)</b>
180°	68.4 (0.7)	71.3 (1.3)	71.3 (0.8)	69.4 (0.6)	67.6 (1.5)	<b>69.6 (1.7)</b>
225°	67.2 (0.9)	71.9 (1.4)	69.8 (0.9)	66.8 (2.0)	64.0 (0.7)	<b>67.9 (3.0)</b>
270°	68.9 (1.0)	72.8 (1.0)	71.6 (0.5)	67.1 (1.5)	61.9 (0.9)	<b>68.5 (4.3)</b>
315°	68.4 (0.6)	74.2 (1.1)	69.2 (1.5)	68.5 (2.6)	62.4 (2.2)	<b>68.5 (4.2)</b>

The ASL's were measured and compared for the SM04-1 and SM600 fibre-optic sensors. The signal-to-noise ratios of the sensors were then defined using the maximum signal amplitudes recorded from the directional sensitivity trials. A comparison of the signal-to-noise ratios for the two sensor types is shown in Table 19. A higher mean signal-to-noise level was observed for the SM04-1-type fibre-optic sensors; it was proposed that this was due to a more uniform refractive index (RI) profile in the fibre cladding compared with SM600 fibre. A high ASL was typically observed from sensors with higher excess-loss. The effect

of the uniformity of the refractive index profile on the excess loss in optical couplers was proposed by Georgiou and Boucouvalas (1985); a review of their findings was presented in Section 4.1.2.

**Table 19 A summary of the signal-to-noise ratios for the square U-channel packaged SM04-1 and SM600-type fibre-optic sensors; standard deviation in parentheses.**

Sensor ID	Excess-loss (dB)	Pre-trigger ASL (dB <sub>AE</sub> )	Maximum recorded amplitude (dB <sub>AE</sub> )	Signal-to-noise ratio (dB <sub>AE</sub> )
SM04-008	1.13	36.7	65.7	29.0
SM04-009	1.28	34.1	69.6	35.5
SM04-010	1.01	37.8	66.6	28.8
SM04-011	0.60	36.4	66.6	30.2
SM04-012	0.81	33.8	71.6	37.8
<b>Mean</b>	<b>0.97 (0.3)</b>	<b>35.8 (1.7)</b>	<b>68 (2.2)</b>	<b>32.2 (4.1)</b>
SM600-001	1.46	50.6	70.1	19.5
SM600-002	1.19	34.6	75.1	40.5
SM600-003	1.25	42.5	72.8	30.3
SM600-004	2.07	40.0	69.4	29.4
SM600-005	0.88	36.8	67.6	30.8
<b>Mean</b>	<b>1.37 (0.4)</b>	<b>40.9 (6.2)</b>	<b>71 (2.6)</b>	<b>30.1 (7.4)</b>

In addition, the overall spread in the data for SM600-type fibre-optic sensors was significantly greater than the SM04-1-type sensors. It was therefore proposed that the SM04-1 fibre provided a more repeatable sensor performance. As a result, the SM04-1 optical fibre was used for subsequent sensor manufacture. In addition, the cost per metre of the SM04-1 fibre was 50% lower than the SM600 fibre.

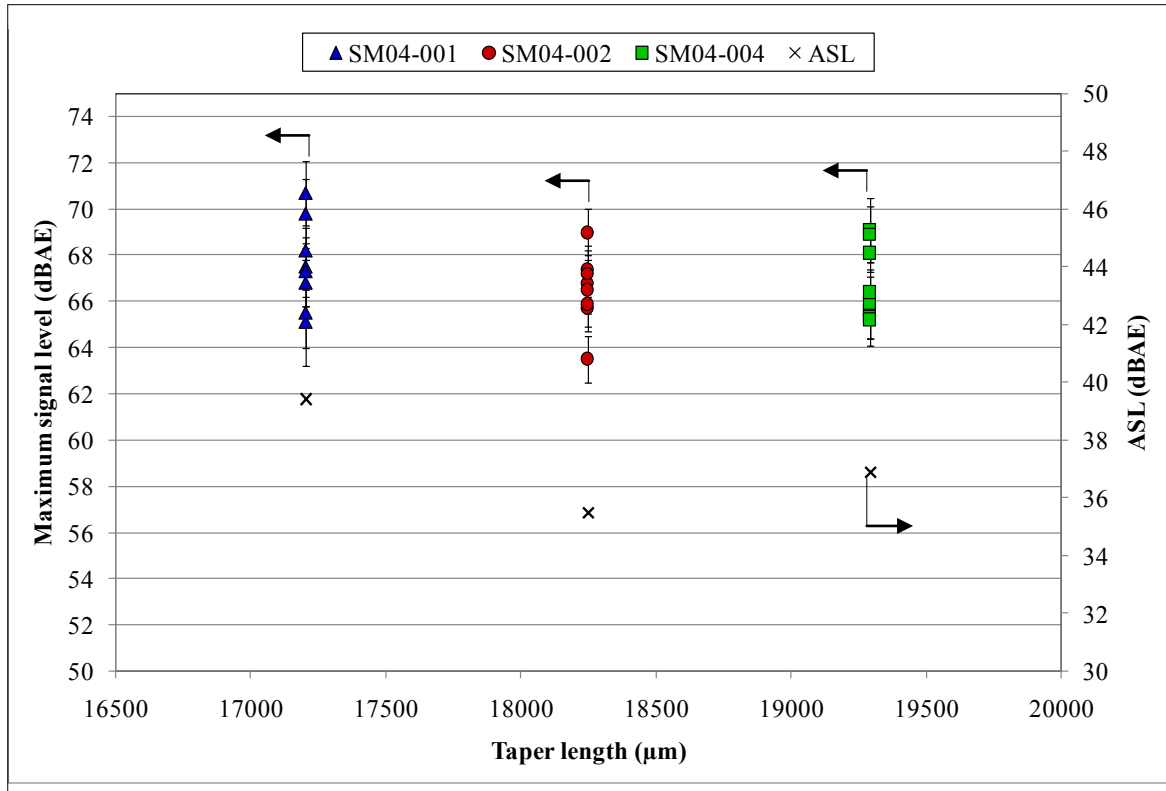
The directional sensitivities of three of the five sensors that were evaluated using optical microscopy in Section 4.1.5 were characterised. The directional sensitivities of the three sensors, SM04-001, SM04-002 and SM04-004 were recorded. Sensors SM04-003 and SM04-

005 suffered damage following image analysis. The performance of the three sensors was evaluated with respect to the following parameters: (i) excess-loss; (ii) coupling ratio; (iii) taper-width; and (iv) taper-length. Table 20 provides a summary of the physical properties of each sensor; in addition, a summary of the signal-to-noise ratios are also shown.

**Table 20 Summary table for sensor fabrication properties, average signal level, maximum signal amplitude and corresponding signal-to-noise ratios for five SM04-1 type sensors packaged using the square U-channel substrates.**

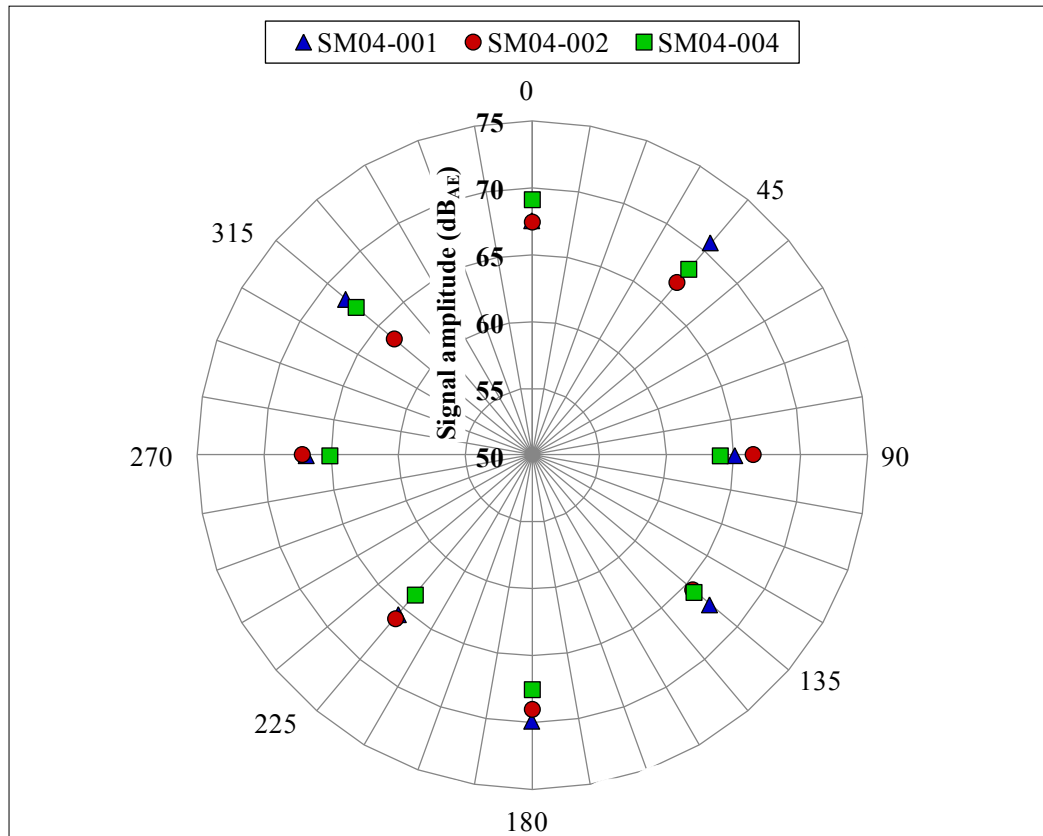
Sensor ID	Excess-loss (dB)	Coupling ratio (%)	Taper-length ( $\mu\text{m}$ )	Taper-width ( $\mu\text{m}$ )	Pre-trigger ASL ( $\text{dB}_{\text{AE}}$ )	Max amplitude ( $\text{dB}_{\text{AE}}$ )	Signal-to-noise ratio ( $\text{dB}_{\text{AE}}$ )
SM04-001	1.37	55.8	17202	13	39.4	70.7	31.3
SM04-002	1.71	52	18246	19	35.5	69.0	33.5
SM04-004	2.79	47.7	19291	13	36.9	69.1	32.2

Figure 70 illustrates the range of signal amplitudes and ASL values for all pencil lead break orientations relative to the longitudinal axis of the sensor; the data in Figure 70 is presented as a function of the taper-length. With reference to the three sensors, the taper-length varied by more than  $1000 \mu\text{m}$ . According to Chen et al. (2003) an increase in the length of the tapered region was assumed to increase the sensitivity of the sensor to AE; a clear increase in the maximum amplitude of the signal was however not observed from analysis of Table 20 and Figure 70. In contrast, the sensors with the narrower taper region, i.e. SM04-001 and SM04-004, demonstrated higher ASL's. It is therefore proposed that as a consequence of the broader taper region, the sensor was less sensitive to vibration induced noise. This result was attributed to the larger mass (Mead, 2000) and a reduction in vibration-induced bending at the taper region (Birks et al., 1996). The sensitivities of the three AE SM04-1-type sensors presented here show close agreement with the sensors previously evaluated.



**Figure 70** A scatter plot illustrating the range of signal amplitudes and ASL values for the different source orientations as a function of taper length for three SM04-1 type fibre-optic sensors; the error bars represent the standard deviation from the mean for each source orientation.

With reference to Figure 71, little directional sensitivity was observed from the three SM04-1 sensors, i.e. the mean signal amplitudes recorded as a function of the orientation of the pencil lead break, were found to be within the same range. This finding further supports the assumption that the response of the fused-tapered fibre-optic AE sensor was not directional dependent.



**Figure 71 Radar plot highlighting mean signal amplitude as a function of orientation for three fibre-optic sensors fabricated using SM04-1 optical fibre.**

The low directional sensitivity indicates that the current sensor design is more suitable for localisation of AE sources compared with other fibre-optic sensor designs presented in the literature. The response of the Fabry-Perot sensor reported by Read et al. (2002) and the fibre Bragg gating sensor reported by Betz et al. (2007) indicated that the recorded amplitude reduced as the incident angle of the propagating wave approached 90° to the axial orientation of the fibre. However, Betz et al. (2007) proposed the use of a three sensor rosette array for detection and localisation of acoustic sources; in this arrangement, the directional sensitivity was minimised as any one sensor was found to demonstrate a high signal response, regardless

of the orientation of the source. A limitation with this setup however was the requirement for multiple sensing heads, thereby adding complexity for signal recovery. Thursby et al. (2008) noted that the dependence of the signal amplitude on the orientation of the source was due to the direction of maximum strain response; for the FBG sensor, this maximum strain response was along the axis of the fibre. In addition, Doyle et al. (2002b) summarised that interferometric sensor designs utilised strain sensing principles to detect AE and were therefore likely to demonstrate a direction dependant response.

The repeatability of remounting the fibre-optic AE sensor on the consistency of the recorded signal amplitude at each source orientation was evaluated. ASTM E-976 addresses the issue of removing and remounting of acoustic sensors; the reference standard proposes that an amplitude range of less than  $3 \text{ dB}_{\text{AE}}$  is deemed as acceptable. A review of the influence of the properties of the adhesive layer on the response of the AE sensor is provided in Section 2.3.1.2. It was proposed here that the viscosity of the couplant (Dugmore et al., 2002) and layer thickness (Qing et al., 2005) were factors that were understood to influence the consistency of the response of the sensor. In addition, owing to the open-top design of the fused-tapered coupler sensor, no weighting blocks were used to reinforce the mounted sensor.

A fibre-optic sensor (SM04-013) was surface-mounted to an aluminium plate using ultrasonic gel; the details of the test setup are provided in Section 3.4.4. The directional sensitivity of the sensor was characterised using pencil lead breaks. The sensor was then removed from the plate, cleaned of any residual adherent and was remounted. The directional sensitivity of the sensor was then re-characterised; this procedure was repeated five times. The mean amplitude of ten pencil lead breaks at each  $45^\circ$  increment around the sensor was used for

comparison. Figure 72 presents a summary of the mean signal amplitudes for the five re-mounting tests. With reference to the minimum and maximum values recorded as a function of the five times that the sensor was re-mounted, the highest recorded variation at a single source orientation was 3.4 dB<sub>AE</sub>; this occurred along the 90° axis. Whilst the recorded value along the 90° axis was outside of the proposed 3dB<sub>AE</sub> limit (ASTM, 2005), this result was found to be an isolated occurrence and was attributed to non-uniform coupling of the sensor. For all other orientations, the typical mean variation in the amplitude of the signal was in the range of 1.2 and 3 dB<sub>AE</sub>.

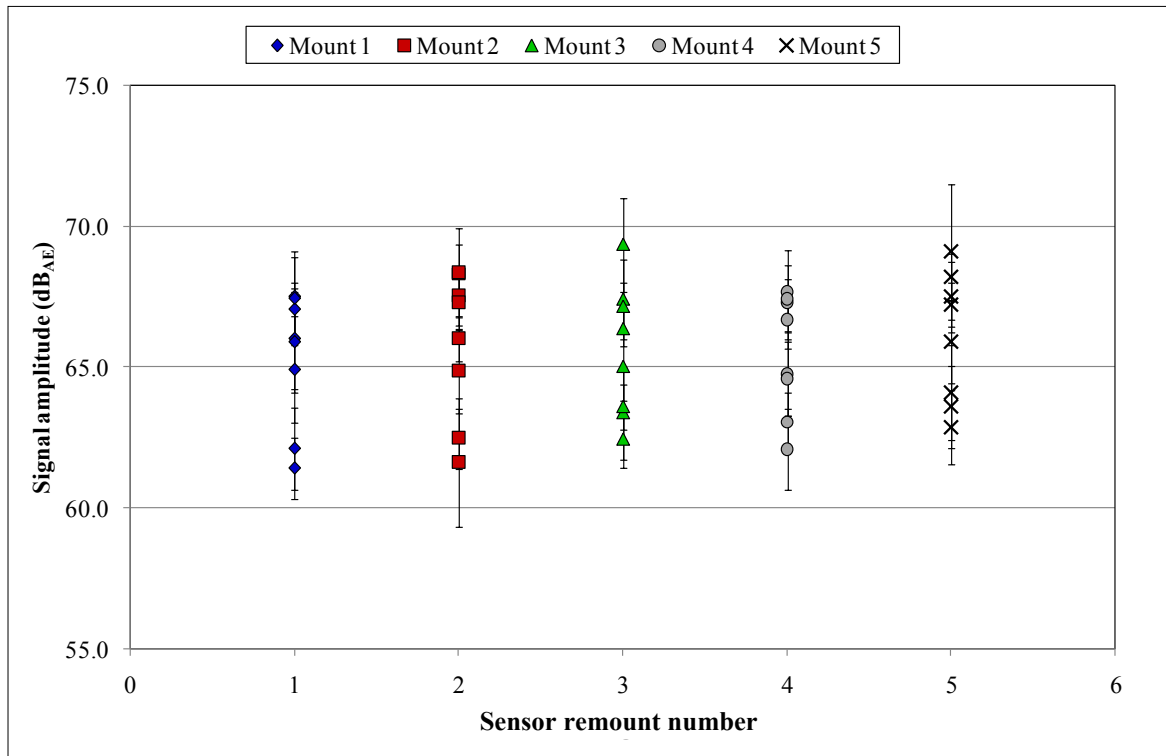


**Figure 72 A scatter plot illustrating the variation in the mean signal amplitude range for repeated removal and remounting trials; the error bars represent the deviation from the mean for each source orientation.**

The results from this trial indicate that a relatively consistent response was obtained from removing and remounting the fibre-optic AE sensor. Dugmore et al. (2002) proposed that for sensors that were mounted using a couplant with a low viscosity, a lower deviation in the signal response could be achieved from remounting. The results from this trial are in close agreement with their findings; the ultrasonic gel was deemed to have the lowest viscosity owing to the nature of the aqueous-based couplant. In addition, the authors proposed that a couplant with a high viscosity provided better coupling of the acoustic energy associated with in-plane particle displacement. As a result of the proposed influence of the properties of mounting adherent on the performance of the sensor, a study was undertaken to evaluate the response of the fibre-optic AE sensor using different coupling media.

The directional sensitivities were compared for sensors mounted using three different coupling media. Four coupling conditions were evaluated; details of the different coupling media conditions and the test setup are presented in Section 3.4.4. The directional sensitivity of a typical fibre-optic AE sensor (SM04-010) as a function of coupling media is presented in Table 21. A pencil lead break error of less than  $\pm 2.2$  dB<sub>AE</sub> was reported from these trials. Therefore any variations in the response of the sensor were attributed to the effect of the coupling media that was used to mount the sensor.

**Table 21 A summary of the mean signal amplitude values recorded using sensor SM04-010 as a function of orientation for the four coupling conditions; standard deviation in parentheses.**

Orientation	Amplitude (dB <sub>AE</sub> )			
	Ultrasonic gel	Silicone rubber	Cured silicone rubber	Cyanoacrylate
<b>0°</b>	65.9 (1.1)	67.8 (1.4)	68.6 (1.4)	70.8 (1.9)
<b>45°</b>	66.6 (1.4)	67.6 (1.6)	68.9 (1.3)	73.1 (0.8)
<b>90°</b>	64.5 (1.3)	63.5 (1.7)	66.8 (1.2)	71.9 (1.4)
<b>135°</b>	66.0 (1.5)	64.7 (1.2)	66.8 (1.2)	70.9 (1.0)
<b>180°</b>	64.3 (0.9)	67.3 (1.2)	66.9 (2.2)	69.4 (1.5)
<b>225°</b>	64.3 (1.3)	64.4 (0.9)	65.5 (1.6)	66.6 (0.9)
<b>270°</b>	63.6 (1.3)	64.0 (0.9)	63.9 (0.7)	70.8 (1.2)
<b>315°</b>	65.6 (1.7)	68.1 (0.7)	68.0 (1.1)	72.8 (1.3)

Figure 73 illustrates the directional sensitivity of the fibre-optic AE sensor as a function of the four coupling conditions that were evaluated. With reference to both Table 21 and the radar plot in Figure 73, it can be observed that the amplitude of the signal increases as a function of stiffness of the couplant used to bond the sensor, e.g. the stiffness of cyanoacrylate is higher than that of ultrasonic gel, therefore resulting in a higher sensitivity to the pencil lead breaks.

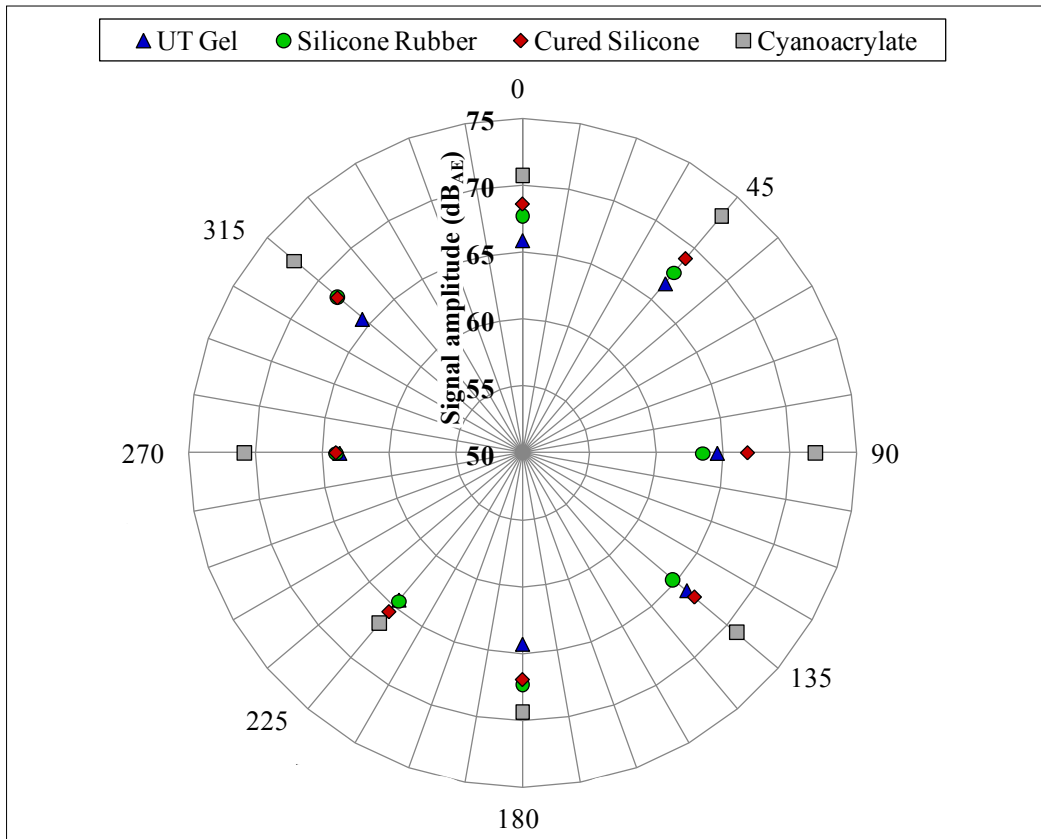


**Figure 73** A radar plot illustrating the mean signal amplitudes as a function of orientation for the four signal couplants.

On inspection of Figure 73, a typical increase in amplitude of  $\sim 6$  dB<sub>AE</sub> was observed from a sensor that was mounted using the cyanoacrylate adhesive compared with the ultrasonic gel. With reference to the two silicone rubber trials, i.e. cured and uncured states, an increase in the signal amplitude was also noted relative to the amplitude of the signal obtained using the ultrasonic gel couplant. The differences in the acoustic impedance of the various coupling media and the sensor package also accounted for the variation in the recorded signal amplitudes. Acoustic impedance is a product of the density and the acoustic velocity of a material. Therefore, since the stiffness of the cyanoacrylate is higher than the other couplants, the velocity of the acoustic wave is higher; as a result, the mis-match in the impedance

between the coupling media and sensor package is significantly lower. For a lower impedance mis-match, scattering and absorption of the energy of the propagating stress wave at the couplant layer will be reduced (Theobald et al., 2008); therefore larger amplitude signals would be anticipated. Theobald (2011) proposed that a rigid-bonded adhesive provided optimal properties for transmission of both shear and longitudinal particle displacements. Typical waveforms recorded by the sensors using the ultrasonic gel and cyanoacrylate adherents are presented in Figure 74. The purpose of this comparison was to evaluate if additional modes could be identified in the recorded waveforms. With reference to Figure 74, no additional modes were identified from using the stiffer adherent. This result confirms that the sensitivity of the fibre-optic sensor to the  $S_0$  mode in the aluminium plate was low and as a result, the sensor signal was triggered from the higher-amplitude  $A_0$  mode. A difference in the amplitude of the waveform using the stiffer coupling media was observed; the waveform profile was more defined with a larger voltage. Interference of the recorded signal was observed in both waveforms beyond 70 microseconds; this results in a significant distortion of the signal. This distortion may result from the arrival of the  $S_0$  reflection signal. As a consequence, destructive and/or constructive interference may have occurred.

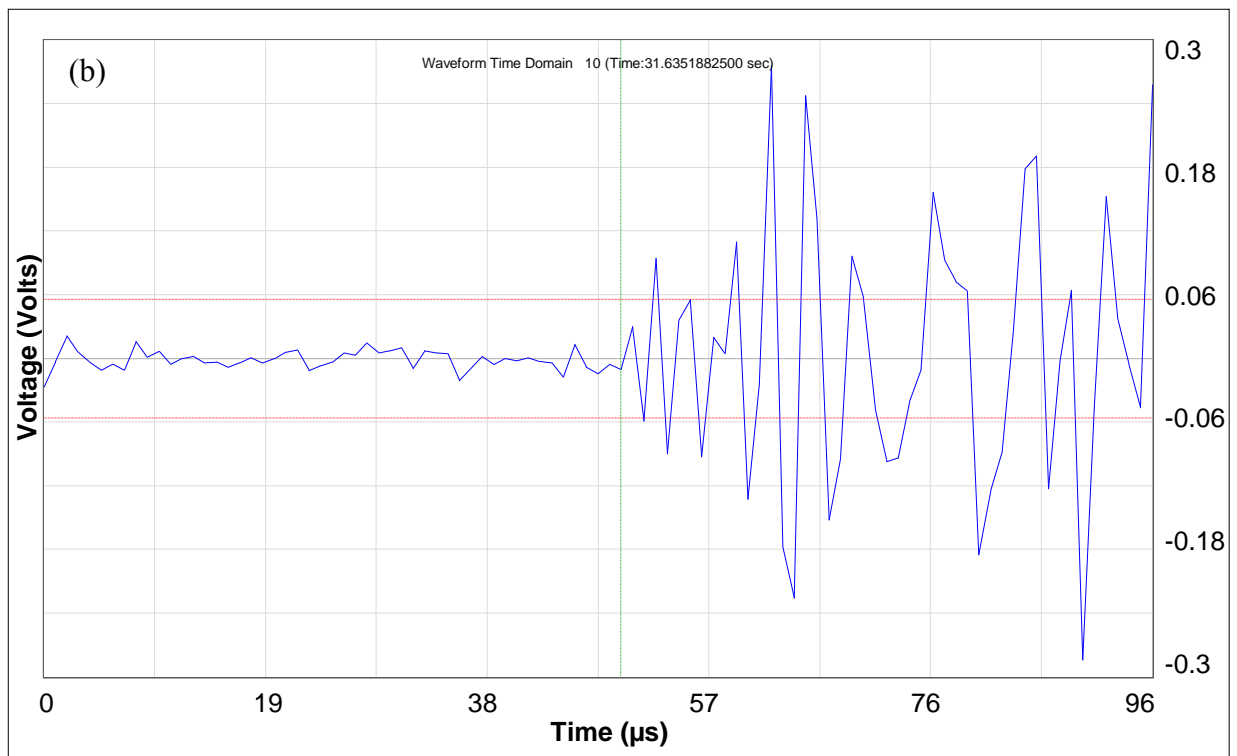
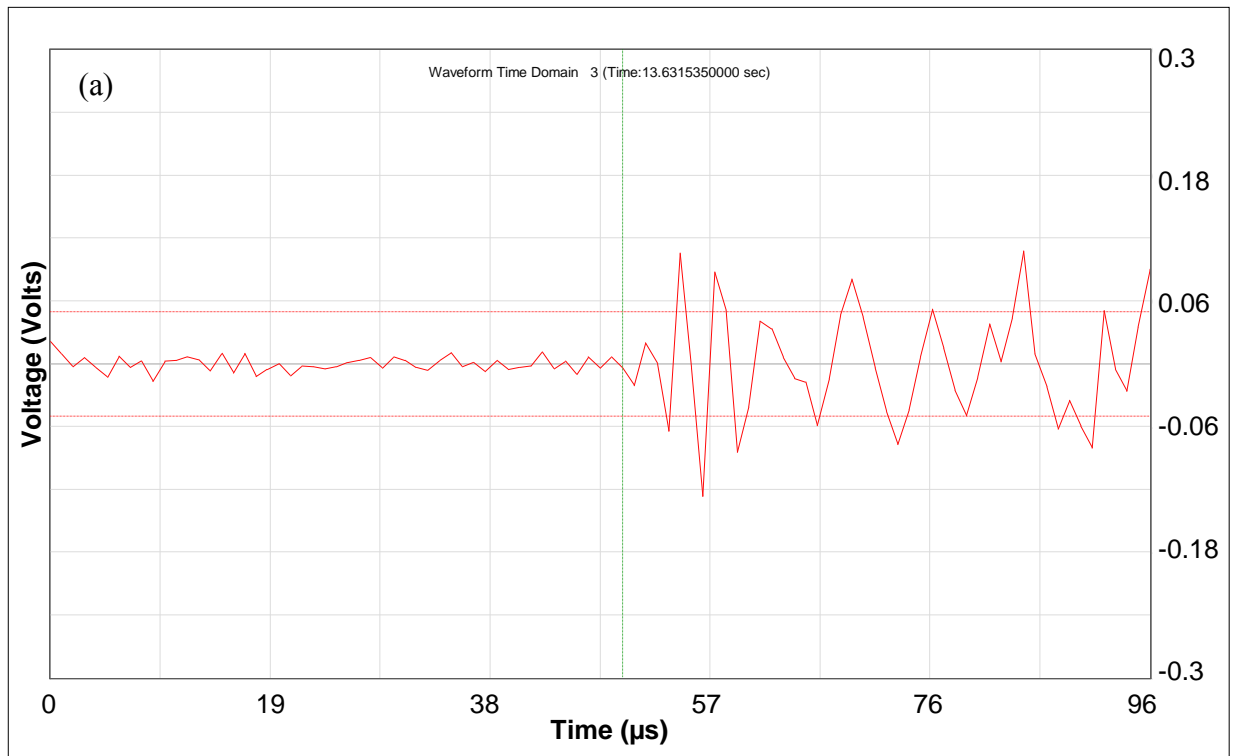


**Figure 74 An example of a typical waveform recorded by the fibre-optic AE sensor (SM04-010) in response to a pencil lead break for: (a) a sensor mounted to an aluminium plate using ultrasonic gel; and (b) a sensor mounted to an aluminium plate using a cyanoacrylate adhesive.**

The mean ASL was obtained from the pre-trigger regions of the waveforms for each coupling media; the corresponding values are presented in Table 22. From analysis of the values obtained, little or no variation in the signal-to-noise ratios was observed for the ultrasonic gel or silicone rubber couplants. With reference to the cyanoacrylate adhesive, an increase in the signal-to-noise ratio of 5.6 dB<sub>AE</sub> was observed. This result was expected due to the increased rigidity of the coupling layer (Theobald, 2011), and as a result, the transmission of the stress wave to the sensor was increased. In addition, the low viscosity of the cyanoacrylate resulted in a good wet-out of the bonding surface; as a result, the thickness of the bonding layer and presence of air-bubbles was minimised (Theobald et al., 2008). For the other couplants evaluated, it was assumed that the bond layer would be thicker due to their lower wetting ability. In addition, the surface tension of the ultrasonic gel and silicone rubber were expected to be higher than that of the cyanoacrylate and therefore entrapment of air bubbles was more likely. A review of the influence of the bond layer thickness on stress transfer is presented in Section 2.3.1.2. It was proposed that the removal and remounting process for application of different adherents did not influence the performance of the sensors; the recorded ASL was found to be within a similar range for all of the conditions investigated.

**Table 22 A summary of the mean ASL, maximum signal amplitude and corresponding signal-to-noise ratios for the four coupling conditions; the sensors were packaged using the square U-channel substrates.**

<b>Coupling Media</b>	<b>ASL (dB<sub>AE</sub>)</b>	<b>Maximum recorded amplitude (dB<sub>AE</sub>)</b>	<b>Signal-to-noise ratio (dB<sub>AE</sub>)</b>
Ultrasonic gel	37.8	66.6	28.8
Silicone rubber	40.7	68.1	27.4
Cured silicone rubber	41.3	68.9	27.6
Cyanoacrylate	38.7	73.1	34.4

In summary, the cyanoacrylate adhesive provided the greatest sensitivity to simulated AE signals; the ultrasonic gel couplant was however preferred due to the ease of removal during sensor evaluation trials. Theobald (2011) and Colombo et al. (2005) suggested that a rigid coupling media should only be used in the event that the sensor was to remain in a fixed location; removal of a rigidly bonded sensor can increase the risk of damage to the packaging. In the current study, whilst acetone could have been used to soften the outer edge of the adhesive bond, there was a risk of fracturing the glass packaging when applying force to remove the sensor from the surface of the material. Furthermore, the removal of cured cyanoacrylate from the under-surface of the package posed additional difficulties. As a consequence, for trials where the removal of the sensor was not required, i.e. mechanical tests, the fibre-optic sensor was bonded using the cyanoacrylate adhesive (see Chapter seven).

With reference to the results presented in Chapter's four, five and six, it has been shown that the response of the fibre-optic sensor is influenced by several factors, namely: (i) the geometry of the tapered region; (ii) the type of optical fibre used to fabrication the sensor; and (iii) the type of coupling media used to bond the sensor to the test specimen. In addition, it is proposed that the dimensions of the packaging also contribute to the response of the sensor. As a result, five sensors were fabricated using the SM04-1 optical fibre and were housed within the circular U-channel packaging substrate. The directional sensitivities of five circular U-channel packaged fibre-optic sensors were characterised using pencil lead breaks. The experimental procedure used to characterise the sensors is further defined in Section 3.4.5. A summary of the response from each sensor is presented in Table 23.

For reference, the circular U-channel packaged sensors were assigned the coding of CP04-xxx, where xxx refers to the database number. All sensors demonstrated a low directional sensitivity. However, on inspection of Table 23, a large scatter in the sensitivities of the five sensors was observed. The amplitudes of the recorded signals for CP04-003 were lower than the signal amplitudes recorded by the other four sensors that were evaluated. A variation in sensitivity of more than 10 dB<sub>AE</sub> was observed; the magnitude of this variation was similar to that of the square U-channel packaged sensors. The minimum and maximum values are highlighted in blue in Table 23. Removal of CP04-003 from the data set resulted in a higher mean signal amplitude with less scatter.

**Table 23 A summary of the signal amplitudes recorded for the five circular packaged fibre-optic AE sensor during the directional sensitivity trials; standard deviations is shown in parentheses.**

Orientation	Amplitude (dB <sub>AE</sub> )					Mean
	CP04-001	CP04-002	CP04-003	CP04-004	CP04-005	
<b>0°</b>	67.5 (1.2)	70.1 (1.4)	65.2 (1.5)	68.1 (1.3)	70.4 (1.4)	<b>68.3 (2.1)</b>
<b>45°</b>	65.0 (0.8)	70.1 (1.4)	61.8 (2.3)	65.6 (2.2)	72.9 (1.3)	<b>67.1 (4.4)</b>
<b>90°</b>	64.4 (1.2)	70.7 (2.4)	60.9 (1.1)	66.9 (2.8)	71.8 (0.9)	<b>66.9 (4.5)</b>
<b>135°</b>	63.2 (0.8)	67.2 (1.8)	61.6 (1.3)	65.7 (1.2)	71.0 (0.5)	<b>65.7 (3.7)</b>
<b>180°</b>	67.0 (2.0)	68.0 (1.3)	62.2 (1.1)	65.2 (2.0)	71.2 (1.1)	<b>66.7 (3.3)</b>
<b>225°</b>	63.0 (1.5)	66.8 (1.0)	61.8 (1.8)	65.5 (1.4)	69.0 (1.7)	<b>65.2 (2.9)</b>
<b>270°</b>	63.8 (2.3)	67.0 (1.2)	61.9 (2.5)	70.1 (2.7)	72.0 (1.3)	<b>67.0 (4.2)</b>
<b>315°</b>	67.5 (1.2)	68.1 (2.2)	61.5 (1.1)	67.0 (1.7)	72.8 (2.0)	<b>67.4 (4.0)</b>

A radar plot highlighting the scatter in the data for the circular packaged sensors is presented in Figure 75. The mean amplitude represents the average of the five sensors that were evaluated. The comparison of the sensitivities of the square and circular U-channel packaged sensors is shown in Figure 75. For an accurate comparison, the data for the square U-channel

packaged sensors was obtained from tests using the cured silicone rubber couplant. On inspection of Figure 75, a low directional sensitivity for all sensors was confirmed. The mean amplitude of the circular U-channel packaged sensors was marginally higher.

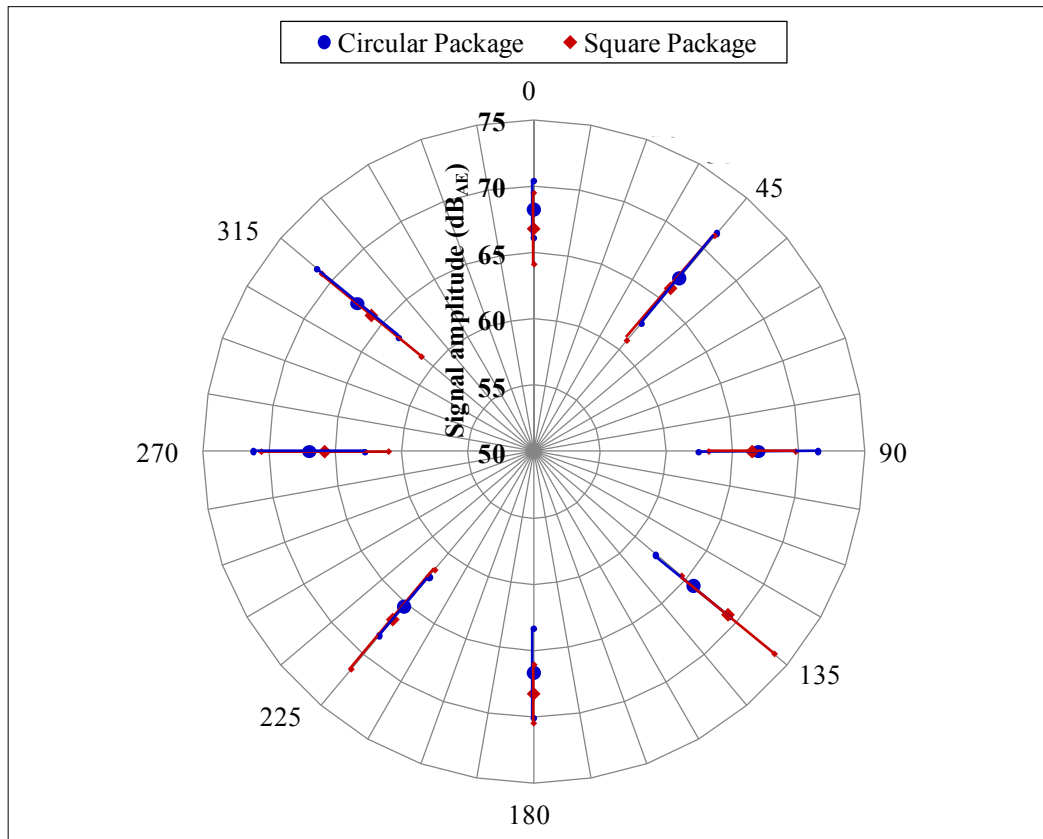


**Figure 75 A radar plot highlighting the scatter in the data sets for SM04-1-type fibre-optic AE sensors, packaged using the circular and square U-channel substrates; the error bars represent the deviation from the mean for the two sensor groups.**

The variation in the sensor-to-sensor sensitivities was attributed to difficulties with surface-mounting the small diameter packaging on the aluminium plate. Owing to the small size and weight of the packaging substrate, there was a tendency for the sensor to become detached if a

low viscosity gel-based adherent was used. As a consequence, silicone rubber was used to mount the sensor to the test specimen. Silicone rubber has a higher viscosity and surface tension and was therefore understood to be more suitable for holding the fibre-optic sensor in position. A limitation with this couplant was however the risk of trapped air bubbles (Theobald et al., 2008; Higo and Inaba, 1991), un-even coverage between the package and the specimen, and variations in the bond layer thickness (Hill and El-Dardiry, 1981). As a result, a more suitable adherent such as cyanoacrylate would have been preferred; this adherent was not used owing to the risk of damaging the sensor during the removal from the test specimen. An evaluation of the effects of couplant on the performance of the circular U-channel packaged sensor should therefore be considered as a topic for further work. A summary of the performance characteristics of the circular U-channel packaged sensor is presented in Table 24.

**Table 24 A summary of the ASL, maximum amplitude and corresponding signal-to-noise ratios for the circular and square U-channel packaged fibre-optic AE sensors; the sensors were fabricated using SM04-1 optical fibre.**

Sensor no.	Excess-loss (dB)	Pretrigger ASL (dB <sub>AE</sub> )	Maximum recorded amplitude (dB <sub>AE</sub> )	Signal-to-noise ratio (dB <sub>AE</sub> )
CP04-001	1.13	35.0	67.5	32.5
CP04-002	1.03	31.7	70.7	39.0
CP04-003	0.96	32.4	65.2	32.8
CP04-004	1.36	40.8	70.1	29.3
CP04-005	1.64	38.7	72.9	34.2
<b>Mean</b>	<b>1.22 (0.3)</b>	<b>35.7 (3.9)</b>	<b>69.3 (3.0)</b>	<b>33.6 (3.5)</b>
SM04-008	1.13	36.7	65.7	29.0
SM04-009	1.28	34.1	69.6	35.5
SM04-010	1.01	37.8	66.6	28.8
SM04-011	0.60	36.4	66.6	30.2
SM04-012	0.81	33.8	71.6	37.8
<b>Mean</b>	<b>0.96 (0.3)</b>	<b>35.8 (1.7)</b>	<b>68.0 (2.5)</b>	<b>32.3 (4.1)</b>

With reference to the mean signal amplitude, the circular U-channel packaged sensor demonstrated marginally higher sensitivity to the pencil lead breaks compared with the square U-channel packaged sensors. This may be attributed to a reduction in the damping of the signal at the region where the sensor was bonded to the U-channel; the polymeric coating was removed from the fibre at this region. The proposed influence of this alternative packaging design on the transmission of the stress-wave to the sensor was presented in Section 5.1.1. A small reduction in the ASL was observed using the circular packaging substrate; a high ASL was recorded for a single sensor which increased in the mean reported value. An increase in the mean signal-to-noise level of 1.3 dB<sub>AE</sub> was obtained from the circular U-channel packaged sensor design.

### 6.3.3 Directional Sensitivity Response of the Fibre-Optic Sensor using Composite Materials

The fibre-optic sensor was surface-mounted to an 8-ply cross-ply carbon-fibre composite. The VTM-264 composite specimen had a lay-up sequence of 0/90<sub>2</sub>/0<sub>s</sub>. The directional sensitivity of the fibre-optic AE sensor was characterised using pencil lead breaks. Further details of the test procedure are provided in Section 3.4.6. As a result of the anisotropic properties of the composite specimen, the wave propagation properties within the material were not comparable with the aluminium plate. As such, a group velocity dispersion curve was calculated using a specialist software program (Disperse; Imperial College, London); the group dispersion curve was calculated from the laminate properties provided by the material technical data sheet supplied by the manufacturer. The laminate properties that were used to define the dispersion curve are shown in Table 25.

**Table 25 A summary of the material properties used to define the group velocity dispersion curve.**

Property	Value
Layup Sequence	0,90 <sub>2</sub> ,0 <sub>s</sub>
Young's Modulus (E)	122 GPa
Shear Modulus (G)	3.94 GPa
Poisson's ratio ( $\nu_{13}$ ):	0.32
Poisson's ratio ( $\nu_{23}$ ):	0.33
Density	1.54 g/cc
Thickness (laminate)	2.4 mm

The calculated group velocity dispersion curve for the 0,90<sub>2</sub>,0<sub>s</sub> composite specimen is presented in Figure 76.

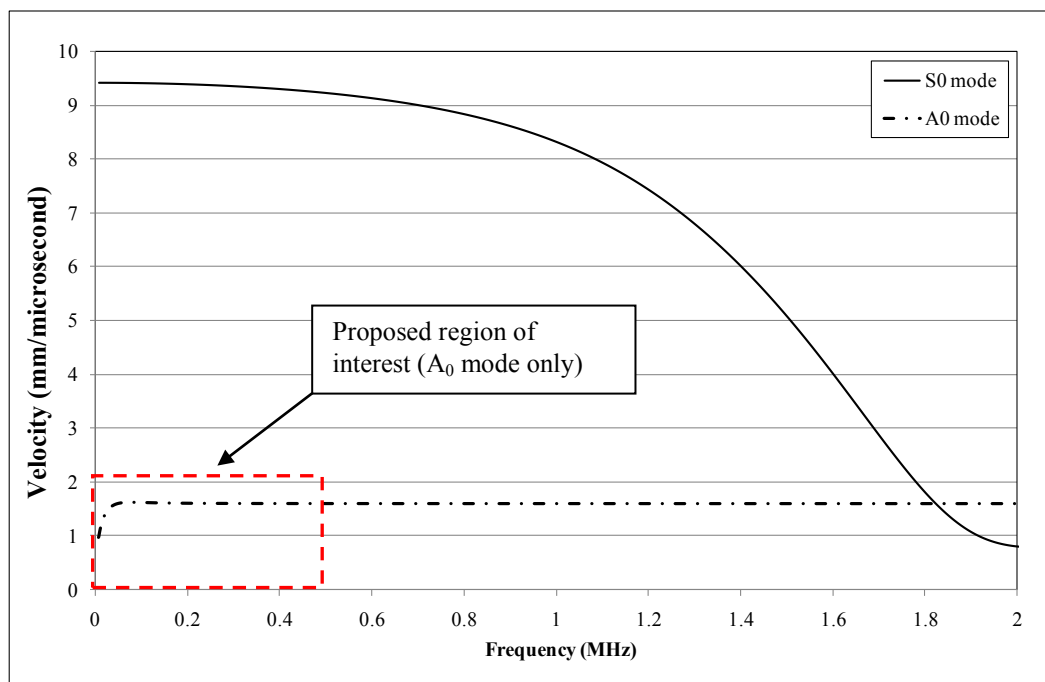


**Figure 76 Group-velocity dispersion curve for the VTM-264 composite specimen; the test specimen had a layup sequence of 0,90<sub>2</sub>,0<sub>s</sub>.**

The wave velocities for the  $A_0$  mode, obtained from the group-velocity dispersion curve shown in Figure 76, were compared with values published in the literature for similar lay-up orientations. Percival and Birt (1997) reported wave velocities of between 1500 and 1600  $\text{ms}^{-1}$  from their experimental trials. Aljets et al. (2010) indicated wave velocities for the  $A_0$  mode to be in the region of 1680  $\text{ms}^{-1}$ . The authors proposed that the flexural mode had a constant velocity around the full 360° circumference, regardless of the fibre orientation. Prosser and Gorman (1992) did however show small variations in wave velocity with orientation, i.e. less than 50  $\text{ms}^{-1}$  at 100 kHz, in the wave speeds for the 0°, 45° and 90° orientations. No reason was given for this observed variation. Wave velocities between 1000 and 1200  $\text{ms}^{-1}$  were reported; these values were limited to signal frequencies between 80 and 160 kHz. The velocities of the  $A_0$  mode proposed in the literature show good agreement with the values presented in the current research. A review of wave propagation theory in cross-ply oriented composite materials is presented in Section 2.3.2.

In order to evaluate the directional sensitivity of the sensor, the wave velocity of the cross-ply composite was measured. The wave velocity was obtained experimentally using the differential time-of-arrival (TOA) of the signal detected at two surface-mounted sensors; the two sensors (SM04-014 and SM04-015) were spaced at a distance of 80 mm. In order to obtain accurate arrival times of the signal at the two sensors, manual correction of the threshold crossing was performed for each channel using the AEwin™ software. The calculated wave velocities are shown in Table 26.

**Table 26 A summary of the time of arrival calculations using two surface-mounted fibre-optic sensors on a cross-ply composite plate; the measurements were obtained along the 90° axis relative to the longitudinal orientation of the sensor.**

Signal No.	Delta TOA (seconds)	Distance (metres)	Velocity (ms <sup>-1</sup> )
<b>1</b>	4.8E-05	0.08	1670
<b>2</b>	5E-05	0.08	1600
<b>3</b>	4.77E-05	0.08	1680
<b>Mean</b>	-	-	<b>1650</b>
<b>SD</b>	-	-	<b>43.6</b>

With reference to Table 26, the mean wave velocity of 1650 ms<sup>-1</sup> shows good agreement with the calculated value of 1620 ms<sup>-1</sup> from the dispersion curve. The calculated value corresponds to a signal frequency of 100 kHz. Based on the results from published literature (see Section 2.3.2), it was assumed in the current research that the wave speed as a function of orientation was nominally similar. Signal boundary reflections that resulted in interference effects in the discrete waveform were minimised using the time-gating procedure reported in Section 6.1. The required segment of the discrete waveform was calculated using the mean wave velocity of the A<sub>0</sub> mode and the known distance over which the first boundary reflection was expected to travel (see Figure 55). The time-gated region of interest of the waveform was calculated; the maximum signal amplitude recorded within the initial 61 microseconds from threshold crossing was used for assessment of the directional sensitivity of the sensor. A typical example of a discrete waveform recorded by the fibre-optic sensor in response to a pencil lead break is provided in Figure 77. The signal frequency corresponding to this waveform is also shown. It is noted that the dominant frequency corresponding to the highlighted region in the waveform was between 50 and 100 kHz.

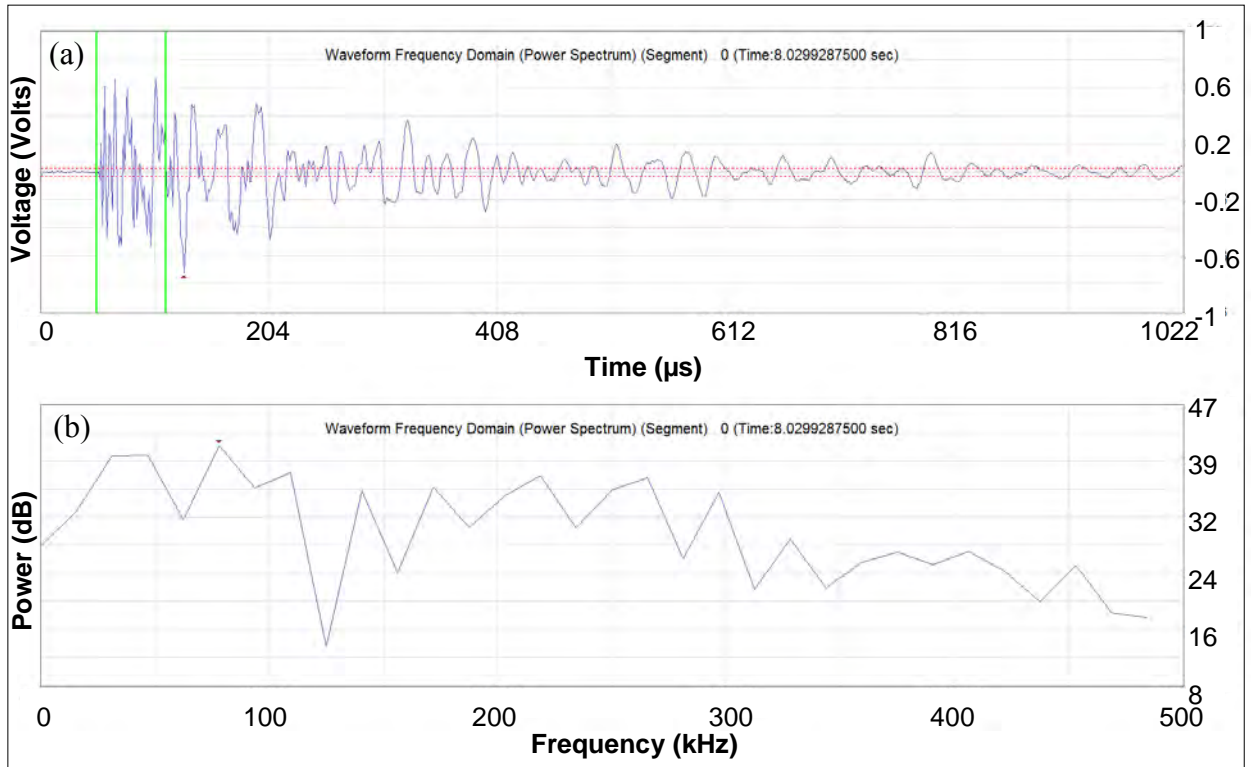


**Figure 77 (a) A typical discrete waveform; and (b) the corresponding FFT recorded by the fibre-optic sensor in response to a pencil lead break on the cross-ply composite specimen.**

With reference to the reported frequency response of the signal in Figure 77, and the measured wave velocity in the composite material (see Table 26), it was proposed that the sensor exhibited sensitivity to the  $A_0$  mode only. The ring-down of the waveform was faster than was observed in the tests using the aluminium plate (see Figure 58). This was due to the higher attenuation in composite materials compared with aluminium. As a result, fewer boundary reflections were generated. The high attenuation in composite materials results from the low mis-match in acoustic impedance between air and the material. In contrast, aluminium has a large mismatch in acoustic impedance with air and its structure is continuous, therefore does not experience any signal scattering (Scholey et al., 2006).

The performance of the fibre-optic AE sensor was compared with the response of a surface-mounted WD piezoelectric transducer. Sensitivity to both the  $S_0$  and  $A_0$  modes was observed from analysis of the discrete waveforms recorded by the piezoelectric transducer. A typical waveform is presented in Figure 78.

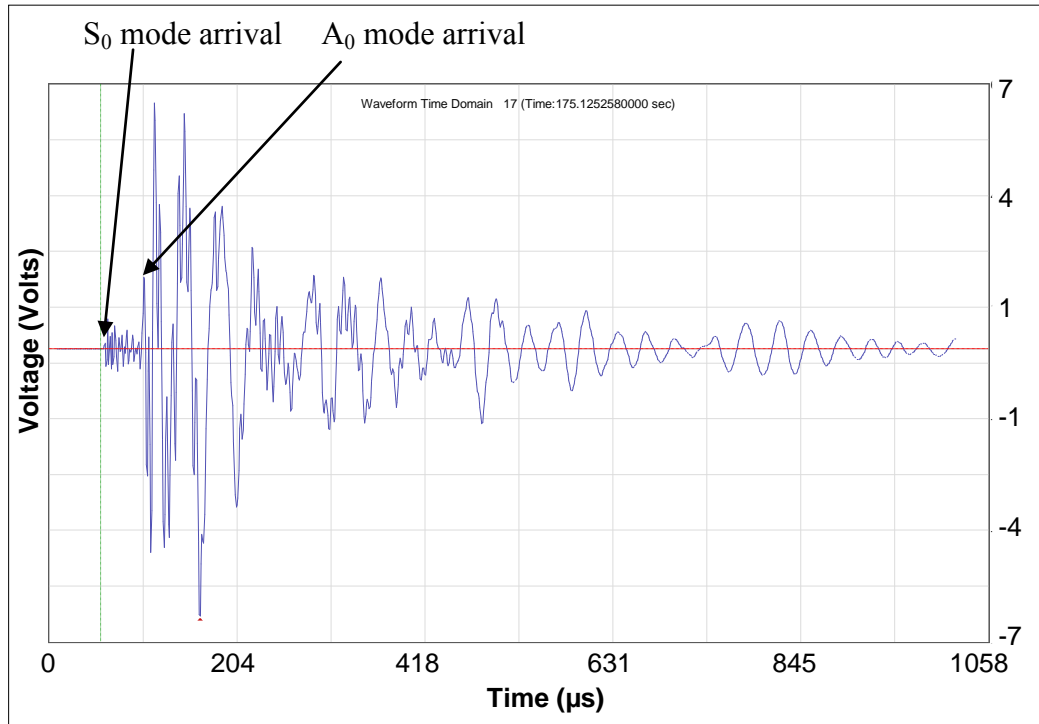


**Figure 78 A typical discrete waveform recorded by the WD piezoelectric transducer in response to a pencil lead break performed on a  $0/90^\circ$  oriented composite plate.**

As a result of the sensitivity to two wave-modes, the initial 61 microseconds after the arrival of the  $A_0$  mode was used to obtain the maximum signal amplitude. This provided a more representative comparison with the fibre-optic sensor. The signal amplitudes recorded by the piezoelectric transducer were notably higher than the fibre-optic device; this was anticipated due to the higher sensitivity of the device. A comparison of the signal amplitude as a function of the orientation of the pencil lead breaks for the two sensors is presented in Figure 79.

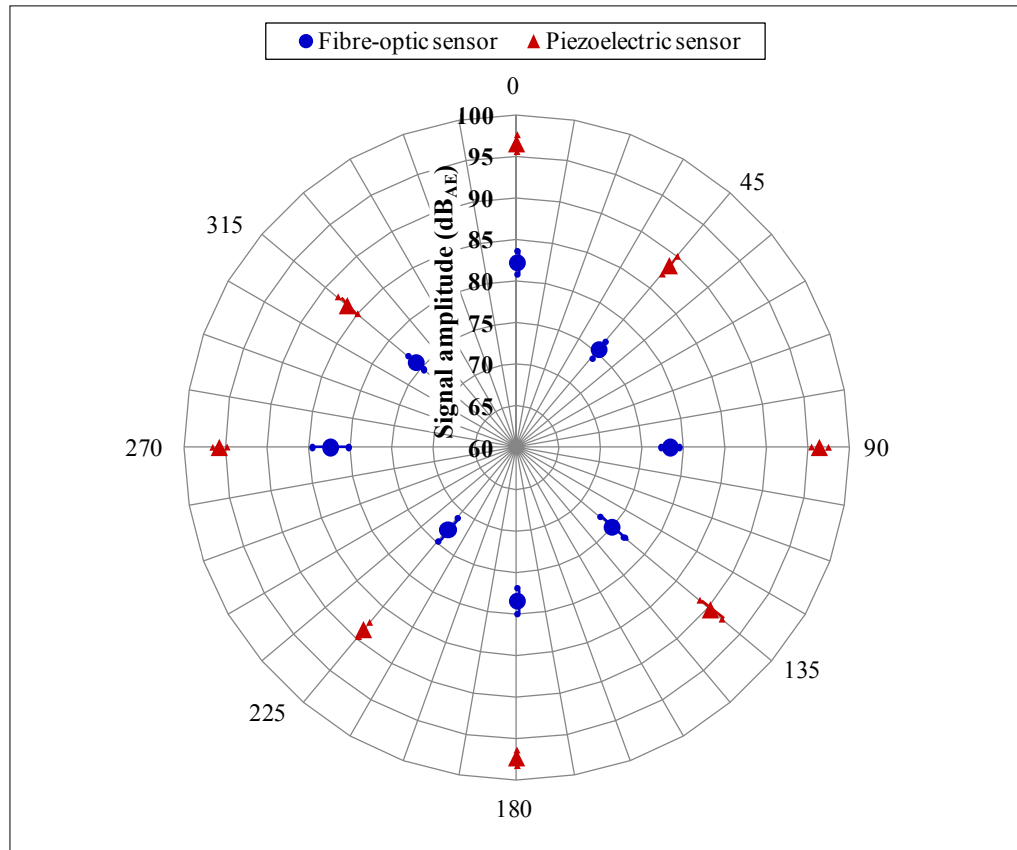


**Figure 79** A radar plot illustrating the mean signal amplitudes as a function of source orientation on the composite specimen for the fibre-optic and piezoelectric transducer; the error bars represent the deviation from the mean relating to lead break error.

With reference to the radar plot, both sensors demonstrated a variation in the recorded signal amplitude as a function of orientation; signals with higher amplitudes were recorded along the 0° and 90° orientations corresponding with the directions of the fibre reinforcement. Along the 45° orientations, the signal amplitude was ~5 dB<sub>AE</sub> lower. Since this phenomenon was not observed in tests using the aluminium plate, it was inferred that this effect was a function of the material. Percival and Birt (1997) proposed that the attenuation of the propagating wave varied between two to three dB<sub>AE</sub> per cm for the 0/90° and ±45° directions in 0/90° oriented composites. Scholey et al. (2006) proposed that a propagating signal was attenuated

at the fibre-matrix interface due to the visco-elastic properties of a composite. In the current work, the variation in the signal amplitude with orientation was attributed to differences in the attenuation coefficients along axes with and without reinforcing fibres. Since there was no fibre reinforcement along the 45° orientations, the signal was attenuated as the wave-front interacted with resin pockets between the overlapping fibres.

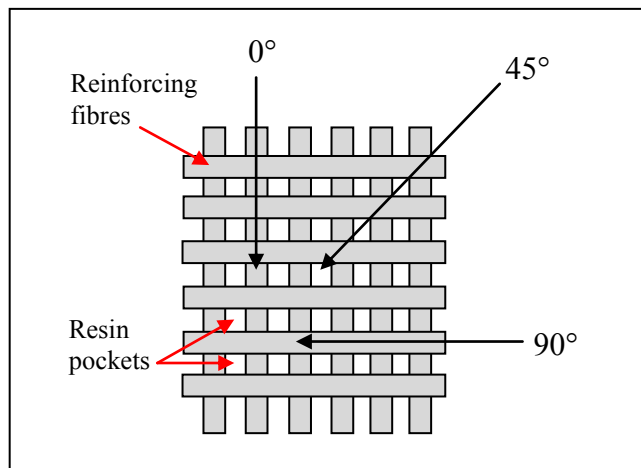


**Figure 80 A schematic illustration of the propagation paths for the wave travelling along 0°, 45° and 90° orientations.**

It is also noteworthy to highlight that the response of the fibre-optic sensor on the composite test-plate was significantly higher than the response of a typical sensor evaluated using an aluminium test-plate. For comparison, Figure 81 illustrates the response of the sensor from trials using both the aluminium and the composite test plates. This effect may be attributed to a lower acoustic impedance mismatch between the composite and ultrasonic gel compared with the aluminium plate and the adherent. Further research is however required to confirm the proposed assumption.

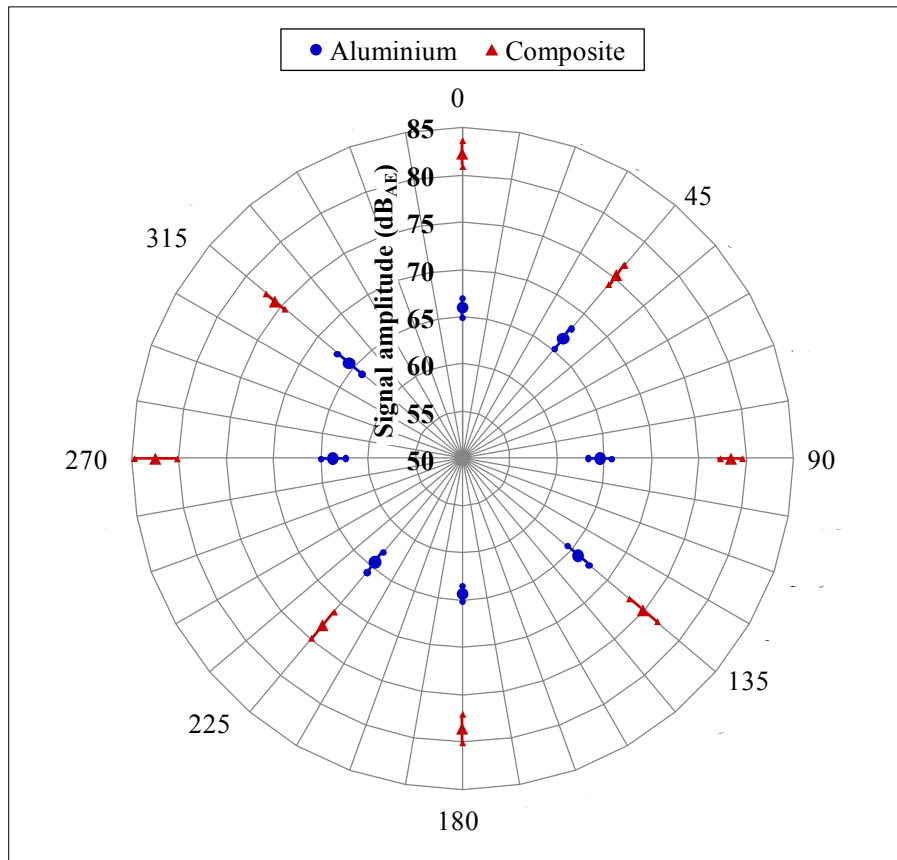


**Figure 81** A radar plot illustrating the mean signal amplitudes recorded by the fibre-optic AE sensor as a function of source orientation for both composite and aluminium test-plates; the error bars represent the deviation from the mean relating to lead break error.

#### 6.3.4 Sensitivity of an Embedded Fibre-Optic AE Sensor

A preliminary investigation was undertaken to evaluate the sensitivity of a fibre-optic AE sensor that was embedded in a composite material; the response of the sensor was evaluated using pencil lead breaks. With reference to experimental procedure in Section 3.4.7, pencil lead breaks were performed at three source-to-sensor distances; the distances were 25, 50 and 75 mm. Owing to the uni-directional layup of the composite, the sensitivity of the sensor was

evaluated along the  $0^\circ$  fibre orientation only. Due to the limited data recorded during this preliminary investigation, a comparison of sensor-to-sensor performance was not feasible; the purpose of this test was to determine if the sensor had sufficient sensitivity to detect a signal generated by the pencil lead break. With reference to Figure 82, the amplitude of the signal was seen to diminish as the source-to-receiver distance increased. Figure 82(c) corresponds to a lead break performed at a distance of 75 mm from the sensor, the peak voltage of the time-gated signal was 680 mV; conversion of this signal voltage to the  $\text{dB}_{\text{AE}}$  scale yields an amplitude of 76.6  $\text{dB}_{\text{AE}}$ . At a distance of 25 mm from the sensor, the amplitude of the recorded signal was 85.9  $\text{dB}_{\text{AE}}$ . The difference in the amplitude of the signal with increasing distance from the sensor was due to signal attenuation. Signal attenuation is governed by four mechanisms, namely: (i) wave-front spreading; (ii) internal friction within the material; (iii) dissipation of the wave into different media; and (iv) dispersion of the signal components (Holford, 2000). The dominant mechanism thought to result in the highest rate of attenuation is wave-front spreading, which occurs in close proximity to the source. For pencil lead breaks performed close to the sensors, the effect of near-field attenuation on the signal will be well pronounced. When considering wave propagation in plates as two-dimensional, the signal amplitude decreases inversely as the square-root of the propagation distance (Holford, 2000). As such, high attenuation occurs if the acoustic emission is close to the sensor. As the source-to-sensor distance increases, i.e. into the far-field, the dominant mode of attenuation is due to the dissipation of the wave energy. This results from either the conversion of sound energy into heat, wave interaction with material in-homogeneities or propagation of energy into surrounding media, e.g. fluid in a pressure vessel. Barbezat et al. (2004) reported that the intersection of the near-field and far-field occurred at a point in between 200 to 300 mm from the sensor. It is therefore proposed that the pencil lead breaks at 75 mm were within the near

field of the sensor and therefore the attenuation of the signal was likely to be high compared with the break at 25 mm; this result was observed. In comparison with the embedded sensor response, the amplitude of a signal recorded by a surface-mounted sensor in response to a signal generated at a distance of 75 mm was 74.9 dB<sub>AE</sub> (see Figure 83). In view of the preliminary result, it can be concluded that the sensitivity of the embedded sensor was of a sufficient level to detect the simulated AE. In addition, the embedded sensor was shown to be more sensitive to the lead break.

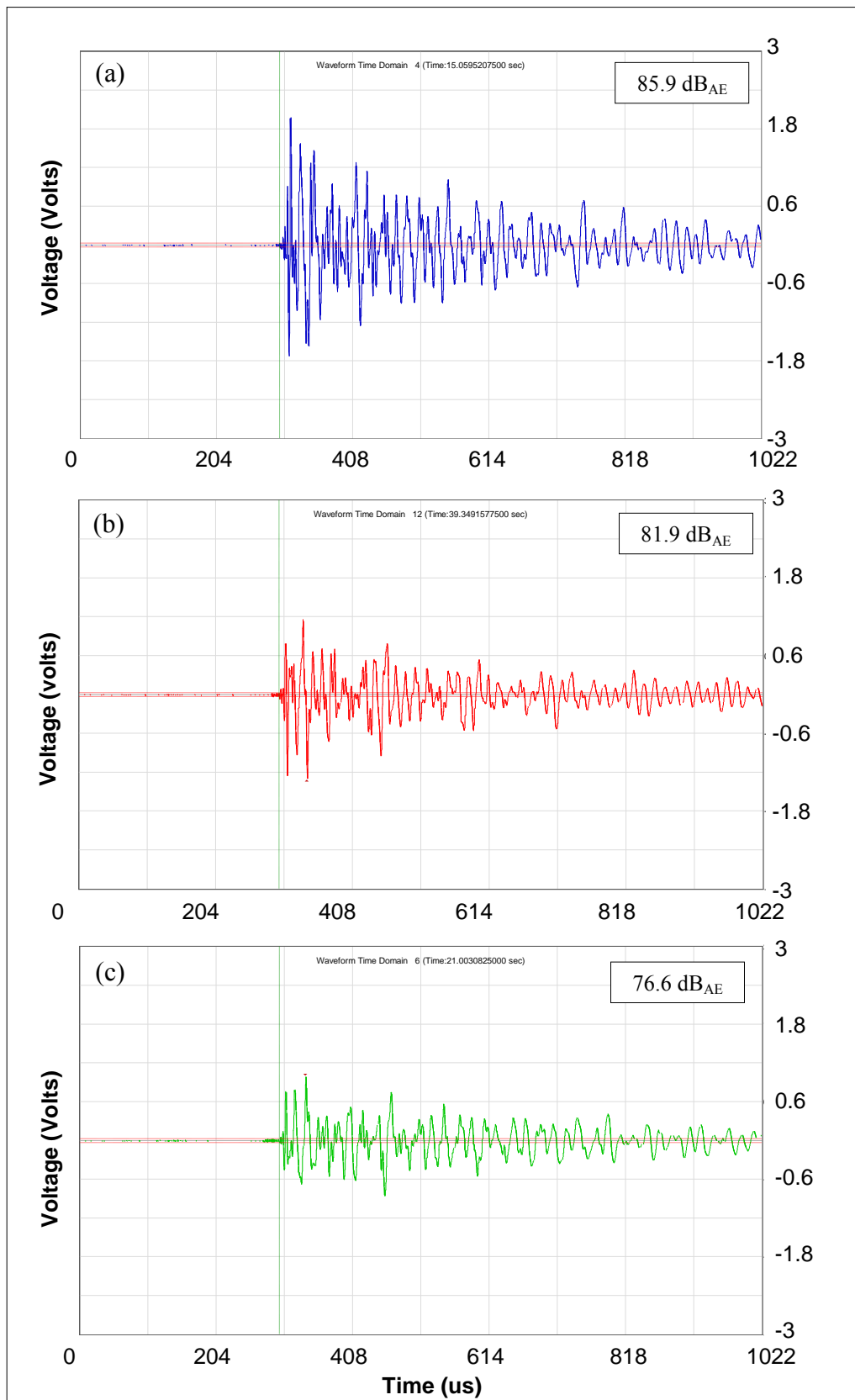


**Figure 82 Typical examples of discrete waveforms illustrating the response of the embedded fibre-optic sensor to pencil lead breaks at: (a) 25 mm; (b) 50 mm; (c) 75 mm from the centreline of the sensor.**

An increase in sensitivity of embedded sensors compared with surface-mounted sensors was also reported in Pierce et al. (1996). To the author's knowledge, this study demonstrates the first instance of successful embedment of the fused-tapered fibre optic coupler in a composite material that was fabricated using conventional autoclave processing.

Fu et al. (2009) reported on the embedment of the fused-tapered coupler in composite materials; in their research, the composite was however fabricated in a press-heater. Fabrication of high-performance composite materials in an autoclave necessitates the application of isostatic pressure to the part using a vacuum-bagging procedure, as well as exposure to high ambient pressure and temperature. As a result, autoclave fabrication yields a composite with low void content (Stringer, 1989; Ramulu et al., 2004) and greater consolidation due to superior compaction pressures (Abraham, 1998). As such, it was anticipated that the fibre-optic AE sensor would be subjected to higher stresses during autoclave fabrication compared with the hot-press technique reported in Fu et al. (2009). Embedment of the fused-tapered coupler was also proposed in Doyle et al. (2002b); however, in this study, the prepregs were cured at room temperature and therefore lower stresses would have been transferred to the sensor compared with autoclave processing.

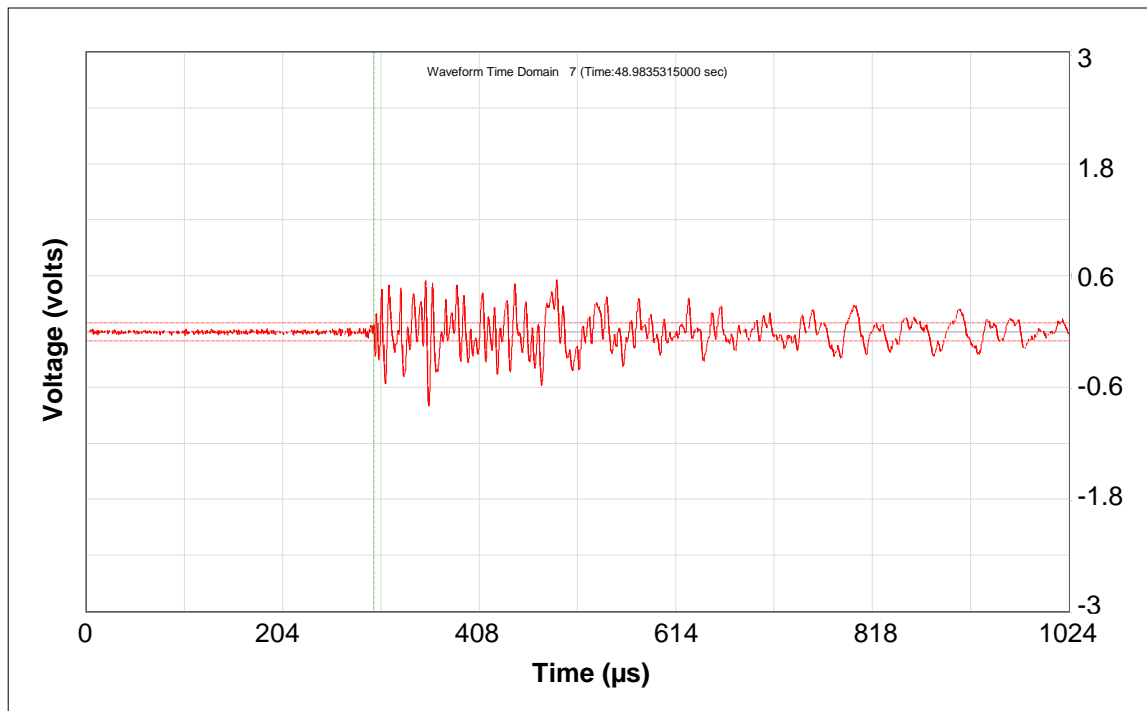


**Figure 83 A typical example of a discrete waveform highlighting the response of a surface-mounted fibre-optic AE sensor (SM04-1-type housed in a square U-channel package) to a pencil lead break at 75 mm from the centreline of the sensor.**

Whilst it has been shown that the embedment of fibre-optic sensors can result in strain concentrations around the optical fibre due to resin-rich areas (Lee et al., 1995), Guemes et al. (2001) reported no influence on the tensile properties of the material. Several authors have also studied the feasibility of embedding piezoelectric elements in composite materials (Hagood et al., 1988; Elpass et al., 1995; Mall and Hsu, 2000). A limitation with their approach was the need to cut holes and/or slits into the prepreg layers in order to accommodate the sensor element; this technique therefore induces significant voids within the material. In addition, for electrically conductive materials, e.g carbon fibre, additional consideration must be given to electrically insulating the element from the surrounding material (Hagood et al., 1988). The proposed advantages of embedded fibre-optic sensors

were illustrated by Pierce et al. (1996) in Section 2.4.2. Kalamkarov et al. (2000) proposed that effective strain transfer was achievable from embedded fibre-optic sensors. In addition, embedded sensors are protected from external environments, rough handling and are resistant to chemical attack (Kalambarov et al., 2000).

As a result of the increased sensitivity to the stress-wave perturbations demonstrated by the embedded sensor, identification of the  $S_0$  mode in waveforms corresponding to signals generated at a distance of 75 mm was possible. Prosser and Gorman (1999) indicated that the  $S_0$  extensional mode was generated from a pencil lead break, albeit with a small amplitude, since the predominant displacement of the material was out-of-plane. Upon inspection of Figure 84, the  $S_0$  mode was observed within the pre-trigger region of the waveform.

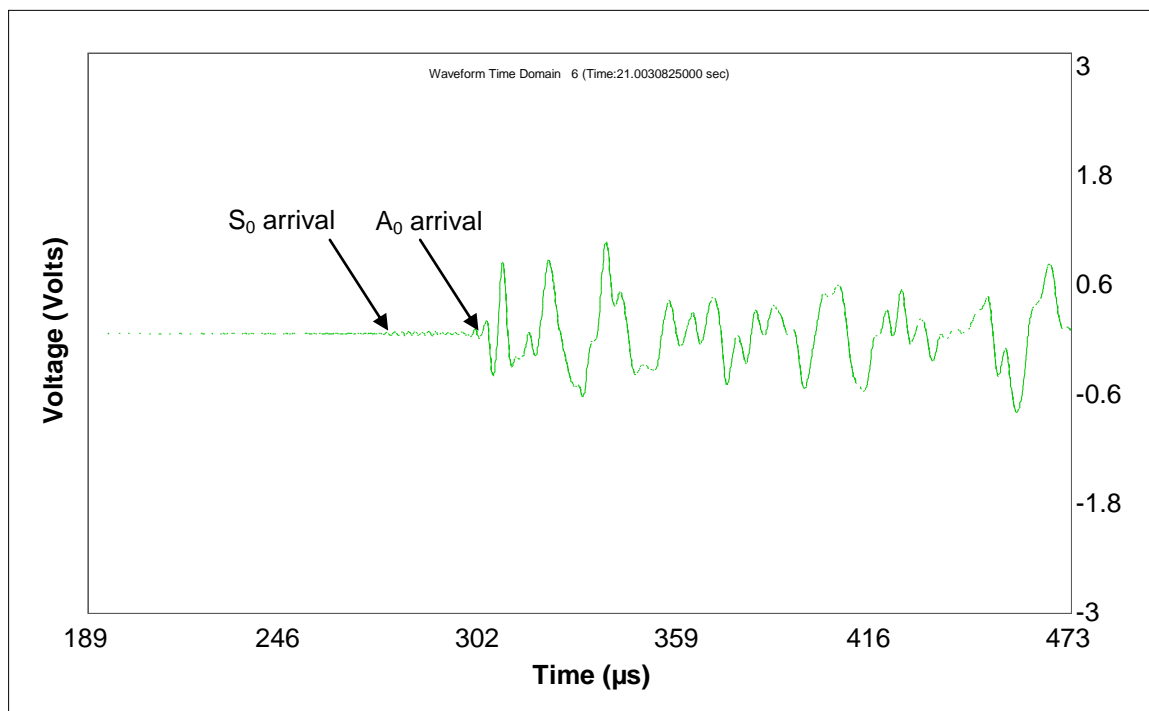


Figure 84 An enlarged view of the discrete waveform in Figure 82(c).

Since the amplitude of the signal was lower than the acquisition threshold, the hit was triggered by the  $A_0$  mode. The same result was observed by Tsuda et al. (2001) using a Michelson interferometer for AE monitoring. Detection of the  $S_0$  mode by the embedded fibre-optic sensor in the current research was attributed to an optimisation in the coupling efficiency between the host material and the sensor; this was understood to be due to the complete encapsulation of the sensor within the composite. Further evaluation of the performance of the embedded fibre-optic sensor is however required to extend the findings of this preliminary investigation. An evaluation of the repeatability of the embedded sensors is required to determine if: (i) the sensitivity of the embedded sensor is higher than that of surface-mounted sensors; and (ii) the sensor-to-sensor response is consistent.

A comparison of the typical directional sensitivities of the fibre-optic sensor in response to the pencil lead breaks as a function of the different testing conditions is presented in Table 27; the purpose of the table was to present a succinct evaluation of the performance of the sensor as a function of the test conditions, e.g. the fibre type and coupling media that was used. With reference to the table and the information presented in Section 6.3, the following observations can be made: (i) the WD piezoelectric transducer demonstrated a higher sensitivity to AE compared with the fibre-optic sensor; (ii) little or no directional sensitivity was observed from SM04-1-type fibre-optic sensors; (iii) a higher sensitivity to AE was observed for the SM600-type sensor compared to the SM04-1 sensors, although the ASL was higher (see Section 6.3.2); (iv) the cyanoacrylate adhesive provided the best signal coupling for the SM04-1-type sensors when bonded on an aluminium plate; (v) the circular U-channel packaged sensors provided a slightly higher sensitivity to AE compared with the square U-channel packaged sensors; (vi) the response of the fibre-optic sensor when bonded to a composite plate was

higher than was observed using the aluminium specimen; and (vii) the directional response of the sensor on the composite material was non-uniform. The latter observation was reportedly due to the properties of the material and not a limitation with the sensor; the WD piezoelectric transducer also demonstrated the same trend.

**Table 27 A table of typical values for the directional sensitivities of the fibre-optic sensor; the typical values represent the response of the sensor under the different test conditions. Standard deviation is shown in parentheses.**

Sensor type & test condition	Source Orientation							
	0°	45°	90°	135°	180°	225°	270°	315°
Aluminium test plate WD sensor Ultrasonic gel	97.0 (1.2)	97.3 (0.9)	96.7 (1.4)	94.9 (1.1)	94.8 (1.5)	95.0 (1.3)	95.2 (1.8)	95.6 (1.1)
Aluminium test plate SM600-type sensor Ultrasonic gel	68.0 (1.3)	68.2 (0.9)	65.1 (1.3)	68.0 (2.0)	69.4 (0.6)	66.8 (2.0)	67.1 (1.5)	68.5 (2.6)
Aluminium test plate SM04-1-type sensor Ultrasonic gel	65.9 (1.1)	66.6 (1.4)	64.5 (1.3)	66.0 (1.5)	64.3 (0.9)	64.3 (1.3)	63.6 (1.3)	65.6 (1.7)
Aluminium test plate SM04-1-type sensor Silicone rubber adhesive	67.8 (1.4)	67.6 (1.6)	63.5 (1.7)	64.7 (1.2)	67.3 (1.2)	64.4 (0.9)	64.0 (0.9)	68.1 (0.7)
Aluminium test plate SM04-1-type sensor Cured silicone rubber	68.6 (1.4)	68.9 (1.3)	66.8 (1.2)	66.8 (1.2)	66.9 (2.2)	65.5 (1.6)	63.9 (0.7)	68.0 (1.1)
Aluminium test plate SM04-1-type sensor Cyanoacrylate adhesive	70.8 (1.9)	73.1 (0.8)	71.9 (1.4)	70.9 (1.0)	69.4 (1.5)	66.6 (0.9)	70.8 (1.2)	72.8 (1.3)
Aluminium test plate Circular packaged SM04-1-type sensor Silicone rubber adhesive	70.1 (1.4)	70.1 (1.4)	70.7 (2.4)	67.2 (1.8)	68.0 (1.3)	66.8 (1.0)	67.0 (1.2)	68.1 (2.2)
Cross-ply composite WD sensor Ultrasonic gel	96.6 (1.0)	88.6 (1.4)	96.4 (1.0)	90.4 (1.7)	97.4 (0.9)	88.6 (1.1)	95.7 (0.9)	86.5 (1.6)
Cross-ply composite SM04-1-type sensor Ultrasonic gel	82.2 (1.4)	75.3 (1.3)	78.4 (1.2)	74.9 (1.9)	78.5 (1.6)	73.0 (1.8)	82.4 (2.2)	75.8 (1.3)

# CHAPTER 7

## Monitoring of Interlaminar Crack Propagation using AE

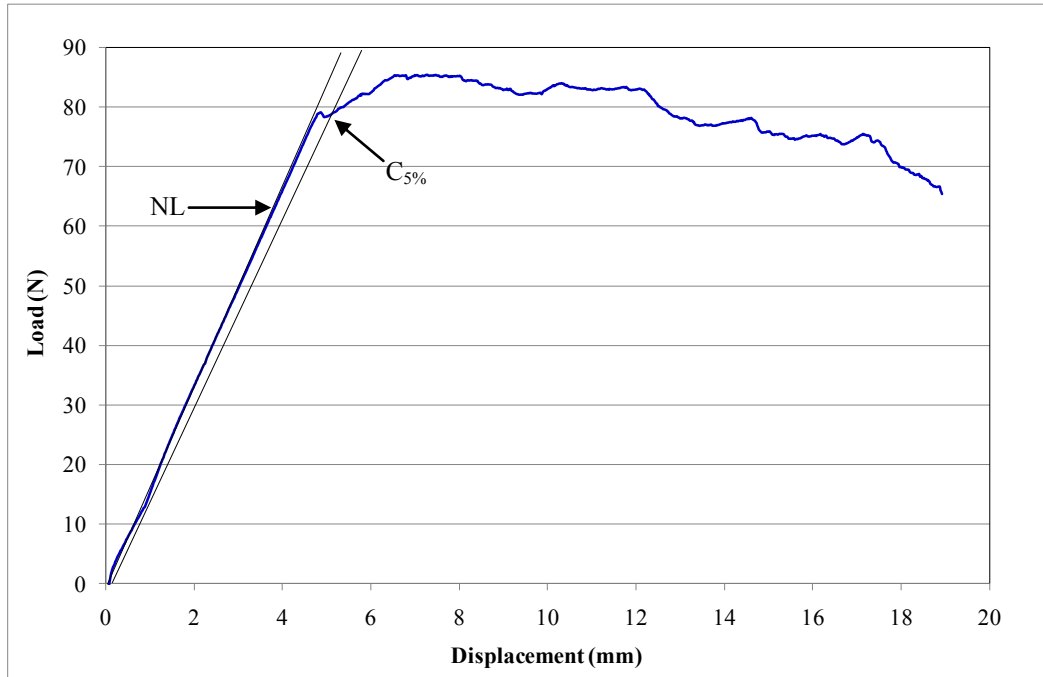
## 7 Monitoring of Interlaminar Crack Propagation using Acoustic Emission

---

### 7.1 Interlaminar Fracture Toughness of Uni-directional Composite Materials

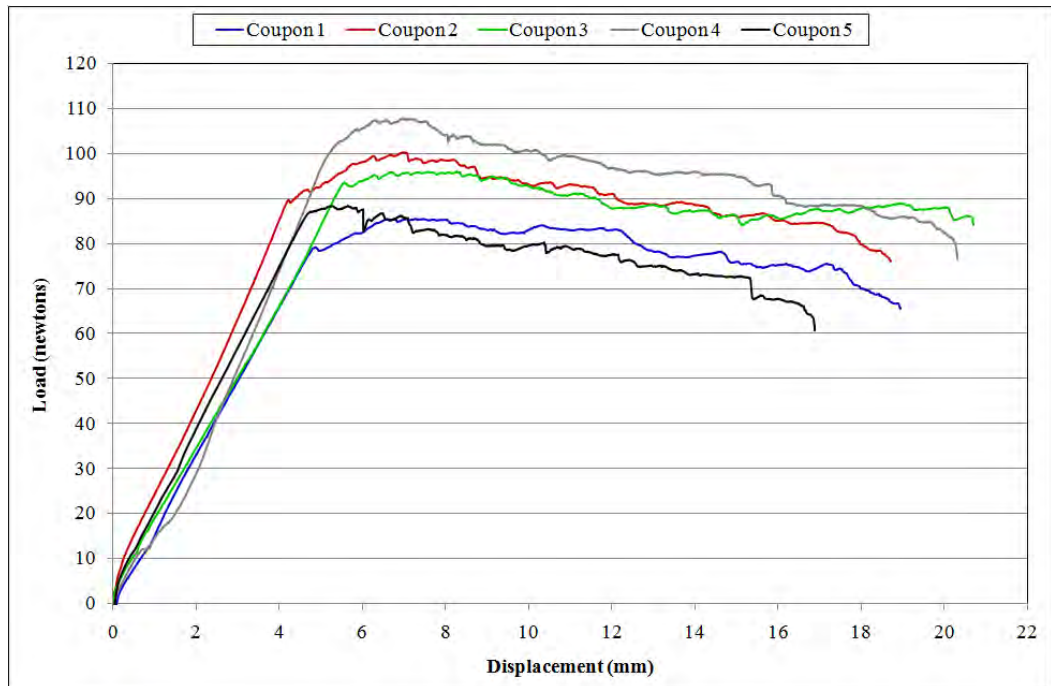
The Mode-I interlaminar fracture toughness of 16-ply uni-directional carbon-fibre epoxy composites was evaluated. The double-cantilever beam (DCB) test method was used to evaluate the fracture toughness of the material. Details of the test coupons and test methodology are provided in Section 3.5.1.

Figure 86 illustrates a typical load versus displacement curve for one of the uni-directional composite specimens. The sample displacement was obtained directly from the cross-head displacement of the Instron testing machine. With reference to this figure, the non-linear (NL) and compliance +5% ( $C_{5\%}$ ) points (BS ISO, 2001) are labelled. The NL point was defined as the deviation from linearity in the initial load versus displacement curve. The  $C_{5\%}$  point was defined by drawing a straight line through the linear region of the load versus displacement curve to obtain the initial compliance; a new line corresponding to a 5% increase in compliance ( $C_{5\%}$ ) was plotted. The intersection of this line on the load versus displacement curve provided the values that were used to define the  $G_{IC}$  initiation of the specimen pre-crack. This method was used owing to the difficulty in defining consistent NL points from the load versus displacement plots (BS ISO, 2001; Blackman and Kinloch, 2001). The  $G_{IC}$  propagation value was obtained from the average of all propagation points beyond crack initiation.



**Figure 85 An example of a load versus displacement curve for the 16-ply VTM264 uni-directional carbon fibre composite test coupon; non-linear (NL) and compliance +5% (C<sub>5%</sub>) are highlighted.**

It was observed in Figure 85 and Figure 86 that crack propagation was stable with few abrupt reductions in applied load; this indicated that the mode of crack propagation was not stick-slip (BS ISO, 2001) but was instead stable. An increase in the recorded load was observed beyond crack initiation; after this initial increase, the load was seen to fall steadily during crack propagation to the end of the test for all samples.



**Figure 86 Combined load versus displacement plots for all five 16-ply VTM-264 uni-directional carbon-fibre epoxy composite test coupons.**

Fibre bridging was observed behind the delamination front. A photograph of a failed DCB specimen after testing showing a high density of fibre bridging is presented in Figure 87.

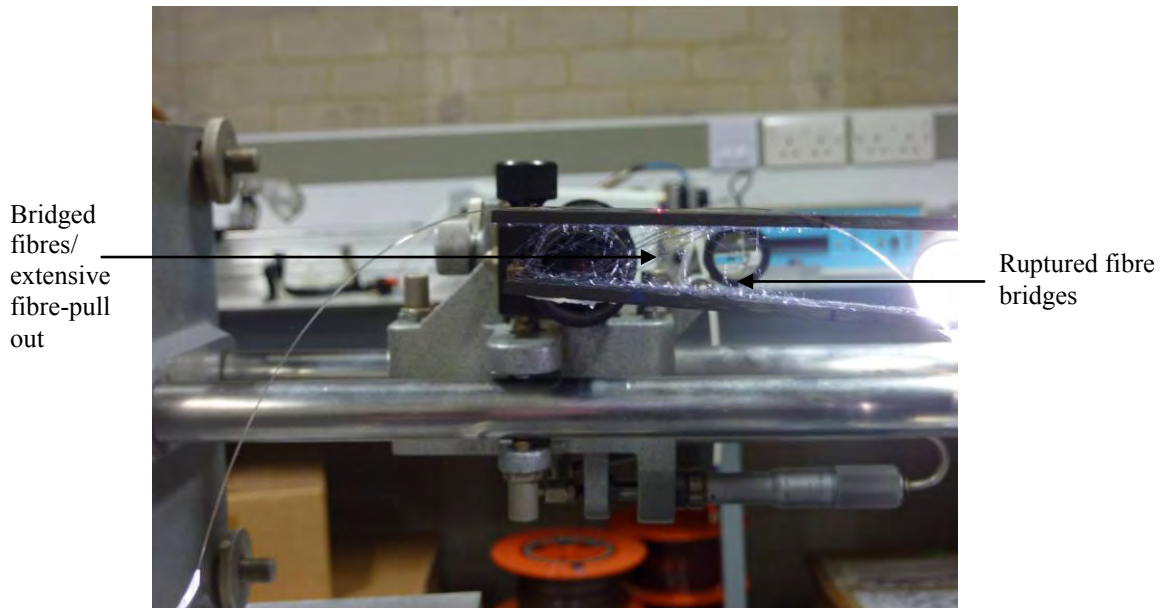


**Figure 87 Photograph of fibre bridging from a post-tested sample.**

Brunner et al. (2006) defined fibre bridging as a mechanism where unbroken fibres straddle the open crack. Davies et al. (1990) and Laffan et al. (2010) proposed that fibre bridging was a major toughening mechanism in the resistance to crack propagation. Hu and Mai (1993) indicated that fibre bridging resulted from misalignment of fibres across the delaminated plane or from multi-layer delamination. It is proposed herein that the bridged fibres served to resist movement of the crack tip by restraining the open crack. This phenomenon may therefore account for the high  $G_{IC}$  values observed in the present research; the resistance curves, i.e. R-curves, for the five samples are shown in Figure 88.

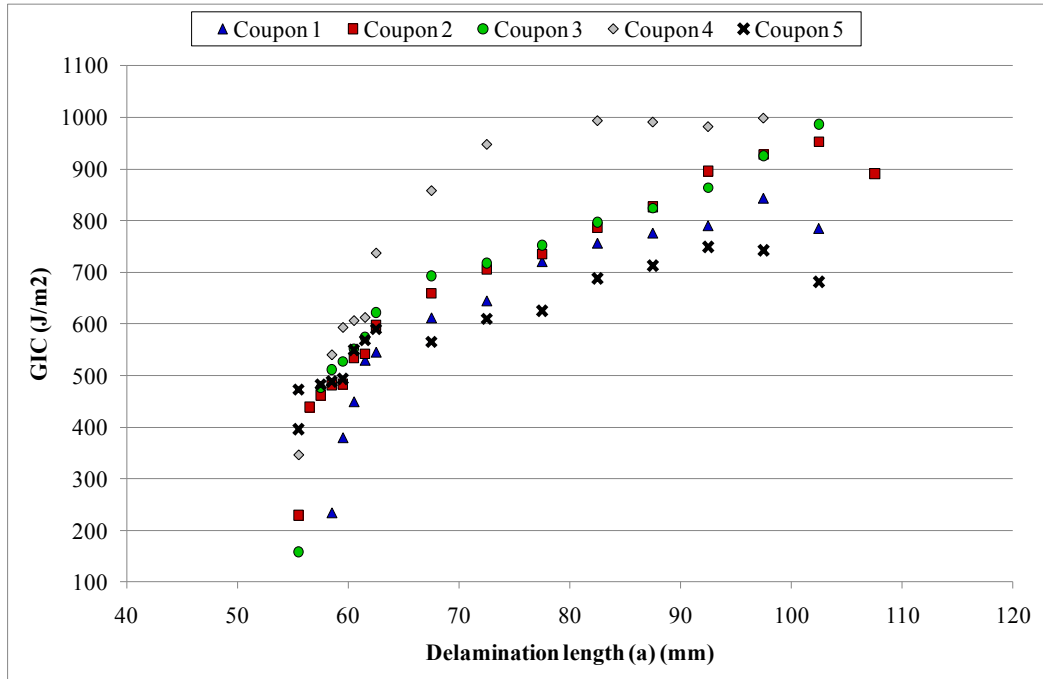


**Figure 88 Resistance curve (R-curve) illustrating the  $G_{IC}$  versus delamination length for the 16-ply VTM-264 uni-directional carbon-fibre epoxy composite test coupons.**

The resistance curve in Figure 88 illustrates an increase in fracture toughness with delamination length beyond crack initiation. Bonhomme et al. (2009) and Al-Khodairi (1996) reported that the  $G_{IC}$  value initially increased after crack initiation and then eventually stabilised during propagation. This effect was attributed to fibre bridging behind the crack tip. In the current research, this effect was also observed in coupons 1 and 4. In coupons 2, 3 and 5, an almost continuous increase in  $G_{IC}$  was observed prior to final failure. Zhang and Fox (2005) also reported this observation using composite specimens that were fabricated using Quickstep™ processing. The authors proposed that this was a function of increasing fibre bridging during crack propagation. Deng and Ye (1999) inferred that the fracture toughness of a composite material was a function of the fibre-matrix adhesion, the interlaminar bonding strength and the extent of fibre bridging. A summary of the  $G_{IC}$  values

for crack initiation and propagation from the pre-crack are presented in Table 28. With reference to the calculated values, it is evident that the  $G_{IC}$  propagation values were higher than the initiation values. This was again attributed to the effects of fibre bridging resisting the propagating crack (Laffan et al., 2010). The  $G_{IC}$  values presented in the table demonstrate low variability.

**Table 28  $G_{IC}$  values for the five 16-ply VTM-264 test coupons. Values obtained using corrected beam theory.**

Specimen ID	Test speed (mm/min)	Maximum load (N)	$G_{IC}$ (J/m <sup>2</sup> )	
			Initiation (C <sub>5%</sub> )	Propagation
VTM-DCB-001	1	85.2	380	677
VTM-DCB-002	1	99.9	439	699
VTM-DCB-003	1	95.8	476	719
VTM-DCB-004	1	107	540	832
VTM-DCB-005	1	88.2	473	602
	<b>Mean</b>	<b>95.2</b>	<b>461.6</b>	<b>705.8</b>
	<b>Standard deviation</b>	<b>8.8</b>	<b>58.4</b>	<b>83.3</b>
	<b>Coefficient of variation (%)</b>	<b>9.3</b>	<b>12.7</b>	<b>11.8</b>

## 7.2 Monitoring of Interlaminar Crack Propagation using Acoustic Emission

Acoustic emission monitoring was carried out to evaluate the development of damage in the DCB specimens during loading. Both the piezoelectric and fibre-optic acoustic emission sensors were used to monitor the DCB tests. The aim of these tests was to evaluate the sensitivity of the fibre-optic sensor to crack propagation in composite materials. The circular U-channel packaged fibre-optic sensors were surface-mounted on the DCB coupons; a photograph of the sensor locations on the DCB coupon is shown in Section 3.5.1.

Figure 89 presents a screen-shot of the AEwin™ software highlighting AE activity during DCB test-2. Load data from the mechanical test machine has been overlaid on this graph to aid comparison with the AE data.

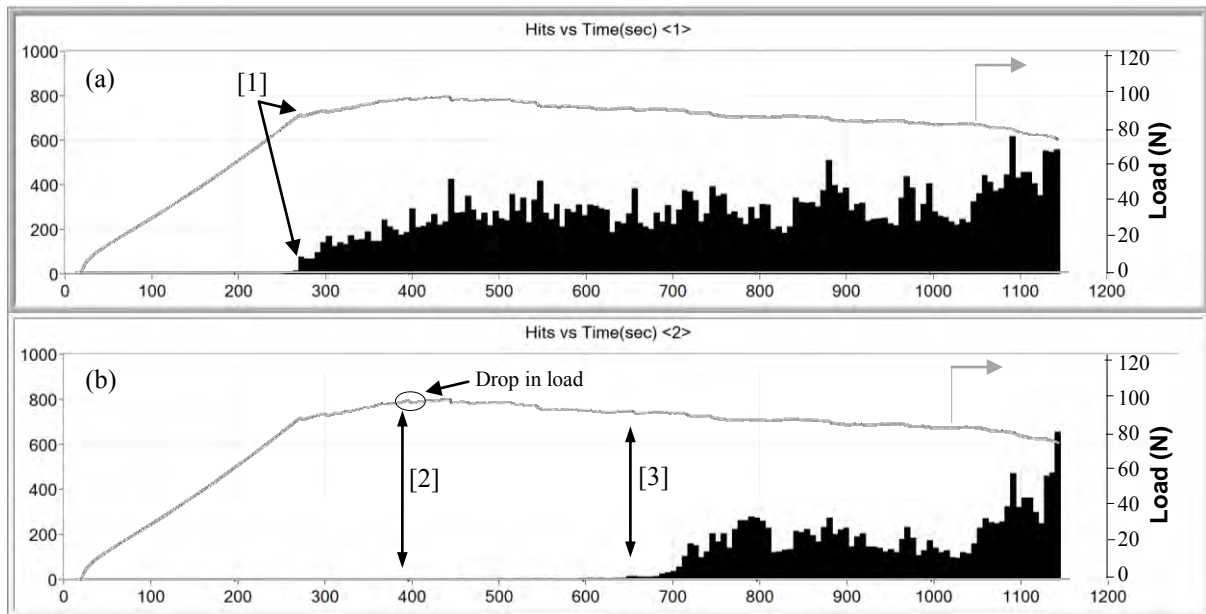


**Figure 89** Screen-shot from the AEwin™ software highlighting AE activity (hits) recorded during the DCB test (coupon 2) for: (a) the piezoelectric transducer; and (b) the fibre-optic sensor.

Owing to the increased sensitivity of the piezoelectric transducer, a greater number of AE hits were recorded; a total of 36406 hits were recorded by the piezoelectric transducer compared with the 12453 hits from the fibre-optic sensor. In addition, the first signals recorded by the piezoelectric transducer were observed well before any activity was recorded from the fibre-optic sensor; the onset of emission occurred close to the change in gradient of the load versus displacement curve. This change in gradient was attributed to the onset of microscopic crack propagation in the sample (de Charentenay et al., 1984) and is indicated by marker [1] in Figure 89. Similar correlations between the onset of AE activity and the onset of crack

propagation have been documented in the literature (Farrow et al., 1994; Benmedakhene et al., 1999; Ducept et al., 2000). The activity levels recorded by the piezoelectric transducer were almost constant up until the end of the test; an increase in the number of hits was observed around 1050 seconds indicating the onset of sample failure.

The detection of acoustic emissions recorded by the fibre-optic sensor began at approximately 380 seconds into the test; the first activity corresponded with a crack length of 10 mm and occurred prior to a sudden small drop in the load. This region is highlighted by marker [2] in Figure 89 and was understood to be associated with a sudden release of energy in the material as the crack propagated in a dynamic manner. A distinct period of activity was recorded by the fibre-optic sensor close to 430 seconds; this period of activity correlated well with the time of test shortly before the maximum load was reached. Bohse *et al.* (2000b) proposed that the point where the load fails from its maximum signifies the onset of macroscopic damage along the whole crack front. It is therefore proposed that the fibre-optic sensor was sensitive to the onset of a change in the crack propagation characteristics, i.e., microscopic to macroscopic. A continuous increase in AE activity from the fibre-optic sensor was observed beyond 650 seconds. At this point, the crack had advanced by ~30 mm; this is highlighted on the curve in Figure 89 (b) by marker [3]. The low sensitivity of the fibre-optic sensor in detecting the microscopic crack front was attributed to: (i) signal attenuation; and (ii) the low energy released during microscopic damage evolution. As the crack moved closer to the sensor, the AE signals were less attenuated and were therefore more easily detected by the sensor.

The intensity, i.e. amplitude, of the AE activity from both sensors is shown in Figure 90. It is noteworthy to illustrate that the signal gain level of the preamplifier used with the piezoelectric transducer was adjustable and was set at 20 dB<sub>AE</sub>; the dynamic range of the AE sensor was therefore altered to provide greater sensitivity to high amplitude emissions.

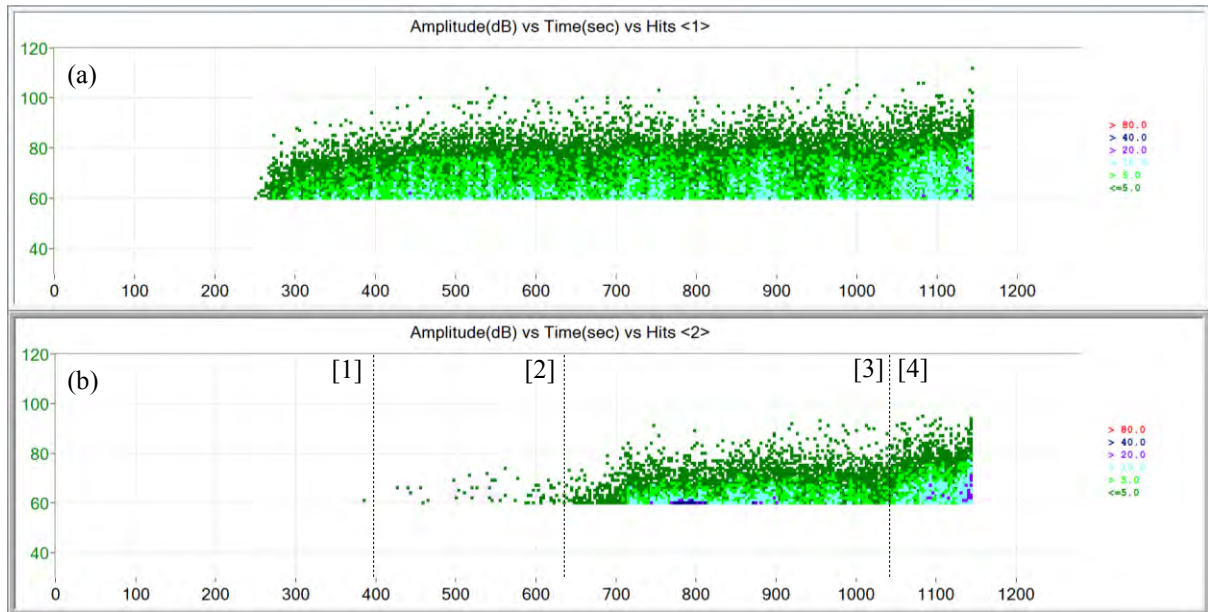


**Figure 90** Screen-shot from the AEwin™ software highlighting signal amplitude versus time recorded during the DCB test (coupon 2) for: (a) the piezoelectric transducer; and (b) the fibre-optic sensor.

The colour-scatter plots in Figure 90 (a) and (b) illustrate the number of hits as a function of amplitude with time. With reference to (b), the onsets of emission [1], as well as the distinct [2] and continuous [3] phases of activity are clearly defined in this plot. It was observed that the level of damage during region [3] was almost continuous indicating stable crack propagation. At 1050 seconds [4], a defined change in the amplitude of the signals was observed; this provided an indication that the coupon was near to failure. The maximum

amplitude of the signal that was recorded by the fibre-optic sensor was 95 dB<sub>AE</sub>; this occurred during the final phase of the test. This result supports the assumption that AE can be used to detect the onset of damage well before catastrophic failure (Finlayson et al., 2001).

As indicated in Valentin et al. (1983), “*b*-value” analysis can be used to provide information on the physical processes involved during failure of a material. The log-sum-amplitude distribution plots for coupon 2 are presented in Figure 91.

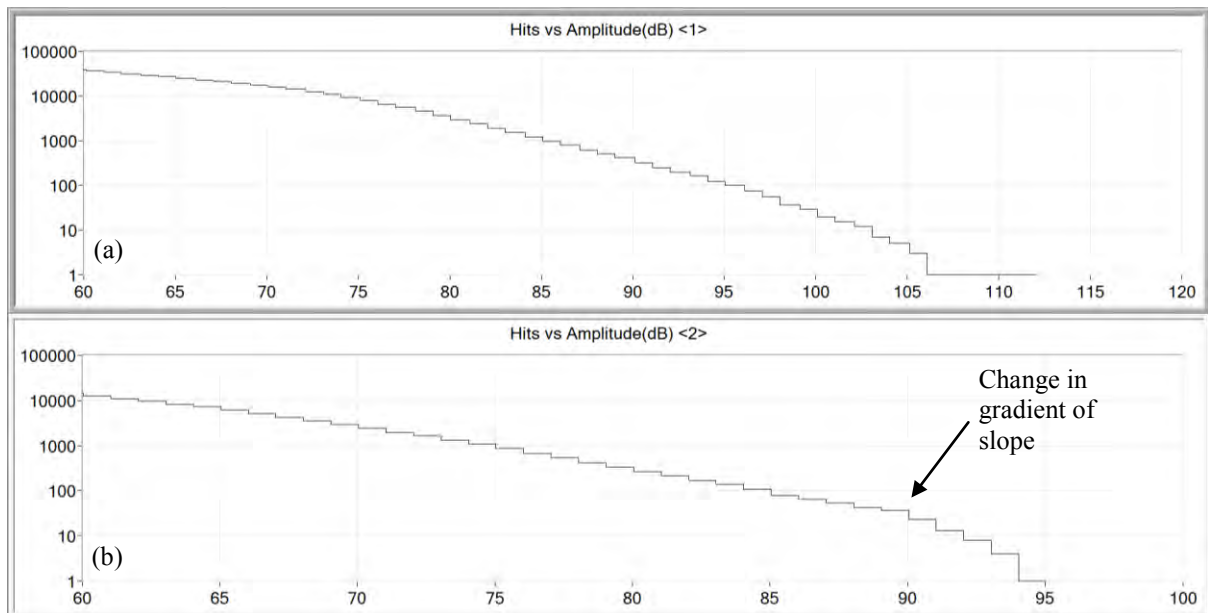


**Figure 91** Screen-shot from the AEwin™ software illustrating a log-sum amplitude distribution plot recorded during the DCB test (coupon 2) for: (a) the piezoelectric transducer; and (b) the fibre-optic sensor.

The “*b*-value” represents the gradient of the slope of activity, and was obtained directly from the amplitude-distribution plots. From analysis of these plots, it was proposed that different physical processes had occurred prior to the failure of the sample. With reference to Figure

(b), the majority of the recorded AE activity, i.e. >12000 hits, was observed within the range of 60 to 90 dB<sub>AE</sub>. This results in a failure process with a high “*b*-value”. In addition, a low number of high amplitude signals, i.e. <50 hits, were observed above 90 dB<sub>AE</sub>, indicating a different failure process with a lower “*b*-value”. The gradient of the amplitude distribution curve was seen to change at this point. The rate of crack propagation over the final 5 mm prior to failure of the sample increased. It was proposed that the high amplitude signals were related to dynamic interlaminar fracture resulting from a combination of the fracturing of bridged fibres as well as matrix cracking within the resin layers. Fibre fracture and matrix cracking were understood to account for the AE signals with amplitude between 60 and 90 dB<sub>AE</sub>; the higher amplitude signals within this range were related to fracturing of fibre bundles that bridged the opened crack. Davies *et al.* (1998) proposed that fibre bridging and multiple crack formations resulted from movement of the crack above and below fibre bundles. The SEM micrographs in Figure 92 (a) and (b) provide evidence to support the proposed assumptions. The micrographs illustrate fibre, and fibre-bundle fracture, fibre-matrix debonding and river markings running adjacent to the fibres. The river markings indicate the direction of matrix crack propagation (Purslow, 1986). The micrographs were acquired from the fracture surface of coupon 2 after final failure. With reference to Figure 88, the fracture toughness of the specimen reduced sharply over the final stages of the test. This also indicates the onset of final failure which correlates well with the observed AE data.

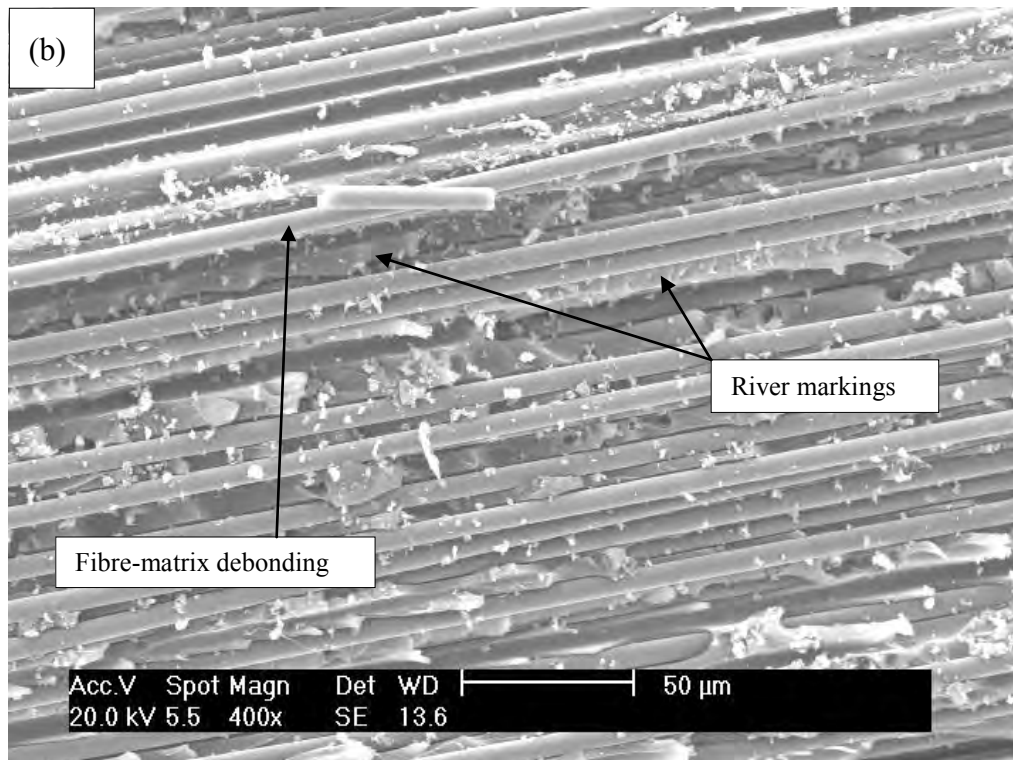
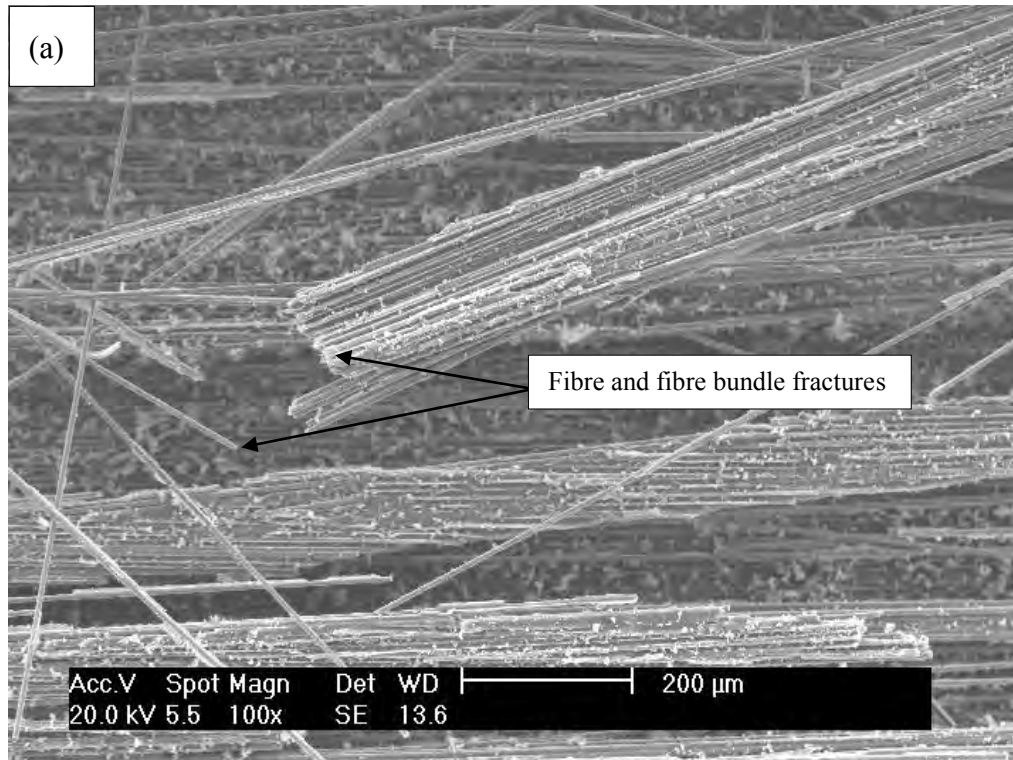


Figure 92 (a) and (b) SEM micrographs of the VTM-264 DCB coupon 2 specimen showing: (i) fibre and fibre bundle fracture; (ii) fibre-matrix debonding; and (iii) river markings.

A summary of the amplitude distributions for the five DCB tests is presented for comparison in Table 29. With reference to the data, the response of the fibre-optic sensor in DCB test-1 was significantly lower than the other four tests. The exact reason for this response was unknown; it was however proposed that the sensitivity of this sensor was lower and/or the coupling of the sensor was poor. The hit-count from the piezoelectric sensor during test-1 was within the same range as tests 2 to 5. The response of the fibre-optic sensors for test-2, 3, 4 and 5 were of equivalent sensitivity.

**Table 29 A summary of the amplitude distributions for the five DCB mode-I tests; FOS refers to the fibre-optic sensor and PZT refers to the piezoelectric transducer.**

Amplitude Range (dB <sub>AE</sub> )	Coupon 1		Coupon 2		Coupon 3		Coupon 4		Coupon 5	
	FOS	PZT	FOS	PZT	FOS	PZT	FOS	PZT	FOS	PZT
60-65	490	9039	6358	11538	4890	9827	5170	12348	4935	6805
65-70	397	6946	3671	9210	3511	7962	3447	10257	3664	6095
70-75	115	5847	1568	7678	1880	7474	1773	7652	2481	4905
75-80	45	3454	595	5042	706	4848	758	3538	1345	2325
80-85	17	1265	183	1981	213	2101	250	1382	457	798
85-90	9	393	55	660	94	689	95	433	141	209
90-95	1	152	23	217	32	254	28	136	54	77
>95	0	57	0	80	0	86	0	45	0	18
<b>Total</b>	<b>1074</b>	<b>27153</b>	<b>12453</b>	<b>36406</b>	<b>11326</b>	<b>33241</b>	<b>11521</b>	<b>35791</b>	<b>13077</b>	<b>21232</b>

Figure 93 presents a plot of absolute energy versus time for both sensors from data acquired during DCB test-2. Absolute energy, measured in attojoules (aJ), is defined as the true energy of the AE hit. Absolute energy is obtained from the integral of the squared voltage signal divided by the reference resistance, i.e. 10 kilohm, over the duration of the AE waveform. The use of the absolute energy parameter provides a convenient method for identifying any changes in the failure processes since its units are not presented on a logarithmic scale. A

“knee” in the curve (Johnson and Gudmundson, 2000) at 1050 seconds in Figure 93 (b) clearly indicates a change in the failure process and subsequently the onset of specimen failure. This data correlates well with the activity plots presented in Figure 89 and Figure 90.

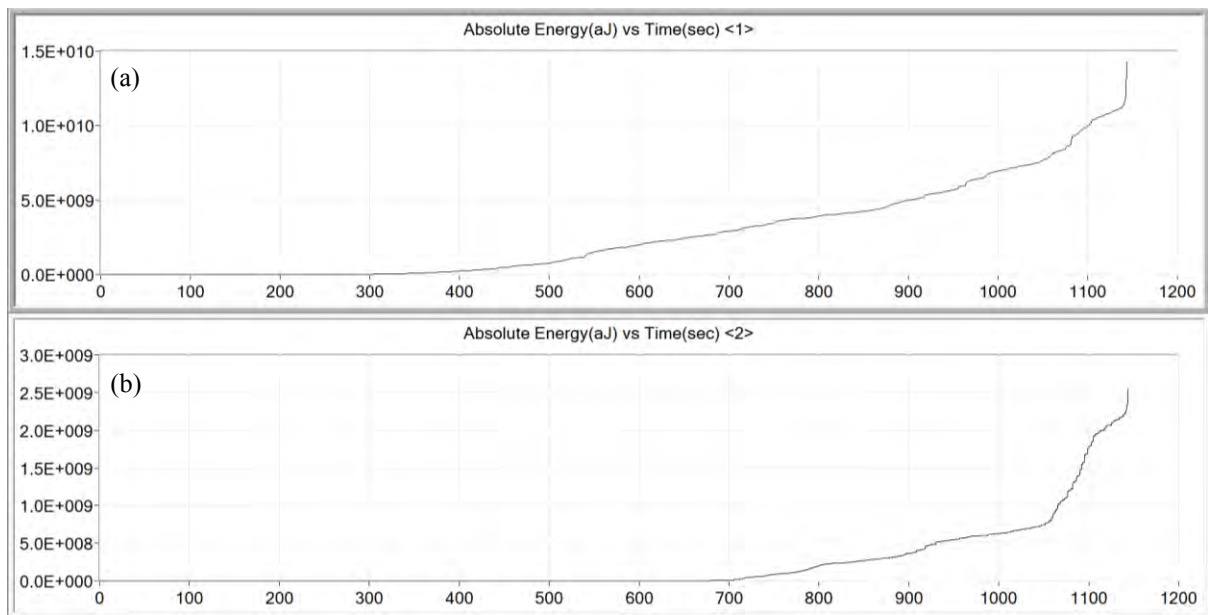


**Figure 93** Screen-shot from the AEwin™ software highlighting hit driven absolute energy versus time plot recorded during the DCB test (coupon 2) for: (a) the piezoelectric transducer; and (b) the fibre-optic sensor.

The frequency response of the AE data was evaluated to determine if this analysis method could yield additional information on the failure mechanisms observed during the DCB tests. Figure 94 presents a coloured scatter plot that shows a comparison of signal amplitude and centroid frequency as a function of time. Three distinct frequency bands are evident in this plot, namely: (i) high-frequency signals greater than 350 kHz; (ii) mid-range frequency signals between 250 and 350 kHz; and (iii) low-frequency signals between 150 and 250 kHz.

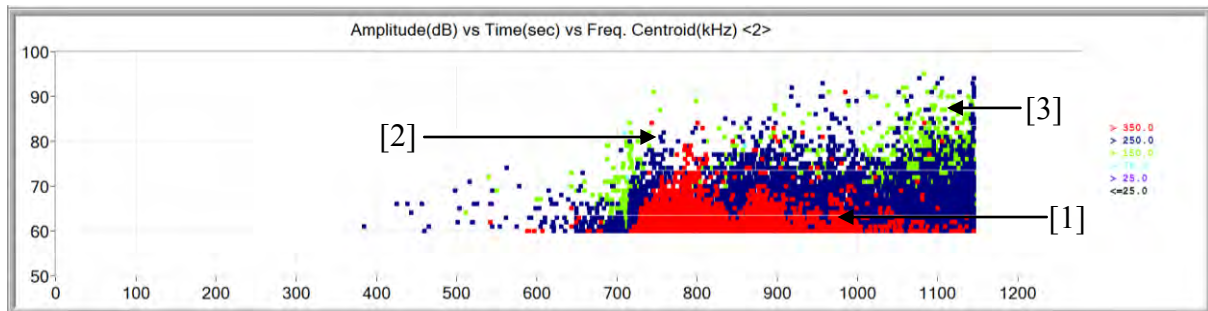


**Figure 94** A screen-shot from the AEwin™ software highlighting centroid frequency as a function of signal amplitude and test time for sample two. Data acquired by the fibre-optic sensor.

A high concentration of low amplitude signals with high-frequency content were noted between 700 and 1000 seconds. During the early stages of the test, significant amounts of fibre debris was observed on the opened crack face. It is therefore proposed that these signals were attributed to breaking of single bridged fibres. Bohse et al. (2002b) suggested that the energy released from fracture of bridged fibres was negligible; the data presented herein supports this assumption since the amplitudes are in the lowest range. Frequency analysis was also performed on discrete waveforms to confirm this assumption. Figure 95 illustrates a time-frequency representation (TFR) of a discrete waveform acquired by the fibre-optic sensor. The waveform represents a signal obtained from region [1] in Figure 94. With reference to the TFR, the dominant frequency content of this signal was approximately 400 kHz. This frequency range is in close agreement with published literature; previous research indicated that fibre fracture generates signals within a frequency range of between 400 and 500 kHz (Suzuki et al., 1991; Komai et al., 1991; Bohse, 2002a; Kim et al., 2005; Gutkin et al, 2010).

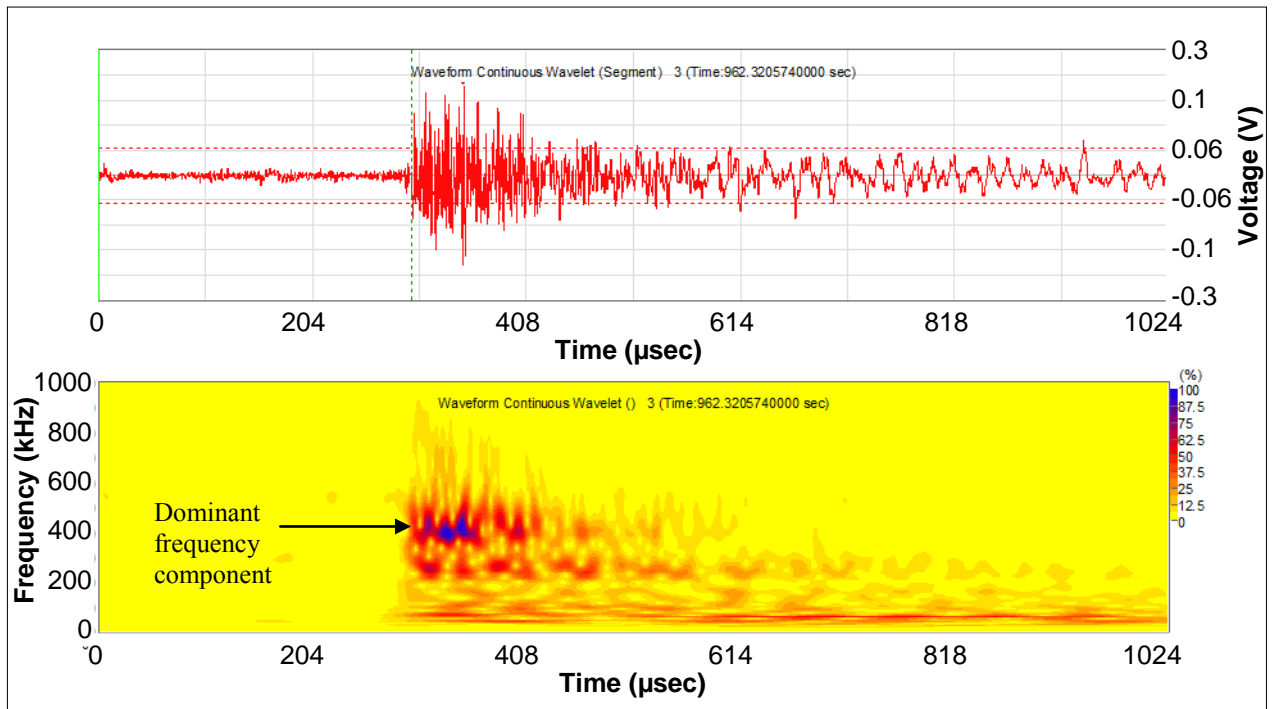


**Figure 95 A typical discrete waveform and wavelet transform for a low amplitude signal recorded by the fibre-optic sensor during sample 2 mode-I test.**

Beyond 1000 seconds, the concentration of the high frequency signals evidently reduced. Signals with a mid-range centroid frequency content and amplitudes of up to 80 dB<sub>AE</sub> were observed. These signals were attributed to fibre bundle pull-out resulting in the generation of additional load bearing bridges across the open crack face. Hwang and Han (1989) proposed that fibre bundles bridged the open crack in a peeling manner over a long distance whereas single fibres had a tendency to break. The SEM micrograph in Figure 92 (b) provides evidence to support the existence of fibre pull-out. In addition, it was also proposed that these signals may have been associated with multiple matrix cracks forming around the fibre bundles (Davies et al., 1998). de Groot et al. (1995) proposed that signals with frequency content between 180 and 250 kHz were associated with fibre-pull out. Iwamoto et al. (2010) suggested that signals with frequency content between 150-350 were related to debonding of the fibre/matrix during DCB tests on uni-directional carbon-fibre composite specimens.

Komai et al. (1991) adopted a more simplified segregation of failure mechanisms; the authors proposed that fibre fracture occurred at frequencies greater than 500 kHz whereas matrix cracking, fibre pull-out and delamination occurred at frequencies less than 300 kHz. In addition, de Groot et al. (1995) highlighted that matrix cracking produced signals with lower frequencies in the range of 50-180 kHz. Figure 96 presents a TFR of a waveform acquired from the higher amplitude region, marked [2] in Figure 94.

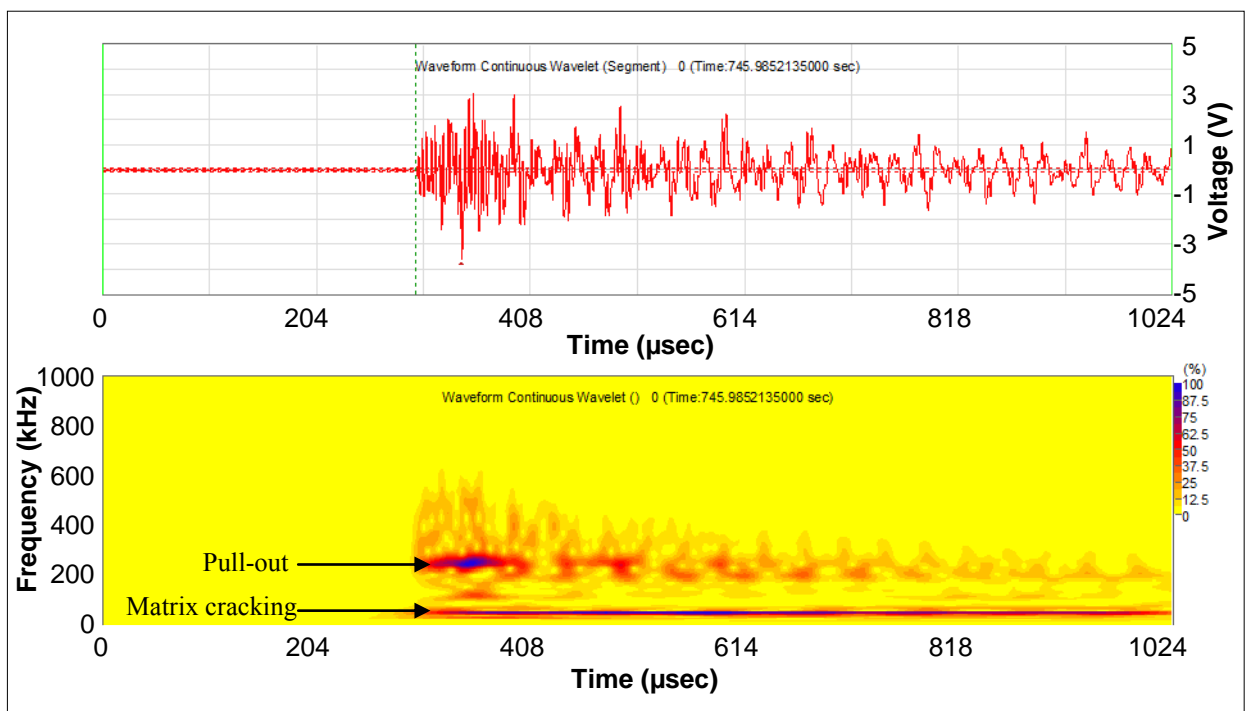


**Figure 96 A typical discrete waveform and wavelet transform for a high amplitude signal recorded by the fibre-optic sensor during sample 2 mode-I test.**

From analysis of this frequency analysis plot, two distinct frequency bands can be observed; the first is evident between 0 and 100 kHz and the second is between 200 and 300 kHz. It is inferred here that two concurrent failure mechanisms contributed to the acquired waveform, namely: (i) fibre pull-out generating the higher frequency content; and (ii) matrix cracking

generating lower frequency content. Ni and Iwamoto (2002) presented the use of wavelet transforms for differentiating failure mechanisms with respect to time. The authors demonstrated that wavelet transforms could be used to obtain additional information on the sequence of the damage mechanisms leading to final failure. The frequency content of signals was first obtained to characterise the peak frequencies. The dominant frequencies were then isolated and their contribution to the signal, with respect to time duration, were determined using wavelets. The authors found that those waveforms exhibiting two or more peak frequencies, contained two or more failure mechanisms that occurred at different time periods within the discrete signal. The signals with low frequency content and high amplitude in Figure 94, highlighted by marker [3], were attributed to delamination of the layers. The increased concentration of these signals towards the end of the test correlates well with the observed reduction in the  $G_{IC}$  fracture toughness.

In summary, complex crack growth resistance behaviour was observed during failure of the DCB specimens. Hwang and Han (1989) also proposed the same conclusion inferring that failure of uni-directional composite under mode-I loading occurs from a combination of fibre breakage, matrix tearing, transverse micro-cracking as well as delamination of the layers. The fibre-optic sensor demonstrated sensitivity to each of these failure mechanisms.

# CHAPTER 8

## Conclusions and Suggestions for Future Work

## 8 Conclusions and Suggestions for Future Work

---

### 8.1 Conclusions

The aims of the work presented in this thesis were threefold: (i) to evaluate and optimise the fabrication and packaging procedures that were used to manufacture a fibre-optic acoustic emission sensor; (ii) to characterise the response of the fibre-optic sensor using simulated AE signal generation; and (iii) to demonstrate the feasibility of using the sensor to monitor real-time damage development in fibre reinforced composite materials. The following provides a summary of the main conclusions of the work presented in this thesis. These conclusions are considered to be novel contributions to this research field.

The type of optical fibre used to fabricate the fibre-optic fused-tapered coupler has been shown to influence the sensor characteristics with respect to: (i) excess-loss; (ii) coupling ratio; and (iii) draw-length. These parameters are understood to influence the sensitivity to acoustic emission detection. The optimal fibre for fabrication of the fused-tapered coupler was found to be the SM04-1-type optical fibre (Beijing Aomolin Photoelectrical Technology Co. Ltd, China).

Differences in the dimensions of packaged fused-tapered fibre-optic sensors were observed using image analysis. These variations were understood to relate to: (i) the method used to bring the fibres into intimate contact prior to fabrication; and (ii) inconsistencies with the conventional packaging substrate used to house the sensor. The variations in the sensor

properties may therefore account for any observed differences in the sensitivity of the device to AE.

Fabrication of the AE sensor using an alternative packaging substrate was undertaken. The use of the alternative substrate was evaluated in order to: (i) reduce the overall dimensions of the sensor; (ii) improve the consistency of sensor packaging, as the conventional substrate demonstrated large variations in its dimensions; and (iii) improve sensitivity.

The post-fabrication properties of the sensors packaged in both the square and circular U-channel substrates were similar. An improvement was however observed in the recorded ASL using the small-diameter circular U-channel packaging substrate.

Embedment of the capillary-sealed fibre-optic AE sensor was demonstrated in a composite laminate that was processed in an autoclave. The post-processing characteristics were found to be in close agreement with the pre-embedment properties.

The use of the HN source method for AE signal generation was found to be a repeatable method for the generation of simulated AE signals; any deviations from the mean amplitude were within the accepted range specified in ASTM E-976 (ASTM, 2005).

The fracture surfaces of pencil lead breaks corresponding to signals with different peak frequencies was evaluated. Large blunted regions were observed on the fracture surface of pencil leads that generated low frequency signals during fracture. The observed blunting was

attributed to a proposed “crushing mechanism”; therefore the surface displacement and corresponding relaxation was assumed to be less dynamic.

Modal analysis was performed on waveforms acquired in response to pencil lead breaks. The fibre-optic AE sensor was shown to demonstrate sensitivity to the anti-symmetrical ( $A_0$ ) wave mode. Previous authors (Gorman and Prosser, 1991; Prosser et al., 1999; Tsuda et al., 2001) have proposed that the pencil lead break generates predominantly out-of-plane displacements; the results presented in the current research show good agreement with the published literature in this field.

The sampling rate that was chosen for data acquisition was shown to have limited influence on the recorded data; no additional wave mode information or an increase in signal amplitude was observed for waveforms sampled at a higher rate.

Whilst the consistency in the sensor-to-sensor response was low, the sensor typically exhibited little or no directional sensitivity. Any minimal variations in the signal amplitude were attributed to the effect of sensor coupling and not the response of the sensor itself. An increased sensitivity to the pencil lead breaks was observed from the SM600-type fibre-optic sensors. The baseline noise level for these sensors was however higher and therefore the overall signal-to-noise ratios were similar for both fibre types.

It was proposed in Chen et al. (2004) that increasing the length and reducing the width of the taper would increase the sensitivity of the device. This response was not observed in the present data. For a sensor with a wider tapered region, the baseline noise level was lower.

This was attributed to the reduction in susceptibility to the surrounding environment, e.g. vibration-based interference from the vacuum chucks and air draughts.

The properties of the couplant were found to influence the sensitivity of the sensor to the pencil lead breaks. An increase in the signal amplitude of  $\sim 5$  dB<sub>AE</sub> was achieved using a cyanoacrylate adhesive compared with the ultrasonic gel.

An increase in the mean signal-to-noise ratio was observed from a batch of sensors that were housed using the small-diameter circular U-channel packaging compared with the square U-channel package. No directional sensitivity was observed for sensors housed in the circular packaging.

The directional response of the sensor was found to be non-uniform when mounted on a 0/90° oriented composite. A reduction in the amplitude of signals recorded along the 45° orientations was observed. This response was understood to be related to the attenuation of the signal along this propagation direction. This was attributed to the influence of the material on the sensor, and not a function of the sensor's properties. A similar trend was observed from the WD piezoelectric transducer.

The fibre-optic sensor was successfully embedded in an 8-ply uni-directional composite laminate that was fabricated using autoclave processing. The embedded fibre-optic sensor provided higher sensitivity to the pencil lead breaks compared with a surface-mounted sensor. This effect was attributed to an optimised signal coupling between the sensor and the host material.

To the author's knowledge, this work represents the first evaluation of interlaminar crack propagation using a fibre-optic acoustic emission sensor.

The fibre-optic sensor demonstrated sufficient sensitivity to the onset of macroscopic damage in the DCB coupon; this type of damage was understood to correspond with an observed reduction in the load bearing properties of the coupon (Bohse, 2002b).

Frequency analysis was performed on the AE data acquired during the DCB tests. The author proposed that this method was sufficient for basic partitioning of the mechanisms associated with failure of the DCB coupons.

The acoustic emission signal analysis was in close agreement with the observed failure mechanisms that were highlighted using electron microscopy. Matrix cracking, fibre fracture and fibre-pull out were observed in SEM micrographs of the DCB coupon fracture surface.

In summary, the work presented in this thesis has demonstrated the feasibility of using the fibre-optic fused-tapered coupler sensor for the detection of acoustic emissions in a range of engineering materials. At the current standing, the author has made aware, the issues that require further investigation. These issues are presented in a succinct manner in the following section.

## 8.2 Suggestions for Future Work

This section discusses the main areas of work where additional research would enhance the current understanding of: (i) the influence of fabrication and packaging variables on the performance of the AE sensor; (ii) the response of the sensor to simulated AE; and (iii) the feasibility of using the AE sensor for real-time damage monitoring in composite materials.

The following research topics should therefore be considered:

The current research presented in Chapter four illustrated variations in the sensor-to-sensor performance; these small variations were understood to have arisen from fabrication-related issues. Development of a semi-automated methodology for controlling the repeatability of the double-twist prior to fibre fusion is proposed. Additional components could be retro-fitted to the coupler fabrication unit to control this stage of the fabrication process.

The type of sensor packaging substrate for surface-mounted applications was shown to have an influence on the performance of the sensor. Further work reviewing alternative packaging designs should be considered. The primary focus would be to maximise the surface area contact between the sensor and host material, whilst maintaining a low overall sensor dimension. In addition, research focused on the fabrication of sensors destined for embedded applications could be investigated. A semi-automated packaging procedure would further improve the success rate for sensors suitable for embedment.

The work presented in Chapter five reported on a preliminary investigation on the feasibility of embedding the capillary-sealed fibre-optic AE sensor within a composite; the preliminary

results indicated that embedment was possible in uni-directional autoclave-processed laminates. Further work should therefore be considered to address the feasibility of embedding the sensors in laminates with cross-ply and quasi-isotropic lay-up sequences. Further research could also be carried out to characterise the response of embedded sensors to simulated AE.

The performance of composite materials with embedded fibre-optic sensors has received much attention in published literature. As such, characterisation of the mechanical performance of composites with and without the embedded fibre-optic AE sensor could be investigated.

The performance of the fibre-optic sensor was characterised using thin isotropic and anisotropic specimens in Chapter six. The sensor demonstrated a dominant sensitivity to the anti-symmetrical ( $A_0$ ) mode that was generated by the pencil lead break. The proposed future work would evaluate the response of the sensor using thick-section materials, i.e. greater than 3 mm; the location of the pencil lead break would be chosen such that the symmetrical ( $S_0$ ) mode could be excited. In addition, further research is required to identify the phenomenon that influences the directional sensitivity of the sensor in cross-ply composite materials.

Whilst it is desirable to identify the presence of damage in a material using acoustic emission, it is of equal importance that the location of the damage is known. In order to detect the location of damage, there is a requirement to have multiple sensing elements configured in either a 1, 2 or 3-dimensional array. The current research can be extended to consider the use of the fibre-optic sensor for source location.

Chapter seven reported on the use of the fibre-optic AE sensor for real-time damage detection in composite materials under Mode-I loading. It is proposed here that further work be undertaken to evaluate the response of the sensor for the detection of different failure modes in composite materials; conventional mechanical test procedures could be used to initiate damage in composite specimens, e.g. static tension/compression and fatigue loading. The response of both surface-mounted and embedded sensors for detecting the onset of damage in these materials should be considered.

Finally, with reference to structural health monitoring of engineering materials and structures, the majority of the fibre optic-based sensor systems reported in the literature infer structural integrity on the basis of strain data. However, it is generally appreciated that access to more than one measurand is necessary to make a meaningful assessment of the structural integrity of engineering materials and structures. It is therefore proposed that the multi-functional capabilities of the sensor be explored; fibre-Bragg gratings can be integrated onto the output leads of the fused-tapered coupler to enable simultaneous detection of AE, strain and temperature.

# CHAPTER 9

## References

## 9 References

---

- A., Moore, D.R., Williams, J.G., (editors) (2001) **Fracture Mechanics Testing Methods for Polymers, Adhesives and Composites**. Amsterdam (Holland): Elsevier Science.
- Abraham, D., Matthews, S., McIlhagger, R. (1998) A comparison of glass fibre epoxy composites produced by wet lay-up with autoclave consolidation and resin transfer moulding. **Composites Part A**, 29A: 795-801.
- Alegria, C.F.G. (2001) **All-fibre devices for WDM optical communications**. PhD Thesis, University of Southampton.
- Aljets, D., Chong, A., Wilcox, S., (2010). "Acoustic emission source location in plate-like structures using a closely arranged triangular sensor array". **In 29th European working group on acoustic emission: AE methods and their practical applications. Vienna, 8-10 September 2010.**
- Al-Khodairi, F.A.A. (1996) **Static and Dynamic Properties of Uni-directional Hybrid Resin and Hybrid Fibre Composites**. PhD Thesis, Brunel University.
- American Society for Testing and Materials. (2007) **E 650-97: Standard guide for mounting piezoelectric acoustic emission sensors**. ASTM International.
- American Society for Testing and Materials. (2005) **E 976-05: Standard guide for determining the reproducibility of acoustic emission sensor response**. ASTM International.
- Ashcroft, I.A., Hughes, D.J., Shaw, S.J. (2001) Mode-I fracture of epoxy bonded composite joints: 1. Quasi-static loading. **International Journal of Adhesion and Adhesives**, 21: 87-99.
- Avdelidis, N.P., Hawtin, B.C., Almond, D.P. (2003) Transient thermography in the assessment of defects of aircraft composites. **NDT&E International**, 36: 433-439.
- Aymerich, F., Meili, S. (2000) Ultrasonic Evaluation of Matrix Damage in Impacted Composite Laminates. **Composites: Part B**, 31: 1-6.
- Bachmaier, S.A. (2008). Event-based acoustic emission techniques for structural health monitoring using wireless sensor networks. **The e-Journal of Nondestructive Testing** [online], 1-10. Available from: [Accessed December 2008].
- Badcock, R.A., Birt, E.A. (2000) The use of 0-3 piezocomposite embedded Lamb wave sensors for detection of damage in advanced fibre composites. **Smart Materials and Structures**, 9: 291-297.

- Ball, R.J., Almond, D.P. (1998) The detection and measurement of impact damage in thick carbon-fibre reinforced laminates by transient thermography. **NDT&E International**, 31(3): 165-173.
- Barbezat, M., Brunner, A.J., Flueler, P., Huber, C., Kornmann, X. (2004) Acoustic emission sensor properties of active fibre composite elements compared with commercial acoustic emission sensors. **Sensors and Actuators A**, 114: 13-20.
- Barnier, F., Dyer, P.E., Monk, P., Snelling, H.V., Rourke, H. (2000) Fibre optic removal by pulsed laser ablation. **Journal of Physics D: Applied Physics**, 33(7): 757-759.
- Barre, S., Benzeggagh, M.L. (1994) On the use of acoustic emission to investigate damage mechanisms in glass-fibre reinforced polypropylene. **Composites Science and Technology**, 52: 369-376.
- Bartelds, G., Hedia, J.H., McFeat, J., Boller, C. (2004) "Introduction". In Staszewski, W.J., Boller, C., Tomlinson, G.R. (ed.) **Health monitoring of aerospace structures**. West Sussex: Wiley and Sons Ltd. Ch 1.
- Bates, D., Smith, G., Lu, D., Hewitt, J.(2000) Rapid thermal non-destructive testing of aircraft components. **Composites: Part B**, 31: 175-185.
- Benmedakhene, S., Kenane, M., Beneggagh, M.,L. (1999) Initiation and growth of delamination in glass/epoxy composites subjected to static and dynamic loading by acoustic emission monitoring. **Composites Science and Technology**, 59: 201-208.
- Bergland, G.,D. (1969) A Guided Tour of the Fast Fourier Transform. **IEEE Spectrum**, 6: 41-52.
- Berthelot, J.M. (1998) **Composite Materials: Mechanical behaviour and structural analysis**. New York: Springer-Verlag.
- Bertholet, J.M., Rhazi, J. (1990) Acoustic emission in carbon-fibre composite. **Composites Science and Technology**, 37: 411-428.
- Betz, D.C., Thursby, G., Culshaw, B., Staszewski, W.J. (2006) Identification of structural damage using multifunctional Bragg grating sensors: I. Theory and Implementation. **Smart Materials and Structures**, 15: 1305-1312.
- Betz, D.C., Thursby, G., Culshaw, B., Staszewski, W.J. (2007) Structural Damage Location with Fibre Bragg Grating Rosettes and Lamb Waves. **Structural Health Monitoring**, 6: 299-308.
- Bilodeau, F., Hill, K.O., Faucher, S., Johnson, D.C. (1990) "Fabrication technique for low-loss fused-tapered directional couplers and pressure sensor produced thereby". **Canadian Patent** 4895423.

- Birks, T.A. (1989) Twist induced tuning in tapered fibre couplers. **Applied Optics**, 28 (19): 4223-4336.
- Birks, T.A., Russell, P-StJ., Culverhouse, D.O. (1996) The acousto-optic effect in single-mode fibre tapers and couplers. **Journal of Lightwave Technology**, 14 (11): 2519-2529.
- Blackman, B.R.K., Kinloch, A.J. (2001) Fracture Tests for Structural Adhesive Joints. **Fracture Mechanics Testing Methods for Polymers, Adhesives and Composites**, 28: 225-267.
- Blitz, J., Simpson, G. (1995) **Ultrasonic methods of non-destructive testing**. London: Chapman & Hall.
- Bock, W.J., Wisniewski, R., Wolinski, T.R. (1992) Fibre-optic strain-gauge manometer up to 100 MPa. **IEEE Transactions on Instrumentation and Measurement**, 41(1): 72-76.
- Bohse, J. (2000) Acoustic emission characteristics of micro-failure processes in polymer blends and composites. **Composites Science and Technology**, 60: 1213-1226.
- Bohse, J., Krietsch, T., Chen, J.H., Brunner, A.J. (2000). "Acoustic emission analysis and micro-mechanical interpretation of mode-I fracture toughness tests on composite materials". **In European Structural Integrity Society; Fracture of Polymer, Composites and Adhesives, 2nd ESIS TC4 Conference on Fracture of Polymers, Composites and Adhesives**, ESIS Publication 27: 15-26.
- Bonesteel, R.M., Piper, D.E., Davinroy, A.T. (1978) Compliance and KI calibration of double cantilever beam (DCB) specimens. **Engineering Fracture Mechanics**, 10: 425-428.
- Bonhomme, J., Arguelles, A., Vina, J., Vina, I. (2009) Fractography and failure mechanisms in static mode-I and mode-II delamination testing of uni-directional carbon reinforced composites. **Polymer Testing**, 28: 612-617.
- Booyesen, A., Spammer, S.J., Swart, P.L. (1991). "Ratiometric fibre-optic sensor utilizing a fused biconically tapered coupler". **In Fibre Optic and Laser Sensors IX Proceedings of SPIE**, Vol. 1584: 273-279.
- Booyesen, A., Swart, P.L., Spammer, S.J., (1993). "Wavelength insensitive fibre optic sensor based on an acially strained fused coupler. **In Fibre Optic and Laser Sensors XI Proceedings of SPIE**. Vol. 2070: 322-332.
- Brewer, J.C., Lagace, P.A. (1988) Quadratic stress criterion for initiation of delamination. **Journal of Composite Materials**, 22 (12): 1141-1155.
- Brunner, A.J., Blackman, B.R.K., Williams, J.G. (2006) Calculating a damage parameter and bridging stress from GIC delamination tests on fibre composites. **Composites Science and Technology**, 66: 785-795.

BS ISO 15024. (2001) **Fibre-reinforced plastic composites. Determination of mode-I interlaminar fracture toughness, GIC, for uni-directionally reinforced materials.** London: BS ISO.

Bunsell, A.R.(1977) Acoustic emission for proof testing of carbon-fibre-reinforced plastics. **NDT International**, 10 (1): 21-25.

Bures, J., Lacroix, S., La Pierre, J. (1983) Analyse d'un coupler bidirectionnel a fibres optiques monomodes fusionnees. **Applied optics**, 22: 1918-1922.

Burns, W.K., Abebe, M., Villarruel, C.A., Moeller, R.P. (1986) Loss mechanisms in single-mode fiber tapers. **Journal of Lightwave Technology**, Vol LT-4 (6): 608-613.

Butter, C.D., Hocker, G.B., (1978) Fibre optic strain gauge. **Journal of Applied Optics**. 17 (18), pp. 2867-2869.

Buttle, D.J., Scruby, C.B. (1989) Acoustic emission monitoring of a fatigue crack in 50D steel in a sea-water environment. **NDT International**, 22 (2): 81-96.

Cantwell, W.J., Morton, J. (1985) Detection of impact damage in CFRP laminates. **Composite Structures**, 3: 241-257.

Cantwell, W.J., Morton, J. (1991) The impact resistance of composite materials – A review. **Composites**, 22 (5): 347-362.

Cawley, P., Adams, R.D. (1988) The mechanics of the coin-tap method of non-destructive testing. **Journal of Sound and Vibration**, 122(2): 299-316.

Chen, J., Su, Z., Cheng, L. (2010) Identification of corrosion damage in submerged structures using fundamental anti-symmetric Lamb waves. **Smart Materials and Structures**, 19: 1-12.

Chen, R. (27 September 2010) **Personal Communication**. Discussion on limitations of oxy-butane flame type for fabrication of couplers.

Chen, R., Badcock, R., Fernando, G.F., Butler, T. (2003) **Project FOAESMIE (Fibre-optic acoustic emission sensors for discharge detection for monitoring in the electrical industry): The performance of the fibre-coupler based AE sensor – Validation of the model with experimental results.** DTI/LINK S3IA Report.

Chen, R., Bradshaw, T., Burns, J., Cole, P., Jarman, P., Pedder, D., Theobald, R., Fernando, G.F. (2006) Linear Location of Acoustic Emission using a Pair of Novel Fibre-optic Sensors. **Measurement Science and Technology**, 17: 2313-2318.

Chen, R., Fernando, G.F., Butler, T., Badcock, R.A. (2004) A Novel Ultrasound Fibre-optic Sensor based on a Fused-Tapered Optical Fibre Coupler. **Measurement Science and Technology**, 15: 1490-1495.

- Chen, R., Theobald, P., Gower, M., Malik, S., Burns, J, Fernandes, E., Bryce, G., Fernando G.F. (2008) A novel fibre-optic acoustic emission sensor. *In Proceedings of SPIE*. Vol. 6932.
- Chiang, C.C., Lee, J.R., Bang, H.J. (2008) Structural health monitoring for a wind turbine system: A review of damage detection methods. **Measurement Science and Technology**, 19: 1-20.
- Colombo, S., Giannopoulos, A., Forde, M.C., Hasson, R., Mulholland, J. (2005) Frequency response of different couplant materials for mounting transducers. **NDT&E International**, 38: 187-193.
- Compton, R. (1971) An inspection system for the non-destructive testing of composites. **Composites** 1971; September: 152-153.
- D’Orazio, T.D., Guaragnella, C., Leo, M., Spagnolo, P. (2005) Defect detection in aircraft composite by using a neural approach in the analysis of thermographic images. **NDT&E International**, 38: 665-673.
- Davies, G.A.O., Zhang, X. (1995) Impact Damage Prediction in Carbon Composite Structures. **International Journal of Impact Engineering**, 16 (1): 149-170.
- Davies, P. et al. (1992) Round-robin interlaminar fracture testing of carbon-fibre-reinforced epoxy and PEEK composites. **Composites Science and Technology**, 43: 129-136.
- Davies, P., Benzeggagh, M.L. (1989) “Interlaminar mode-I-fracture testing”. *In*: Freidrich K, (ed). **Application of fracture mechanics to composite materials**. London: Elsevier Science: Ch 3.
- Davies, P., Blackman, B.R.K., Brunner, A.J. (1998) Standard test methods for delamination resistance of composite materials - current status. **Applied Composite Materials**, 5: 345-364.
- Davies, P., Cantwell, W., Kausch, H (1989) Measurement of initiation values of GIC in IM6/PEEK composites. **Composites Science and Technology**, 35: 301-313.
- Davies, P., Moulin, C., Kausch, H.H., Fischer, M. (1990) Measurement of GIC and GIIC in Carbon/Epoxy Composites. **Composites Science and Technology**, 39: 193-205.
- de Charentenay, F.X., Harry, J.M., Prel, Y.J., Benzeggagh, M.L. (1984) Characterizing the effect of delamination defect by Mode-I delamination test. *In Effects of defects in composite materials*, ASTM STP 836, American society for testing and materials: 84-103.
- de Groot, P.J., Wijnen, P.A.M., Janssen, R.B.F. (1995) Real-time Frequency Determination of Acoustic Emission for Different Fracture Mechanisms in Carbon/epoxy Composite. **Composite Science and Technology**, 55: 405-412.
- De Oliveria, R., Lavanchy, S., Chatton, R., Costantini, D., Michaud, V., Salathé, R., Manson, J,A.E. (2008) Experimental investigation of the effect of the mould thermal expansion on the

development of internal stresses during carbon-fibre composite processing. **Composites: Part A**, 39: 1083-1090.

De Oliveria, R., Ramos, C.A., Marques, A.T. (2008) Health monitoring of composite structures by embedded FBG and interferometric Fabry-Perot sensors. **Computer and Structures**, 86: 340-346.

Deng, S., Ye, L. (1999) Influence of Fibre-Matrix Adhesion on Mechanical Properties of Graphite/Epoxy Composite: II. Interlaminar Fracture and Inplane Shear Behaviour. **Journal of Reinforced Plastics and Composites**, 18: 1041-1057.

Di Scalea, H., Bartoli, I., Srivastava, A., Park, G., Farrar, C. (2006) "The fundamental response of piezoelectric guided-wave sensors and applications to damage and impact location". **In Proceedings of the third European workshop on structural health monitoring 2006**. Lancaster PA.

Donaldson, S.L. (1987) The effect of interlaminar fracture properties on the delamination buckling of composite laminates. **Composites Science and Technology**, 28: 33-44.

Doyle C, Chen R, Liu T, Zheng G, Fernando GF. (2002) "Fibre-optic acoustic emission sensor based on a fused-tapered coupler". **In Smart Structures and Materials-Smart Sensor Technology and Measurement Systems, Proceedings of SPIE, San Diego, 18 March 2002**: 28-35.

Doyle, C., Porada, S., Fernando, G. (2002b) "Development of a new type of fibre-optic sensor for detection of AE in composites". **In Conference proceedings of Structural Health Monitoring. Paris, 2002**.

Drzal, L.T. (1990) The role of the fiber-matrix interphase on composite properties. **Vacuum**, 41 (7-9): 1615-1618.

Ducept, F., Davies, P., Gamby, D. (2000) Mixed mode failure criteria for a glass/epoxy composite and an adhesively bonded composite/composite joint. **International Journal of Adhesion and Adhesives**, 20: 233-244.

Dugmore, K., Jonson, D., Walker, M. (2002) A comparison of signal consistency of common ultrasonic couplants used in the inspection of composite materials. **Composite Structures**, 58: 601-603.

Elspace, W. J., Kunzmann, J., Flemming, M., Baumann, D. (1995) "Design, manufacturing and verification of piezoceramics embedded in fiber-reinforced thermoplastics". **In Smart Structures and Materials; Smart Structures and Integrated Systems, Proceedings of SPIE**, 2443: 327-333.

Enoki, M., Kishi, T. (2000). "Acoustic emission source characterization in materials". **In Kishi, T., Ohtsu, M., Yuyama, S., (ed). Acoustic Emission – Beyond the Millennium**. 1st ed. Elsevier Science; 2004. Ch 1.

Farrow, G.J., Hughes, J.D.H., Darby, M.I. (1994) Acoustic Emission from Single Carbon-fibres and Model Microcomposites. **J.Phys. D; Appl. Phys**, 27: 644-651.

Favre, J.P., Laizet, J.C. (1989) Amplitude and counts per event analysis of the acoustic emission generated by the transverse cracking of cross-ply CFRP. **Composites Science and Technology**, 36: 27-43.

Fernando, G.F., Degamber, B. (2006) Process monitoring of fibre reinforced composites using optical fibre sensors. **International Materials Reviews**, 51(2): 65-106.

Fernando, G.F., Hameed, A., Tetlow, J., Winter D., Leng, J., Barnes, R., Mays, J., Kister, G. (2003) Optical fibre sensors for structural health monitoring of concrete: Part 1: Sensor design, modelling and protection systems. **Invited paper – Journal of Structural health monitoring**, 2 (2): 123-135.

Fernando, G.F., Liu, T., Crosby, P.A., Doyle, C., Martin, A., Brooks, D., Ralph, B., Badcock, R.A. (1997) A multi-purpose optical fibre sensor design for fibre reinforced composite materials. **Journal of Measurement Science and Technology**, 8: 1065-1079.

Finlayson, R.D., Friesel, M., Carlos, M., Cole, P., Lenain, J.C. (2001) Health monitoring of aerospace structures with acoustic emission and acousto-ultrasonics. **Insight**, 43 (3).

Foote, P., et al. (2004) “Operational load monitoring using optical fibres”. In: Staszewski WJ, Boller C, Tomlinson GR, (ed). **Health monitoring of aerospace structures**. West Sussex: Wiley and Sons Ltd: Ch 3.

Friebele, E.J., Askins, C.G., Bosse, A.B., Kersey, A.D., Patrik, H.J., Pogue, W.R, Putnam, M.A., Simon, W.R., Tasker, F.A., Vincent, W.S., Vohra, S.T. (1999) Optical fibre sensors for spacecraft applications. **Smart Materials and Structures**, 8: 813-838.

Fu, T., Liu, Y., Li, Q., Leng, J. (2009) Fibre optic acoustic emission sensor and its applications in the structural health monitoring of CFRP materials. **Optics and Lasers in Engineering**, 47: 1056-1062.

Fuhr, P.L., Huston, D.R., Ambrose, T.P. (1994) “Remote monitoring of instrumented structures using the INTERNET information superhighway”. **In Proceedings of the 2nd European Conference on Smart Structures and Materials**, Glasgow.

Fuhr, P.L., Huston, D.R., Ambrose, T.P., Mowat, E.F. (1995) An internet observatory: remote monitoring of instrumented civil structures using the information superhighway. **Smart Materials and Structures**, 4: 14-19.

Georgiou, G., Boucouvalas, A.C. (1985) Low-loss single-mode optical couplers. **IEEE proceedings**, 132(5): 297-302.

Giallorenzi, T.G., Bucaro, J.A., Dandridge, A., Sigel, Jr G.H., Cole, J.H., Rashleigh, S.C. (1982) Optical fibre sensor technology. **IEEE Journal of Quantum Electronics**, Vol QE-18(4): 626-665

Giordano, M.L., Zielinski, M. SFAR 88/Relative operating rules; special maintenance requirements and compliance planning briefing. Keynote address. [internet] c2007 [cited 19th January 2011] Available from: [http://www.caasd.org/atrac/FAA\\_PI-Engineer\\_Workshop/2002/SFAR-88-Related-Operating-Rules-and-Special-IMaintenance-Requirements.pdf](http://www.caasd.org/atrac/FAA_PI-Engineer_Workshop/2002/SFAR-88-Related-Operating-Rules-and-Special-IMaintenance-Requirements.pdf)

Gorman, M.R., Prosser, W.H. (1991) AE Source Orientation by Plate Wave Analysis. **Journal of Acoustic Emission**, 9 (4): 283-288.

Gower MRL. (2008) Project ACLAIM (Advanced Composite Life Assessment and Integrity Management): Measurement of Mode-I and II fracture toughness for mixed materials used in ACLAIM case studies. **NPL REPORT MAT 19**.

Gray, G.R., Roy, R. (1991) Bistability and mode hopping in a semiconductor laser. **J. Opt. Soc. Am.**, 8 (3): 632-638.

Green, A.T. (1969) Detection of incipient failures in pressure vessels by stress wave emissions. **Nuclear Safety**, Vol 10(1).

Gu, H., Chattopadhyay, A. (1999) An experimental investigation of delamination buckling and postbuckling of composite laminates. **Composites Science and Technology**, 59: 903-910.

Guemes, J.A., Menedez, J.M., Frovel, M., Fernandez, I., Pintado, J.M. (2001) Experimental analysis of buckling in aircraft skin panels by fibre-optic sensors. **Smart. Materials and Structures**, 10: 490-496.

Gutkin, R., Green, C.J., Vangrattanachai, S., Pinho, S.T., Robinson, P., Curtis, P.T. (2010) On acoustic emission for failure in CFRP: Pattern recognition and peak frequency analyses. *Mechanical Systems and Signal Processing*, Available online: December 2010.

Hamstad, A. (1982) Acceptance testing of graphite/epoxy composite parts using an acoustic emission monitoring technique. **NDT International**, 15 (6): 307-314

Hamstad, M. An Illustrated Overview of the use and Value of a Wavelet Transform to Acoustic Emission Technology [internet] [cited 5th July 2011] Available from: <http://www.vallen.de/zdownload/pdf/hamstad.pdf>.

Hamstad, M.A., O’Gallagher, A., Gary, J. (2002) A Wavelet Transform Applied to Acoustic Emission Signals: Part 1- Source Identification. **Journal of Acoustic Emission**, 20: 39-61.

Han, L., Wang, X.D., Sun, Y. (2008) The effect of bonding layer properties on the dynamic behaviour of surface-bonded piezoelectric transducers. **International Journal of Solids and Structures**, 45: 5599-5612.

- Hati, A., Nelson, C.W., Taylor, J., Ashby, N., Howe, D.A. (2008) Cancellation of vibration-induced phase noise in optical fibers. **IEEE Photonics Technology Letters**, 20(22): 1842-1844.
- Henneke II, E.G. (1987) Destructive and Non-destructive tests. **Engineered Materials Handbook**, Volume 1: 774-778.
- Hensman, J.J., Cristodaro, C.V., Pierce, S.G, Worden, K. (2006) On the reproducibility of transducer coupling for acoustic emission testing. **Advanced Materials Research**, 2006; Vol 13-14: 117-124.
- Higo, Y., Inaba, H. (1989) "The general problems of AE sensors". In Sachse W, Roget J, Yamaguchi K, (ed). **Acoustic emission: current practise and future directions**. ASTM International, 1989. Ch 1.
- Hill, K.O., Meltz, G. (1997) Fibre Bragg Grating Technology: Fundamentals and Overview. **Journal of Lightwave Technology**, 15 (8): 1263-1276.
- Hill, R., El-Dardiry, S.M.A. (1981) Variations in the use and design of acoustic emission transducers. **Ultrasonics**, 19 (1): 9-16.
- Holford, K.M. (2000) Acoustic emission – Basic principles and future directions. **Strain**, 36 (2): 51-54.
- Hou, J.P., Jeronimidis, G. (1999) Vibration of delaminated thin composite plates. **Composites: Part A**, 30: 989-995.
- Hsieh, C.S., Wu, T.L., Cheng, W.H. (2001) An optimum approach for fabrication of low loss fused fibre couplers. **Materials Chemistry and Physics**, 69: 199-203.
- Hu, X.Z., Mai, Y.W. (1993) Mode-I Delamination and Fibre Bridging in Carbon-Fibre/Epoxy Composite With and Without PVAL Coating. **Composites Science and Technology**, 46: 147-156.
- Hull, D., Clyne, T.W. (1996) **An Introduction to Composite Materials**. 2nd ed. Cambridge: Cambridge University Press.
- Hull, D., Shi, Y.B. (1993) Damage mechanism characterization in composite damage tolerance investigations. **Composite Structures**, 23(2): 99-120.
- Hwang, H., Han, K.S. (1989) Interlaminar fracture behaviour of fibre bridging of glass-epoxy composite under mode I static and cyclic loadings. **Journal of Composite Materials**, 23: 396-430.
- Iwamoto, M., Ni, Q.Q., Fujiwara, T., Kurashiki, K. (1999). Intralaminar fracture mechanism in uni-directional CFRP composites Part I: Intralaminar toughness and AE characteristics. **Engineering Fracture Mechanics**; 64: 721-745.

Jacobs, J.M. (2001) "Suggested guidelines for the handling of optical fibre". **Corning white paper**: WP3627.

Jian, X., Bin, M. (2010) "Experimental investigation of coupling fiber-optic sensor for vibration measurement". **In International Conference of Electrical and Control Engineering, 25-27 Jun 2010**: 936-939.

Johnson, M., Gudmundson, P. (2000) Broad-band transient recording and characterization of acoustic emission events in composite laminates. **Composite Science and Technology**, 60: 2803-2818.

Joinwit Optoelectronic Technical Co., Ltd. (date unknown). User manual for JW2101 fused bi-conical taper system. 47-48.

Kaczmarek, H., Maison, S. (1994) Comparative ultrasonic analysis of damage in CFRP under static indentation and low-velocity impact. **Composites Science and Technology**, 51: 11-26.

Kalamkarov, A.L., Fitzgerald, S.B., MacDonald, D.O., Georgides, A.V. (2000) The mechanical performance of pultruded composite rods with embedded fibre-optic sensors. **Composites Science and Technology**, 60 (8): 1161-1169.

Kersey, A.D. (1996) A Review of Recent Developments in Fibre Optic Sensor Technology. **Optical Fibre Technology**, 2: 291-317.

Kersey, A.D., Davis, M.A., Patrick, H.J., LeBlanc, M., Koo, K.P., Askins, C.G., Putnam, M.A., Friebele, J.E., (1997). Fibre grating sensors. **Journal of lightwave technology**. 15(8). pp. 1442-1463.

Kersey, A.D., Jackson, D.A., Corke, M. (1983) A Simple Fibre Fabry-Perot Sensor. **Optics Communications**, 45(2): 71-74.

Kessler, S.S. (2002a) **Piezoelectric-based in-situ damage detection of composite materials for structural health monitoring systems**. PhD Thesis, Massachusetts Institute of Technology.

Kessler, S.S., Spearing, M.S., Atalla, M.J., Cesnik, C.E.S., Soutis, C. (2002b) Damage detection in composite materials using frequency response methods. **Composites: Part B**; 33: 87-95.

Kim, I.G., Lee, H.Y., Kim, J.W. (2005) Impact damage detection in composite laminates using PVDF and PZT sensor signals. **Journal of Intelligent Material Systems and Structures**, Vol 16: 1007-1013.

Kim, J.K., Sham, L.M. (2000) Impact and delamination failure of woven-fabric composites. **Composite Science and Technology**, 60: 745-761

Kinra, V.K., Ganpatye, A.S., Maslov, K. (2005) Ultrasonic ply-by-ply detection of matrix cracks in laminated composites. **Journal of Non-Destructive Evaluation**, 25 (1): 39-51.

- Koh, Y.L., Chiu, W.K., Rajic, N. (2002) Effects of local stiffness changes and delamination on Lamb wave transmission using surface mounted piezoelectric transducers. **Composite Structures**, 57: 437-443.
- Komai, K., Minoshima, K., Shibutani, T. (1991) Investigations of the fracture mechanism of carbon/epoxy composites by AE signal analyses. **JSME International Journal**, 34.
- Konur, O., Matthews, F.L. (1989) Effect of the properties of the constituents on the fatigue performance of composites - A review. **Composites**, 20(4): 317-328.
- Kuang, K.S.C., Kenny, R. (2001) Whelan MP, Cantwell, W.J., Chalker, P.R. (2001) Embedded fibre Bragg grating sensors in advanced composite materials. **Composites Science and Technology**, 61: 1379-1387.
- Kyriazoglou, C., Le Page, B.H., Guild, F.J. (2004) Vibration damping for crack detection in composite laminates. **Composites: Part A**, 35: 945-953.
- Laffan, M.J., Pinho, S.T., Robinson, P., Iannucci, L. (2010) Measurement of the in situ fracture toughness associated with mode-I fibre tensile failure in FRP. Part II: Size and lay-up effects. **Composites Science and Technology**, 70: 614-621.
- Lee, D.C., Lee, J.J., Yun, S.J. (1995) The mechanical characteristics of smart composite structures with embedded optical fibre sensors. **Composite Structures**, 32: 39-50.
- Lee, D.G., Mitrovic, M., Friedman, A., Carman, G.P. (2002) Characterisation of fibre-optic sensors for structural health monitoring. **Journal of Composite Materials**, 36 (11): 1349-1366.
- Lee, J.R., Dhital, D., Yoon, D.J. (2011) Investigation of cladding and coating stripping methods for specialty optical fibres. **Optics and Lasers in Engineering**, 49: 324-330.
- Lee, J.R., Tsuda, H. (2005) A novel fibre Bragg grating acoustic emission sensor head for mechanical tests. **Scripta Materialia**, 53: 1181-1186.
- Lemaire, P.J., Atkins, R.M., Mizrahi, V., Reed, W.A. (1993) High pressure H<sub>2</sub> loading as a technique for achieving ultrahigh photosensitivity and thermal sensitivity in GeO<sub>2</sub> doped optical fibres. **Electron. Lett**, 29: 1191-1193.
- Liu, K., Ferguson, S.M., Measures, R.M. (1990) Interferometric sensor for the detection of acoustic emission within composite materials. **Optics Letters**, 15 (22): 1255-1257.
- Liu, T., Fernando, G.F., Rao, Y.J., Jackson, D.A., Zhang, L., Bennion, I. (1998) Simultaneous strain and temperature measurements using a multiplexed fibre Bragg grating sensor and an extrinsic Fabry-Perot sensor. **Journal of Smart Structures and Materials**, 7: 550-556.
- Lloyd, P.A. (1989) Ultrasonic system for imaging delaminations in composite materials. **Ultrasonics**, 27: 8-18.

Machavaram, V.R. (2006) **Micro-machining Techniques for the fabrication of Fibre Fabry-Perot Sensors**. PhD Thesis, Cranfield University.

Mall, S., Hsu, T.L. (2000) Electromechanical fatigue behaviour of graphite/epoxy laminate embedded with piezoelectric actuator. **Smart Materials and Structure**, 9 (1): 78-84.

Marec, A., Thomas, J.H., El Guerjouma, R. (2008) Damage characterisation of polymer-based composite materials: Multivariable analysis and wavelet transform for clustering acoustic emission data. **Mechanical Systems and Signal Processing**, 22: 1441-1464.

Marshall, D.B., Cox, B.N., Evans, A.G., (1985) The mechanics of matrix cracking in brittle-matrix fibre composites. **Acta Metall**, 33(11): 2013-2021.

Maslov, K., Kundu, T. (1997) Selection of Lamb modes for detecting internal defects in composite laminates. **Ultrasonics**, 35: 141-150.

Matthews, A.L., Murphy, K.A., Rogers, R.E., Claus, R.O. (1987) Acoustic fiber waveguide coupler. **Ultrasonics Symposium**, 629-633.

Matthewson, M.J., Kurkjian, C.R., Hamblin, J.R. (1997) Acid stripping of fused silica optical fibers with strength degradation. **Journal of Lightwave Technology**, 15: 490-497.

Mba, D., Rao, Raj, B.N.K. (2006). Development of acoustic emission technology for condition monitoring and diagnosis of rotating machines; bearings, pumps, gearboxes, engines and rotating structures. **The Shock and Vibration Digest**, 38 (1): 3-16.

Mead, D.J.(2000) *Passive vibration control*. Chichester (UK): John Wiley & Sons.

Miao, P., Kukureka, S.N., Metje, N., Chapman, D.N., Rogers, C.D.F. (2004) Mechanical properties of optical fibres for tunnel displacement monitoring in a “wet” environment. **Reliability of Optical Fibre Components, Devices, Systems and Networks II**, 5465: 80 – 83.

Miravete, A., Jimenez, M.A. (2004) Application of the finite element method to predict the onset of delamination growth. **Journal of composite materials**, 38 (15): 1309-1335.

Mistras products and systems. PAL Provides Severn River Crossing with AE Monitoring for Long-Term Evaluation of Suspension Bridge Cables [internet]. c2008 [Cited 30th December 2010]. Available from: <http://www.ndt.net/search/docs.php?id=6824&content=1>

Mix, P.E. (1987) **Introduction to non-destructive testing: A training guide**. Canada: Wiley Interscience.

Moore DR, Williams JG, (ed). (2001) **Fracture Mechanics Testing Methods for Polymers, Adhesives and Composites**. Amsterdam: Elsevier Science.

- Hagood, N. W., Crawley, E. F., de Luis, J., Anderson, E.H. (1988) “Development of integrated components for control of intelligent structures”. In **Smart materials, structures, and mathematical issues, U.S. Army Research Office Workshop; Sept 1988**. Blacksburg VA: 80-104.
- Nagata, H., Miyamoto, N., Saito, T., Kaizu, R. (1994) Reliable jacket stripping of optical fibers. **Journal of Lightwave Technology**, 12 (5): 727-729.
- Nairn, J.A., Hu, S., (1992) The initiation and growth of delaminations induced by matrix microcracks in laminated composites. **International Journal of Fracture**, 57 (1): 1-24.
- NASA Preferred Reliability Practises: Design and Manufacturing Guideline for Aerospace Composites. Guideline no. GD-ED-2205.
- Ni, Q.Q, Iwamoto, M. (2002) Wavelet transform of acoustic emission signals in failure of model composites. **Engineering Fracture Mechanics**, 69: 717-728.
- Nielson, A. (1980) Acoustic emission source based on pencil lead breaking. **The Danish Welding Institute Publication**, 90: 15.
- Ohtsu, M., Shigeishim, M., Sakata, Y. (1998) Nondestructive evaluation of defects in concrete by quantitative acoustic emission and ultrasonics. **Ultrasonics**, 36: 187-195.
- Pal, B.P., Chaudhuri, P.R., Shenoy, M.R., Kumar, N. (2006) Fused Fibre couplers: Fabrication, modelling and applications. **Guided wave optical components and Devices: Basics, Technology and Applications**: 205-223.
- Paternotte, A., Molpeceres, F., Montero de Espinosa, F.R., Carbo, R., Chinchurreta, F.J., Muriel, M.A. (1993) Acoustic-field fibre-optic sensor. **Sensors and Actuators A**, 37-38: 489-493.
- Payne, F.P., Hussey, C.D., Yataki, M.S. (1985) Modelling fused single-mode-fibre couplers. **Electronics Letters**, 21 (11): 461-462.
- Percival, W.J., Birt, E.A. (1997) A study of Lamb wave propagation in carbon-fibre composites. **Insight**, 39: 728-735.
- Perez, I.M., Cui, H.L., Udd, E. (2001) Acoustic emission detection using fiber Bragg gratings. In: **Proceedings of SPIE**, Vol.4328: 209-215.
- Physical Acoustics Ltd. (2007) PCI-2 Based AE system: Users manual 3rd rev. (USA) Princeton, New Jersey.
- Pickering, S., Almond, D. (2008) Matched excitation energy comparison of the pulse and lock-in thermography NDE techniques. **NDT&E International**, 41: 501-509.

- Pierce, S.G., Phip, W.R., Gachagan, A., McNab, A., Hayward, G., Culshaw, B. (1996) Surface-bonded and embedded optical fibres as ultrasonic sensors. **Applied Optics**, 35 (25): 5191-5197.
- Pietrzakowski, M. (2001) Active damping of beams by piezoelectric system: effects of bonding layer properties. **International Journal of Solids and Structures**, 38: 7885-7897.
- Pollock, A.A. (1967) Stress-wave emission – A new tool for industry. **Ultrasonics**, 6 (2): 88-92.
- Pollock, A.A. (1981) Acoustic Emission Amplitude Distributions. **International Advances in Nondestructive Testing**, 7: 215-239.
- Poole, P., Young, A., Ball, A.S. (1994) Adhesively bonded composite patch repair of cracked aluminium alloy. AGARD: Advisory group for aerospace research and development: Composite repair of military aircraft structures. AGARD conference proceedings 550, 3.1 – 3.12.
- Preuss, T., Clarke, G. (1988) Use of time-of-flight C-scanning for assessment of impact damage in composites. **Composites**, 19 (2): 145-148.
- Prosser, W.H., Gorman, M.R. (1992) Propagation of flexural mode AE signals in GR/EP composite plates. *In* Proceedings of the fourth international symposium on acoustic emission from composite materials. 418-427.
- Prosser, W.H., Hamstad, M.A., Gary, J., O’Gallagher, A. (1999) Reflections of AE waves in Finite Plates: Finite Element Modelling and Experimental Measurements. **Journal of Acoustic Emission**, 17, (1-2): 37-47
- Purslow, D. (1986) Matrix fractography of fibre-reinforced epoxy composites. **Composites**, 17(4): 289-303.
- Qing, X.P., Chan, H.L., Beard, S.J., Ooi, T.K., Marotta, S.A. (2006) Effect of adhesive on the performance of the piezoelectric elements used to monitor structural health. **International Journal of Adhesion and Adhesives**, 26: 622-628.
- Ramirez-Jimenez, C.R., Papadakis, N., Reynolds, N., Gan, T.H., Purnell, P., Pharaoh, M. (2004) Identification of failure modes in glass/polypropylene composites by means of the primary frequency content of the acoustic emission event. **Composites Science and Technology**, 64: 1819-1827.
- Ramulu, M., Stickler, P.B., McDevitt, N.S., Datar, I.P., Kim, D., Jenkins, M.G. (2004) Influence of processing methods on the tensile and flexure properties of high temperature composites. **Composites Science and Technology**, 64: 1763-1772.
- Read, I., Foote, P., Murray, S. (2002) Optical fibre acoustic emission sensor for damage detection in carbon-fibre composite structures. **Measurement Science and Technology**, 13: N5-N9.

Redder, J.R., Demarco, K., Whitley, K.S. (2002) "The Use of Doublers in Delamination Toughness Testing". **In Proceedings of the American Society of Composites 17th Technical Conference, Oct 21-23; Purdue University.**

Rose, J. (2004) **Ultrasonic waves in solid media**. Cambridge: Cambridge University Press.

Rotem, A. (2003) The discrimination of micro-fracture mode of fibrous composite material by acoustic emission technique. **Fibrous Science and Technology**, 10 (2): 101-121.

Russell, S.S., Henneke, E.G. (1977) Signature analysis of acoustic emission from graphite/epoxy composites. **Interim report, NASA Grant NSG 1238, Report No. VPI-E-77-22.**

Saktioto, J.A., Fadhali, M., Zainal, J. (2008) "Estimation of coupling power parameter of fused coupled fibres". **In Proceedings of SPIE**. Vol; 2008. 679309.

Santulli, C. (2000) **Impact damage evaluation in woven composites using acoustic and thermoplastic techniques**. PhD Thesis, University of Liverpool.

Schmid, S.R., Toussaint, A.F. (2007) **Optical fibre coatings, Specialty optical fibre handbook**: 95-122.

Scholey, J.J., Wilcox, P.D., Lee, C.K., Friswell, M.I., Wisnom, M.R. (2006) Acoustic Emission in Wide Composite Specimens. **Advanced Materials Research**, 13-14: 325-332.

Schuster, J., Bauer, C., Friedrich, K. (1993) Influences on signal/noise ratio during ultrasonic inspection of composites. **NDT&E International**, 26 (5): 255-260.

Seale, M.D., Smith, B.T., Prosser, W.H. (1998) Lamb wave assessment of fatigue and thermal damage in composites. **Journal of Acoustical society of America**, 103 (5): 2416-2424.

Sela, N., Ishal, O. (1989) Interlaminar fracture toughness and toughening of laminated composite materials - A review. **Composites**, 20 (5): 423-435.

Shi, Z., Ren, S., Wu, W. (2002) "High-reliable fused couplers. Optical fibre and planar waveguide technology II". **In Proceedings of SPIE**, Vol. 2904, 28-36.

Shiotani, T. (2008) Parametric AE Analysis. In: Grosse CU, Ohtsu M, (ed). **Acoustic emission testing – Basics for research: Applications in Civil Engineering**: Berlin: Springer-Verlag; Ch 4.

Short, D., Summerscales, J. (1984) Amplitude distribution acoustic emission signatures of uni-directional fibre composite hybrid materials. **Composites**, 15 (3): 200-206.

Song, G.B., Olmi, C., Gu, H. (2006) An overheight collision detection and evaluation system for bridge girder using piezoelectric transducer. In: Ou. J.P., Li. H., Duan. Z.D, (ed). **Structural health monitoring and intelligent infrastructure**, Volume 1.

Soutis, C., Curtis, P.T. (1996) Prediction of the post-impact compressive strength of CFRP laminated composites. **Composites Science and Technology**, 56: 677-684.

Steinberger, R., Valadas (), Leitao., T.I., Ladstatter, E., Pinter, G., Billinger, W., Lang, R.W. (2006) Infrared thermographic techniques for non-destructive damage characterisation of carbon-fibre reinforced polymers during tensile fatigue testing. **International Journal of Fatigue**, 28: 1340-1347.

Steiner, K.V. (1992) Defect classifications in composites using ultrasonic non-destructive evaluation techniques. In: Masters J, (ed). Damage detection in composite materials: ASTM STP 1128, American Society for testing and materials: 72-84.

Steiner, K.V., Eduljee, R.F., Huang, X., Gillespie, Jnr, J.W. (1995) Ultrasonic NDE Techniques for the Evaluation of Matrix Cracking in Composite Laminates. **Composite Science and Technology**, 53: 193-198.

Suh, K.S., Lee, C.R., Park, K.H., Park, J.W. (1991) In-situ monitoring of failure and fracture mechanisms in carbon fiber/epoxy composite by an optical fibre sensor. **Polymer (Korea)**, 16: 15-21.

Suhir, E., (1992). Vibration frequency of a fused biconical taper (FBT) lightwave coupler. **Journal of Lightwave technology**, 10(7), pp. 898-902.

Sun, L., Li, H.N., Ren, L., Jin, Q. (2007) Dynamic response measurement of offshore platform model by FBG sensors. **Sensors and Actuators A**, 136: 572-579.

Surgeon, M., Wevers, M. (1999) Modal analysis of acoustic emission signals from CFRP laminates. **NDT&E International**, 32(6): 311-322.

Suzuki, M., Kida, S., Shimbo, M., Miyano, Y. (1991) "Effects of fiber content on fracture mechanisms of short fiber reinforced PET composites". In Proceedings of the 8th International conference on Composite materials. Vol 3.

Suzuki, M., Nakanishi, H., Iwamoto, M., Jinen, E. (1988) "Application of static fracture mechanisms to fatigue fracture behaviour of class A-SMC composite". In **Proceedings of the 4th Japan-US conference on composite material, Japan**. 297-306.

Takeda, N., Okabe, Y., Kuwahara, J., Kojima, S., Ogisu, T. (2005) Development of smart composite structures with small-diameter fibre Bragg grating sensors for damage detection: Quantitative evaluation of delamination length in CFRP laminates using Lamb wave sensing. **Composites Science and Technology**, 65: 2575-2587.

Takeuchi, Y. (1996) Thermodynamic analysis of WDM fibre couplers fabricated by using a microheater. **Journal of Non-Crystalline Solids**, 202: 272-278.

Tarpey, J., Kukureka, S.N., Jurkschat, K. (2002) The mechanical reliability of stripped and recoated polyimide fibres for optical fiber sensors. **Optical Fiber and Fiber Component Mechanical Reliability and Testing**, 4639: 141-151.

Teti, R. and Alberti, N. (1990) Ultrasonic identification and measurements of defects in composite material laminates. **Annal of the CIRP**, 39: 527-530.

Theobald, P. (2011) Guide on Acoustic Emission Sensor Couplants. NPL Report [internet] [cited 23rd June 2011]. Available from: <http://www.npl.co.uk/acoustics/ultrasound/research/guide-on-acoustic-emission-sensor-couplants>.

Theobald, P., Zeqiri, B., Avison, J. (2008) Couplants and their influence on AE sensor sensitivity. **J. Acoustic Emission**, 26: 91-97.

Thursby, G., Culshaw, B., Botsev, Y., Arad, E., Zeyde, R., Tur, M., Kressel, I. (2008) "The use of Fibre Bragg Gratings to Detect Ultrasound in Anisotropic Materials". In **Proceedings of SPIE: Smart Sensor Phenomena, Technology, Networks and Systems, March; San Diego, CA**.

Toyama, N., Koo, J.H., Oishi, R., Enoki, M., Kishi, T. (2001) Two-dimensional AE source location with two sensors in thin CFRP plates. **Journal of Material Science Letters**, 20: 1823-1825.

Tsuda, H., Ikeguchi, T., Takahashi, J., Kemmochi, K. (1998) Damage Monitoring of Carbon-fibre Reinforced Plastics using Michelson Interferometric Fibre-optic Sensors. **Journals of Material Science Letters**, 17: 503-506.

Tsuda, H., Koo, J-H., Kishi, T. (2001) Detection of simulated acoustic emission with Michelson interferometric fibre-optic sensors. **Journal of Materials Science Letters**, 20: 55-56.

Tsuda, H., Takahashi, J., Urabe, K., Ikeguchi, T. (1999) Damage monitoring of carbon-fibre-reinforced plastics with Michelson interferometric fibre-optic sensors. **Journal of Materials Science**, 34: 4163-4172.

Tsuda, H., Toyama, N., Urabe, K., Takatsubo, J. (2004) Impact damage detection in CFRP using fibre Bragg gratings. **Smart Materials and Structures**, 13: 719-724.

Valentin, D., Bonniau, P.H., Bunsell, A.R. (1983) Failure mechanism discrimination in carbon-fibre reinforced epoxy composites. **Composites**, 14 (4): 345-351.

Van Otterloo, D.L., Dayal, V. (2003) How isotropic are quasi-isotropic laminates. **Composites: Part A**, 34: 93-103.

Viktorov, I. (1967) **Rayleigh and Lamb waves**. New York: Plenum Press.

Waller, J.M., Saulsberry, R.L., Andrade, E. (2010) The use of acoustic emission to monitor progressive damage accumulation in Kevlar 49 composites: Nasa Technical Report Server [internet] c2010 [cited 16th August 2010]. Available from: [http://ntrs.nasa.gov/archive/nasa/casi.ntrs.nasa.gov/20090026552\\_2009026831.pdf](http://ntrs.nasa.gov/archive/nasa/casi.ntrs.nasa.gov/20090026552_2009026831.pdf).

Wei, C.T., Ye, C.C., James, S.W., Tatam, R.O., Irving, P.E. (2001) "An experimental approach to quantify strain transfer efficiency of fibre Bragg grating sensors to host structures". **In The 13th International Conference on Composite Materials: ICCM-13. Beijing, 25-29 Jun 2001.**

Whittingham, B., Li, H.C.H., Herszberg, I., Chiu, W.K. (2006) Disbond Detection in Adhesively Bonded Composite Structures using Vibration Signatures. **Composite Structures**, 75: 351-363.

Wong, B. et. al. (1999) Thermographic evaluation of defects in composite materials. **Insight**, 41(8): 504-509.

Xie, T. (1991) "Fused 3x3 single-mode fibre optic couplers for fibre interferometric sensors and coherent communications". **In Proceedings of the 41st Electronic Components & Technology Conference; 11-16 May; Atlanta, GA.**

Yo, Y.L., Sirkis, J.S. (1994) Active Homodyne Demodulation of Mach-Zehnder Interferometric Optical Fiber Sensors. **Experimental Techniques**, 18 (6): 33-36.

Zhang, J., Fox, B. (2005) "Manufacturing process effects on the mode-I interlaminar fracture toughness and nanocreep properties of CFRP. SAMPE Europe". **In Proceedings of the 26th International SAMPE Europe Conference - Nanotechnology Assists Leadership and Success of the Composite Technology; 5-7 April 2005. Paris.**

Zhao, J-H, Shi, Y-K, Shan, N., Yuan, X-Q. (2008) Stabilized fiber-optic extrinsic Fabry-Perot sensor system for acoustic emission measurement. **Optics & Laser Technology**, 40: 874-880.

Zheng, S.X., McBride, R., Barton, J.S., Jones, D.C., Hale, K.F., Jones, B.E. (1992) Intrinsic optical fibre sensor for monitoring acoustic emission. **Sensors and Actuators A**, 31: 110-114.

## Appendices

---

### Appendix-A: Theory of the Fibre-Optic AE Sensor

#### A.1 Strain-Optics Theory

Equations (12) to (17) illustrate derivation of equations that define the change in refractive index as a function of applied strain. Equation (12) illustrates the change in the optical indicatrix  $\left(\frac{1}{n^2}\right)_i$  in the presence of applied strain.

$$\Delta\left(\frac{1}{n^2}\right)_i = \sum_{j=1}^6 P_{ij}S_j \quad \text{Eq. 12}$$

With reference to equation (12),  $P_{i,j}$  are defined as Pockel's co-efficient for the strain-optic tensor (Kersey et al. 1997). As the fibre is isotropic, the strain-optic tensor is expressed using the matrix in equation (13).

$$P_{ij} = \begin{bmatrix} P_{11} & P_{12} & P_{12} & 0 & 0 & 0 \\ P_{12} & P_{11} & P_{12} & 0 & 0 & 0 \\ P_{12} & P_{12} & P_{11} & 0 & 0 & 0 \\ 0 & 0 & 0 & P_{44} & 0 & 0 \\ 0 & 0 & 0 & 0 & P_{44} & 0 \\ 0 & 0 & 0 & 0 & 0 & P_{44} \end{bmatrix} \quad \text{Eq. 13}$$

The strain vector,  $S_j$ , as a function on an applied longitudinal strain is given in equation (14).

$$S_j = \begin{bmatrix} \varepsilon \\ -\nu\varepsilon \\ -\nu\varepsilon \\ 0 \\ 0 \\ 0 \end{bmatrix} \quad \text{Eq. 14}$$

With reference to equation (14), the strain in the transverse direction, i.e. around the fibre diameter is related to the longitudinal strain using Poisson's ratio,  $\nu$ . Equation (15) is derived from solving equations (12), (13) and (14); this assumes no shear strain.

$$\Delta \left( \frac{1}{n^2} \right)_{2,3} = \varepsilon(1 - \nu)P_{12} - \nu\varepsilon P_{11}. \quad \text{Eq. 15}$$

Equation (16) (Butter and Hocker, 1978) illustrates the relationship between a change in the refractive index ( $\Delta n$ ) and a change in the indicatrix.

$$\Delta \left( \frac{1}{n^2} \right)_{2,3} = -2 \frac{\Delta n}{n^3}. \quad \text{Eq. 16}$$

The change in the refractive index as a function of applied longitudinal strain is expressed in equation (17).

$$\begin{aligned} \Delta n &= -\frac{1}{2} n^2 \Delta \left( \frac{1}{n^2} \right) \left( \frac{1}{n^2} \right)_{2,3} \\ &= -\frac{1}{2} n^3 [\varepsilon(1 - \nu)P_{12} - \nu\varepsilon P_{11}]. \end{aligned} \quad \text{Eq. 17}$$

## A.2 Strain-Optic Effect: Fused-tapered Coupler

The change in coupling ratio as a function of applied strain can be related closely to the elasto-optic effect within the fused-tapered coupler. For a fused-tapered coupler with a coupling ratio of 50:50, the output powers are nominally equal. The corresponding output powers from the two fibres can be expressed as follows.

$$P_1(l) = P_0 \left\{ 1 - \sin^2 \left[ \int_0^l C(z) dz \right] \right\} \quad \text{Eq. 18}$$

$$P_2(l) = P_0 \sin^2 \left[ \int_0^l C(z) dz \right] \quad \text{Eq. 19}$$

where  $P_0$  represents the optical power launched into the coupler and  $P_1(l)$  and  $P_2(l)$  are the optical powers from the output fibres of the coupler.  $C(z)$  refers to the coupling coefficient and  $l$  is the length of the coupling region. With reference to equations (18) and (19),  $P_0 = P_1(l) + P_2(l)$ . The coupling ratio of the fibre coupler can be expressed as follows.

$$\eta = P_2(l) / [P_1(l) + P_2(l)] \quad \text{Eq. 20}$$

Equations (18) and (19) can therefore be rewritten.

$$P_1(l) = \{1 - \eta\} P_0 \quad \text{Eq. 21}$$

$$P_2(l) = \eta P_0 \quad \text{Eq. 22}$$

Where  $\eta = \eta_0 + \Delta\eta$ ;  $\eta_0$  refers to the coupling ratio prior to application of axial strain and  $\Delta\eta$  is the change in the coupling ratio due to applied strain ( $\epsilon$ ). According to Booyesen et al.

(1991),  $\eta_0$  and  $\Delta\eta$  are finite and differentiable respectively. This analytic function can be expanded in the form of a Taylor series in the vicinity of  $\varepsilon = \varepsilon_0$  and is expressed as follows.

$$\eta - \eta_0 = \Delta\eta(\varepsilon) = \sum_{m=0}^{\infty} \frac{1}{m!} \frac{\partial^m \eta(\varepsilon_0)}{\partial \varepsilon^m} \varepsilon^m \quad \text{Eq. 23}$$

In the expanded form,  $\Delta\eta(\varepsilon)$  can be expressed as.

$$\Delta\eta(\varepsilon) = \frac{\partial \eta(\varepsilon_0)}{\partial \varepsilon} \varepsilon + \frac{1}{2!} \frac{\partial^2 \eta(\varepsilon_0)}{\partial \varepsilon^2} \varepsilon^2 + \frac{1}{3!} \frac{\partial^3 \eta(\varepsilon_0)}{\partial \varepsilon^3} \varepsilon^3 + \dots \quad \text{Eq. 24}$$

In respect of a linear relationship between strain ( $\varepsilon$ ) and the strain induced change in coupling ratio ( $\Delta\eta(\varepsilon)$ ), equation (24) can be re-written as.

$$\Delta\eta(\varepsilon) = \alpha(\varepsilon)\varepsilon \quad \text{Eq. 25}$$

where:

$$\alpha(\varepsilon) = (\alpha_0 + \beta_0\varepsilon + \gamma_0\varepsilon^2 \dots \dots) \quad \text{Eq. 26}$$

and:

$$\alpha_0 = \frac{\partial \eta(\varepsilon_0)}{\partial \varepsilon} \quad \text{Eq. 27}$$

$$\beta_0 = \frac{1}{2!} \frac{\partial^2 \eta(\varepsilon_0)}{\partial \varepsilon^2} \quad \text{Eq. 28}$$

$$\gamma_0 = \frac{1}{3!} \frac{\partial^3 \eta(\varepsilon_0)}{\partial \varepsilon^3} \quad \text{Eq. 29}$$

For small strains applied to the coupler, equation (30) applies.

$$\alpha(\varepsilon) \approx \alpha_0 \quad \text{Eq. 30}$$

Generally,  $\alpha$  can be a function of strain ( $\varepsilon$ ), coupling ratio ( $\eta_0$ ) before the application of strain and the power-cross points ( $m$ ) at the point where the fibre coupler fabrication process was terminated. The change in the coupling ratio due to applied strain can be expressed as follows.

$$\Delta\eta(\varepsilon) = \alpha(m, \eta_0, \varepsilon)\varepsilon \quad \text{Eq. 31}$$

Booyesen et al. (1993) discussed a model that could be applied to evaluate the performance of a weakly-fused biconically tapered coupler subjected to axial strain. With reference to Figure 97, the coupling ratio can be expressed as per equation (32).

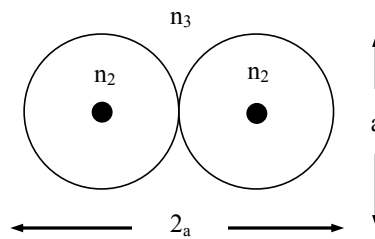


Figure 97 A schematic illustration of a weakly-fused coupler cross-section.

$$C_0 = \frac{1}{2} [1 + \cos((K_x + K_y)L) \cos((K_x - K_y)L)] \quad \text{Eq. 32}$$

Where:

$$K_x + K_y = \frac{2^{\frac{7}{2}}(n_2^2 - n_3^2)^{\frac{1}{2}}U_\infty^2}{n_2 a \sqrt{\pi V^2}} \quad \text{Eq. 33}$$

$$K_x - K_y = \frac{2^{\frac{5}{2}}(n_2^2 - n_3^2)^{\frac{1}{2}}U_\infty^2}{n_2^3 a \sqrt{\pi V^2}} \quad \text{Eq. 34}$$

and:

$$V = \frac{2\pi a}{\lambda} (n_2^3 - n_3^2)^{\frac{1}{2}} \quad \text{Eq. 35}$$

With reference to equations (32) to (35):  $C_0$  is the coupling ratio,  $l$  and  $a$  are the length and diameter of the coupling region respectively,  $K_x$  and  $K_y$  are the coupling coefficients of the two orthogonal polarisation states in the fibre,  $n_2$  and  $n_3$  are the refractive indices of the cladding and potting compounds respectively,  $\lambda$  defines the wavelength and  $U_\infty = 2.405$ . The refractive index of the core was neglected in this model owing to the small dimensions of the core after tapering. Applied strain results in a change in the refractive index of the fibre cladding. The expression used to define this relationship is provided in equation (36).

$$\frac{1}{n_{2e}^2} = \frac{1}{n_2^2} + \rho \epsilon \quad \text{Eq. 36}$$

$n_{2e}$  describes the refractive index as a result of the elastic-optic effect and  $\rho$  defines the strain-optic coefficient; for fused silica fibres, a value of 0.27 is given. Chen et al. (2003) further propose that the equations describing the response of the coupler to applied strain can be simplified if the assumption is made that the coupling region is at the centre of the taper, i.e.

in a region of constant cross section. As such, Poisson's contraction can be neglected. The simplified equation providing the relationship between applied strain on the coupling region and the change in the coupling ratio of the coupler is as follows.

$$\frac{d\eta}{d\varepsilon} = -\frac{1}{2}(T\sin P\cos Q + U\cos P\sin Q) \quad \text{Eq. 37}$$

where:

$$P = (K_x + K_y)L \quad \text{Eq. 38}$$

$$Q = (K_x - K_y)L \quad \text{Eq. 39}$$

$$T = \frac{dP}{d\varepsilon} = P \left\{ 1 + \frac{\rho\eta_{2e}^2}{2} \left[ 1 + \frac{1.5n_{2e}^2}{(n_{2e}^2 - n_3^2)} \right] \right\} \quad \text{Eq. 40}$$

$$Q = \frac{dQ}{d\varepsilon} = Q \left\{ 1 + \frac{\rho\eta_{2e}^2}{2} \left[ 3 + \frac{2.5n_{2e}^2}{n_{2e}^2 - n_3^2} \right] \right\} \quad \text{Eq. 41}$$

### A.3 Magnification of the mechanical strain effect

Analysis of the strain effect in the fused-tapered coupler was evaluated with respect to both longitudinal and transverse stresses. A model, proposed by Suhir (1992), was used to describe the relationship between the strain effects in the coupler as a function of coupler geometry. With reference to Figure 98, the proposed model assumes that the cross-section of the fibre coupler and the taper transitions either side of the narrow waist region have a constant radius of curvature; this allows for simplification of the model whereby the taper region is treated as a cylindrical rod with a varying radius. Moreover, with reference to conventional beam theory, the model assumes that the coupler is fixed at each end.

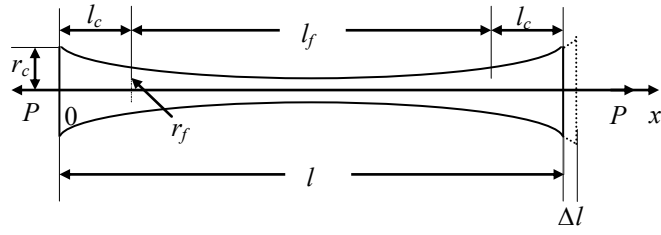


**Figure 98** A schematic illustration of the simplified waist region of a fused-tapered coupler.

The stress distribution acting along the sensing region, i.e. the fibre taper, varies due to the difference in cross-sectional area. The stress  $\sigma(x)$  in any cross section ( $x$ ) if the coupler can be evaluated using the following expression.

$$\sigma(x) = \frac{P}{\pi r^2(x)} = \sigma_f \frac{r_f^2}{r^2(x)} \quad \text{Eq. 42}$$

where  $r_f$  is the radius of the fused mid-portion,  $\sigma_f = P/\pi r_f^2$  is the stress in that portion.  $r(x)$  of the couplers cross-section is defined as.

$$r = \begin{cases} r_c - (r_c - r_f) \frac{x}{l_c}, & 0 \leq x \leq l_c \\ r_f, & l_c \leq x \leq l_c + l_f \\ r_c - (r_c - r_f) \frac{l-x}{l_c}, & l_c + l_f \leq x \leq l \end{cases} \quad \text{Eq. 43}$$

With reference to equation (43),  $l$ ,  $l_c$  and  $l_f$  refer to the total length of the coupler, the length of a single conical region and the length of the fused mid-portion respectively. The origin of the coordinate  $x$  is at the left side of the coupler. For tensile strains not exceeding the 5% of the elastic behaviour for silica fibres, the stress-strain relationship can be expressed as.

$$\sigma = E_0 \varepsilon \left( 1 + \frac{1}{2} \alpha \varepsilon \right) \quad \text{Eq. 44}$$

Here  $\zeta$  is the stress,  $\varepsilon$  is the strain,  $E_0$  is the Young's modulus of silica at low strains and  $\alpha$  is the parameter of non-linearity. For silica,  $E_0 = 72$  GPa and  $\alpha = 6$ .

Using equation (44), the strain in the fibre can be expressed as follows.

$$\varepsilon = \frac{1}{\alpha} \left( \sqrt{1 + 2\alpha \frac{\sigma}{E_0}} - 1 \right) = \frac{1}{\alpha} \left( \sqrt{1 + \beta^2 \frac{r_f^2}{r^2}} - 1 \right) \quad \text{Eq. 45}$$

$$\text{where: } \beta^2 = 2\alpha \frac{\sigma_f}{E_0} = 2\alpha \frac{P}{\pi E_0 r_f^2} \quad \text{Eq. 46}$$

With reference to equation (45), the overall elongation of the coupler can be calculated. The expression used to define  $\Delta l$  is as follows.

$$\Delta l = \int_0^l \varepsilon(x) dx = \frac{1}{\alpha} \left( \int_0^l \sqrt{1 + \beta^2 \frac{r_f^2}{r^2}} dx - l \right) \quad \text{Eq. 47}$$

The integral of equation (47) can be expressed as:

$$\begin{aligned} \int_0^l \sqrt{1 + \beta^2 \frac{r_f^2}{r^2}} dx &= 2 \int_0^{l_c} \sqrt{1 + \beta^2 \frac{r_f^2}{r^2}} dx + \sqrt{1 + \beta^2} l_f \\ &= 2f_c l_c + f_f l_f \end{aligned} \quad \text{Eq. 48}$$

where:

$$f_c = \frac{1}{l_c} \int_0^{l_c} \sqrt{1 + \beta^2 \frac{r_f^2}{r^2}} dx \quad \text{Eq. 49}$$

$$f_f = \sqrt{1 + \beta^2} \quad \text{Eq. 50}$$

Using equations (49) and (50), the equation (51) can be defined which can be used to evaluate the strain  $\Delta l/l$  in the coupler as a function of a specified force  $P$ .  $\rho$  refers to the radii ratio where  $\rho = r_f/r_c$ .

$$\frac{\Delta l}{l} = \frac{1}{\alpha} \left[ \frac{2l_c}{l} f_c(\beta, \rho) + \frac{l_f}{l} f_f(\beta) - 1 \right] \quad \text{Eq. 51}$$

Using the above equation, Suhir (1992) showed that for a low overall strain acting on the coupler, the strain in the mid-portion of the taper was significantly higher. Chen et al. (2003) further proposed that for small strains, the expression presented in equation (52) can be simplified to.

$$\sigma(x) = E_0 \varepsilon(x) \quad \text{Eq. 52}$$

Using equations (42) and (52), the relationship between strain ( $\varepsilon$ ) and the radius of the couplers cross-section ( $r(x)$ ) for a specified effective force ( $P$ ) is as per equation (53).

$$\varepsilon(x) = \frac{P}{\pi E_0 r^2(x)} \quad \text{Eq. 53}$$

Using equation (53), Chen et al. (2003) demonstrated that the measured strain increased as the radius of the couplers cross-section reduced; the authors also proposed that sensors with a

large taper angle will also present high sensitivity. From the results presented by Suhir (1992) and Chen et al. (2003), it is proposed that the tapered region of the coupler acts as a stress-raiser and therefore this region would provide the highest sensitivity to acoustic perturbations.

Chen et al. (2003) further demonstrated the effect of transverse stresses acting on the coupling region. The authors demonstrated that these stresses result in an increased strain at the coupling region of the sensor. An additional model was presented; for simplicity, the fused-tapered coupler can be considered as a beam clamped at each end. When the flexural acoustic wave interacts with the coupler, the “beam” vibrates along the transverse direction (see Figure 99).

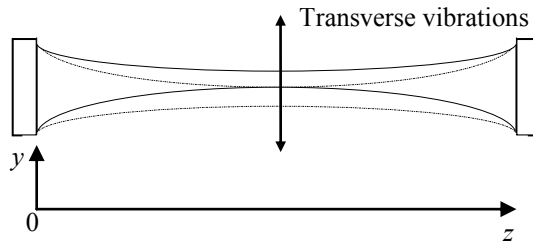


**Figure 99 A schematic illustration of transverse beam vibration.**

The Euler equation for transverse beam vibration is as follows.

$$\frac{\partial^2}{\partial z^2} \left[ EI(z) \frac{\partial^2 y(z, t)}{\partial z^2} \right] + \rho_l(z) \frac{\partial^2 y(z, t)}{\partial t^2} = F(t) \quad \text{Eq. 54}$$

Where the following notation is used:  $EI$  represents the Young’s modulus of elasticity,  $I(z)$  is the moment of inertia,  $\rho_l$  is the linear density,  $F(t)$  is the effective force acting on the coupling

region and  $y(z,t)$  is the transverse beam displacement. Assuming isotropic beam properties, simplification of equation (54) provides the following expression.

$$EI \frac{\partial^4}{\partial z^4} y(z, t) + p_l(z) \frac{\partial^2}{\partial t^2} y(z, t) = F(t) \quad \text{Eq. 55}$$

Using the separation of variable method and attempting the solution of the following:

$$y(z, t) = \sum_{n=1}^{\infty} \psi_n(z) \xi_n(t) \quad \text{Eq. 56}$$

Where  $\psi_n(z)$  represents the mode shape of the beam and  $\xi_n(t)$  represents the modal amplitude. The strain experienced by the fibre coupler when subjected to transverse stresses can be expressed as follows.

$$\varepsilon(z, t) = \frac{\partial^2 y(z, t)}{\partial z^2} \quad \text{Eq. 57}$$

$y(z,t)$  denotes the deflection of the beam away from the point of equilibrium.

According to equations (54) to (57), transverse vibrations result in strain along the length of the coupling region which results in a change in the coupling ratio of the sensor. The authors note that the coupling region is subjected to an elongation which can be calculated by integrating the strain along the coupling region.

A.4 The effect of an acoustic-wave on the optical response of the fused-tapered coupler.

The basic optical performance of a fused-tapered coupler and the effects of sensor geometry on the sensing response have been discussed. Whilst the refractive index change due to the elastic-optic effect will result in a variation in the coupling coefficient, the change in the coupling length of the sensing region was found to contribute the largest effect on the coupling ratio and power output ratio change in the coupler (Chen et al., 2004). The theoretical basis for the power output ratio change from the interaction of an acoustic wave is presented in equations (58) to (68) (Chen et al., 2004).

For a stable fused-tapered coupler with a coupling ratio of 50:50, the optical power outputs from  $P_1$  and  $P_2$  (see Figure 8, Section 2.4.5) relative to the input power  $P_0$  are expressed as follows.

$$P_1 = P_2 = P_0 / 2 \text{ and } \sin^2 \left\{ \int_0^L C(z) dz \right\} = \cos^2 \left\{ \int_0^L C(z) dz \right\} = 1/2 \quad \mathbf{Eq. 58}$$

where  $P_1$  and  $P_2$  are the optical intensities of the output ports,  $P_0$  is the input power,  $z$  is the refractive index of the fibre, and  $C(z)$  is the coupling coefficient. For a dynamic strain  $\varepsilon(z,t)$  along the length of the coupling region due to the perturbation from an acoustic wave, the optical output from each port ( $P_1$  and  $P_2$ ) can be expressed as:

$$P_1(l, t) = P_0 \cos^2 \left\{ \int_0^l C(z) [1 + \varepsilon(z, t)] dz \right\} \quad \text{Eq. 59}$$

$$P_2(l, t) = P_0 \sin^2 \left\{ \int_0^l C(z) [1 + \varepsilon(z, t)] dz \right\} \quad \text{Eq. 60}$$

For a sinusoidal acoustic wave, equation (61) applies, where  $\Lambda$  is the wavelength and  $f$  is the frequency of the acoustic wave (Birks et al., 1996):

$$\varepsilon(z, t) = \varepsilon_0(z) \cos\left(\frac{2\pi}{\Lambda} z - 2\pi ft\right) \quad \text{Eq. 61}$$

The effective strain amplitude,  $\varepsilon_0(z)$ , is dependent on acoustic power, material properties and the diameter of the coupling region:

$$\varepsilon_0(z) = \frac{F}{\pi E_0 r^2(z)} \quad \text{Eq. 62}$$

The coupling coefficient  $C(z)$  is highest in the narrow waist region of the sensor. Therefore a minimum coupling region diameter is necessary to provide high sensitivity since the tapered region acts as a strain-concentrator. Using Equations (59) to (62), the power outputs from either port can be expressed as:

$$\left\{ \begin{array}{l} P_1(l, t) = P_0 \cos^2 \left\{ \int_0^l C(z) dz + \int_0^l \varepsilon_0 C(z) \times \cos\left(\frac{2\pi}{\Lambda} z - 2\pi ft\right) dz \right\} \\ P_2(l, t) = P_0 \sin^2 \left\{ \int_0^l C(z) dz + \int_0^l \varepsilon_0 C(z) \times \cos\left(\frac{2\pi}{\Lambda} z - 2\pi ft\right) dz \right\} \end{array} \right. \quad \text{Eq. 63}$$

Assuming the coupling ratio of the sensor is 50:50, equation (63) can be re-written using trigonometric functions to express the change in the output powers due to the interaction of an acoustic perturbation on the sensing region:

$$\begin{cases} \Delta P_1(l, t) = P_1(l, t) - \frac{1}{2} P_0 = -\frac{1}{2} P_0 \sin \left[ \int_0^l 2\varepsilon_0 C(z) \cos \left( \frac{2\pi}{\Lambda} z - 2\pi f t \right) dz \right] \\ \Delta P_2(l, t) = P_2(l, t) - \frac{1}{2} P_0 = \frac{1}{2} P_0 \sin \left[ \int_0^l 2\varepsilon_0 C(z) \cos \left( \frac{2\pi}{\Lambda} z - 2\pi f t \right) dz \right] \end{cases} \quad \text{Eq. 64}$$

Equation (64) can be expanded in the form of a Taylor series in the vicinity of  $\varepsilon_0 = 0$ . The higher order terms are thus neglected:

$$\begin{cases} \Delta P_1(l, t) = -\frac{1}{2} P_0 \int_0^l 2\varepsilon_0 C(z) \cos \left( \frac{2\pi}{\Lambda} z - 2\pi f t \right) dz \\ \Delta P_2(l, t) = \frac{1}{2} P_0 \int_0^l 2\varepsilon_0 C(z) \cos \left( \frac{2\pi}{\Lambda} z - 2\pi f t \right) dz \end{cases} \quad \text{Eq. 65}$$

However, it is assumed that  $C(z) = \bar{C}$  is the average over the coupling region. Integration of equation (65) provides the outputs of each fibre in a simpler form:

$$\begin{cases} \Delta P_1(l, t) = -P_0 \bar{C} \varepsilon_0 l \left[ \frac{\sin(\pi l / \Lambda)}{\pi l / \Lambda} \right] \cos \left( \frac{\pi l}{\Lambda} - 2\pi f t \right) \\ \Delta P_2(l, t) = P_0 \bar{C} \varepsilon_0 l \left[ \frac{\sin(\pi l / \Lambda)}{\pi l / \Lambda} \right] \cos \left( \frac{\pi l}{\Lambda} - 2\pi f t \right) \end{cases} \quad \text{Eq. 66}$$

In conclusion, the operating principle for the sensor is to monitor the output power variation at  $P_1$  and  $P_2$ . The differential of the two can be obtained by:

$$\Delta P = P_2 - P_1 \quad \text{Eq. 67}$$

With reference to equation (67), the coupler response can be expressed as:

$$\Delta P(l, t) = 2P_0 \bar{C} \varepsilon_0 l [\sin(\pi l / \Lambda) / (\pi l / \Lambda)] \cos\left(\frac{\pi l}{\Lambda} - 2\pi f t\right) \quad \text{Eq. 68}$$

With reference to equation (68), the term  $(\frac{\pi l}{\Lambda}) / (\frac{\pi l}{\Lambda})$  represents the relationship between: (i) the coupling ratio variation, the length of the coupling region, and the acoustic frequency or wavelength.

## Appendix-B: Autoclave Processing

### B.1 Autoclave Details

A conventional autoclave (99/20; Leeds and Bradford Boiler Company UK) was used for processing the laminated prepregs throughout the duration of the project. The autoclave was equipped with temperature, vacuum and pressure control capabilities. The dimension of the autoclave chamber was 750 mm (diameter) x 2000 mm (length). A carbon-fibre tooling plate was used for the production of the composite specimens. The autoclave was computer-controlled via a personal computer which used a commercially available software package (SV32 Version 2; Specview Ltd, UK). A photograph of the autoclave is presented in Figure 100.



**Figure 100** A photograph of the autoclave that was used for processing the laminated prepregs.

## B.2 Prepregs

A VTM 264 (Advanced Composites Group, UK) variable curing pre-impregnated (prepreg) material was used in this project. The prepreg was a T700S (24K) 300 g/m<sup>2</sup> unidirectional carbon/epoxy material. The VTM prepreg was a general purpose variable temperature moulding material. The cure schedule used to process the laminated prepregs is provided in Table 30. The prepregs were stored in a chest freezer at a temperature of -18 °C in sealed polyethylene bags. Silica gel was placed inside the sealed bags to absorb any moisture. The freezer temperature was routinely monitored to confirm correct storage conditions. Prior to use, the material was removed from the freezer and allowed to thaw for a period of 6 hours. This procedure was performed to equilibrate the prepreg to ambient temperature.

**Table 30 Details of the programmed processing schedule for the VTM264 prepregs**

TEMPERATURE CONTROL					PRESSURE CONTROL				
Profile segment	Ramp rate (°C/minute)	Target temperature (°C)	Time (mins)	Cycle end command	Profile segment	Ramp rate (MPa/minute)	Target pressure (MPa)	Time (mins)	Vacuum command
1	2	65		On	1	0.007	0.007		On
2			1.0	On	2			20	On
3	2	120		On	3	0.021	0.138		On
4			60.0	On	4			1	Off
5	2	50		On	5	0.021	0.482		Off
6			2.0	On	6			67	Off
7	1	25		Off	7	0.014	0		On

### B.3 Lay-up Procedure

Once the prepreg had been allowed to equilibrate to room temperature, the material was cut to the required specimen dimensions using a craft knife. Prior to lamination, each prepreg layer was laid flat to avoid fibre warping. During lamination, each layer was consolidated using a wooden roller to expel entrapped air. An aluminium set-square was secured to the table-top as a reference for the alignment of the plies. A vacuum plate was fabricated to further aid with prepreg alignment during the lamination stage of processing. The plate was fabricated using two acrylic polymer plates with dimensions 300 (*w*) x 300 (*l*) x 5 (*d*) mm. The two plates were fixed together using a double layer of vacuum tape along all four edges. Equally spaced 1 mm holes were machined throughout the bottom plate to enable a vacuum to be drawn onto the pre-cut material. A 30 mm hole was machined in the centre of the upper plate to allow for a vacuum cleaner hose to be attached. Metal handles were attached to the upper face of the top plate for handling convenience. A schematic illustration of the vacuum plate is presented in Figure 101.

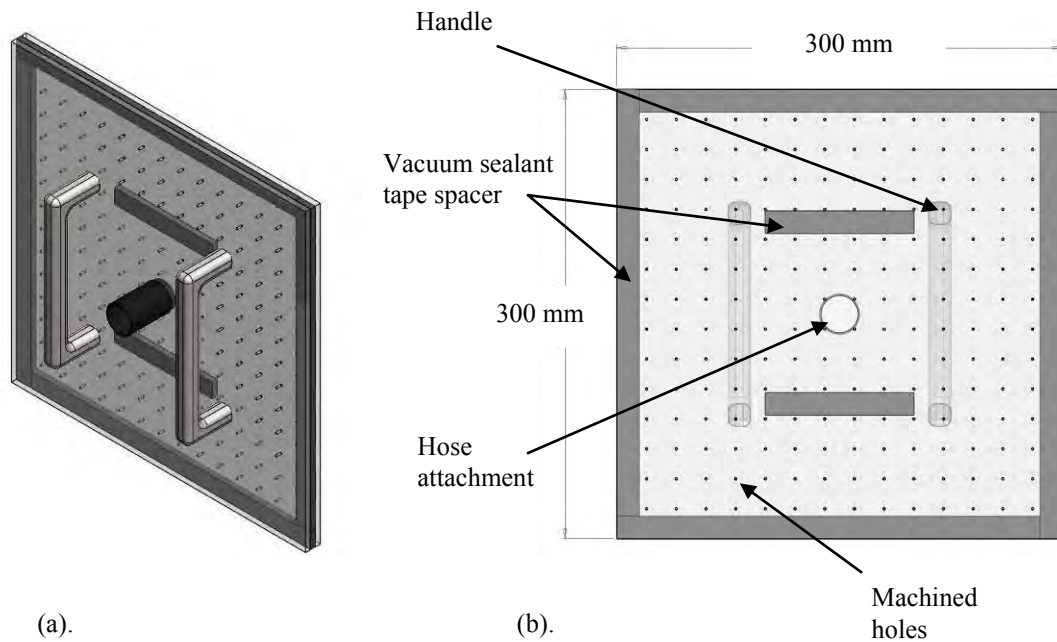


**Figure 101 Schematic illustrations of the vacuum plate that was used for assisting with the alignment and stacking of the prepreg lay-up: (a) trimetric view; and (b) rear view.**

#### B.4 Vacuum Bagging

Composite specimens were fabricated using a conventional vacuum bagging procedure and processed according to the manufacturers recommended cure schedules (see Table 30). The vacuum bagging procedure is illustrated in Figure 102. All the consumables used in this process were supplied by Amber Composites Ltd, UK. The main components used in the vacuum bagging procedure highlighted in Figure 102 are described in Table 31 below.

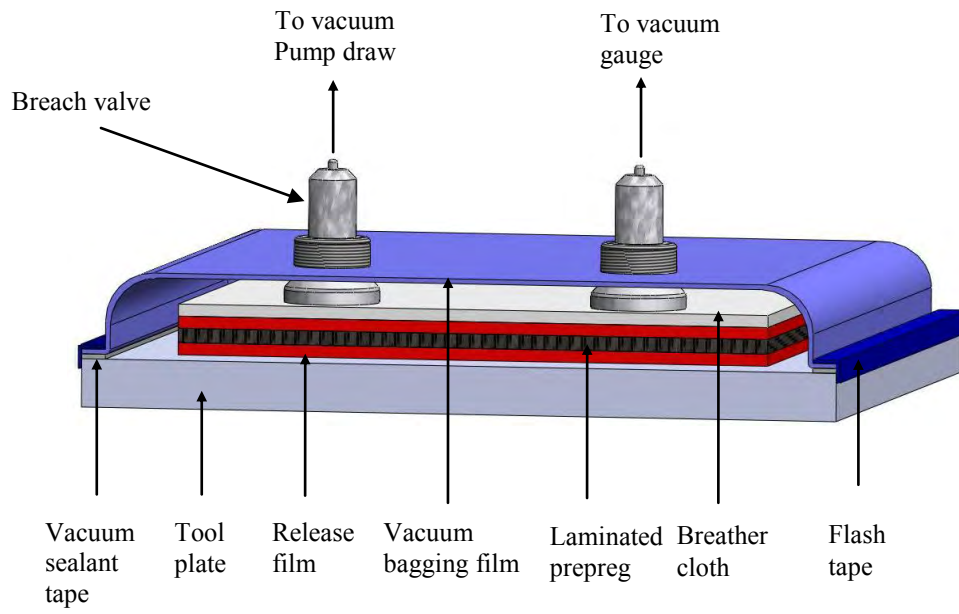


**Figure 102 A schematic representation of the vacuum bagging assembly (not to scale).**

**Table 31 Descriptions of the components used for processing the prepregs in the autoclave.**

<b>Component</b>	<b>Description</b>
Breach valves	Two screw-lock breach valves were required for the purpose of: (i) drawing vacuum on the bagged composite; and (ii) monitoring the degree of vacuum during cure. The breach valves were connected to ports on the inside wall of the autoclave chamber.
Tool plate	A woven carbon-fibre composite plate with dimensions (600 x 2000 x 10 mm) was used for composite processing.
Release film	A layer of FEP fluoropolymer release film (VAClease20R1.2) was positioned above and the below the prepreg stack during processing to avoid adhesion of the specimen to the tool plate and breather cloth.
Breather cloth	A layer of needled polyester breather cloth (VAC B 4) was positioned onto the top layer of the release film. The purpose of the breather cloth was to enable air and volatiles to be removed from the vacuum bag during cure and to absorb any residual resin.
Vacuum bagging film	A nylon vacuum bagging material (VACTiteG6) was used to seal the prep-preg during cure. The film was temperature rated up to 180 °C.
Vacuum sealant tape	Vacuum sealant tape (VAC-seal) was used to secure the vacuum bagging film around the prepreg stack.
Flash tape	A layer of polyester flash tape (FT25BS) was used around the edge of the vacuum bag (attached to tool plate). This helped to reduce the likelihood of a vacuum bag failing at the sealant tape/tool plate interface.